MECHANICAL CHARACTERIZATION OF BORON-BASED ONE-DIMENSIONAL NANOSTRUCTURES BY VARIOUS TECHNIQUES

by

Youfei Jiang

A dissertation submitted to the faculty of
The University of North Carolina at Charlotte
in partial fulfillment of the requirements
for the degree of Doctor of Philosophy in
Nanoscale Science

Charlotte

2015

Approved by:

_____
Dr. Terry T. Xu

_____
Dr. Jordan Poler

_____
Dr. Howie Fang

_____
Dr. Stuart Smith

_____
Dr. Aixi Zhou

ABSTRACT

YOUFEI JIANG. Mechanical characterization of boron-based one-dimensional
nanostructures by various techniques.
(Under the direction of DR. TERRY T. XU)

One-dimensional (1D) nanostructures, such as nanotubes, nanowires and
nanobelts, have attracted considerable interests in the last two decades because of their
exceptional physical, chemical, and electrical properties. Engineering applications of
these nanostructures such as in nanocomposites and nanoelectronics require accurate
characterization and complete understanding of their mechanical properties. In this
dissertation, the mechanical properties of boron-based 1D nanostructures, a promising
class of high temperature thermoelectric nanomaterials, are investigated. The work
includes three parts: (1) nanoindentation of α-tetragonal boron nanoribbons and
nanoplatelets, (2) implementation of a nanomanipulator system for *in situ* mechanical
testing of 1D nanostructures within a scanning electron microscope, and (3) study of
mechanical properties of boron carbide (B_4C-type) nanowires both experimentally and
numerically. All experimental mechanical tests were on individual nanostructures. This
dissertation work resulted in a nanomanipulator with better performance, as well as
provided more reliable data related to the fundamental properties which currently are
quite scarce for boron-based 1D nanostructures.

Nanoindentation was employed to characterize mechanical properties of α-
tetragonal boron nanostructures such as nanoribbons and nanoplatelets. Optimal
experimental conditions for indentations at shallow depths were systematically
investigated. Following this mechanical characterization on α-tetragonal boron platelets
using nanoindentation was performed. The results demonstrate that the substrate used to
support the nanostructure plays a critical role in determination of the measured

properties. To rule out the substrate effect, a new simple approach was proposed to extract the intrinsic properties of boron nanoplatelets. The derived Young's modulus of α-tetragonal boron nanostructures is 69 ± 4 GPa, which is comparable to that reported for α-rhombohedral boron nanobelts.

To realize *in situ* mechanical characterization of 1D nanostructures within a scanning electron microscope, a nanomanipulator system was designed and implemented. The system is desired to test 1D nanostructures whose cross sections are circular and their mechanical properties are not suitable to be studied by nanoindentation. The system consists of three linear motion and two rotation stages. It has positioning resolutions in XYZ directions at 20-30 nm, and has around 0.04° resolution in rotation. The system is capable of performing resonance vibration, tensile and buckling tests on individual 1D nanostructures. Compared to other home-built nanomanipulator systems reported, the current one has the following improvements. Frist, each individual nanowire can now be tested by two different techniques so that direct comparison of experimental data can be made. Second, the force measurement resolution is improved as compared to others' work. Third, the accuracy of determination of the length of a tested nanowire is increased with the help of the additional rotational stage. These improvements facilitate more accurate mechanical characterization of 1D nanostructures.

Mechanical properties of boron carbide nanowires were studied both experimentally and numerically. The experimental work, with a focus on resonance vibrational testing, was conducted on individual boron carbide nanowires using the home-built nanomanipulator system. Mechanical properties such as Young's modulus and fracture strength, were obtained. The numerical finite element modeling (FEM) work was done by the commercial software ABAQUS. Various factors (*e.g.*, the non-

uniformity of a nanowire, the amorphous carbon coating resulted from the electron beam induced deposition (EBID) process, *etc*.) which could affect the accuracy of measured properties were studied. There are two significant contributions of this part of the dissertation work. (1) For each measured nanowire, its mechanical properties were correlated to its microstructure (*e.g.*, diameter, orientation of planar defects, the preferred growth direction of a nanowire, *etc*.), so that more accurate values of mechanical properties of boron carbide nanowires have been obtained. (2) The effect of amorphous carbon coating formed during EBID was systematically studied for the first time.   Results showed that the orientation of planar defects played an important role in determining the Young's modulus of boron carbide nanowires. The Young's modulus of a nanowire whose planar defects are perpendicular to its preferred growth direction (*i.e.*, a transverse-faulted TF nanowire) could be up to 67% higher than that of a nanowire whose planar defects are parallel to its preferred growth direction (*i.e.*, an axial-faulted AF nanowire). Although the TF nanowires are as stiff as bulk boron carbide (E_{bulk} = 432-480 GPa), they exhibit excellent flexibility which is unusual for brittle ceramic material. Results also indicated that the amorphous carbon coating had profound effects to the measured results. For example, depending on the aspect ratio of a nanowire, the addition of amorphous carbon coating could result in up to 153% overestimation of the Young's modulus. This study provided a guideline for further study on amorphous coatings on nanowires, and also offered an alternative explanation of large variations in results from *in situ* scanning electron microscopy-based tests widely observed in the field.

ACKNOWLEDGEMENTS

It is a pleasure to thank many people who made this dissertation possible.

First, I would like to express my sincere gratitude to my advisor Professor Terry Xu for the continuous support of my study and research. Prof. Xu shows her kindness by always respecting my decisions, and her patience and enthusiasm when we had discussions. She encouraged and sponsored me to attend many professional activities to develop myself. She is an excellent mentor to me not only in study, but also in life.

Besides my advisor, I also like to thank Prof. Stuart Smith, who inspired me with his hard-working and modesty spirits. He is so knowledgeable that provides many critical suggestions and discussions to me. I am also very grateful to the rest of my committee members: to Prof. Howie Fang for his many meaningful guides in the simulation works, to Prof. Jordan Poler for his encouragement and insightful comments, and to Prof. Aixi Zhou.

I would like to thank Prof. Haitao Zhang for his continuous helpful discussions in my research, Prof. Weiqiang Ding at Clarkson University for sharing his experiences about experiments and data analysis, and Prof. Xiaodong Li at University of South Carolina for providing an opportunity of visiting to his lab, and Prof. Deyu Li at Vanderbilt University for many helps during the collaboration.

In addition, I want to thank to many people at UNCC, three former group members Dr. Xiaoxia Wu, Dr. Zhe Guan and Dr. Baobao Cao, my current group members Zhiguang Cui and Siang Yee Chang, and my best friends Dr. Weihua Yin and Jianghua Shen, Jason Marmon, Zhiqiang Ma and Yong Sun, and my lovely girlfriend Xiaoyu Chen, for helping me get through the difficult times, and for all the emotional support and entertainment they provided.

Lastly, and most importantly, I want to thank my parents – Xiaoxin Jiang and Jinzi Li, and my dear old sister – Hongyan Jiang. They raised me, supported me, and taught me, and loved me. To them I dedicate this dissertation.

TABLE OF CONTENTS

LIST OF FIGURES

LIST OF TABLES

CHAPTER 1:   INTRODUCTION

1.1   Motivation

Nanotechnology has rapidly developed over last few decades, which is due to the advancing capabilities of instrumentation, and the emergence of new nanostructures. One definition of nanostructures is having at least one functional dimension less than 100 nm. In 1991, Iijima discovered carbon nanotubes (CNTs), which sparked an entirely new paradigm in the development of nanoscience and nanotechnology [1]. After this, many new one-dimensional (1D) nanostructures, such as nanowires (NWs), nanobelts (NBs), nanorods (NRs), nanotubes (NTs), were successfully synthesized in laboratories [2]. Over the past two decades, these 1D nanostructures have received intensive interest because of their many extraordinary properties compared with their respective bulk counterparts [2]. A couple of examples are discussed below. (i) The electronic properties of 1D nanostructures were revealed to be very interesting [3]. For NWs, they exhibited similar transport properties to their bulk materials when their diameters were larger than the carrier mean free path. However, the electron transport properties became diameter-dependent at very small diameters [2]. Many studies indicated that metal NWs might become semiconducting as their diameters were reduced below certain values, which was proposed as a result of quantum confinement [4]. In addition, NTs and NWs with sharp tips were reported to have enhanced field electron emission properties [5, 6]. Hence, the exceptional electronic properties of 1D nanostructures make them promising as building blocks in electronic and optoelectronic nanodevices [7]. Taking advantage of that the electrical properties of 1D nanostructures are extremely sensitive to species

absorbed on surfaces, resulted from their extremely high surface-to-volume ratios, these 1D nanostructures could also be developed into biological and chemical nanosensors for medicine and the life sciences [8, 9]. (ii) In terms of thermal properties, it was found that thermal conductivities of 1D nanostructures are lower than those of bulk materials, and reduced with decreasing the diameters of NWs [10]. 1D nanostructures, possessing both lower thermal conductivity and higher electrical conductivity, had potential applications for thermoelectric energy conversion. (iii) Originated from quantum confinement effects, some unique optical properties have also been discovered for nanostructures. For instance, interesting highly polarized photoluminescence [11], lasing properties [12, 13], and photoconducting properties [14] were observed in many semiconductor NWs, which suggested that they were good candidates for many applications in nanoscale photonics, such as photodetectors, optical switches, nanolasers, LEDs, waveguides and nonlinear optical converters [15]. Studies on photovoltaic (PV) properties of single NWs were carried out to give promises of NWs as single nanoscale PV solar cells. The PV performance of NWs solar cells could be enhanced by controlling key nanomaterial parameters, including chemical/dopant composition, diode junction structure, size, and morphology [16].

Besides aforementioned properties of 1D nanostructures, mechanical properties have been intensively investigated as well. Many unusual mechanical properties of 1D nanostructures have been discovered. For example, extremely high Young's moduli and strengths were found in single-walled CNTs [17, 18] and multi-walled CNTs [19]. Ultra-high strengths were also found in many other 1D nanomaterials, such as SiC NRs [20], Au and Ag NWs [21, 22]. Some covalence-bonded NWs exhibited superplasticity at low temperatures [23-25]. In addition, size dependency of mechanical properties of 1D nanostructures has been widely observed [26-28]. These exceptional mechanical

properties in 1D nanostructures have been proposed to be caused by the size confinement (as a result of a small amount of defects) and high surface-to-volume ratios. A large number of theoretical works also proposed that the surface effects (i.e., surface elasticity and residual surface tension), owing to the increasing ratio of surface area to volume in nanostructures, played an important role in the physical properties of nanomaterials and could explain their size dependency [29-31]. Nevertheless, the excellent mechanical properties of 1D nanostructures make them viable candidates for many applications, such as in nanocomposites , nanoscale actuators, and force sensors [32, 33]. From an application's point of view (e.g., a reliable design of nanoscale devices) for 1D nanostructures, it is essential to understand mechanical responses of them. For example, the mechanical properties of piezoelectric nanostructures are required to know prior to their applications in devices, such as strain sensors [34], and nanogenerators [35], so that the deformation limits can be outlined to avoid the malfunctions of devices. It is also known that the stabilities of nanostructures are extremely sensitive to environmental changes, such as temperature fluctuation, residual stress variation, and external loadings. Therefore, there is no doubt that the mechanical properties of 1D nanostructures need to be understood primarily for fundamental science studies and applied research applications, which motivates this dissertation work.

The difficulties of characterizing nanostructures include, but are not limited to, preparation of test specimen, controllable loading, and accurate measurement of load and displacement. In addition, precise determination of geometrical information of 1D nanostructures are essential to evaluate accurate their mechanical properties. Therefore, nanomechanical characterization tools are required to equip with high resolution microscopy tools, including atomic force microscopy (AFM), scanning electron microscopy (SEM), and transmission electron microscopy (TEM).

In this chapter, the current available techniques for experimental characterization of 1D nanostructures are first reviewed and compared. Following this, the current research status of the boron-based 1D nanostructures, a promising class of high temperature thermoelectric nanomaterials, are reviewed.

1.2   Nano-mechanical Characterization Techniques

To realize mechanical characterizations of 1D nanostructures with low uncertainties, both the development of novel experimental methods and improvement to the existing techniques are required. So far, the state-of-the-art experimental techniques to characterize mechanical properties of nanostructures are included but not limited to nano-tensile test [36], nano-bending test [37], nanoindentation [38], and resonance vibration test [39]. Because specimens can be prepared for testing by simply depositing the nanostructures on a hard and flat substrate [40], nanoindentation is the first choice among these testing techniques. Compared with nanoindentation, other techniques require a precise manipulation system. For the manipulation system functioning at the nanometer scale, an accurate and sensitive force transducer and actuators with high resolution are necessary. Usually, most of the manipulation systems are operated in electron microscopes instead of under optical microscopes, due to the higher magnification can be achieved in the range of hundreds of nanometers to a few nanometers. This limits the testing environment to vacuum conditions. Although AFM is capable of imaging nano-objects, it is not in real-time which makes the manipulation of nano-objects difficult to operate. To better understand these testing techniques, they are reviewed in details in sections 1.2.1 to 1.2.3.

1.2.1   Nanoindentation Technique

Nanoindentation, also called instrumented indentation technique, was introduced in 1992 for measuring hardness and Young's modulus of monolithic material by analysis

of load versus depth curves [41]. Because it directly determines the mechanical

properties of materials without the need to image and measure the hardness impression,

this method has been widely adopted and improved after it was introduced. Generally,

the instrumented indentation technique is performed by using a force actuator to apply

a known force to an indenter in order to drive the indenter into the sample. The applied

load and the displacement of the indenter into the sample are recorded by the electronics,

as shown in FIGURE 1.1. Through analyzing this load and displacement data package,

the hardness and elastic modulus of the tested materials can be derived [42].
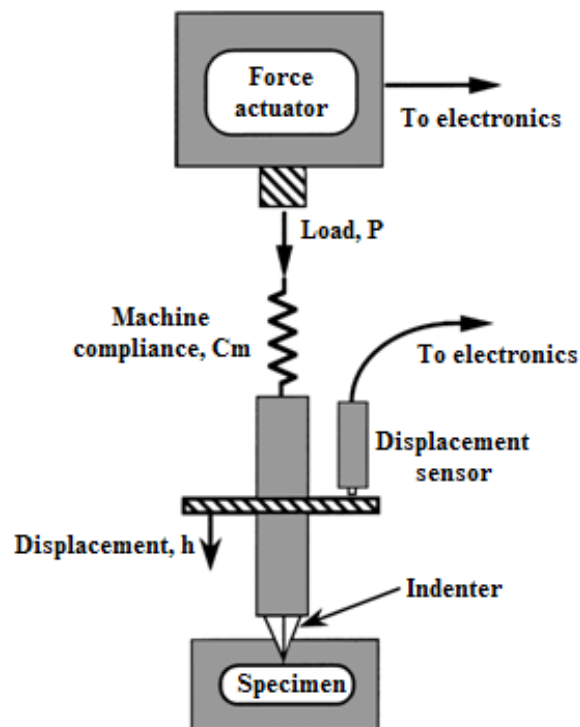
FIGURE 1.1: Schematic representation of the nanoindentation technique [42].

A typical curve of load versus displacement is presented in FIGURE 1.2, where

the symbol S is the contact stiffness, and defined as the slope of the upper portion of the

unloading curve during the initial stage of the unloading. The variables, P and P_{max} are

the applied load and the maximum applied load respectively. Similarly, h and h_{max} are

the displacement and the maximum displacement of the indenter into the sample respectively.
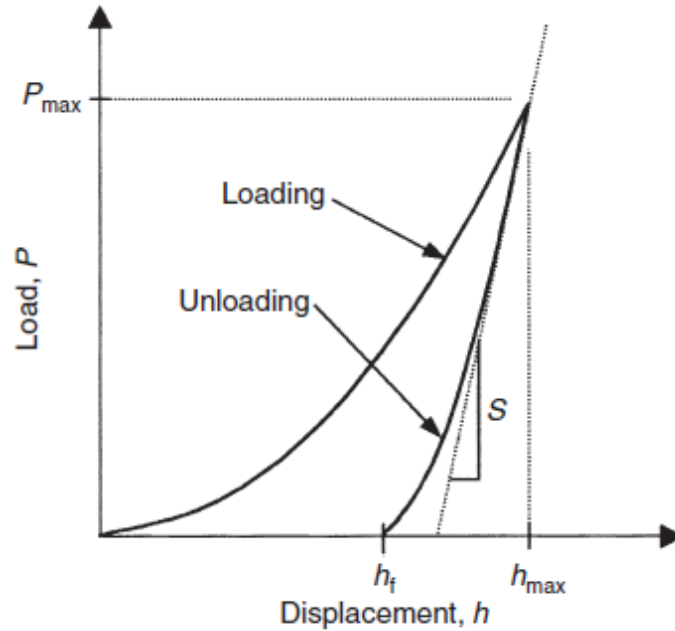
FIGURE 1.2: Schematic graph of load-displacement curve for one complete cycle of loading and unloading [41].

For many materials, the unloading curves are usually well approximated by the power law relation (1):

$$P = \alpha(h - h_f)^m \tag{1}$$

where, α and m are empirically determined fitting parameters, and h_f is the final displacement after complete unloading, also determined from the curve fit [41]. Based on the above model, the contact stiffness can be calculated by equation (2).

$$S = \left.\frac{dP}{dh}\right|_{h_{max}} = \alpha m(h_{max} - h_f)^{m-1} \tag{2}$$

The basic assumption of the method is that the contact periphery sinks in, schematically shown in the FIGURE 1.3, which is referred to as the "Oliver-Pharr

model". The specimen surface sinks in when the indenter penetrates into the surface. Then the relationship between the contact depth h_c and the maximum depth h_{max} can be represented by equation (3),

$$h_c = h_{max} - h_s = h_{max} - \varepsilon \frac{P_{max}}{S}$$ (3)

where, h_s is the elastic displacement of the surface at the edge of the contact, and ε is the geometric factor for the indenter. The amount of surface that sinks in relates to (i) the maximum load, (ii) the contact stiffness, and (iii) the geometry of the indenter.
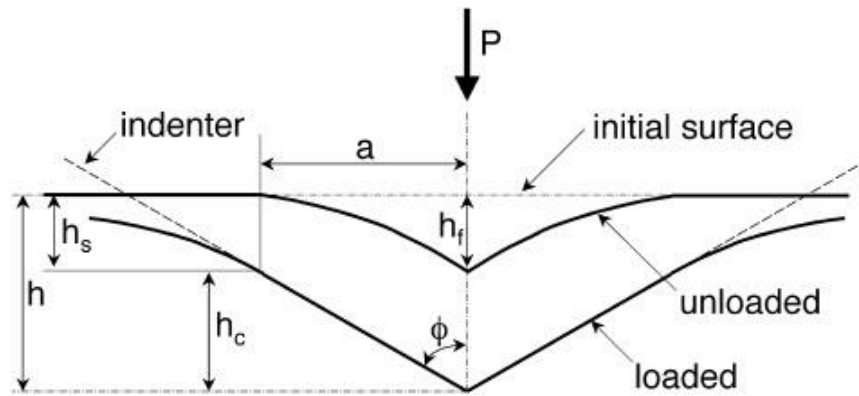
FIGURE 1.3: Schematic illustration of surface periphery under load and after unload [41]. Each label is defined in the texts.

The surface contact area function $A(h_c)$ describes the cross sectional area of the indenter at a distance from its tip. It can be calibrated by analyzing the results of a batch of tests on a standard sample, like refused silica. Once the contact area is calculated, the hardness and the reduced modulus can be computed by equation (4) and equation (5), respectively [41].

$$H = \frac{P_{max}}{A}$$ (4)

$$E_r = \frac{\sqrt{\pi} \cdot S}{2\beta\sqrt{A}}$$ (5)

where β is a constant depending on the geometry of the indenter, which is equal to 1.304

for Berkovich indenter, and E_r is the reduced elastic modulus, defined by equation (6)

[41].

$$\frac{1}{E_r} = \frac{1-v^2}{E} + \frac{1-v_i^2}{E_i} \tag{6}$$

The reduced elastic modulus takes into account the fact that elastic

displacements occur in both the specimen and the indenter [41]. The Berkovich indenter

is made of diamond with the known Young's modulus and Poisson's ratio. Although the

Poisson's ratio of the sample is required to calculate the Young's modulus, the

sensitivity is weak. It was proved that a generous uncertainty of 40% in the Poisson's

ratio results in only a 5% uncertainty in the Young's modulus [43]. Therefore, based

upon the above equations, both the Young's modulus and the hardness of a specimen

can be determined if the load and displacement data set is obtained.

The continuous stiffness measurement (CSM) is a new technique that was

recently incorporated with nanoindentation, and provides significant improvements.

Instead of measuring the static contact stiffness at maximum load in the unloading

portion, it directly measures the dynamic contact stiffness during the whole loading

portion of an indentation test. The advantages of CSM are that this technique is

insensitive to thermal drift, and provides a more accurate determination of mechanical

properties for small volume deformation [44].

The basic concept of CSM is to impose a small and sinusoidal oscillating signal

to the primary load signal which is driving the motion of the indenter, FIGURE 1.4. By

using a frequency specific amplifier, the displacement response of the indenter at the

excitation frequency and the phase angle between these two signals are measured

continuously in the loading portion [44].
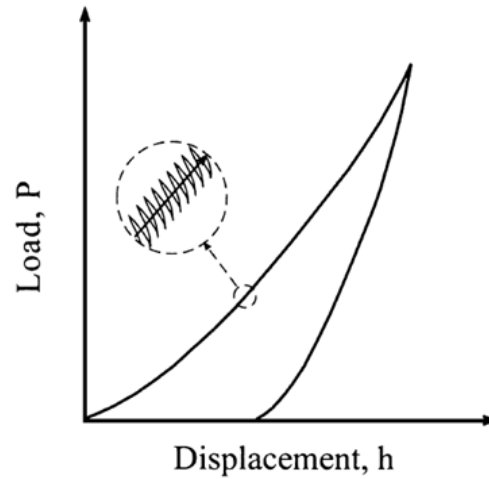
FIGURE 1.4: Scheme of loading and unloading curve with CSM [44]. The zoom-in of dashed circle line represents the imposed small and sinusoidal oscillating singal.

Then the dynamic contact stiffness, S, which is a function of penetration depth, can be calculated by equation (7),

$$S = \left| \frac{1}{\dfrac{F_0}{Z_0}\cos\phi - (K_s - m\omega^2)} - \frac{1}{K_f} \right|^{-1} \tag{7}$$

where F_0 is the force excitation amplitude, Z_0 is the magnitude of the resulting displacement oscillation, ϕ is the phase angle between the force and displacement signals, ω is the excitation frequency. These parameters are measured during the indentation test, and are altered with increasing the indentation depth. While, K_s is the stiffness of the support springs in the machine, m is the mass of indenter column, and K_f is the load frame stiffness. They are the fixed values obtained from the initial system calibrations. Therefore, the contact stiffness is represented as a function of the indentation depth. According to the above definitions, the CSM technique is capable of continuously measuring mechanical properties of materials as a function of the indentation depth.

The nanoindentation technique was widely employed to determine the mechanical properties of thin films [44]. Several studies present the nanoindentation experiments as methods to measure the mechanical properties of 1D nanostrucutures, including NBs [45-47], and NWs [38, 48]. The advantages of nanoindentation for mechanical characterization of 1D nanostructures were a relatively simple sample preparation, and excellent force and displacement resolutions. However, the configuration of indentation on a nanostructure differs from that on a half-space, so the standard Oliver-Pharr method of analysis was not applicable [49]. Moreover, the compliance between the nanostructure and the substrate results in the underlying substrate affecting the measurement results significantly [50]. Therefore, to achieve reliable mechanical properties of nanostructures by nanoindentation, additional numerical modeling may be needed to correct the experimental results.

1.2.2 AFM Based Testing Techniques

AFM is a type of scanning probe microscopy, with high resolution on the order of a nanometer. By integrating force mode and imaging modes, AFM had been widely applied to study mechanical properties of 1D nanostructures [51]. Generally, AFM can be operated in two different modes to mechanically test of 1D nanostructures, including lateral force mode, and contact mode.

In the lateral force mode, there are two different testing configurations according to different specimen preparations. In the first configuration, nanostructures were dispersed randomly on a substrate, and some of them were pinned with one end by microfabrication (FIGURE 1.5A). Then the cantilevered nanostructures were laterally bent at the free end by AFM tip (FIGURE 1.5B). The data of measured lateral force and deflection were analyzed to obtain their mechanical properties, such as the elastic modulus, strength and toughness [20]. It was relatively simple to perform this test, but

effects from adhesion and friction between nanostructures and substrate were inevitable and not negligible. Therefore, a second testing configuration has been used more extensively [52]. In this configuration, nanostructures were suspended over a trench, with two ends fixed on the substrate by electron beam induced deposition (EBID). Then the AFM tip is used to apply force to bend the double-clamped nanostructure laterally (FIGURE 1.5C). The measured force versus deflection (*F-d*) curves, see an example in FIGURE 1.5D, were analyzed to determine the mechanical properties of nanostructures [52]. For example, for a nanowire with radius *r* and suspended length *L*, the Young's modulus *E* can be calculated by equation (8),

$$E = FL^3 / 192dI \tag{8}$$

where the second moment of area of the nanowire *I* is determined by $I = (\pi r^4)/4$.
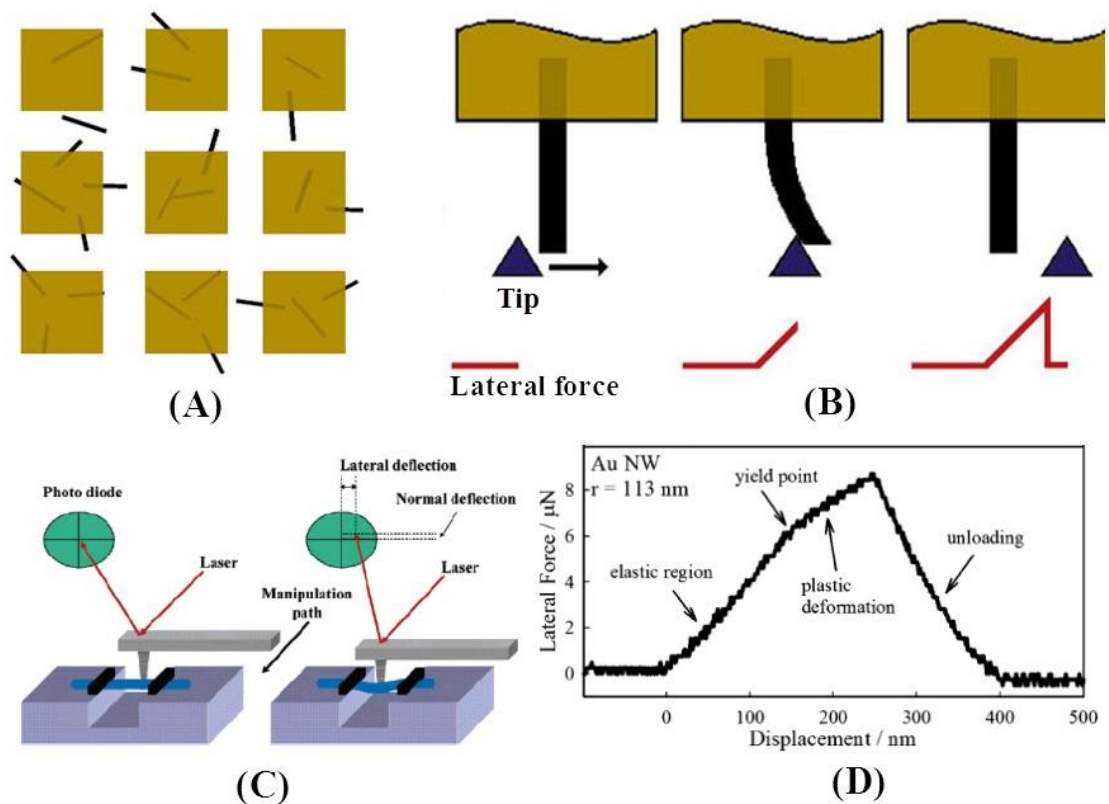
FIGURE 1.5: (A) nanostructures were ultrasonically dispersed on substrate, and then pinned by deposition of a grid of square pads [20]. (B) Schematic of beam bending by an AFM tip with lateral force [20]. (C) Schematic drawings of lateral bending of

double-clamped nanostructures by AFM [52]. (D) A typical *F-d* curves obtained by lateral bending on a gold nanowire [52].

In the contact mode, four different testing configurations were used to characterize mechanical properties of 1D nanostructures. The first testing configuration was normal three-point bending (Figure 1.6A) [53]. A nanostructure was suspended over on a trench with two ends clamped on the substrate. Then an AFM tip was used to apply a normal force on the midpoint of the suspended part of the nanostructure. The applied normal force and corresponding vertical deflection of the suspended nanostructures were measured to determine their mechanical properties. The second one is so called AFM assisted nanoindentation (FIGURE 1.6B) [54]. The principle of this testing system is similar to that of a commercial nanoindenter. AFM is used directly to make indents on nanostructures after precisely locating their positions. Commercially available AFM cantilevers with sharp and hard tips and well-calibrated force constants were used as force sensors. Then mechanical properties of nanostructures could be estimated by analyzing the load and displacement into nanostructures, as described in section 1.2.1. But the normal nanoindentation by a commercial nanoindenter is better than the AFM assisted nanoindentation, because it has a higher load and displacement resolutions than AFM. It is also worthy to note that the AFM assisted nanoindentation is different with the three-point bending test, because nanostructures for this technique are laid on a flat substrate, whereas they are suspended across a trenched substrate for three-point bending test. Characterizing mechanical properties of vertically aligned nanostructures was the third configuration (FIGURE 1.6C) [55]. In this configuration, nanostructures were grown vertically on the substrate without any manipulations before tests. AFM was operated in contact mode during the scanning while a constant normal force was kept between the tip and sample surface. When the tip contacted the nanostructure, the

cantilever was twisted to maintain a constant normal force which resulted in existence of lateral force. By measuring the maximum lateral deflection (δ) and corresponding lateral force (F), the elastic modulus was determined by $E = FL^3/3\delta I$, where I was the second moment of area of nanostructures. The last configuration was contact resonance atomic force microscopy (CR-AFM) (FIGURE 1.6D), which is capable of determining radial indentation elastic moduli of NWs [56]. A NW was laid on a substrate, then an AFM tip was moved to contacting with the NW. The resonant frequency of the AFM cantilever was changed before and after contact with the NW. The amount of frequency shift was related to the mechanical property of the NW. Therefore, the mechanical properties of NWs were determined by measuring the shift of resonant frequency of the AFM cantilever before and after contacting with them.
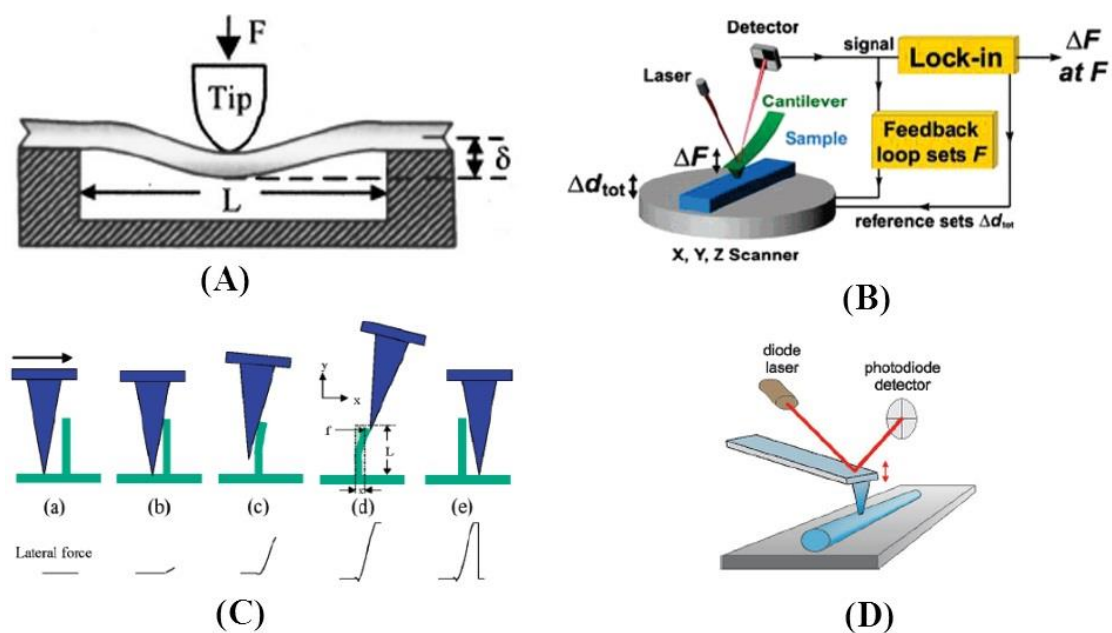
FIGURE 1.6: Schematic of AFM based techniques in contact mode. (A) Normal three-point bending on a suspended nanostructure [53]. (B) AFM assisted nanoindentation on a nanostructure on a substrate [54]. (C) Procedures of bending a vertically aligned nanostructure [55]. (D) CR-AFM experiments on a nanostructure to measure its radial indentation modulus [56].

AFM based techniques have high capability of precise measurement of force and deflection, but some limitations restrict its applications for mechanical characterization of 1D nanostructures. For example, a sharp tip using in three-point bending tests may cause indentation or damage nanostructures as well. For techniques in lateral force mode, it is difficult to calibrate the lateral spring constant of the AFM cantilever. In addition, AFM is incapable of structural characterizing and imaging during the test. Therefore, alternative testing techniques are developed inside electron microscopies with the same idea that AFM cantilever is employed as a force sensor while imaging using the electron beam.

1.2.3 *In Situ* SEM-Based Testing Techniques

Electron microscopies, including SEM and TEM, are capable for imaging nanostructures with high magnifications and in real time observation modes, and obtaining the compositional information of a specimen surface. With additional testing instruments, various mechanical tests, such as resonance vibration, tensile, bending and buckling tests, can be performed inside SEM or TEM. Compared with SEM, TEM has a relatively higher imaging resolution, so it is capable of imaging nanostructures at atomic resolution, and observing defect nucleation and propagation in real time during the mechanical testing. However, SEM is more compatible with *in situ* testing instruments because it has a larger space to house additional apparatus. For TEM, a delicate testing apparatus only a few millimeters in size or microelectromechanical systems (MEMS) must be designed to fit in a specimen holder, which is more expensive than developing a testing device to incorporate into a SEM [57]. In addition, SEM is more flexible to prepare sample and perform tests for *in situ* tests. Therefore, *in situ* SEM tests, employed to characterize mechanical properties of as-synthesized 1D

nanostructures in our lab, are reviewed here. However, it is worth noting that the principles of in situ testing techniques are applicable to SEM or TEM.

1.2.3.1 Tensile Test

Tensile testing, or tension testing, is one of most commonly used mechanical stress-strain tests in which a sample is in uniaxial tension until failure. Usually, a gradually increasing uniaxial tensile load is applied to a specimen along the long axis to elongate the specimen. The test specimen is permanently deformed and eventually fractured, FIGURE 1.7A. In the tensile testing device, the applied load and the resulting elongations are measured simultaneously. Then the engineering stress and engineering strain are determined by analyzing the recorded applied load and elongation.
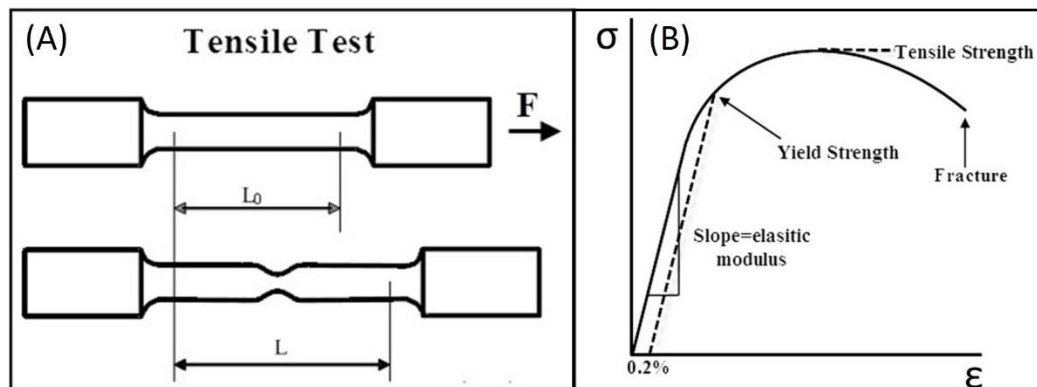
FIGURE 1.7: (A) Schemes of tensile test; and (B) typical tensile stress-strain curve.

According to the fundamental mechanics of materials, the engineering stress σ and engineering strain ε are calculated by equations (9) and (10),

$$\sigma = \frac{F}{A_0} \tag{9}$$

$$\varepsilon = \frac{L - L_0}{L_0} = \frac{\Delta L}{L_0} \tag{10}$$

where F is the applied load perpendicular to the cross section of the specimen, A_0 is the original cross-section area of the specimen before any load is applied, L_0 is the original length before any load is applied, L is the instantaneous length, and ΔL is the elongation in the length.

Eventually, based on the stress-strain curve (FIGURE 1.7B) that is plotted from the calculation of above equations, the tensile properties of nanostructure such as elastic modulus, yield strength, tensile strength, and the maximum strain can be achieved.

In situ tensile testing was initially introduced to characterize nanostructures by Yu in 1999 using a home-built nanomanipulator inside an SEM [58]. This manipulation device inside the SEM was designed to manipulate and characterize carbon nanotubes (CNTs) and is shown in FIGURE 1.8.

FIGURE 1.8: Schematics of the nanomanipulator inside SEM [58].

In Yu's work, there are two stages on the SEM platform, including X-Y stage and Z-θ stage. The motions of the stages are driven by picomotor actuators. The AFM tips or STM probes and the sample holder are mounted on the top of the stages. The

tensile test of CNT was realized by precisely moving the stage to control the movement of AFM tip, FIGURE 1.9. Two different AFM tips (*i.e.*, stiff and soft) were mounted on two separated stages. Both two ends of A CNT was clamped on the soft and stiff cantilevers. The SEM images (FIGURE 1.9b-e) showed that the deflection of the soft cantilever increased as the stiff cantilever was moved upward until the CNT was broken, FIGURE 1.9f. The elongation of the CNT was measured by capturing the instantaneous SEM images. The applied load to the CNT was determined by the deflection of the soft cantilever, multiplied by the spring constant of the cantilever. When the applied load and elongation of CNT were obtained, the tensile properties of the CNT were determined using the equations (9) and (10).
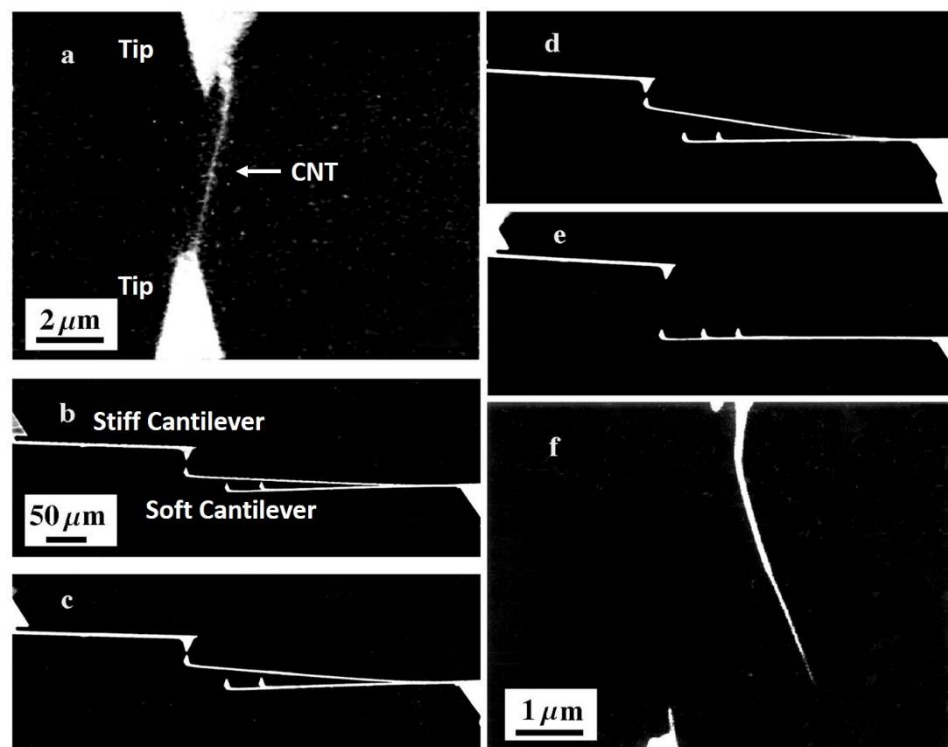
FIGURE 1.9: SEM images represent a complete process of tensile test [58]. (a) a CNT was attached on two AFM tips; (b-d) the deflection of soft cantilever increased when the stiff cantilever was moved upward; (e) the soft cantilever recovered after the CNT was fractured; (f) zoom-in image of the CNT after failure.

The development of a nanomanipulator inside SEM is capable of characterizing many nanostructures with round cross sections, such as NTs, NRs, and NWs. Besides the tensile test, a SEM-based nanomanipulator is capable of performing other testing techniques: resonance vibration, buckling, and bending tests.

1.2.3.2 Resonance Vibration Test

Different from the tensile test, which is a static mechanical test, resonance vibration test is a dynamic test. Nanostructures were resonantly excited at the fundamental frequency and higher harmonics inside SEM for determining their elastic moduli. For example FIGURE 1.10 shows a boron NW, which was attached to an AFM tip, was excited at the first two harmonic resonance modes [59].
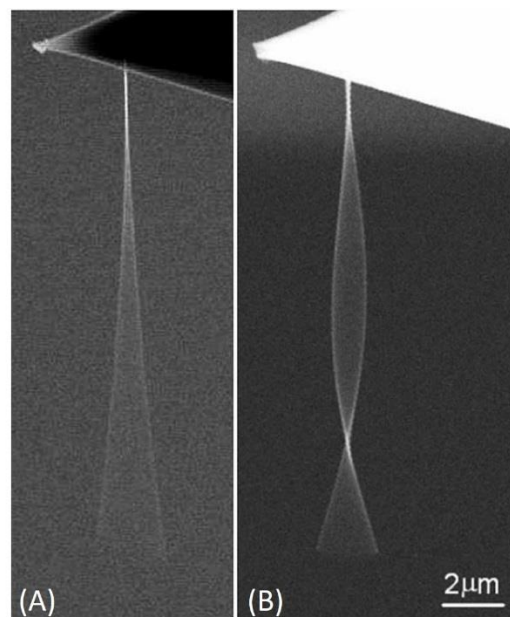
FIGURE 1.10: SEM images of a boron NW at (A) fundamental mode of resonant vibration; (B) second mode of resonant vibration [59].

It is known that the resonances of nanostructures can be reached by mechanical or electrical excitations *in situ* SEM [60]. For instance, a NW was first attached to a conductive AFM or metallic tips. The electrical field excitation of NW was achieved by applying AC voltages between the conductive AFM cantilever and a grounded counter

electrode, FIGURE 1.11A. For mechanical excitation, one AFM cantilever with a NW on the tip was attached to a piezoelectric bimorph actuator. Then the vibration of NW can be driven by applying AC voltages to this piezoelectric actuator, as shown in FIGURE 1.11B. Compared with the mechanical excitation, the electrical excitation was used more often for resonance vibration tests on nanostructures because it was easier to observe the resonances of nanostructures. The details of the electrical excitation is discussed later in the section 3.4.1.
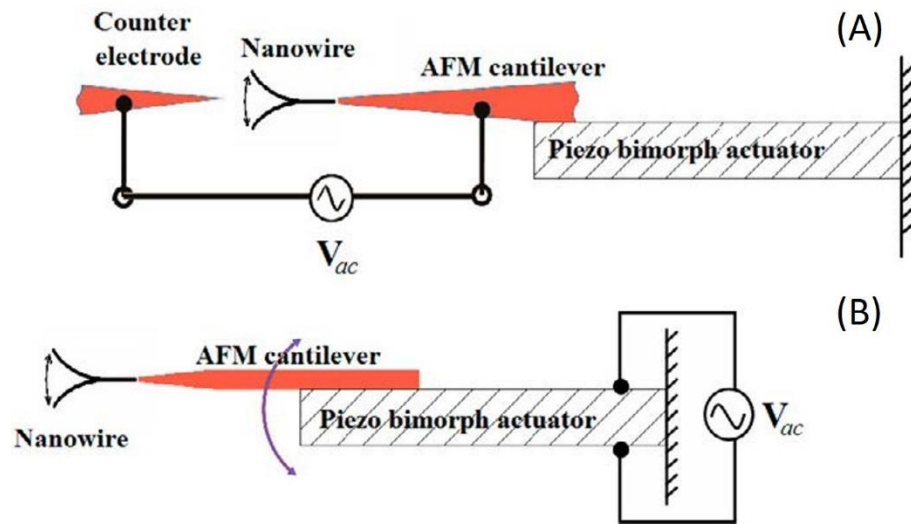
FIGURE 1.11: (A) Electrical and (B) mechanical excitations of a cantilevered boron NW attached on an AFM cantilever [61].

According to simple beam theory, the nth mode resonance frequency f_n for a cantilevered uniform beam is calculated by equation (11) [62],

$$f_n = \frac{\beta_n^2}{2\pi}\sqrt{\frac{E_b I}{mL^4}} \qquad (11)$$

where, E_b is the bending modulus of the beam, I is the second moment of area, m is the unit mass per length, and L is the beam length. The β_n is the eigenvalue of the characteristic equation: $\cos\beta_n \cosh\beta_n + 1 = 0$, which determines $\beta_0 = 1.875$,

β_1=4.694, β_2=7.855 and β_3=1.099.6 correspond to the first four modes of resonance frequency [62].

For a solid and uniformly circular cross-section NW, the Young's modulus E can be determined from [59],

$$E = \frac{64\pi^2 \rho}{\beta_n^4} \frac{L^4}{D^2} f_n^2 \qquad (12)$$

where ρ is the material density and D is the diameter of NW. For *in situ* SEM resonance vibration test of a NW, the density of NW (ρ) is assumed to be the same as that of bulk counterpart. The diameter of NW (D) is measured on captured TEM images before test, which is employed for all *in situ* SEM tests in this work. The effective length of NW (L) during the test is measured on the captured SEM images. The resonant frequencies of NW (f_n) are read directly from an external instrument that provides AC signals.

1.2.3.3 Bending Test

In situ bending test was also introduced to examine nanostrucutures inside SEM [63]. As shown in FIGURE 1.12, a silicon NW was attached to the probe and the AFM cantilever, and then bent by moving the probe upward. The deflection of NW increased with the moving of the probe, as marked with a black "I" in FIGURE 1.12b-f. The applied force was determined by measuring the deflection of the AFM cantilever.
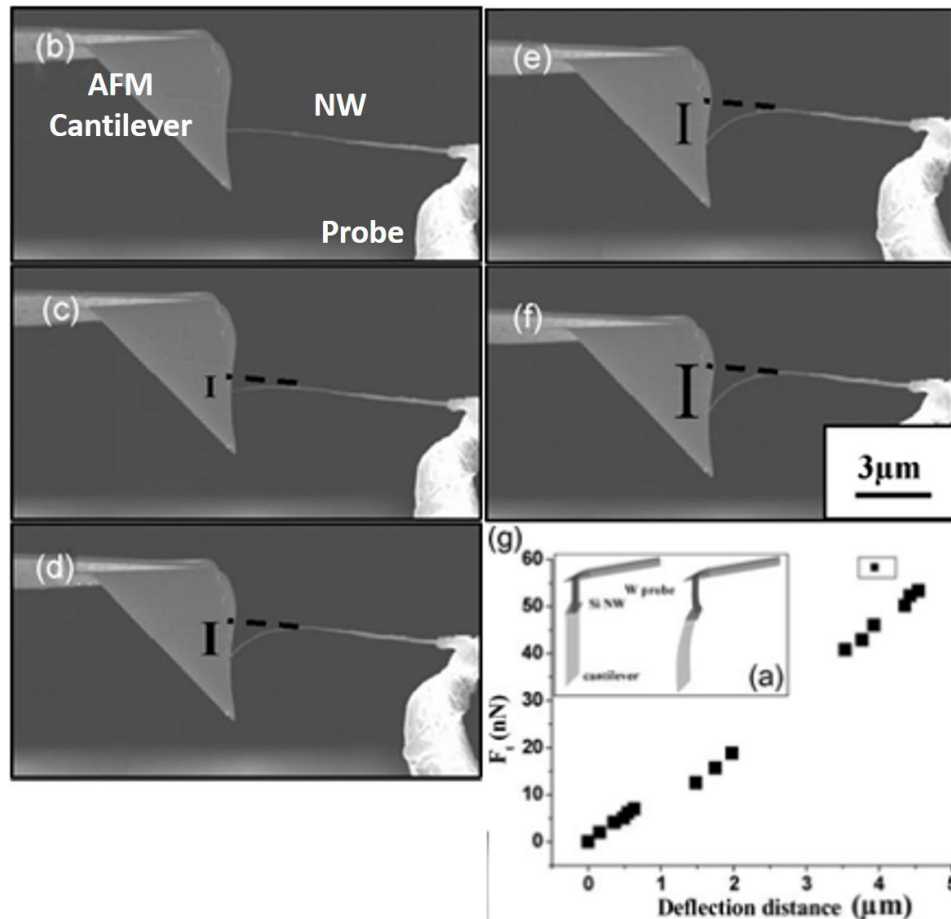
FIGURE 1.12: (a) Schematic diagrams illustrating the bending test; (b-f) SEM images of the bending testing process of NW; (g) the force versus NW deflection curve [63].

For this *in situ* SEM bending test, the NW was clamped at both ends. The disadvantage of this testing configuration was that the NW endured the tension as well during the bending process. Therefore, an *in situ* lateral bending test of a clamped-free NW is more appropriate [64]. A simple illustration of the *in situ* lateral bending test is shown in FIGURE 1.13. A nanostructure with one end clamped on a substrate (or a fixed tip) is laterally bent by a compliant AFM cantilever.
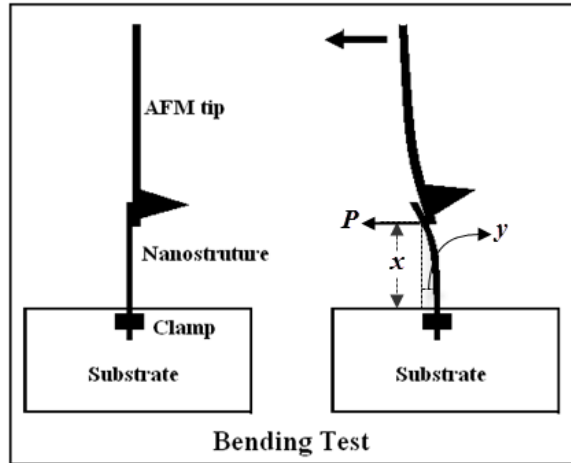
FIGURE 1.13: Simplified representations of bending test on nanostructure.

For the lateral bending test of NW, the elastic modulus E is calculated by equation(13),

$$P = 3EI\frac{y}{x^3} \qquad (13)$$

where, P is the applied load, x the height from the fixed end to the point where the lateral force is applied, y is the lateral displacement perpendicular to nanostructure (FIGURE 1.13), and I is the second moment of area of nanostructure ($I = \pi D^4\big/64$ for nanowire, where D is the radius of nanowire) [20, 55]. The applied load (P) is calculated by multiplying the spring constant of AFM cantilever with its instantaneous deflection measured on captured SEM images. The effective length (x) and the lateral displacement (y) of NW are also measured on SEM images captured at every loading step.

1.2.3.4 Buckling Test

Buckling occurs when compression test is carried out to a slender column. Hence, buckling happens if 1D nanostructures like NWs, NTs and NRs are compressed, which is the reason why it is usually called buckling tests on nanostructures, instead of compression tests.

In situ buckling test was reported to be carried out by a commercial nanomanipulator inside a SEM to achieve the mechanical properties of nanowires [63, 65], as shown in FIGURE 1.14. Similar with *in situ* bending test, there have two testing configurations for *in situ* buckling test: clamp-free and clamp-clamp. FIGURE 1.14A showed that a Si NW was clamped on the rigid probe (top), but free against a soft AFM cantilever (bottom). But two ends of a ZnO NW were both fixed on a rigid probe (right) and a soft AFM cantilever (left), FIGURE 1.14B. The two NWs were both buckled if the rigid probe was moved close to the soft cantilever.

For *in situ* buckling test of a NW, the Young's modulus of nanostructure E is determined, according to the Euler's formula, by the equation (14),

$$E = \frac{P_{cr}L_e^2}{\pi^2 I} \tag{14}$$

where P_{cr} is the critical force for buckling, L_e is the effective length depending on boundary conditions (e.g., $L_e = 2L$ for clamp-free, and $L_e = L/2$ for clamp-clamp, where L is the actual length of NW), and I is the second moment area of NW [63, 65]. The critical buckling force is determined from the curve of force versus the displacement, as shown in the curve on FIGURE 1.14A-g. The length of NW (L) is measured through SEM images.
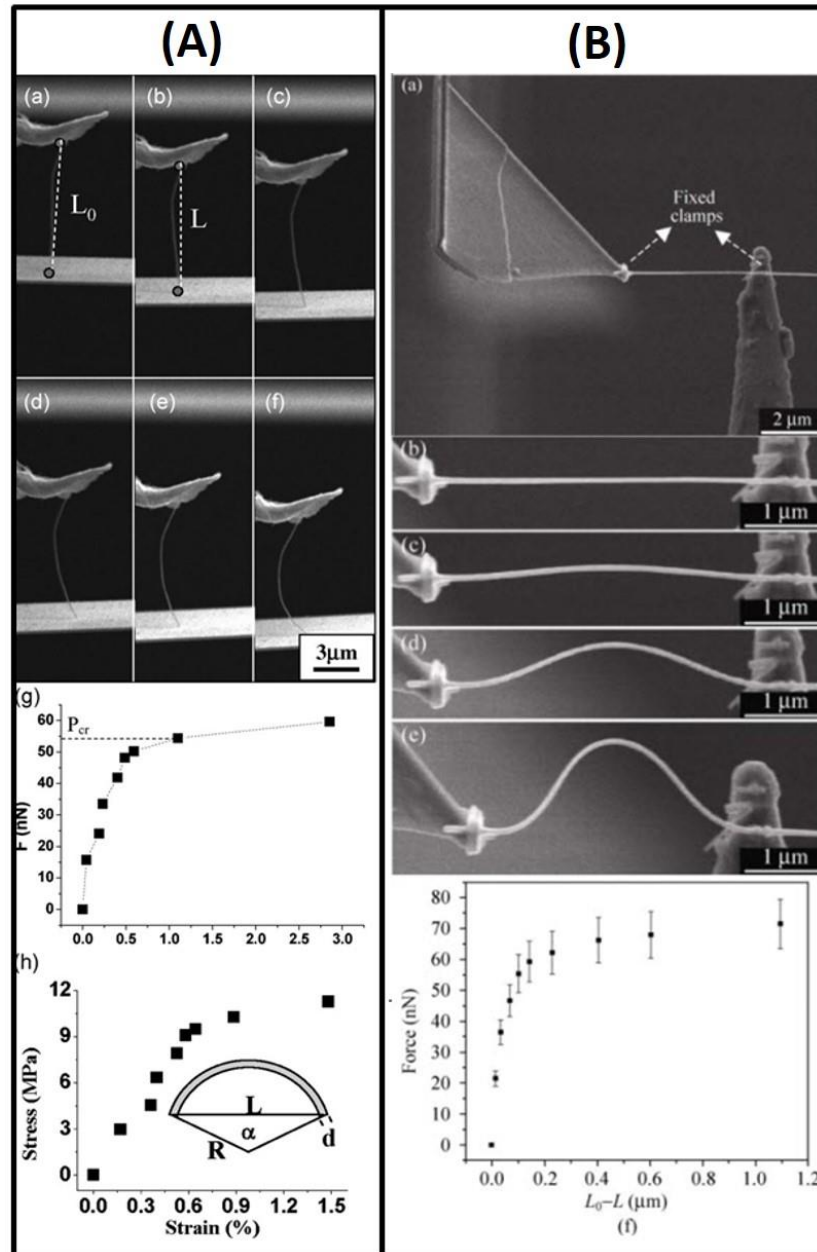
FIGURE 1.14: SEM images and resultant graphs represent the buckling tests on (A) a Si NW [63]; and (B) a ZnO NW [65].

1.2.4   Summary of Nano-Mechanical Characterization Techniques

In summary, significant development has been made in mechanical tests of 1D nanostructures, by specimen preparation and manipulation, precise loading control, and accurate measurement of applied force and nanostructures' deformations. Detailed comparisons of these reviewed techniques, including pros and cons, are shown in

TABLE 1.1. Taking into considerations of current limitations, there are some areas that can be further developed: improving the resolutions of force and deflection measurements; exploring the relations between the mechanical properties and crystalline structures and defects, different loading modes, and size effects; performing dynamic testing on nanostructures. In this dissertation work, a home-made manipulator with improved performance for *in situ* SEM tests is developed to answer following questions:

- Can each individual nanowire be tested by two different techniques so that direct comparison of experimental data can be made?

- Can the measurement accuracy of cantilever deflection be improved so that the force measurement resolution is better than any other published works?

- Can the accuracy of determination of the length of a tested nanowire be increased to minimize the experimental error (e.g., in resonance vibration test, 5% error in length measurement can lead to 20% error in the calculated Young's modulus)?

- Can a rational experimental procedure be developed to realize pre- and post-materials characterization of each individual tested NW, so that the relations between the mechanical properties and microstructures, as well as various effects on experimental results of *in situ* SEM tests, can be explored?

If all above questions can be solved, more accurate mechanical properties of 1D nanostructures are expected to be obtained.

TABLE 1.1: Summary of different nanomechanical characterization techniques.

Instruments	Test methods	Pros	Cons
Nanoindenter	*Nanoindentation*	Simple sample preparation; high force and displacement resolution; measure both Young's modulus and hardness.	Basic assumption for calculation is not applicable; substrate effect; tip bluntness effect; etc.
AFM	*Lateral bend*	Mechanical properties is extracted based on simple beam theory	It's difficulty to calibrate lateral force constant; Torsion may exist during bending.
	Three-point bend	Mechanical properties is extracted based on simple beam theory	Hard to precisely locate at the middle point on nanostructures; indentation may exist during test.
	Nanoindentation	Simple sample preparation; measure both Young's modulus and hardness.	It's difficulty to calibrate the area function of AFM tip; It's impossible to achieve perfect vertical indentations.
	CR-AFM	Contact frequency of AFM cantilever can be measured accurately; nondestructive.	Inaccuracy of analyzing AFM cantilever dynamics and modeling tip-sample contact geometry.
Electron Microscopy	*Resonance vibration test*	Easy to excite nanostructures to resonance; nondestructive.	Inaccurately determine the resonance frequency by visually observing the vibration; only elastic modulus can be obtained.
	Tensile test	It's straightforward to perform the tests; both elastic and plastic behaviors can be studied.	Axial misalignment causes large errors; difficulty to achieve precise measurement of force and deflections, etc.
	Buckling test		
	Bending test		

1.3 Boron-based 1D Nanostructures

The focus of this dissertation work is to measure mechanical properties of boron-based 1D nanostructures by rational techniques. In this section, the reason why we are interested in studying of boron-based 1D nanostructures is discussed. Then a review on

current research status of two types of boron-based 1D nanostructures: α-tetragonal boron nanoplatelets and boron carbide (B_4C-type) nanowires is given.

1.3.1 Why Boron-Based 1D Nanostructures?

Boron is an electron-deficient atom, possessing the nature of the chemical bonds: 1) having ligancy (*i.e.,* coordination number) higher than the numbers of valence electrons and stable orbitals; 2) causing adjacent atoms to increase their ligancy to a value larger than the orbital number [66]. This bonding nature of boron results in that boron-based materials contain many complex elemental clusters, such as B_6 octahedron, B_{12} icosahedron, B_{20} and B_{28} units [67]. Then various crystal structures of boron-based materials are formed by linking these complex boron clusters in different modifications. Their structural complexity but not close-packed feature lead to many interesting properties, including high thermal and chemical stability, low density, and high modulus and hardness [68]. One promising application of boron-based materials is for high temperature TE energy conversion [69]. It is known that the performance of TE materials can be evaluated by the dimensionless quantity *ZT*, where *T* is the absolute temperature, and *Z* is the figure of merit given by $Z = S^2\sigma/k$, when *S* is the Seebeck coefficient, σ is the electrical conductivity, and *k* is the thermal conductivity. With increasing temperature, the Seebeck coefficients and electrical conductivities of boron-based materials are usually enhanced, while their thermal conductivities remain at relatively low values because of their structural complexity [69]. Therefore, large figures of merit of boron-based materials are achieved at high temperature, which shows promise for applications in high temperature TE power generation.

About two decades ago, theoretical studies predicted that nanostructured TE materials could have enhanced ZT, owing to quantum effects related to carrier confinement and pronounced phonon scattering at the surface boundaries [70, 71]. These

theoretical predictions were experimentally confirmed [72-74]. However, it has been found that electronic confinement and subsequent changes in the electronic band structure are not the main sources for the enhancement of ZT. Instead, the significant reduction of the thermal conductivity is found out to be a major contribution to the improved ZT, which is due to the increased phonon-boundary scattering [75]. Thus, by applying the same principle, if the boron-based materials can be synthesized to nanometer scale, the increased surface area, which in turn will result in the increased phonon-boundary scattering and lower thermal conductivities, lead to the expectation that boron-based 1D nanostructures could have enhance TE properties.

Two p-type TE boron-based nanostructures, α-tetragonal boron nanostructures (FIGURE 1.15A,C) and single-crystalline boron carbide (B_4C) NWs (FIGURE 1.15B,D), have been synthesized and studied in our laboratory. It is worth noting that both nanostructures can be produced in one synthesis process. During the process of co-pyrolysis of diborane (B_2H_6) and methane (CH_4) in a low pressure chemical vapor deposition (LPCVD) system at temperatures below 1000 °C, the aforementioned two boron-based 1D nanostructures with different morphologies were synthesized in different temperature zones [76]. The α-tetragonal boron nanostructures were produced in the 630-750 °C temperature zone [77], while B_4C NWs were synthesized in the temperature range of 964-997 °C. The focus of this dissertation work is to measure mechanical properties of these two boron-based 1D nanostructures by suitable techniques.
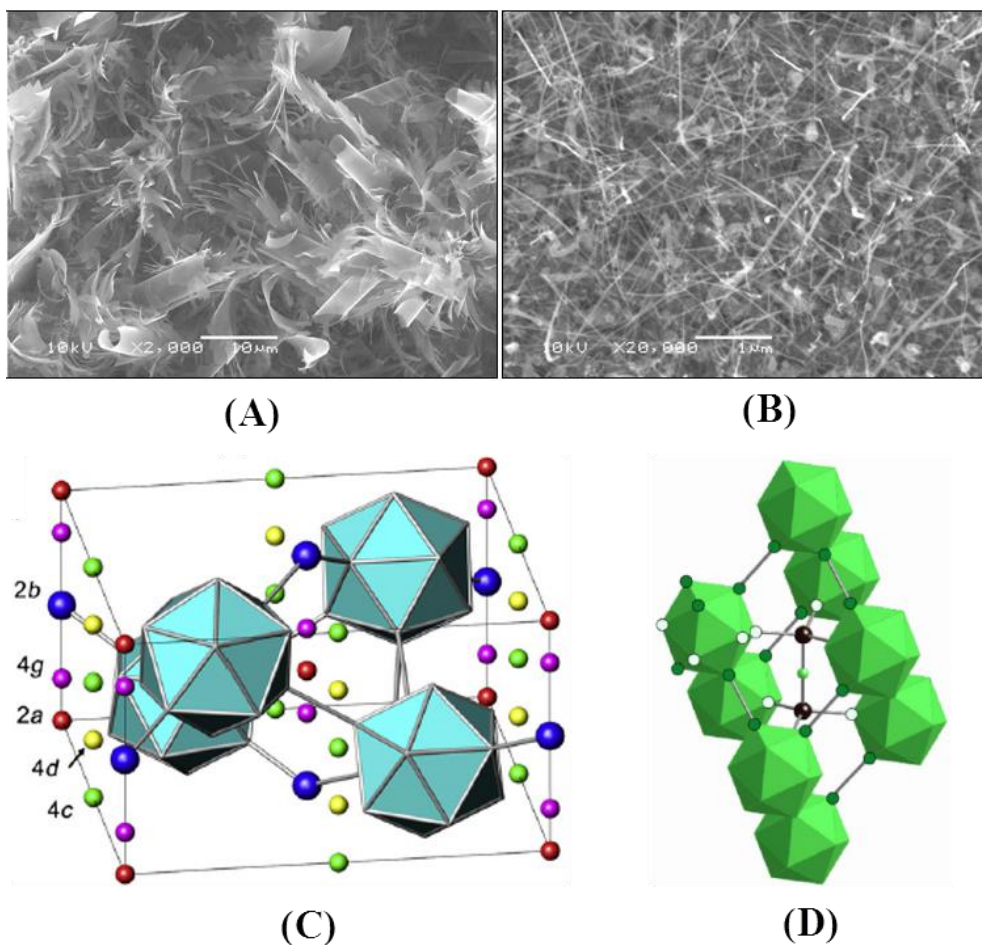
FIGURE 1.15: SEM image of as-synthesized (A) α-tetragonal boron nanoribbons and nanoplatelets; (B) B_4C NWs. Unit structure of (C) α-tetragonal boron, 50 boron atoms are distributed with four B_{12} icosahedra and other two boron atoms are in interstitial sites, such as 2a (red), 4c (green), 4d (yellow), and 4g (pink), and 2 carbon or nitrogen atoms are in 2b sites (dark blue) [78]; (D) B_4C, B12 icosahedra is located on the vertex of rhombohedra, and 3-atom chain is along the main diagonal [79].

1.3.2 α-tetragonal Boron Nanostructures

Boron has been described to have a variety of crystalline modifications such as α-rhombohedral, β-rhombohedral, α-tetragonal, and β-tetragonal. Since α-tetragonal boron was synthesized first and described to be pure crystalline B_{50} in 1943 [80], for a long time researchers believed that pure α-tetragonal boron existed until both quantum mechanics analysis and theoretical calculations proved the impossibility of B_{50} [81, 82]. Instead, both $B_{50}C_2$ and $B_{50}N_2$ can crystalize in α-tetragonal structure [82]. Within the tetragonal unit cell (FIGURE 1.15C), the fifty boron atoms are composed of four B_{12}

icosahedral clusters and two other boron atoms distributed in the interstitial positions, and two carbon or nitrogen atoms are in interstitial sites between icosahedrons to form strong covalent bonds [82]. The first structure of α-tetragonal boron was synthesized in the form of micro-needles and micro-plates [80]. Recently, crystals of α-tetragonal boron have been grown with a variety of nanostructures, such as NWs [83, 84], nanocones [85], NBs [86], NTs [87], nanoribbons [77], and nanoplatelets. Some properties of α-tetragonal nanostructures, including electrical transport and field emission [83-87], and thermal conductivity [88, 89], were investigated. However, there is no report so far on studying of the mechanical properties of α-tetragonal boron nanostructures. Most previous studies reported mechanical characterization of boron 1D nanostructures with α-rhombohedral crystalline or amorphous structures. For example, the elastic moduli of amorphous and α-rhombohedral crystalline boron NBs were reported to be 92.8 ± 4.5 GPa and 72.7 ± 3.9 GPa by nanoindentation, and 87.8 ± 3.5 GPa and 72.2 ± 2.4 GPa by AFM three-point bending, respectively [90]. Another paper showed that the elastic modulus of α-rhombohedral crystalline boron NWs was 196.72 GPa by *in situ* buckling test. The difference in elastic moduli of those α-rhombohedral boron nanostructures was considered to be due to the anisotropic elasticity characteristics of the boron crystal structures [91]. It is also reported that the elastic moduli of orthorhombic crystalline (without unknown structures) boron nanowires were measured to be range from 91.9 to 410 GPa by mechanical resonance test, and around 320 GPa by *in situ* tensile test [59, 61]. Generally, the elastic moduli of amorphous and crystalline boron nanostructures in previous studies were lower than that of bulk boron (380-400 GPa). As mentioned above, it is important to understand the mechanical reliability of α-tetragonal boron nanostructures prior to their applications. Furthermore, the Young's modulus of nanostructures are required to calculate the phonon velocity , in helping study the

phonon transmission on the interface between two nanostructures when they are bundled together for TE applications [89]. In this work, the elastic modulus and hardness of as-synthesized α-tetragonal boron nanostructures were determined using the nanoindentation technique.

1.3.3 Boron Carbide (B_4C-type) Nanowires

Boron carbide has a rhombohedral unit cell, with eight icosahedrons are located at the vertex of rhombohedra, and one 3-atom chain is along the longest diagonal (FIGURE 1.15D) [79]. It is a compositionally disordered material, with a stoichiometric range from $B_{11}C$ (~8 at.% C) to B_4C (20 at.% C), because boron atoms at several positions can be replaced by carbon atoms [92, 93]. For example, the general structural configuration of boron carbide is $(X_{12})XXX$, where (X_{12}) represents icosahedral atoms (*i.e.*, B_{12} or $B_{11}C$), and XXX stands for the three-atoms chains (*i.e.*, BBB, BCB, CBC, CCC).

Bulk boron carbide, as an interesting refractory ceramic and semiconductor, has many excellent properties such as high melting point, low density, high stability, high resistance to wear [94], extreme hardness and high modulus [95], a high Seebeck coefficient [96], and a large neutron absorption cross-section [97]. It is the third hardest material known at room temperature after diamond and cubic boron nitride, and becomes the hardest above 1100 °C [98]. Due to these properties, boron carbide has many applications, including uses as lightweight armor, an abrasive wear-resistant material, a neutron moderator in nuclear reactors, and potentially high-temperature thermoelectric power generation [92, 94, 96-99].

Recently, several studies have shown that boron carbide NWs exhibit some novel properties differing from bulk material [33, 76, 100-102]. It was observed that a blue-shift of peak at 638 nm in the photoluminescence spectrum of boron carbide nanowires

from the 795 nm peak of bulk boron carbide, implying potential applications in visible optical emission devices [100]. A high field emission current density with an enhancement factor of 106 for boron carbide NWs was revealed, which illustrates potential applications as semiconductor field emitters [102]. Excellent elastic and ductile properties of boron carbide NWs make them promising for nanocomposites, as proved by achieving a superior reinforcing effect in epoxy composites [33]. A significant reduction of thermal conductivity of boron carbide NWs compared to the reported values of bulk material was also found [76]. Although these properties of boron carbide nanowires are promising for many applications, they are still a long away from being commercialized, mostly due to issues of reliability and robustness, as well as performance optimization, which remain to be addressed [103]. Therefore, to understand the mechanical properties of boron carbide NWs is required before they are used in applications. In contrast to the intensive studies on mechanical properties of bulk boron carbide materials, few works have been done for investigating mechanical characteristics of boron carbide nanostructures. The only reported data showed the boron carbide NWs had Young's modulus as 428.1 ± 9.3 GPa [33]. There is no doubt that more studies on mechanical properties of boron carbide nanostructures are needed. In this work, mechanical characterization of boron carbide NWs was carried out by various *in situ* SEM testing techniques.

1.4   Layout of Dissertation

The objectives of this dissertation work are to develop a nanomanipulator with improved performance as compared to all reported ones for conducting in situ SEM-based mechanical testing of 1D nanostructures, perform systematic mechanical characterization of two different types of boron-based nanostructures using respectively rational techniques, understand the effects of different factors which could affect the

accuracy of measured data, and attempt to establish the microstructure-mechanical property relation of as-measured nanostructures.

This dissertation is divided into five chapters. This chapter includes the motivations of this study, reviews of the current available nanomechanical testing techniques, and introductions of two types of boron-based 1D nanostructures: α-tetragonal boron nanostructures and B_4C NWs. In Chapter 2, nanoindentation technique is employed to characterize the mechanical properties of α-tetragonal boron platelets. It includes nanoindentation tests to boron platelets on sapphire substrates, and application of a new approach to extract intrinsic modulus values from measurements that include the substrate effect. Chapter 3 presents the complete development of setting up a nanomanipulator system inside an SEM. Results of *in situ* testing of B_4C NWs are present in Chapter 4. It covers the experimental procedures and data analysis, discussions of various effects, and the utilization of numerical modeling tools to analyze and understand the experimental data. In the last chapter, conclusions from this study and future considerations are presented.

CHAPTER 2:   NANOINDENTATION OF BORON NANOSTRUCTURES

2.1   Preliminary Study for Nanoindentation Test

As described above, the α-tetragonal boron nanostructures were produced by co-pyrolysis of B_2H_6 and CH_4 in a LPCVD system at temperatures zone of 630-750 °C in the laboratory. They had two types of nanostructures in general: nanoribbons and nanoplatelets. The morphologies of these two α-tetragonal boron nanostructures were examined by SEM, as shown in FIGURE 2.1(A) and (C). Then these nanostructures were scanned by AFM for their morphological and dimensional details. Three-dimensional (3D) AFM image demonstrated that nanoribbons on the substrate were twisted (FIGURE 2.1B). The twist-shaping nanoribbons were considered as unqualified samples for nanoindentation tests. However, nanoplatelets on the substrate were flat (FIGURE 2.1D). Therefore, only boron nanoplatelets were used for nanoindentation tests.
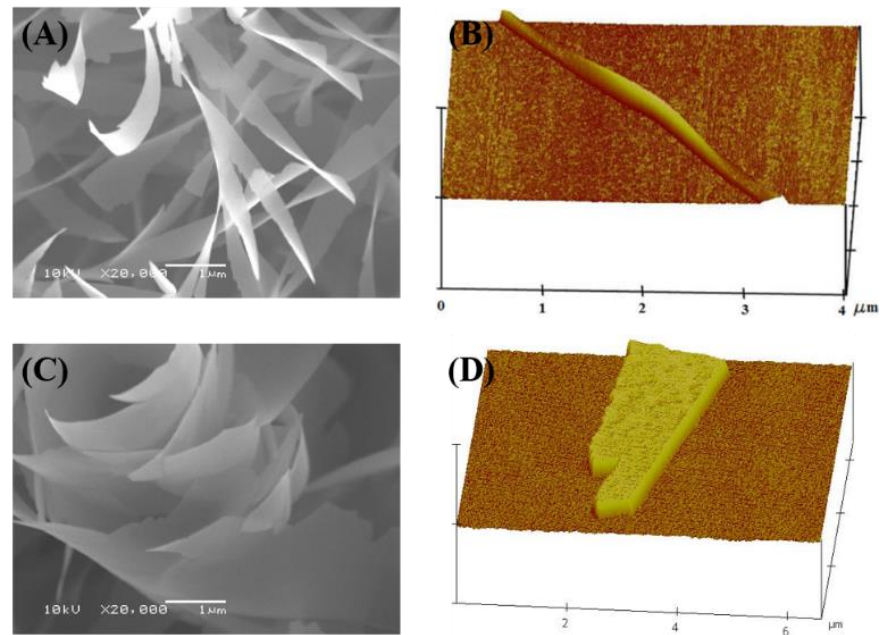
FIGURE 2.1: SEM image (A) and AFM image (B) show the morphologies of nanoribbons; SEM (C) and AFM (D) images of nanoplatelets.

By measuring the thicknesses of 100 boron nanoplatelets or nanoribbons using AFM, around 90% of them were in the range between 10 nm and 40 nm (FIGURE 2.2). Most boron platelets were found to have some small dots or particles on their surfaces, which were considered unsuitable for nanoindentation tests. This was because the surface roughness effect was influential for indentations with tens of nanometers depth. After carefully filtering out unsuitable boron nanoplatelets on substrates, a large number of chosen nanoplatelets were systematically tested. The first challenge of nanoindentation on these platelets was to determine indentation depths. For a nanoplatelet with around 20 nm thickness, was it suitable to set the indentation depth to 10 nm, which was 50% of the thickness? It was widely accepted that the indentation depth should be less than 10 % [104] or 30% [105] of the thickness of a tested sample. So with the indentation depth about 50% of the thickness of platelet, the substrate would definitely affect the measured mechanical properties, especially for Young's modulus [106]. But if the "Buckle's 10% rule" or "Nix's 30% rule" was obeyed, the indentation

depth should be around 2 nm to 6 nm. Then the measured results might be less or not affected by the substrate effect, but they would have large uncertainties caused by the surface roughness, tip bluntness effect, environmental vibrations and other factors [107]. Hence, it was difficult to make a compromise between the errors from substrate effect and the uncertainties from extremely small indentation volume. In our experiments, the influence from the substrate was admitted first, then the measured values are corrected by subtracting the substrate effect. So the elastic modulus achieved directly from the software was just the system modulus, or named as effective elastic modulus of film-on-substrate systems [108]. From an experimental standpoint, it is difficult to decouple the deformation behavior of platelets from substrate effects. Finite element modeling (FEM) was considered in the beginning to extrapolate the intrinsic elastic modulus of nanostructures with a goal of subtracting the influence of the substrate, which has been done in our group for other boron-based nanomaterials [50]. However, after carefully evaluating the FEM model for correction of experimental results from nanoindentation, several difficulties existed. First of all, it was difficult to determine the sharpness of a Berkovich indenter based on the contact area function, which was achieved by tip calibration on standard fused silica sample [109]. The approach used to calculate the tip radius of indenter before in our group considered it as a spherical indenter, which in fact was not appropriate for a three-sided pyramidal Berkovich indenter. In addition, the Berkovich indenter was replaced by a conical indenter in the FEM simulation. It was known that the edges of the Berkovich indenter could increase the stresses around the edges and influence the plastic strain distribution under the deformation compared with a conical indenter [110]. So it was not ideal to use a conical indenter to simulate the nanoindentation on nanostructures with a Berkovich indenter. Furthermore, the contact

conditions between nanostructure and substrate or between indenter and nanostructures were required to define with cautions.

Measurements of 100 boron nanostructures by AFM
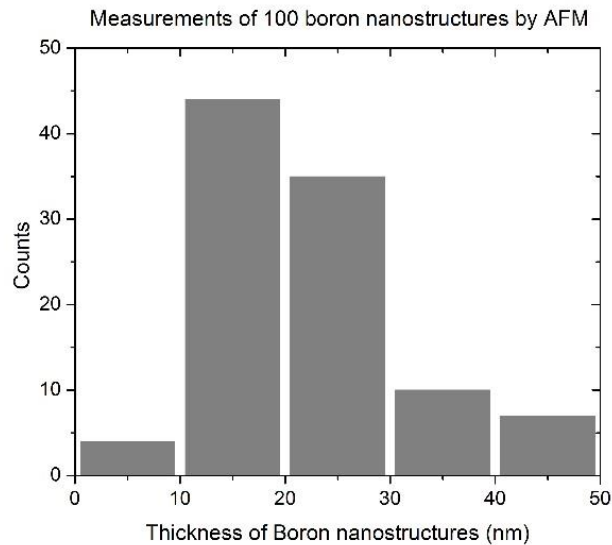
FIGURE 2.2: Thickness measurement of 100 boron nanostructures by AFM.

Therefore, a new simple method is proposed in this work to rule out the substrate effect only by manipulating experimental data without doing any simulations. Another advantage of this is that the indenter size effect can be also minimized. It is well known that these effects are two most influential factors for determining the Young's modulus of thin film or nanostructures on a substrate. The details of theoretical principles of this method and its application in this work are discussed in section 2.3. In addition, it is essential to ensure that the measured results from nanoindentations on nanoplatelets were reliable before manipulating them by this method. Therefore the optimal experimental conditions should be specified for nanoindentations on boron platelets.

To determine the optimal experimental conditions, a series of systematic experiments were carried out. This study was discussed in my master thesis, so the details of experimental procedures and results were only briefly presented in APPENDIX A. Results demonstrated the optimal experimental conditions for

nanoindentation on boron nanostructures should be using the continuous stiffness measurement (CSM) method, dynamic contact module (DCM), the displacement oscillation amplitude at $0.2 - 0.5$ nm, and manually defining surface point for each test. So these optimal experimental conditions were used consistently for nanoindentations on boron nanoplatelets.

2.2   Nanoindentation of Boron Nanoplatelets on Sapphire Substrate

A large number of nanoindentation tests were performed on boron nanoplatelets on sapphire substrates. The reason for choosing a sapphire substrate was that the Young's modulus of this substrate (440 GPa) was comparable to that of boron bulk materials (380-400 GPa) [77]. So if the Young's moduli of the a-tetragonal boron nanostructures were close to those of the boron bulk, then the substrate effect from a sapphire substrate should be less because the system can be considered as quasi-monolithic.

2.2.1   Experimental Details

These α-tetragonal boron nanostructures were synthesized in clusters as like powders on a silicon substrate. First, these powders were scrapped off from the substrate, and then were uniformly dispersed in an absolute alcohol to form a nanostructures solution by ultrasonication for 5 minutes. Two or three drops of solution were then deposited on a sapphire (0001) substrate. After the substrate was dried, the nanostructures were left on the sapphire substrate. Then this sapphire substrate was flatly mounted on an aluminum sample disk and fixed using a small amount of the mounting adhesive (Crystalbond 509). Boron nanoribbons and nanoplatelets on the substrate were observed under optical microscope (Olympus BX51 reflective microscope) both in the bright field and the dark field, so that the nanostructures with smooth surfaces were found, FIGURE 2.3A and C. The locations of these nanostructures on the substrate were

also documented and marked in the captured images by drawing a specific feature around it in order to easily find them under Atomic Force Microscope (AFM) and Nanoindenter. An AFM (Veeco Dimension 3100) with the tapping mode was used to scan these chosen nanostructures to determine their topographical and geometric features, FIGURE 2.3B and D. By comparing AFM images of different nanoplatelets, some nanoplatelets with dots and uneven surface were filtered out. For example, the nanoplatelet shown on FIGURE 2.3B was chosen for nanoindentation tests, but another one shown on FIGURE 2.3D is filtered out. Nanoindenter (Agilent Technology G200) was applied to perform the indentation tests on these boron nanoplatelets. The nanoindenter was combined with NanoVision nanomechanical microscopy option under DCM module with CSM method. A Berkovich indenter with a calibrated tip area function was used in all experiments.
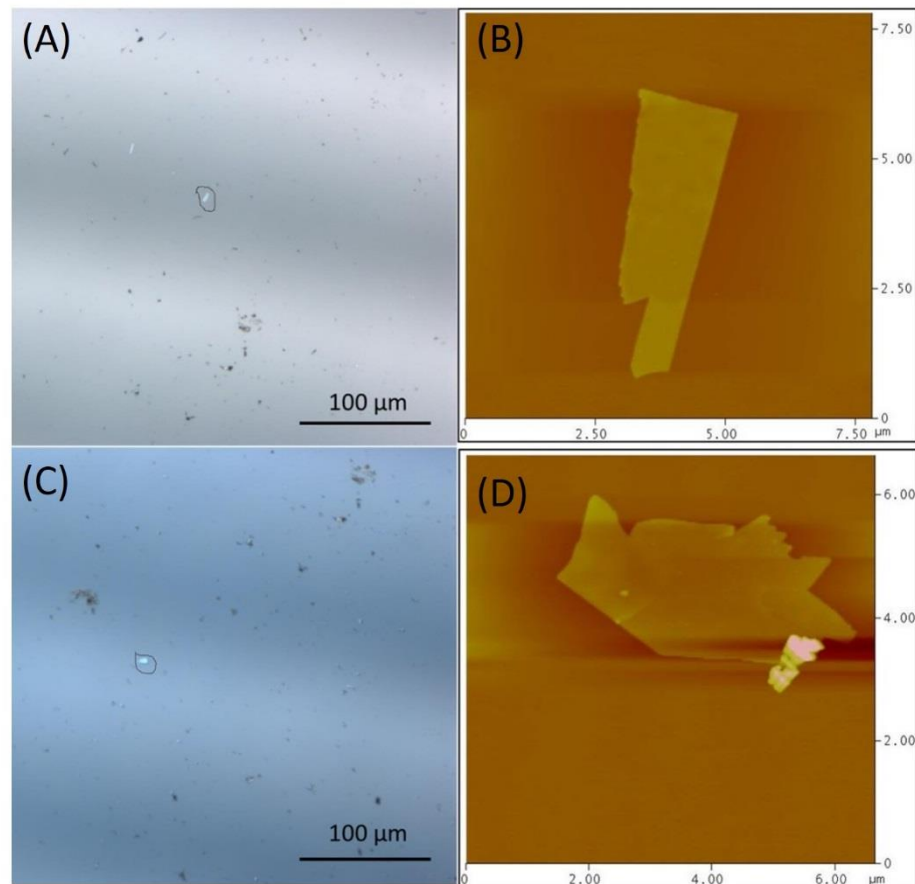
FIGURE 2.3: Images of optical microscope and AFM of two different boron plates: (A) and (B) represent one good platelet; (C) and (D) represent a platelet unsuitable for nanoindentation test.

The detailed process of nanoindentation on the nanoplatelets was specified as following. First of all, the operating method was selected to be the scan and indent interactive method in NanoVision package. After the sample disk was installed in the nanoindenter, the desired nanoplatelet was searched under an optical microscope inside the nanoindenter. After the nanoplatelet was found with the optical microscope, the sample disk was then moved under the indenter. Consecutively, several 100 nm indentations on sapphire substrate were made to check the stability and performance of nanoindenter system, which usually consumed half to one hour. The system was considered as stable only if the results of nanoindentation on sapphire were repeatable. Then the selected nanoplatelet was scanned by a scanned force microscope equipped in

nanoindenter to obtain its surface roughness and thickness. Nanoplatelets with surface roughness less than 3 nm were accepted for the further indentation tests. After required settings were prescribed, the Berkovich indenter started to approach the nanoplatelet with a 10 nm/s approaching velocity from a distance of around 1000 nm above the sample surface. The nanoplatelet surface was detected by the indenter with 25% or 40% sensitivity. Then the indenter was loaded into the sample with a constant strain rate of 0.05 /s to the prescribed depth. The indenter was held on the maximum load for 10 seconds, and begun to unload with the same strain rate. It was held for 100 seconds for correction of thermal drift when it reached at the 10% of the maximum load. Eventually, the indenter was completely unloaded. Load versus displacement into surface curves were achieved after subtracting the thermal drift, and were used to extract elastic modulus and hardness.

In the whole process, the same Berkovich indenter was used to image and indent the nanostructures, and again image the residual indentation impressions after tests. Pre-test imaging of the nanostructures on substrate was not only to determine surface roughness, but also to accurately locate the nanostructures and positions for indentations. Post-test imaging of the residual indentation impressions was to verify that the indentations were carried out in the anticipated locations, such that the validity of data were assured.

2.2.2   Results and Discussions

To briefly understand the test samples, one boron nanoplatelet was tested before the systematic experiments. The thickness of the platelet was 30 nm, as shown in AFM images FIGURE 2.4A and B. The surface of this platelet was flat enough for this qualitative examination. Three indentations with different penetration depths were performed on the platelet. These three penetration depths were 24 nm, 33 nm and 61 nm,

which were selected intentionally to be smaller than, equal to and larger than its thickness, respectively. Three different residual impressions after tests were observed both by the nanoindenter and AFM. The AFM image of these residual impressions on the nanoplatelet was illustrated in FIGURE 2.4C. For the first indentation with 24 nm depth, the residual impression was sink-in. The pile-up shape was observed for the 33 nm indentation, and crack occurred for the 61 nm indentation. Curves of the loads as a function of displacement into surface for these three tests were plotted, see FIGURE 2.4D. The inset graph showed the corresponding elastic modulus versus displacement curves. From this qualitative test, results guided us that if the indentation depth were prescribed at 80% or less of thicknesses of nanoplatelets, the impression shape should be sink-in. The occurrence of pile-up at 33 nm indentation manifested that the boron platelets are softer than the substrate. The sink-in model was referred as the original Oliver-Pharr model [41], which was adopted in the software of our nanoindenter system [111]. Therefore the measured results from this nanoindenter system will not be reliable if the pile-ups are observed in post-test imaging, because the assumed contact area A less than the actual area results in the over-estimation of elastic modulus and hardness. These over-estimations could be up to 50% in some cases [112]. Therefore, as long as the residual impression shape is sink-in, that is prescribing the indentation depth less than 80% of thickness of nanoplatelets in this study, the measured results obtained in the system are considered to be reliable for further analysis.
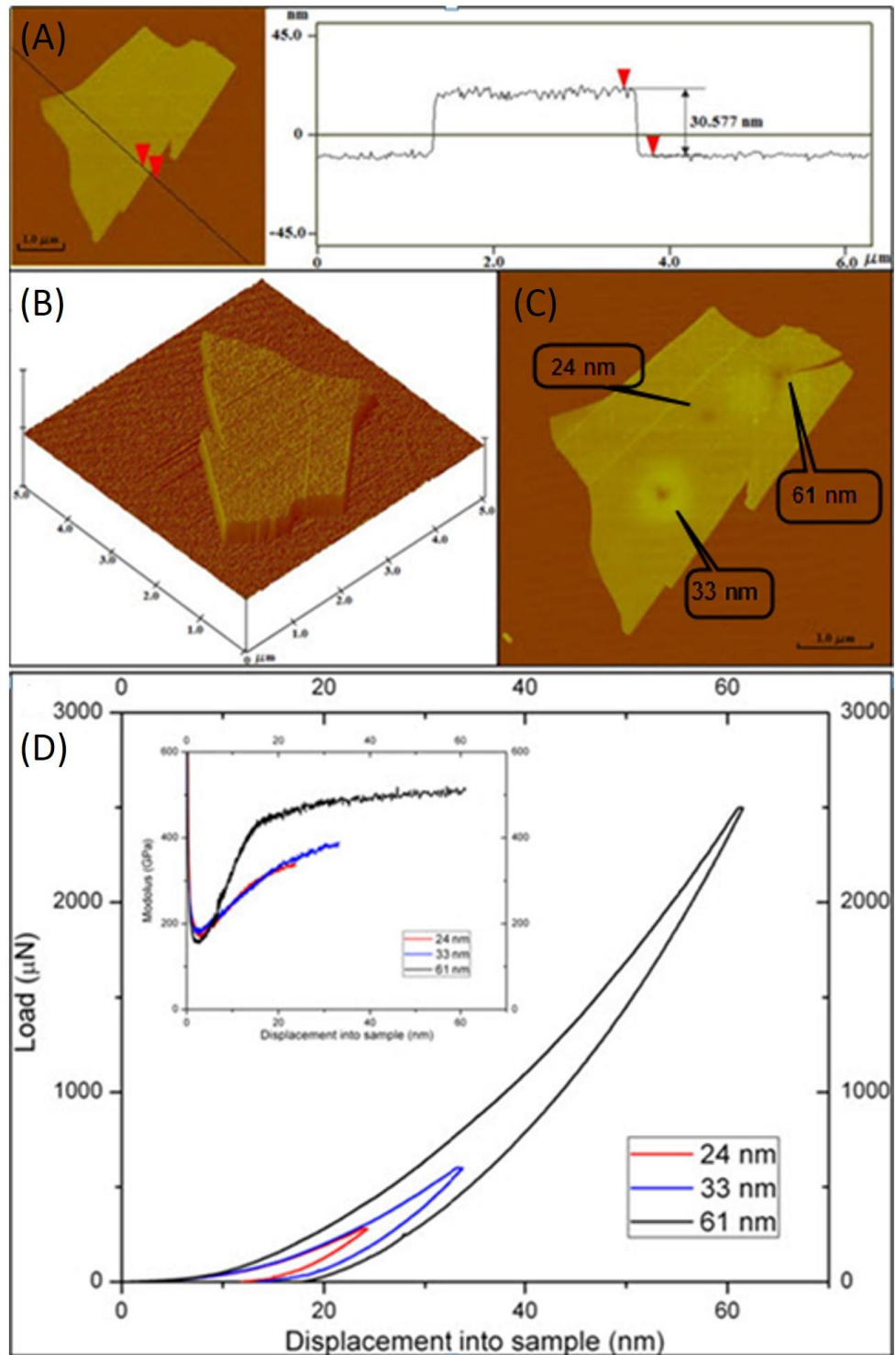
FIGURE 2.4: (A) AFM image of one boron platelet and the corresponding height profile, (B) Three dimensional image of this boron platelet, (C) AFM image of the boron platelet with residual impressions after indentation tests, (D) the load vs. displacement curves from nanoindentation tests on the platelet; the inset is the corresponding Young's modulus vs. displacement curves.

Generally multiple indentations were performed on one platelet. The distance between two neighboring indents should be more than 200 nm such that the second indent was not in the influential area of residual impression from the first indent. The representative AFM images are shown in FIGURE 2.5A and B to exhibit the morphology of one boron platelet with 20 nm thickness and five residual indentation impressions on it. Triangular-shaped impressions are observed on the platelet. The image shows that these residual impressions are more than 300 nm away from the edge of the platelet, so the measured results from these indentation tests are considered to be valid. If the residual impressions are close to the edge of the platelet or other indents (i.e. < 200 nm), then the measured values extracted from these tests are not used. A typical curve of applied load versus displacement into surface for a 10 nm indentation test is illustrated in FIGURE 2.5C. FIGURE 2.5D presents the corresponding curve of the measured Young's modulus as a function of penetration depth. From this modulus curve, the measured modulus value increases with increasing penetration depth. The inconsistent modulus values may be due to the uncertainties at depths less than 10 nm, or because of the substrate effect. The intrinsic modulus of nanoplatelet directly from this modulus curve could not be determined to within an acceptable uncertainty.
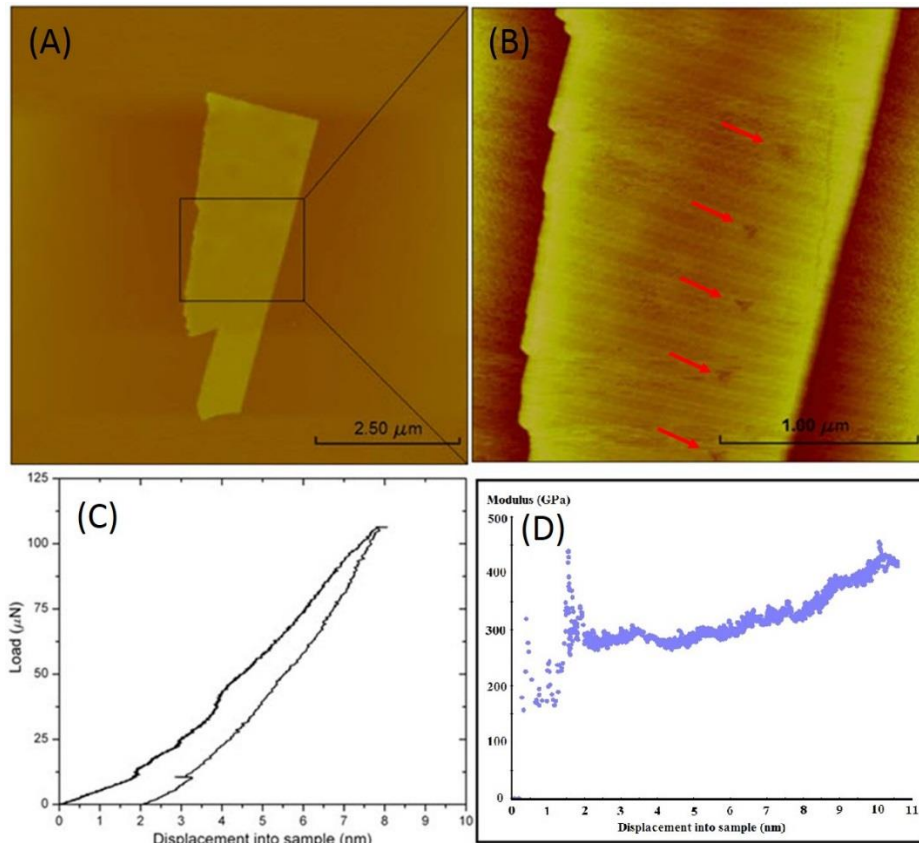
FIGURE 2.5: (A) AFM image of one boron platelet; (B) AFM image of five residual indentation impressions (pointed by red arrows) on the part of the boron platelet where is marked in (A); (C) a typical load versus displacement curve of one indentation on boron platelets on sapphire substrate; (D) the corresponding curve of Young's modulus as a function of indentation depth.

To avoid the uncertainties from the shallow depth at 10 nm, four indentation depths at 20 nm, 30 nm, 40 nm, and 50 nm were performed on a 54 nm-thick platelet on a sapphire substrate. FIGURE 2.6A shows the AFM image of this tested boron platelet with four indentation impressions, indicated by four arrows with different penetration depths. The measured modulus curves for these four indentations are present in FIGURE 2.6B. It is clearly shown that the results under 10 nm depth (the part on the left of red dash line on the graph) have larger variations and uncertainties. So the measured values under 10 nm indentation depth are not reliable. In addition, the substrate effect was also proven to exist in the measured results of indentation tests on the platelet, because the

all modulus curves increase with the increment of penetration depth. For the modulus

curve of 50 nm indent, the modulus value suddenly decreases, as pointed by an arrow,

because the crack occurred when the indenter penetrated through the platelet, shown in

FIGURE 2.6A. The increasing trends for all modulus curves also manifest that boron

platelet is softer than the sapphire substrate [107].
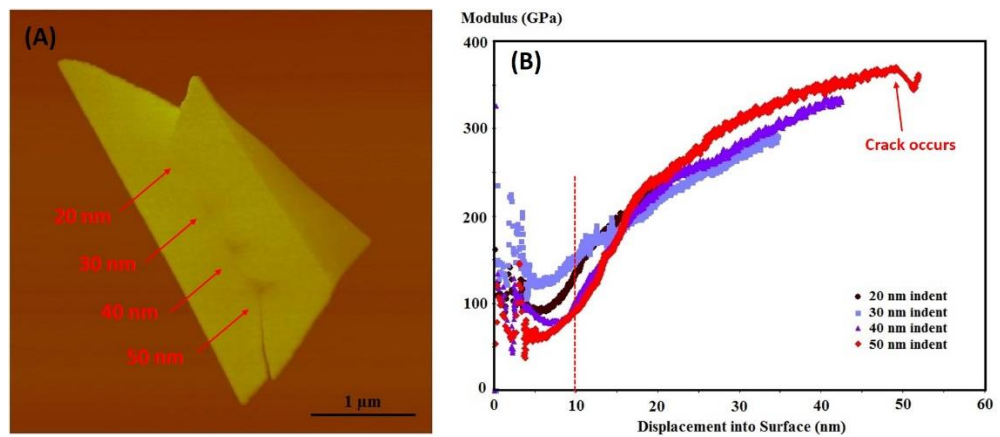
FIGURE 2.6: (A) AFM image of a 54 nm-thick boron platelet; (B) measured Young's
modulus curves of four different-depth indentations on the boron platelet.

2.2.3 Summary

Boron nanoplatelets with thickness at tens of nanometers were used for

nanoindentation tests. The nanoplatelets were both imaged under AFM and

Nanoindenter to determine the surface roughness, because flat surfaces are required for

nanoindentation tests. Conclusions can be made based on the results of nanoindentations

to boron platelets on sapphire substrates: (1) indentation depth should not exceed the

thickness of a tested nanoplatelet (for safety, keep the indentation less than 80% of its

thickness), otherwise pile-up or crack may occur. (2) boron platelets are softer than the

sapphire substrate; (3) the indentation depth at 10 nm or less is inappropriate for our

case, because many other effects play more profound roles in the measured results of

nanoindentation at a shallow depth; (4) the substrate effect is significant for a nanoindentation with depth more than 10 nm on boron nanoplatelets.

2.3   A New Approach to Extract Intrinsic Modulus of Nanostructures

This new method is developed to rule out the substrate effect from the experimental results. The principle of this method is introduced here. A nanoplatelet (NP) is laying on a substrate with a perfect bond for their contact condition, which is concluded from the experimental observation that no nanoplatelet was lift up during the test. An indenter is controlled to penetrate into a substrate with an indentation depth h. Then the same indentation depth (h) is applied on a NP with thickness t on the substrate, as shown in FIGURE 2.7. As discussed above, the indentation depth should be less than 80% of the thickness (i.e. h<0.8t). The measured moduli of indentation on the NP 1 and indentation on the substrate 1 are named as the measured system modulus (E_{meas_sys}) and the measured substrate modulus (E_{meas_sub}), respectively. The E_{meas_sub} is expected to be a constant. However, the modulus values for a substrate vary with the indentation depth at tens of nanometers because of many error sources in a small indentation depth. Hence, E_{meas_sys} and E_{meas_sub} at the same depth should be subject to the same influence. In other words, if the E_{meas_sub} at 10 nm is 10% higher than the exact value, then E_{meas_sys} at 10 nm should be also around 10% higher than the real system modulus. Then the substrate 1's influence factor (r) is defined as the ratio of E_{meas_sys} to E_{meas_sub}, i.e. $r = \frac{E_{meas\_sys}}{E_{meas\_sub}}$ at the ratio of indentation depth to the thickness of nanoplatelet (h/t). This dimensionless term r not only reflects the substrate effect, but also minimizes the tip size effect.

Then indentations to a new system of NP2 on substrate 2 are performed with the similar procedures. Since the thickness of NP 2 (t') is different, and in order to keep the ratio of indentation depth to the thickness of NP constant, the penetration depth on NP 2 is set to h' in order to have $h'/t'=h/t$. Eventually, the substrate 2's influence factor (r')

will be achieved. Then more NPs on different substrates are indented with similar processes. Consequently, various influence factor values corresponding to every substrate are obtained, and then the relationship between the influence factor and intrinsic modulus of substrate can be estimated by curve fitting. If the intrinsic modulus of NP is same with that of a substrate, then the substrate effect will not exist because the NP-on-substrate system is considered as a monolithic material, which means the influence factor should be equal to 1. Therefore, the intrinsic modulus of substrate (i.e. the intrinsic modulus of NP) can be calculated by inputting the influence factor value 1 into that relationship.
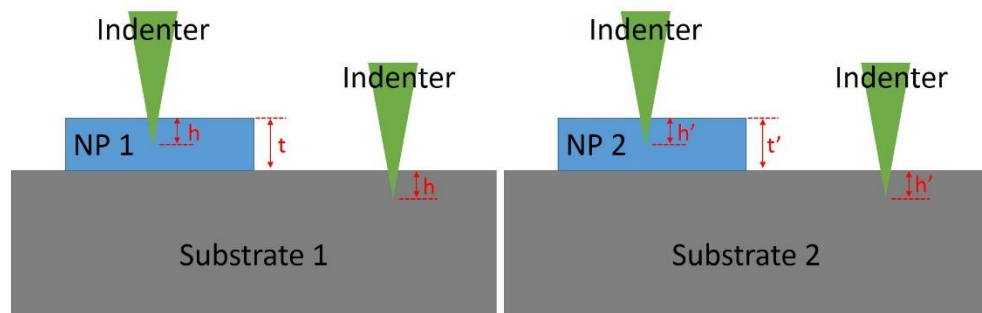
FIGURE 2.7: Schematics of indentations to two nanoplatelets on two different substrates.

According to the principle of this new approach, more nanoindentation tests to boron platelets on different substrate were performed. Besides the sapphire(0001) substrate, three more substrates including 1 μm SiO_2/Si substrate, Si(100) substrate and quartz(0001) substrate were employed for the study. The experimental conditions and detailed procedures of this study were same with those described above for nanoindentations to platelets on sapphire substrates.

First, a new tip calibration was conducted based on results of nanoindentations on standard fused silica sample. The measured Young's modulus for fused silica was 72

± 1 GPa, which indicated that this newly calibrated tip area function provided accurate modulus extraction. Many batches of 200 nm indentations were then performed on these four substrates in order to achieve their intrinsic Young's moduli. The measured Young's moduli were 429 ± 3 GPa for sapphire(0001) substrate, 165 ± 2 GPa for Si(100) substrate, 119 ± 2 GPa for quartz(0001) substrate and 81 ± 1 GPa for SiO_2/Si substrate. The measured Young's moduli for sapphire and Si substrate were consistent with those reported elsewhere [106], and the measured value for quartz substrate was also consistent with that in the publication [113]. However, all measured values were slightly lower than the reported values in our group [50]. The reason for the difference was because a new indenter with a new tip area function was used. These measured values are used as intrinsic Young's moduli of four substrates for the further data analysis.

Nanoindentations on boron platelets on sapphire substrates were explored above, but it was carried out with an old indenter. Since a new indenter was used to study this method, it was necessary to perform more nanoindentations on boron platelets on sapphire substrates with this new indenter. The results discussed above showed that the Young's moduli of boron platelets were less than that of sapphire substrate. The measured results of nanoindentations on boron nanoplatelets on sapphire substrates using the new indenter lead to a similar conclusion, as shown in FIGURE 2.8. The figure shows the measured modulus curves of three indentations. The black curve, representing a 80 nm indentation on a sapphire substrate, shows that the measured moduli of sapphire substrate at the shallow indentation depth are higher than its intrinsic modulus. This should be due to the inaccuracy of tip area function at the shallow depth. The indenter tip is blunt at the apex, so it is difficult to have an accurate tip area function at tens of nanometers depth. By using this rough tip area function at the shallow depth, the modulus values calculated by the software are higher than the intrinsic ones. Therefore,

the measured system moduli of boron platelets on substrates should be higher than the real measured system modulus values. This is the advantage of this method that the effect of inaccurate tip area function can be minimized.

There are two platelets with different thickness on a sapphire substrate. The thin plate is 38 nm thick, while another one is 68 nm thick. The red curve in FIGURE 2.8 presents the resultant moduli of a 20 nm indentation on the thin platelet. And the blue one is the modulus curve of a 50 nm indentation on the thick platelet. The blue curve is below the red one at the same displacement is because the indentation on the thick platelet is less affected by the substrate than that on the thin platelet at the same indentation depth. It is reported that the influence from the substrate should be equal if the ratio of indentation depth to thickness is same [106]. So the results shown in FIGURE 2.8A are transformed to the results in FIGURE 2.8B. The overlap of these two curves validates this model. Therefore, a curve of modulus versus indentation depth/thickness is considered as a representation of all nanoindentations of boron nanoplatelets on one kind of substrate.
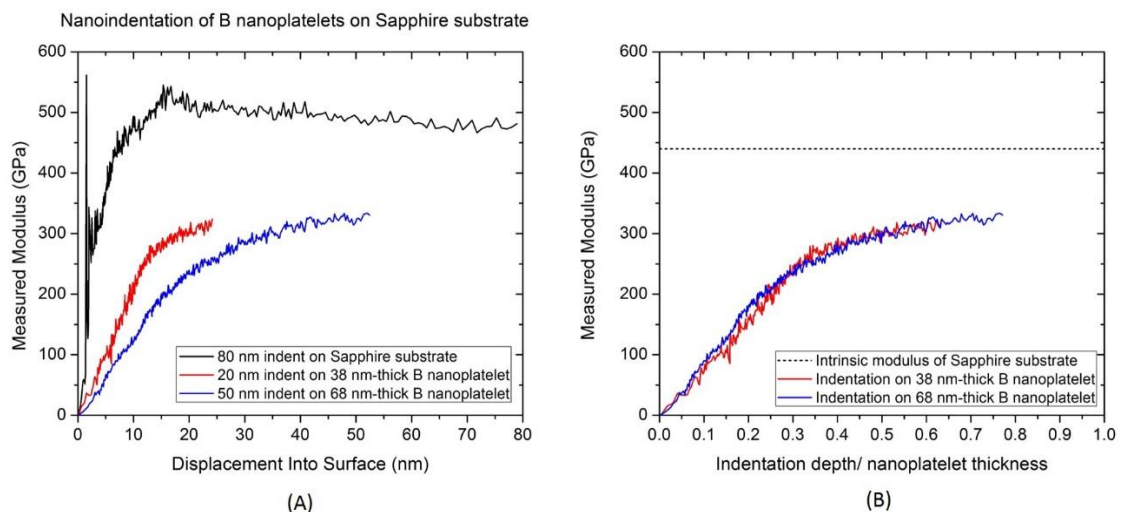
FIGURE 2.8: Measured modulus results of 20 nm and 50 nm nanoindentations to a 38 nm-thick and 68 nm-thick boron platelets on a sapphire substrate versus (A) displacement into surface, and (B) indentation depth/ thickness, respectively.

The moduli of boron platelets are confirmed to be softer than the sapphire substrate. Then Si substrate, a softer substrate than sapphire substrate, was used to support boron platelets. The modulus curves of nanoindentations on a Si substrate and on a 38 nm-thick boron platelets on the Si substrate are present in FIGURE 2.9. The green and black curves are the measured moduli of 20 nm and 30 nm indentations on the Si substrate, respectively. Similar as sapphire substrate, the measured modulus of Si substrate is higher than its intrinsic modulus. The blue and red curves represent the measured moduli of 20 nm and 30 nm indentations on this 38 nm-thick boron platelet on the Si substrate. Results also indicate that boron platelets are also softer than the Si substrate. The consistency of the blue and red curves verifies that the modulus curves at different indentation depths on the same platelet are consistent.
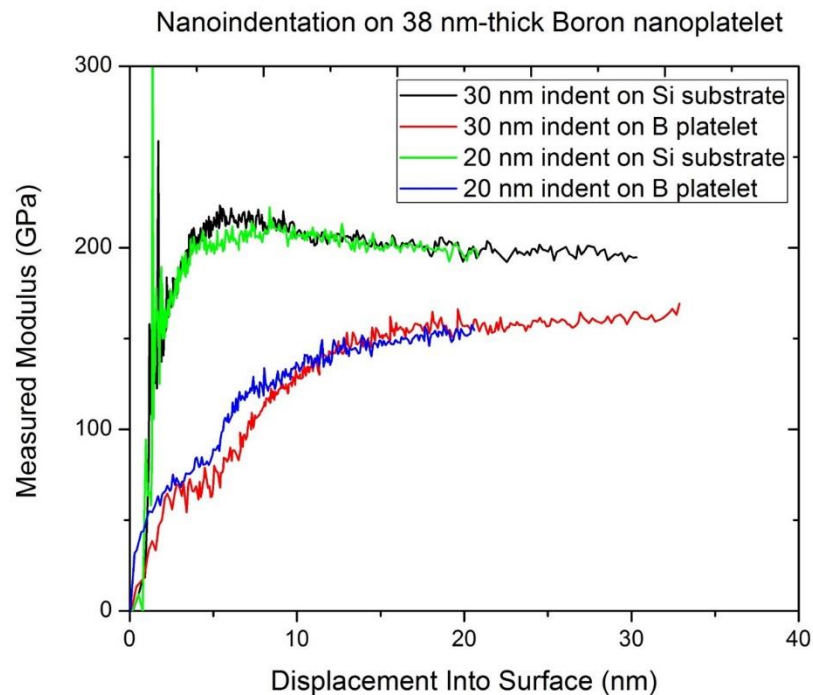
FIGURE 2.9: Comparison of measured modulus results of 20 nm and 30 nm nanoindentations on a 38 nm-thick boron platelet on a Si substrate and the substrate.

Then a softer substrate, quartz, was employed. FIGURE 2.10 shows the measured modulus curves of 30 nm indentations on a quartz substrate (black) and on a 47 nm-thick boron platelet on it (red). It apparently demonstrates the quartz is harder than boron platelets.
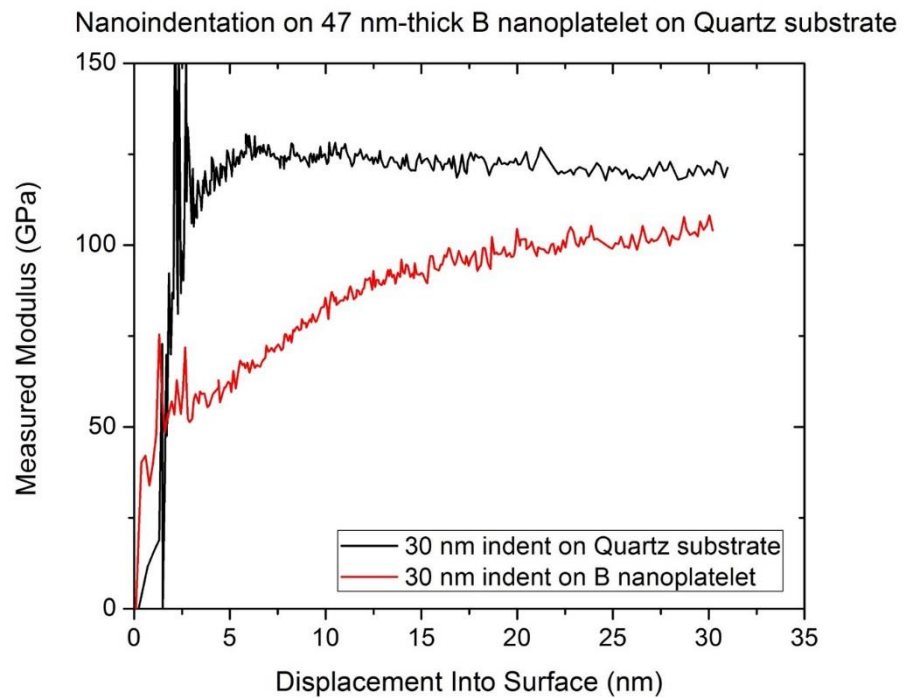
FIGURE 2.10: Comparison of measured modulus results of 30 nm nanoindentation on a 47 nm-thick boron platelet on quartz substrate and the substrate.

Therefore, 1 μm SiO_2/Si substrate was used, because it was softer than quartz substrate. The resultant moduli of 20 nm indentations on a SiO_2/Si substrate (black) and on a 32 nm-thick boron platelet on the SiO_2/Si substrate (red) are displayed on FIGURE 2.11. Again, it exhibits that boron platelets are softer than the SiO_2/Si substrate. However, there is one major difference compared with modulus curves of nanoindentations on boron platelets on other three substrates, which is this modulus curve (red) does not have a rising trend with increasing the indentation depth. The curve becomes almost flat after 10 nm depth. The variations on the curves before 10 nm depth are caused by the

uncertainties from surface roughness and tip roughness effect. The flatness of the measured modulus curve for boron platelets on the SiO_2/Si substrate implies that the Young's moduli of boron platelets and SiO_2/Si substrate are close. So the Young's modulus of a-tetragonal boron nanostructures should be slightly lower than that of the SiO_2/Si substrate.
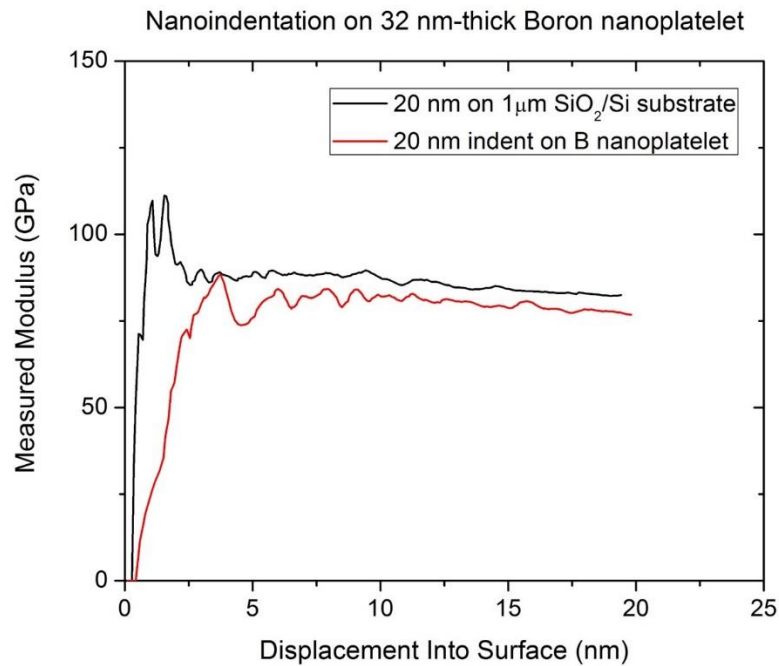
FIGURE 2.11: Comparison of measured modulus results of 20 nm nanoindentations on a 32 nm-thick boron platelet on 1 μm SiO_2/Si substrate and on the substrate.

All curves of measured moduli as a function of indentation depth are converted to those of modulus versus indentation depth/platelet thickness, such that results of nanoindentations on boron nanoplatelets on these four substrates can be represented by four modified curves, FIGURE 2.12. Measured moduli of boron platelets on four substrates are all lower than the intrinsic moduli of the corresponding substrates, which are indicated with arrows on the figure. Moreover, it shows that the "Buckle's 10% rule" is not technologically suitable for any nanostructures with thickness less than 100 nm, because the results have large variations with the indentation depth less than 10 nm. In

addition, the "Nix's 30% rule" is not optimal for our case, because the modulus curves are already subjected to the substrate effect with the indentation depth/thickness less than 0.3.
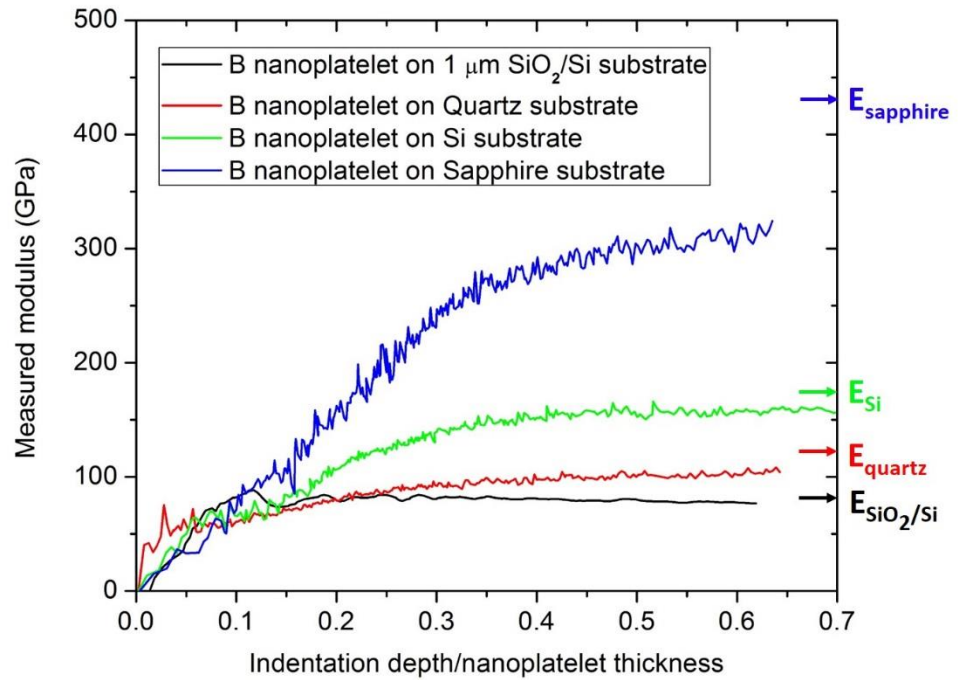
FIGURE 2.12: Measured modulus of boron platelets on SiO_2/Si substrate, quartz, Si and sapphire substrate, as a function of indentation depth/nanoplatelet thickness.

From modulus curves of nanoindentations on substrates at shallow depths, the measured values are relatively higher than the intrinsic values of these substrates. Therefore, the influence factor (r) introduced here. The r values are different for boron platelets on different substrates, or for different ratios of indentation depth/platelet thickness. The r values corresponding to four h/t ratios on four different substrates are list on TABLE 2.1. The r values are the typical results of nanoindentation on one platelet on each substrate.

TABLE 2.1 Summary of *r* values for different *h/t* ratios for different substrates.

Substrate	Intrinsic E_{sub} (GPa)	*Thickness of platelet (nm)*	*h/t*=0.3 *r*	*h/t*=0.4 *r*	*h/t*=0.3 *r*	*h/t*=0.3 *r*
SiO₂/Si	81	32	0.9165	0.9554	0.9611	0.9719
Quartz	119	47	0.7570	0.8154	0.8286	0.8427
Si	165	38	0.6772	0.7566	0.7642	0.7850
Sapphire	429	38	0.5298	0.5945	0.6356	0.6508
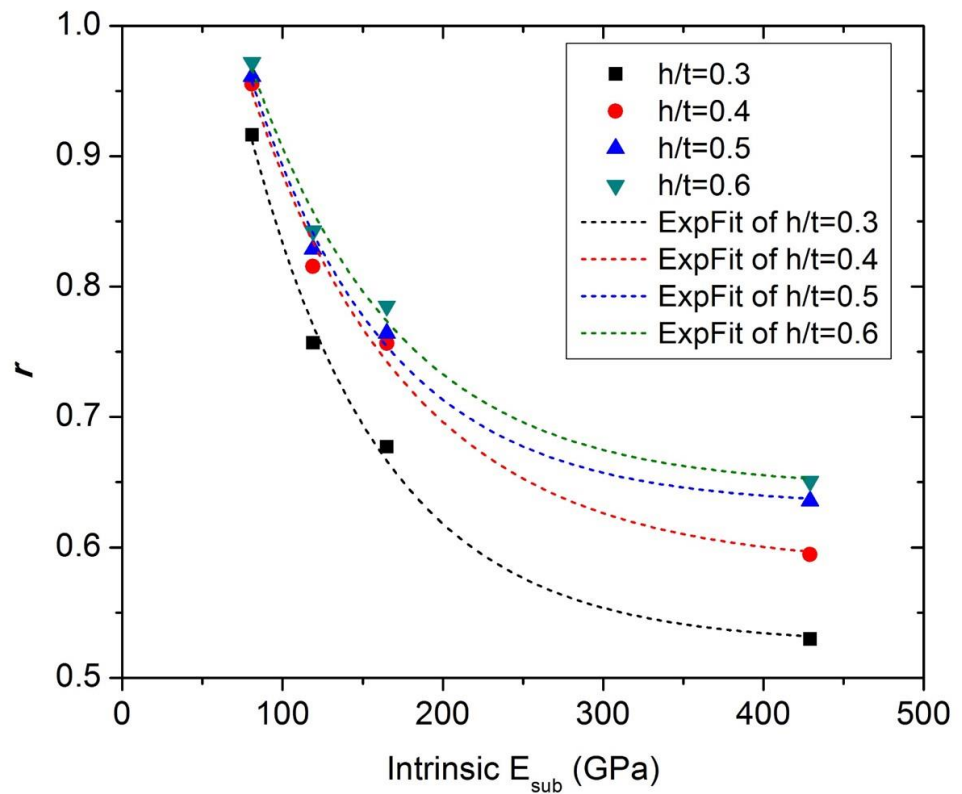
FIGURE 2.13: The experimental results and curve fitting of influence factor *r* values corresponding to intrinsic Young's moduli of these four substrates for two *h/t* ratios.

The curves of r values corresponding to the intrinsic Young's moduli of substrates for these four h/t ratios are plotted in FIGURE 2.13. The results can be fitted into exponential decay functions for both h/t ratios. For the h/t ratio from 0.3 to 0.6, the fitting relationship between r and the intrinsic modulus of substrate E are

$$\frac{h}{t} = 0.3, r = 1.02e^{-\frac{E}{83}} + 0.53 \tag{15},$$

$$\frac{h}{t} = 0.4, r = 0.81e^{-\frac{E}{100}} + 0.59 \tag{16},$$

$$\frac{h}{t} = 0.5, r = 0.83e^{-\frac{E}{86}} + 0.63 \tag{17},$$

$$\frac{h}{t} = 0.6, r = 0.78e^{-\frac{E}{91}} + 0.65 \tag{18}.$$

Theoretically, these four fitting curves should intersect at the point where r is equal to1. According to the principle described at first, its corresponding intrinsic modulus of the substrate E should be equal to the intrinsic modulus of boron platelets when $r = 1$. So E is reversely calculated by inputting $r = 1$ into the above four fitting equations. The E values are calculated to be 64 GPa, 68 GPa, 69 GPa, and 73 GPa for the fitting equations from 0.3 to 0.6, respectively. Therefore, the intrinsic Young's modulus of α-tetragonal boron nanostructures derived by this method is 69 ± 4 GPa.

It is worthy to point out that the excellent curve fitting for the experimental results is because of that all boron platelets on four substrates are belong to one system: a soft film on a hard substrate. If a substrate softer than boron platelets is used in this study, then its experimental results is not suitable to combine with others for the curve fitting, because the influence from a substrate is completely different for a hard film on a soft substrate system.

2.4   Conclusions

   In this chapter, the α-tetragonal boron nanostructures were mechanically characterized by nanoindentation. Preparation works were conducted first before nanoindentation tests, which include extensive investigation of morphologies and thickness of boron nanostructures, and systematic study to determine optimal experimental conditions for nanoindentations on boron nanoplatelets. Then, nanoindentations on boron nanoplatelets on sapphire substrates were performed. This part of the study was included in my thesis work. More details can be obtained in my master thesis. Related results were briefly present and summarized here. The last part about using a new approach to rule out the substrate effect from the experimental results was expanded in this dissertation work. More nanoindentation experiments were conducted on boron platelets on four different substrates. Then the experimental data were analyzed to extract the intrinsic Young's modulus of α-tetragonal boron nanostructures at 69 ± 4 GPa. The derived intrinsic modulus of α-tetragonal boron nanostructures is comparable to the reported values for α-rhombohedral boron NBs [90].

CHAPTER 3:   DEVELOPMENT OF A NANOMANIPULATOR SYSTEM

3.1   Background

As discussed in Chapter 2, the mechanical properties derived from nanoindentation tests are affected by many factors such as substrate effect, tip geometry and so on. Besides, nanoindentation is suitable for testing on nanostructures with flat surfaces, not with round surfaces like NWs and NTs. In this dissertation work, nanoindentation was initially used to study the mechanical properties of as-synthesized B_4C NWs. It was later found out that the technique was not suitable to test NWs. This is because there were various problems found in the experiments, such as the movement of NWs under applied load, uncertain contact areas between indenter and NWs, the sliding of the indenter when it was not contacting the center top of the NW, and etc. Therefore, an alternative mechanical characterization technique has been developed to obtain more reliable results. For current available techniques, such as nano-tensile, nano-bending and resonance vibration tests, precise manipulation and positioning of nanostructures are required. It was reviewed in the Chapter 1 that AFMs were capable of both imaging and manipulating nanostructures with nanometer resolution, so they were sometimes applied to laterally bend nanostructures in the lateral force mode [20], vertically bend nanostructures in the contact mode [114], and/or axially stretch nanostructures in the force microscopy mode [115]. But AFM-based testing system had a similar drawback as a nanoindenter that the characterization process was not able to be observed in real-time. To overcome this limitation, electron microscopies were employed for imaging during the mechanical characterizations. Since it has more space

inside the vacuum chamber compared to TEM, it is easier to build a testing stage within a SEM. In this work, a home-built nanomanipulator for *in situ* SEM was designed, manufactured, assembled, evaluated, and improved.

3.2   Procedure of Building a Nanomanipulator inside SEM

To set up a complete nanomanipulator system in SEM, FIGURE 3.1, many components, such as a nanomanipulator stage inside vacuum chamber, vacuum feedthrough, picomotor drivers, and computers are necessary. For components such as function generator, DC source and a joystick, they are optional. But they can be included for providing more user friendly functionality.
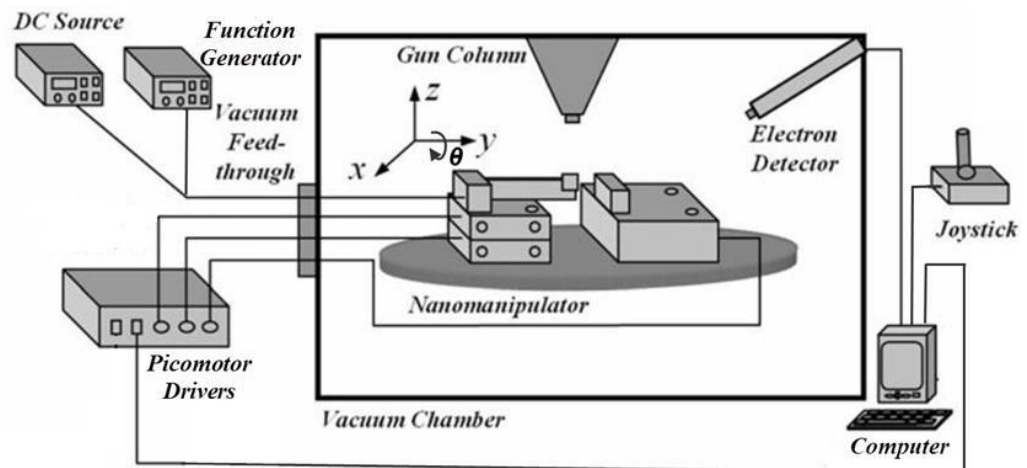
FIGURE 3.1: The instrumentation diagram of the home-made SEM nanomanipulator system [116].

The SEM instrumentation used in this study is a JEOL JSM6480 SEM with a large specimen chamber. The microscope is also equipped with secondary and backscattered electron detectors. The resolution of this microscope is specified as 3.0 nm at 30 kV with an 8 mm working distance [117]. In reality, the processes of manipulations and tests are observed under "Scan 2" that is a video imaging mode, so the resolution is lower than this. High resolution images can be achieved under the slowest-scan mode (Scan 4).

3.2.1   Nanomanipulator Stage

The nanomanipulator stage is the main part of the whole nanomanipulator system. It basically contains the supporting platform, two independent motion stages (*X-Y*) and (*Z-θ*), one piezoelectric benders (not shown in the image), and AFM tip and sample holders, as shown in FIGURE 3.2. All electrical wires are connected to the picomotor actuators and external electronic devices through a vacuum-side plug of vacuum feedthough connector.
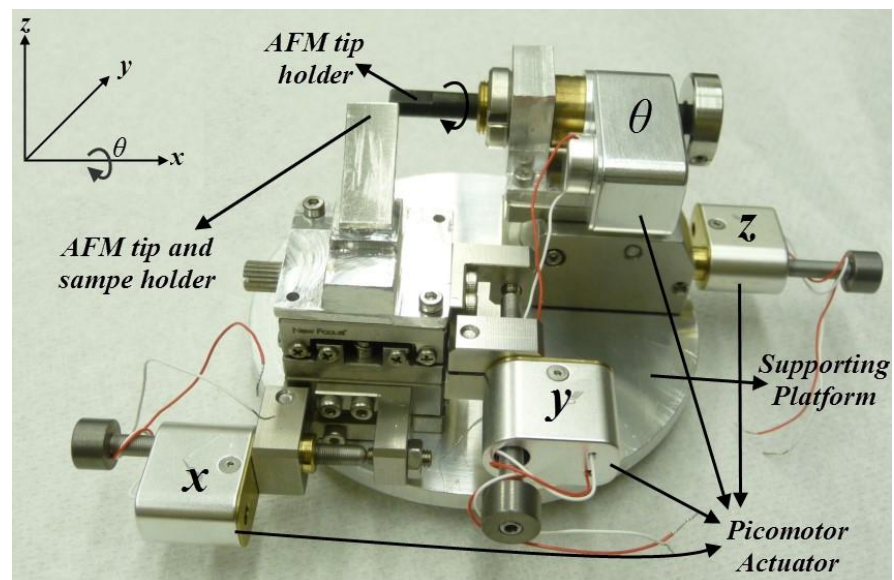
FIGURE 3.2: The photograph of the old nanomanipulator stage.

The *X* and *Y* linear motion stages (9061-XY), three picomotor actuators (8353-V), one rotating actuator (8341-V), and two picomotor drivers (8753) were all purchased from New Focus (now called Newport Corporate). The *Z* pivot stage (122-1155) was bought from OptoSigma corporate. Other components, including the supporting platform, piezo bender holders, and sample holders, were designed and manufactured at UNC Charlotte. The *X-Y-Z* motion stages are controlled by the three picomotor

actuators, and the θ rotation stage is controlled by the rotating actuator. These four actuators are connected to, and controlled by, the two picomotor drivers.

The supporting platform was made of aluminum alloy 6061T6, and manufactured to fit onto the 51 mm round SEM specimen holder. The solid model of this support platform is shown in FIGURE 3.3. The outer diameter of the supporting platform is 80 mm, which is compacted in order to have more space to move the testing stage around without touching any detectors or chamber walls inside the SEM. There are eight M2 threads (20 mm × 20 mm) on the top of the platform for mounting two motion stages.
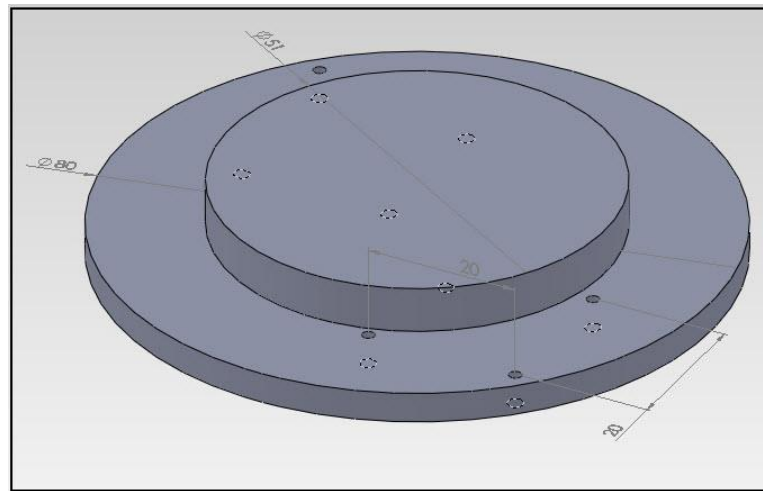
FIGURE 3.3: Solid model of the supporting platform.

After this manipulator stage were assembled, its overall dimensions were measured. In X direction, the size including actuator is around 130 mm. The dimension in Y direction is around 100 mm. For Z axis, the height is not fixed because of the required motion of Z stage. It is less than 50 mm in Z direction when the Z stage is at its highest position. Hence, the nanomanipulator stage occupies approximately 650 cm^3, which is compact enough to operate inside the SEM vacuum chamber.

3.2.2   Vacuum Feedthrough

To create a vacuum feedthrough, a flange with a hole and a welding lip was manufactured to replace the flange of one port on SEM chamber wall. On the flange, the diameter of the circular hole must be 28.45 ± 0.02 mm, which is in order to match the outer diameter of the double-end connector (CeramTec, 16003-02-W). It is a 19-pin connector with air-side and vacuum-side plugs. The material for the flange was chosen to be stainless steel 304, which had excellent machinability and weldability, and low outgas pressure. The following image shows the vacuum-side faces of the manufactured flange and the connector, FIGURE 3.4. The O-ring trench on the flange was made for an O-ring to create a seal at the interface between the flange and the SEM chamber wall. The welding lip on the flange was manufactured to match the welding lip on the connector, so that they could be welded easily.
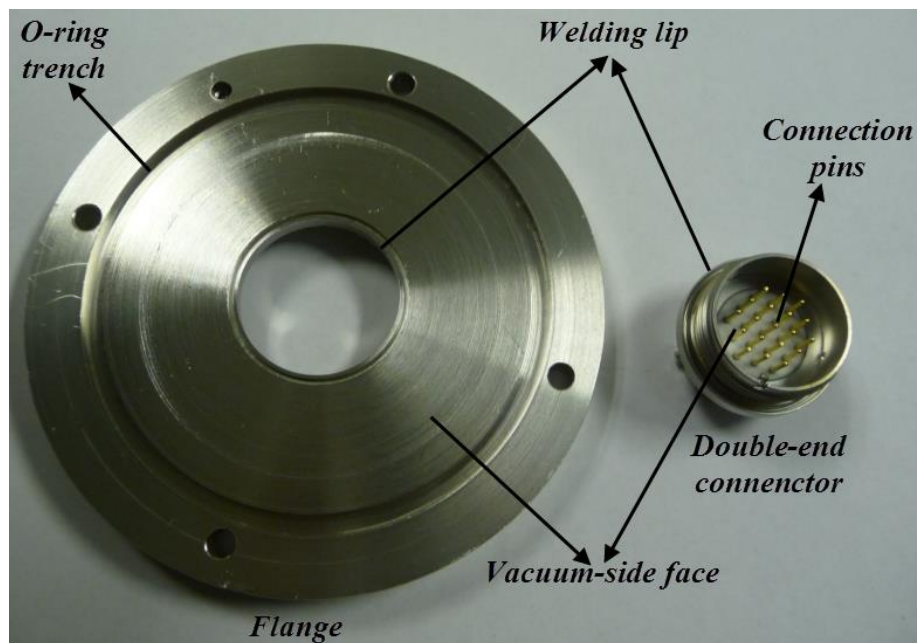
FIGURE 3.4: The image of the flange fabricated in-house and electrical connector for building a vacuum feedthrough.

The flange and the connector were sent to precision instrument machine shop in North Carolina State University for welding. Because the staff there had not followed the welding instructions when the connector was welded to flange, the connector was damaged by overheating as described below. This 19-pin connector was sealed by glass-ceramic materials, which is high-temperature tolerant. However, the glass seal did not survive under the high temperature during the welding process. Therefore, a gas leak was found when the welded feedthrough was mounted on SEM. Then, a vacuum-compatible epoxy (Epoxy Technology, 353NDT, Part A&B) was used to make a thin layer covered on the surface of glass-ceramic material. After the epoxy was cured, the gas leak problem was solved. The vacuum feedthrough was functional eventually, and mounted on SEM (see FIGURE 3.5).

3.2.3 Picomotor Actuator Drivers and Control Software

The driver for controlling picomotor actuators was the intelligent open-loop picomotor driver module, which had three channels capable of driving three different actuators, as shown in FIGURE 3.5. The drivers were connected to the air-side plug of the connector on the vacuum feedthrough, while the picomotor actuators were connected to the vacuum-side plug, such that it established a continuous conductive path between the drivers and the picomotor actuators. Then the drivers were connected to a computer where the controlling software and hardware interfaces were installed.
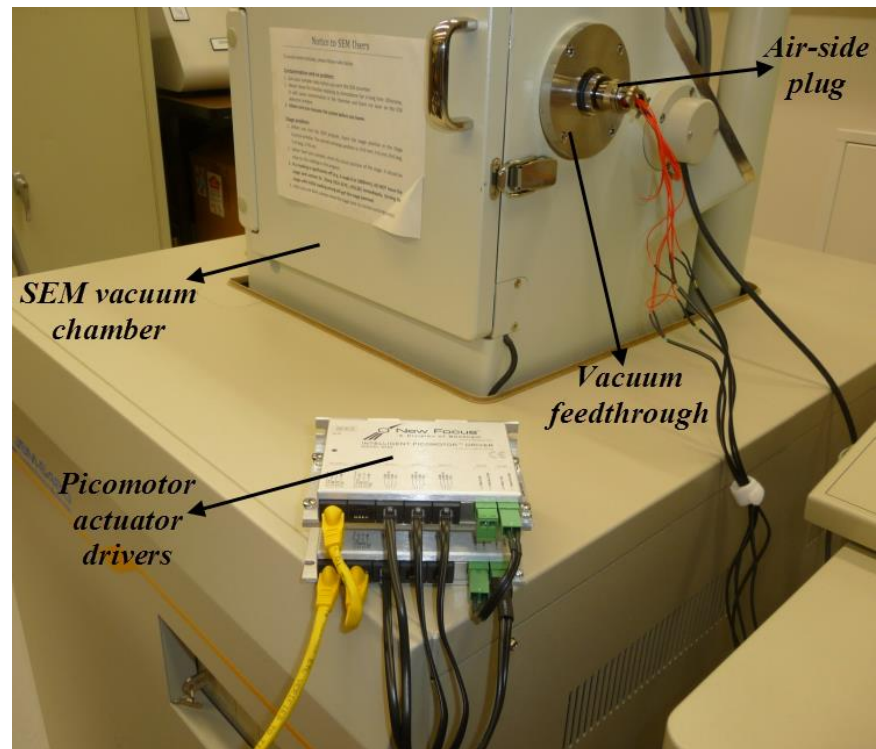
FIGURE 3.5: The photograph presents two picomotor actuator drivers and vacuum feedthrough.

The software controlling the drivers is the NewFocus picomotor distributed control network (DCN) set-up and diagnostic utility, which enables users to test the basic functionality of the picomotor drivers. It was written in Visual Basic and uses dynamic link library (DLL) functions to communicate with the modules. The picomotor driver control panel is shown in the FIGURE 3.6. It has two motion control modes: velocity and position. In velocity mode, desired velocity and acceleration are input independently. The range of input velocity value is -2000 to 2000 pulses/second. The positive or negative symbol represents the different motion directions. In position mode, the actuator moves the number of steps which is entered in Jog Step, which is currently grey in the figure meaning it is not enabled.
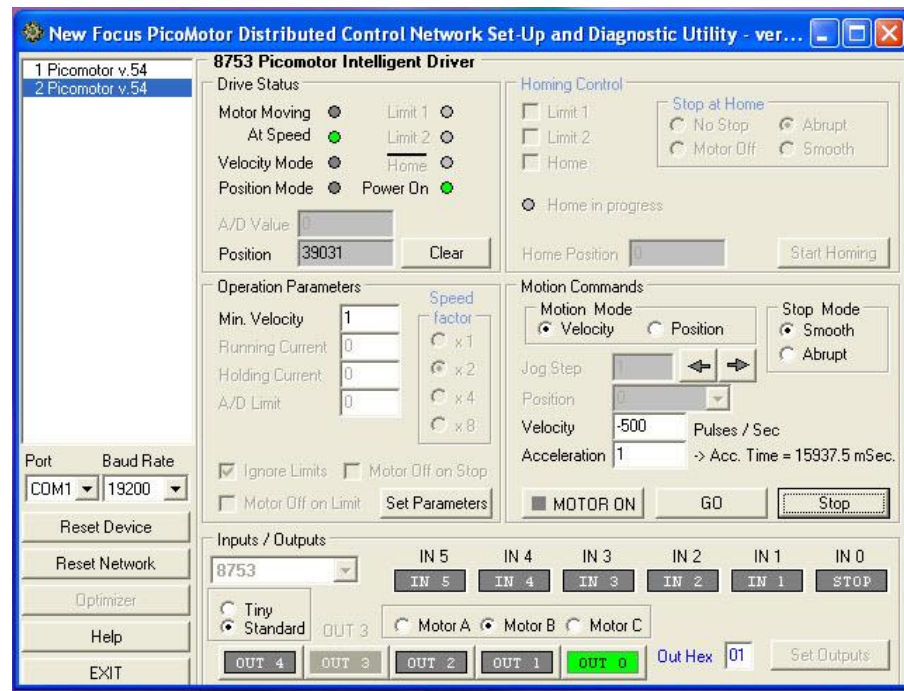
FIGURE 3.6: A screenshot of the DCN control panel for the picomotor drivers.

3.2.4   Piezoelectric Plate Bender

After the basic nanomanipulator system was complete, it was capable of performing basic functions, such as manipulating and stretching nanostructures. To perform mechanical resonance vibration testing, a piezoelectric plate bender (Noliac, CMBP05; FIGURE 3.7A) was needed to vibrate the probe, in turn to vibrate nanostructures attached on the probe. Basically, the piezoelectric plate bender has two control modes, FIGURE 3.7B and C.

When the piezoelectric plate bender is connected to alternative current (AC) source, a so-called differential voltage control mode is activated and the bender deflects both upwards and downwards with tiny amplitudes (FIGURE 3.7B). If the applied electrical signal is a continuous function with a known frequency, then the bender will vibrate the probe and the attached nanostructure at the same frequency. By sweeping across a range of frequencies, the resonant frequencies of nanostructures can be determined through finding their maximum oscillations under SEM. Another purpose of

providing AC to the piezoelectric plate bender is to measure the spring constant of AFM cantilever in vacuum if this AFM cantilever is used as a force sensor. When the piezoelectric plate bender is connected to direct current (DC) source, the single side voltage control mode (FIGURE 3.7C) is activated, and the bender only bends to single side. With providing a small DC voltage to the piezoelectric plate bender, it can result in fine movement of probes attached on the bender.
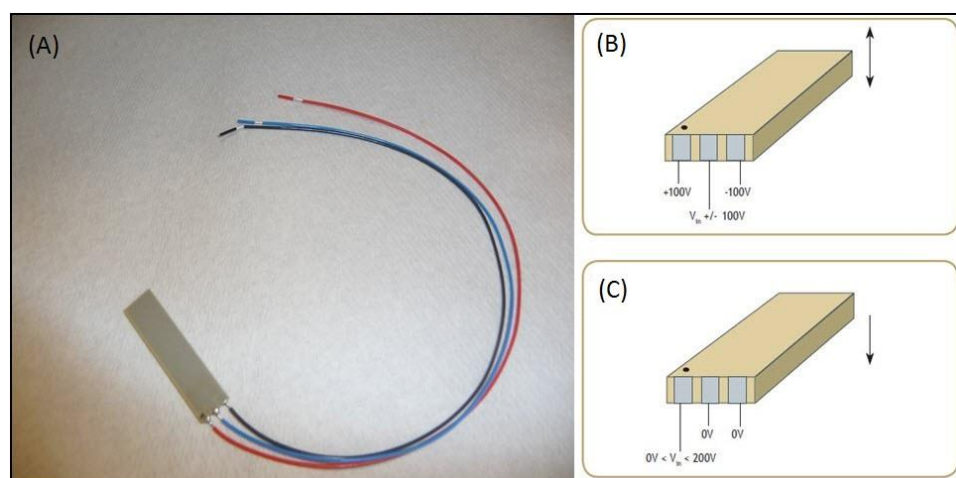
FIGURE 3.7: The images of piezoelectric plate bender (A) and its two control modes: (B) differential voltage control; (C) single side voltage control.

3.3 Performance of the Nanomanipulator

3.3.1 Performance of Motion Stages

Three linear motion stages (*X-Y-Z*) are controlled to move stepwise. The total travel ranges are 8 mm both for *X* and *Y* stages, and 6 mm for the *Z* stage. Two rotation stages can be continuously rotated. One rotation stage θ is controlled automatically, while another one ψ is controlled manually. The step resolutions of *X* and *Y* motions are limited by the picomotors, which the minimal step is specified to be less than 30 nm according to the vendor. The way to calibrate the step resolution was measuring the displacement after a large number of steps. It was difficult to distinguish the difference

of one step movement because of the limitation of image resolution under SEM. It was assumed that each step movement driven by the same type of actuator was equivalent, and then the step resolution was determined by the total movement divided to the step amount. For example, the stage moved a distance of 5.43 ± 0.30 μm after 214 steps, which meant the step displacement was 25.4 ± 1.4 nm. With a systematic study in SEM, the step resolution was found between 20 nm and 30 nm, which was consistent with the vendor's specification. Yu claimed that the step sizes were measured to be around 4 nm in one direction and 10 nm in the reverse when the actuator was driving in slow motion (1 step/second), because there appeared to be a settle-back effect of the stage, although the single step of picomotor in fast motion ($\geq$ 2 steps/second) was between 20 and 30 nm [58]. This was consistent with our results achieved in fast motion. The higher step resolution was not found in slow motion in our study, which was consistent with other reported results, that this type of picomotors had a step resolution in the range of 20 − 30 nm either in slow or fast motion [116, 118-120]. The rotating picomotor controlling the rotation of the θ stage had angular step size of around 0.04°, which was little higher than the reported value as 0.02° [58, 118]. The rotation resolution was determined by counting the steps for a 90-degree rotation.

3.3.2   Performance of Piezoelectric Plate Bender

The piezoelectric plate bender is an important element served as an actuator and an oscillator for the AFM tips and probes. Therefore, it is necessary to study the performance of this plate bender. The changes of the deflection of plate bender were inspected with altering the applied DC voltage from a DC power supply (BK Precision, 1787B). In the beginning of the study, a nanofeature (one nanowire with two small nanowires attached) was clamped on an AFM tip fixed on the piezoelectric plate bender, and pulled out from a TEM grid, FIGURE 3.8A. This nanofeature was considered as a

pointer, FIGURE 3.8B, which indicates the position of the nanofeature reached after applying the voltage. Then a series of SEM image were captured for measuring the distance of the nanofeature movement at each applied voltage, for example at 1V (FIGURE 3.8C) and at 16V (FIGURE 3.8D).
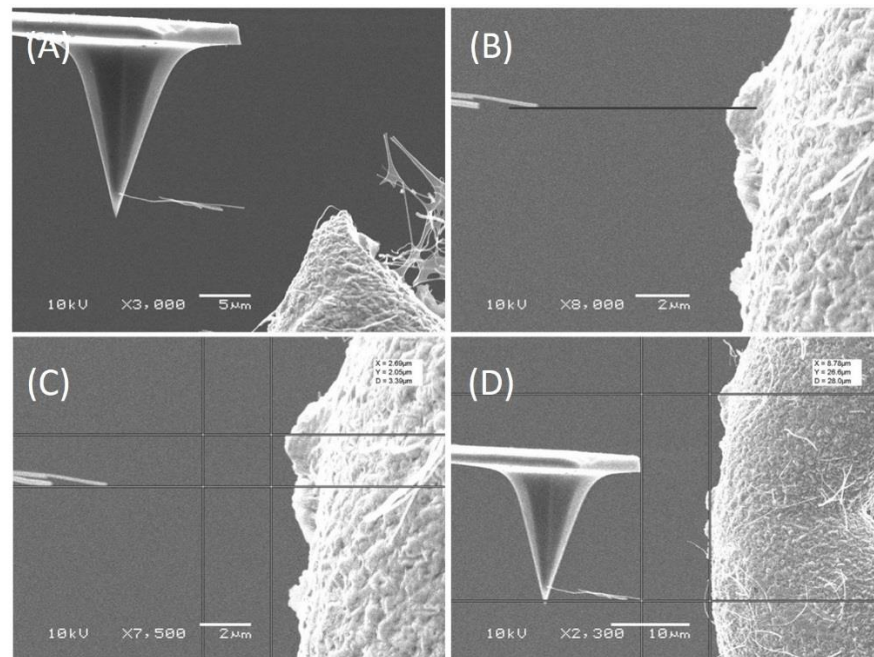
FIGURE 3.8: The SEM images representing the performance of piezoelectric plate bender: (A) a nanofeature was pulled out; (B) the nanofeature was used as a pointer; (C) the displacement of the pointer at 1 V; (D) the displacement of the pointer at 16 V.

In this study, a set of applied voltages and corresponding displacements data were recorded, and plotted as FIGURE 3.9. The graph demonstrates that the overall performance of the plate bender with deflection in a large voltage range (e.g., 0 – 30 V) can be best fitted into a second order polynomial equation (17),

$$y = 0.026x^2 + 1.217x + 0.331 \tag{19}$$

where, x and y are the applied voltage and the corresponding deflection of piezoelectric plate bender in unit of μm. However, the piezoelectricity of this plate bender in a range of lower voltage (e.g., 0 – 5 V) is better fitted into a linear equation (18),

$$y = 1381x + 331 \tag{20}$$

where the deflection of the plate bender is in the unit of nm.
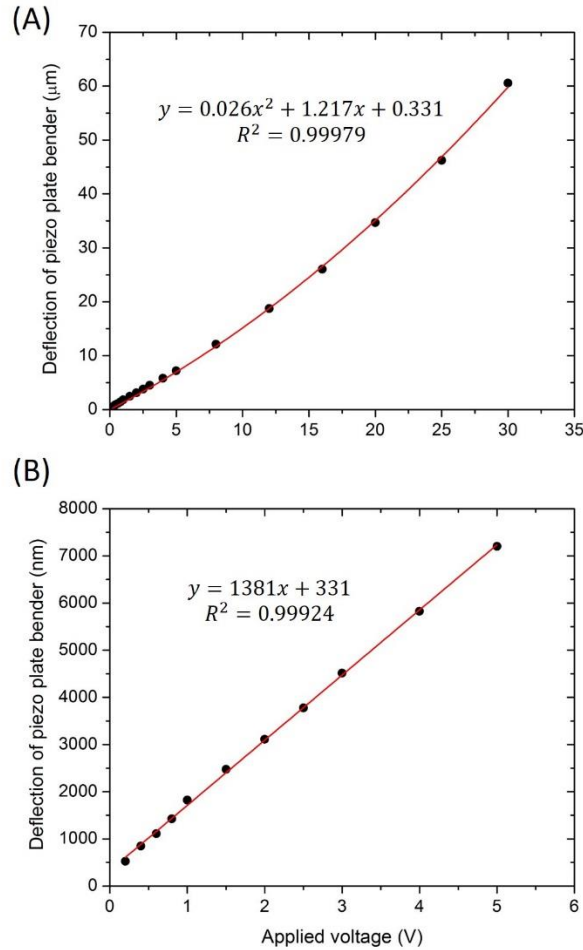
FIGURE 3.9: The deflections of piezoelectric plate bender in the voltage range of $0-30$ V (A) and $0-5$ V (B), with their fitting curves and equations.

The two fitted curves are both intercepting at 331 nm on the y axis when x is equal to 0. It is not real that the piezoelectric plate bender deflects 331 nm with no applied voltage. So this value (i.e., 331 nm) should be a system error which may be from the image analysis software, or SEM instrument, or the piezoelectric plate bender itself. For the DC power supply used in this study, it has the minimal voltage change as 0.01 V. Therefore, in the range of $0-5$ V, the deflection resolution of the piezoelectric plate bender is 13.81 nm, which is rounded to 14 nm. For the range of $5-30$ V, its deflection

resolution can be calculated based on the first derivative of equation (17) as the equation (19),

$$\frac{\Delta y}{\Delta x} \approx \frac{dy}{dx} = 0.052x + 1.217 \tag{21}$$

where Δy is the deflection resolution when the minimal voltage change Δx is 0.01V. Since the voltage x is in the range of $5 - 30$ V, the amount of $\Delta y/\Delta x$ is in the range of $1.477 - 2.777$ μm/V. Therefore, the deflection resolution Δy should be in the range of $0.01477 - 0.02777$ μm, which is around $15 - 28$ nm. The deflection resolution of the piezoelectric plate bender can be improved by providing DC voltage with a lower minimal voltage change.

3.3.3 Summary

According to results of systematic performance studies, technical specifications of the home-made nanomanipulator system are summarized in TABLE 3.1.

TABLE 3.1: Technical specifications of the home-made nanomanipulator system.

Items	Specifications
Testing stage	• Max stage size: 13 cm x 10 cm x 5 cm • Degrees of freedom: 5
X	• Step resolution: 20-30 nm
Y	• Range of motion: 8 mm
Z	• Step resolution: 20-30 nm • Range of motion: 6 mm
θ	• Rotation resolution: 0.04° • Automatic control
ψ	• Rotation resolution: 1° • Manual control
Piezoelectric plate bender	• Deflection resolution: 14 nm at 0-5 V • Deflection resolution: 15-28 nm at 5-30 V
Picomotor actuator driver	• Speed resolution: 1 step/second • Speed range: -2000 -- +2000 steps/second
Vacuum feedthrough	• 19-pin connector: flexible to add on more functionalities • User installable and removable
Function generator	• Voltage range: 0-10 V • Frequency range: 0-16 MHz
DC power supply	• Voltage range: 0-30 V • Voltage resolution: 0.01 V

3.4   Improvements to the Nanomanipulator System

The aforementioned nanomnipulator system was first investigated for the feasibility of *in situ* SEM tests, which is part of my Master's thesis work. Results, present in Appendix B, show that it is capable of performing *in situ* tests. However, to obtain more accurate results from this system compared to other reported nanomanipulator systems, several improvements were implemented. FIGURE 3.10 shows the updated version of the nanomanipulator stage. Compared to the old one shown in FIGURE 3.2, the new stage has incorporated in one new piezo plate bender (Noliac, CMBP02), one continuous rotation stage ψ (OptoSigma, 122-1155) and one re-designed sample/tip holder. The addition of these features significantly enhances the performance of the nanomanipulator system in turn producing more precisely controlled testing.
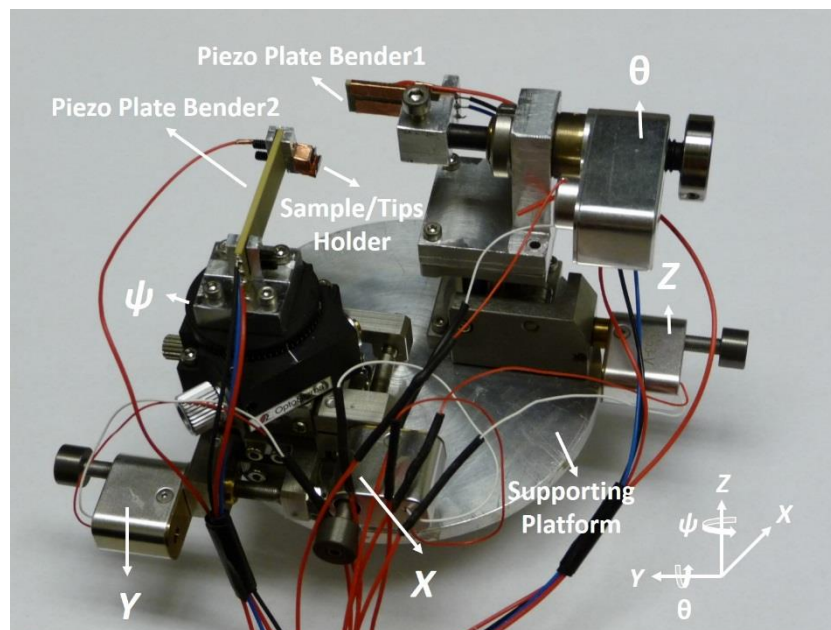
FIGURE 3.10: The updated version of the nanomanipulator stage.

3.4.1   Implementation of Two Different Tests on Individual NWs

In some reports of mechanical characterization of nanostructures, different testing techniques were applied to the same batch of nanostructures for the cross

comparison of results from different tests [59, 65]. However, there was no report claimed to use different testing techniques to characterize the same individual nanostructure. In this dissertation work, we proposed to perform two different tests on individual B_4C NWs with our unique testing setup. Because it is a non-destructive test, the first testing technique must be resonance vibration test. The NWs subject to this test only undergo elastic deformation, which results in no change to their intrinsic properties. The second testing technique, either tensile test or buckling test, can still measure the intrinsic properties of the tested NWs. Results obtained from the two different tests can then be compared.

To perform two different tests on individual NWs, a new sample/tip holder and a new piezo plate bender 2 were added into the system as shown in FIGURE 3.10. The schematic set up is shown in FIGURE 3.11. The tungsten tip 1 is fixed on the piezo plate bender 1, while the tungsten tip 2 is fixed on the sample/tip holder. Two tungsten tips are connected to a function generator, which is capable of providing an AC signal with a DC bias. If an AC signal is applied to the piezo plate bender 1, then the NW clamped on the tungsten tip can be mechanically excited. If an AC signal with a DC bias is applied between two tungsten tips, then the NW can be electrically excited. In the second testing technique, the AFM tip mounted on the sample/tip holder is used as a force sensor, so it is required to calibrate its spring constant. The resonant frequency of the AFM cantilever can be measured by applying an AC signal to the piezo plate bender 2, then its spring constant is determined via combining with the dimensional information of the AFM cantilever, as discussed in Appendix B.
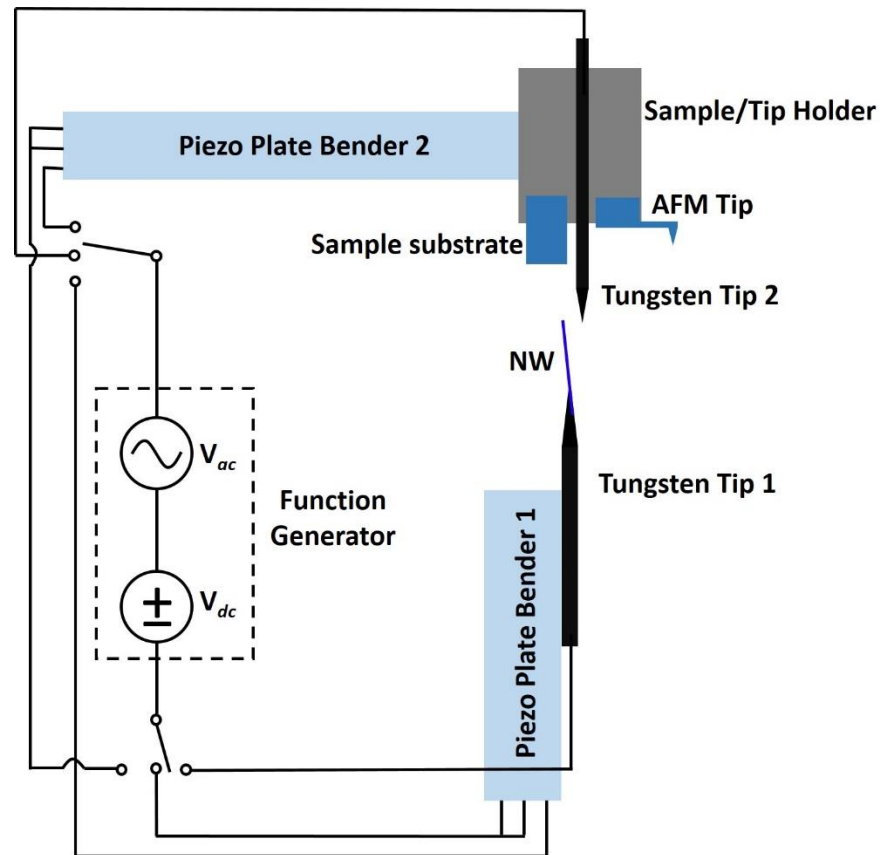
FIGURE 3.11: Schematics of setup for performing two tests on individual NWs.

For testing individual NWs are originally laid on the edge of sample substrate, and then they are fixed on the tungsten tip 1 by depositing a clamp by EBID. The NW is pulled out from the substrate, and moved close to the tungsten tip 2. The resonance of the NW is measured either by electrical or mechanical excitation resonance vibration tests. After its resonant frequency is determined, the NW is moved close to AFM tip. The free end of NW is then clamped onto the AFM tip by EBID. Consecutively, the tensile or buckling test is carried out by moving the AFM tip towards or away from the tungsten tip 1, respectively.

The reason why the function to perform electrically excited resonance vibration tests is added to the nanomanipulator system is discussed below. Mechanically excited resonance vibration test was first used to test several B_4C NWs. But it was found that it

was difficult to observe resonances of those NWs whose resonant frequencies were larger than 2 MHz. This was because more energy was needed to reach visible vibration by the mechanical excitation from the root end of a NW. However, it was much easier to reach a large vibration by the electrical excitation from its free end. In electrical excitation, the force between the NW and the counter electrode (which is the tungsten tip 2) was known as a function of the applied electric filed and its frequency [39]. When an AC signal ($V_{ac}\cos\omega t$) with a DC bias (V_{dc}) is applied between two electrodes, the force acting on the NW is:

$$
\begin{aligned}
F\left(t\right) &= \alpha\left(\Delta V + V_{dc} + V_{ac}\cos\omega t\right)^2 \\
&= \alpha(\Delta V + V_{dc})^2 + \frac{1}{2}\alpha V_{ac}^2 + 2\alpha\left(\Delta V + V_{dc}\right)V_{ac}\times\cos\omega t + \frac{1}{2}\alpha V_{ac}^2\cos 2\omega t
\end{aligned}
\tag{22}
$$

where, ΔV is the work function difference between the NW and the counter electrode, and a is the proportionality constant [39, 59]. Theoretically, based on this equation, the NW can vibration when the frequency of applied signal is at half-harmonic or harmonic frequency of the NW. So it is necessary to check the response of NW at $2f$ or $0.5f$, if the NW is resonated at a frequency f. The differences of resonant frequencies of NWs obtained from both mechanical and electrical excitations are found to be within 1%, so it is reasonable to use either excitation method for resonance vibration test.

3.4.2   Development of Measuring Deflection of Cantilever

It is known that the AFM cantilever is playing a role as a force sensor in *in situ* tensile and buckling tests. The applied force P of this cantilever-based force sensor can be calculated by multiplying the deflection of cantilever d and its spring constant k, that is $P=k\times d$. This Hooke's law was obeyed only if the cantilever deflection was within the linear regime, which was the case for most tensile tests since the maximum cantilever deflection was usually less than 5% of the length of the cantilever [59]. To obtain a reliable value of P, the cantilever deflection d needs to be accurately measured.

There are several reported approaches to determine the cantilever deflection [36, 58, 59, 65, 91, 121]. All of them were tried in this dissertation work, and none of them was found to be suitable for testing B4C NWs, as discussed below. The first approach is to directly measure the deflection of the soft cantilever by comparing the instantaneously-captured SEM images during unloading and loading. The deflection of the soft cantilever is the change of lateral distance between its root end and free end, as red lines marked in FIGURE 3.12. Two ends of a NW was fixed on a soft and stiff cantilevers. The soft cantilever deflected when it moved away from the stiff cantilever (as shown in the direction of arrow in FIGURE 3.12A). When the NW was fractured, the soft cantilever recovered to unloaded position, FIGURE 3.12B. The difference of these two later distance in loaded and unloading conditions was the measured cantilever deflection. The major drawback of this method is that the whole cantilever is required to be imaged, which means SEM images are captured in lower magnification with lower resolution.
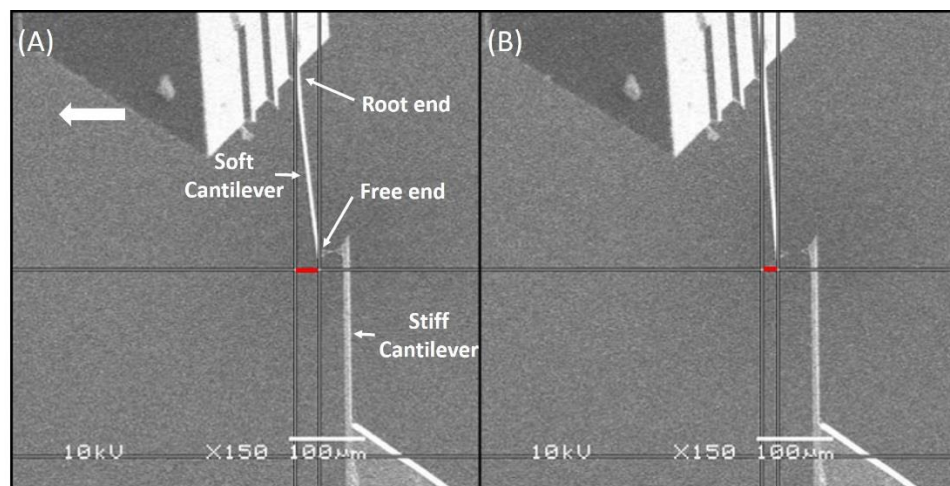
FIGURE 3.12: The demonstration of directly measuring cantilever deflection by comparing the lateral distances between its root and free ends (red lines) in (A) loaded and (B) unloaded conditions.

The second method, measuring the deflection slope of the cantilever, was also used to calculate the cantilever deflection, by the relationship as equation (23),

$$\delta = \frac{2}{3}\theta L \qquad (23)$$

where δ is deflection, θ is the deflection angle at the free end, L is the length of the cantilever [59]. It was found that this method was practically unsuitable for detecting a small force. For example, a cantilever with the length of 300 μm is used here. Based upon the above equation, 1 degree of deflection angle can be measured if around 3.5 μm deflection. In another expression, if 100 nm cantilever deflection happens, there is only 0.029° angle change at the free end of cantilever, which was not possible to detect and measure. With many attempts in our experiments, this method was proved to have more uncertainties so that it was no adopted.

The third method to measure the deflection of cantilever was by calibrating the response of the piezoelectric plate bender, if the bender was employed to actuate the tension of nanostructures. During the tensile tests, each applied DC voltage corresponded to one deflection of the cantilever that was captured instantaneously by SEM. After tests, the same sequence and magnitudes of DC voltages were applied again, and then the corresponding cantilever deflections were captured as well. The deflection discrepancy (D_n) of unloaded and loaded cantilever at each applied voltage was determined by analyzing the SEM images, FIGURE 3.13 [121].
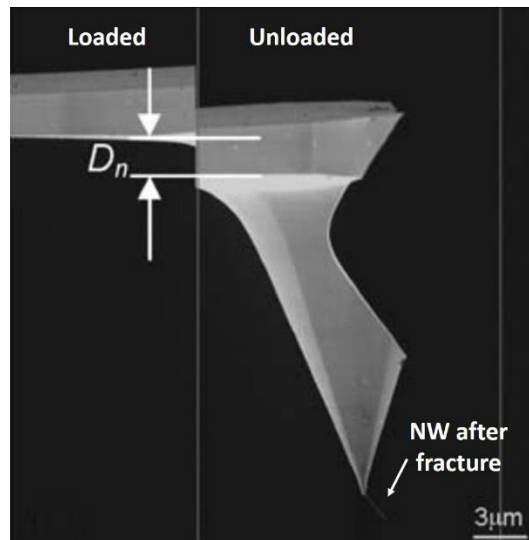
FIGURE 3.13: SEM images recorded for the unloaded and loaded cantilever at the same applied voltage [121].

This approach was not employed in this work because it was not applicable for *in situ* buckling test for B_4C NWs. Because the method required the AFM tip to relax after loading, then the positions of unloaded and unloaded cantilever were compared. However, B_4C NWs were not fractured under buckling test, so the AFM cantilever could not be relaxed. Moreover, this method was more time-consuming.

Instead of measuring the deflection directly by viewing the single cantilever as shown in the above three methods, a fourth method was tried. This method attempted to use a reference cantilever to measure the deflection in a more accurate way. A type of AFM chip with three different cantilevers was chosen to employ this method in buckling test, FIGURE 3.14A. The shortest cantilever was employed as a force sensor. The deflection of this shortest cantilever was determined by measuring the change of vertical distance between the shortest and longest cantilevers. For example, the initial vertical distance between these two cantilevers was L_0 at moment of $t=0$, and the distance was L_1 at next moment $t=1$ during buckling test. Then the deflection of cantilever at moment of $t=1$ is L_1-L_0, FIGURE 3.14B. SEM images at each moment of buckling test were captured. Then the distances between two cantilevers were measured by an image

processing software, ImageJ. However, two cantilevers were not at the same height. The

height distance between two cantilevers was around 80 µm for the AFM tip that we used.

As shown in FIGURE 3.14C, the edge of reference cantilever was vague, which leads

to a large the measurement error in cantilever deflection. This is the major disadvantage

of this approach.
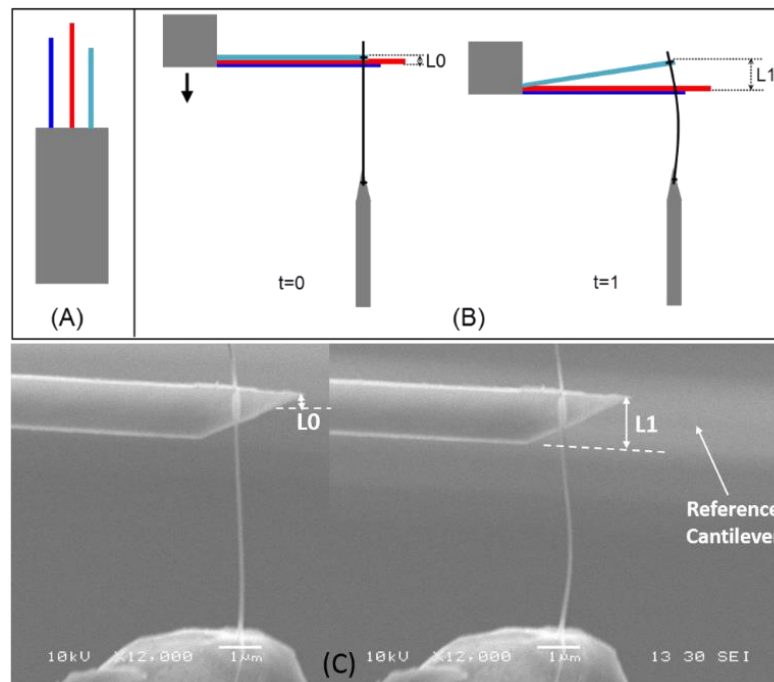
FIGURE 3.14: (A) Schematic drawing shows the top view of an AFM chip
with three cantilevers. The longest one is used as a reference to determine the
deflection of the shortest cantilever during buckling test; (B) Schematics of buckling
test process at two different moments. The AFM chip present is by side view, when the
shortest cantilever is at the top; (C) SEM images of buckling process to demonstrate
the deflection of AFM cantilever.

All four methods discussed so far were proposed by other researchers [36, 58,

59, 65, 91, 121]. While adopting them into this dissertation work, disadvantages of each

method were clear. Therefore, a new method was developed. The principle of the new

method is same as the third one, (i.e., reference cantilever based method), but the

reference cantilever is now being replaced by a reference feature that is very close to the

cantilever used for force sensing, such that the edges of both the reference feature and the sensing cantilever can be clearly seen in the same SEM images during tests.

An arbitrary micro-feature was picked up and manipulated to perpendicularly attach on a reference cantilever, FIGURE 3.15A and B. Such that the micro-feature was used as a reference feature with the almost same height as the cantilever used for testing, which maked the reference feature in focus as well during the testing, as shown in FIGURE 3.15C and D. The distance between the cantilever and the reference feature could be determined more accurately, in turns to achieve more accurate measurement of the deflection of cantilever.
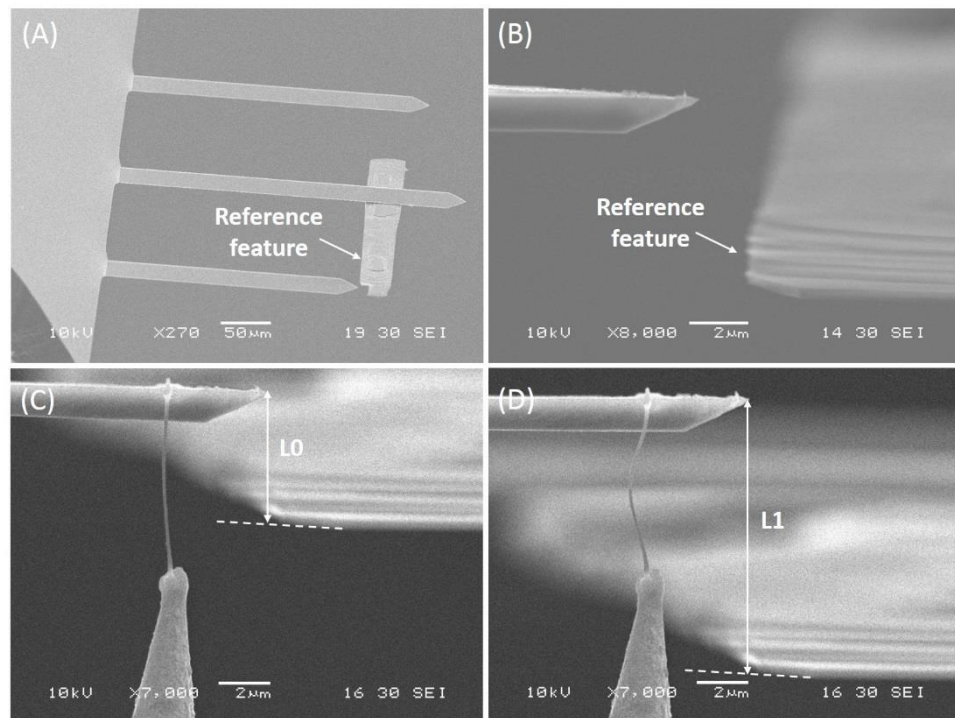
FIGURE 3.15: SEM images of (A) top view of a micro-feature attached on a reference cantilever to be a reference feature; (B) side view of this reference feature; (C) and (D) show the buckling process with clear distance determination.

The buckling forces in buckling tests of B_4C NWs were found to be less than 1 µN, so an extremely compliant cantilever was desired so that large deflections of cantilever could be observed and measured under these small forces. However, the

compliant cantilever was not suitable for tensile tests of B_4C NWs. For example, as shown in FIGURE 3.16, a B_4C NW was subjected to tensile test with a soft cantilever. The deflection angle of the cantilever was 12°, which is much larger than the limiting range of 5°. Furthermore, the misalignment of NW in XY plane was 18°, which made the NW twisted at the clamped ends and eventually fractured at the clamp locations. It was reported that the misalignment angle should be less than 10° to have lower relative error for calculated Young's modulus [122].Therefore, a stiffer cantilever should be utilized for *in situ* tensile test. However, with a stiff cantilever, the deflection of cantilever under a small tensile load will be difficult to measure. So it is important to find a compromise between an accurate measurement of the cantilever's deflection and the planar alignment of NW.
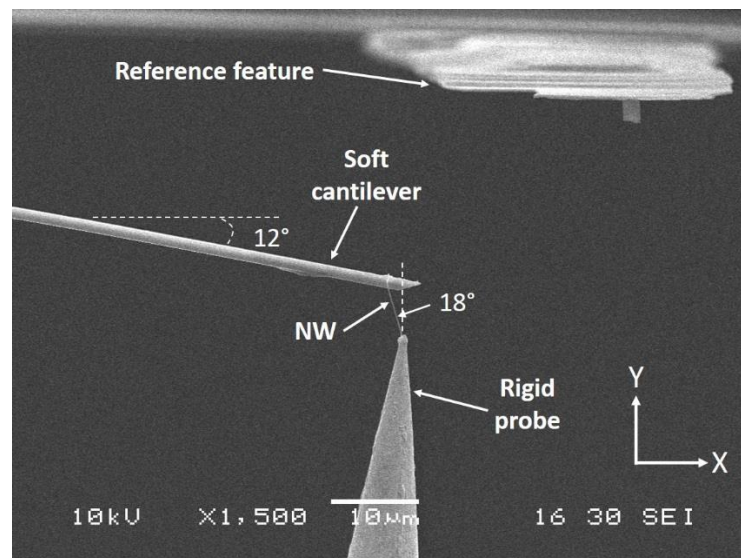
FIGURE 3.16: SEM image of tensile test of a B_4C NW with a soft cantilever.

To the best of my knowledge, other researchers chose to measure the accurate deflection with the sacrifice of the alignment of NW. The method proposed in this work is especially fit for tensile testing of strong nanostructures with considering both aspects. For example, a cantilever with stiffness about 15 N/m was used for tensile test on B_4C

NWs. Similarly, a carbon fiber was manipulated to attach on the AFM chip and close to the cantilever as a reference bar, FIGURE 3.17A. The SEM images of tensile testing process showed that the offset angle of NW and deflection angle of the cantilever were both small, FIGURE 3.17B. Then the deflection of cantilever was the difference of the vertical distance between the cantilever and the reference bar (*i.e., L1 – L0*).
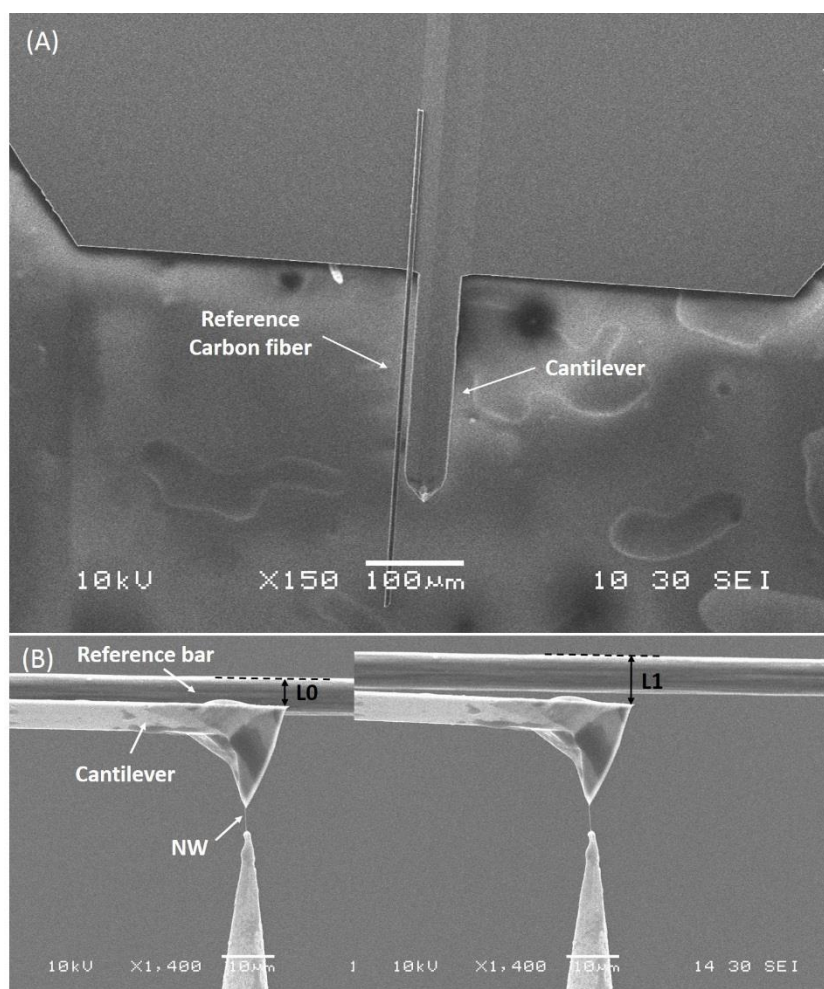
FIGURE 3.17: SEM images of (A) a carbon fiber attached nearby a stiff cantilever; (B) tensile testing process to determine the deflection of the cantilever (*L1-L0*).

3.4.3 Implementation of Probe Rotation

According to the equation (13) for resonance vibration test of nanostructure introduced in Chapter 1, the Young's modulus is proportional to the effective length of

nanostructure to the fourth power. So the error in length measurement will be dramatically amplified in the calculated modulus. For example, about 20% error in calculated modulus can be produced if a 5% error is existed in length measurement. Therefore, it is crucial to accurately measure the effective length of nanostructure. However, SEM imaging only provides two-dimensional (2D) projections of nanostructures. Thus the determination of the length of nanostructure from a 2D image is not accurate because the nanostructure does not position exactly in the XY plane for many experiments. So it needs to develop a method to determine the true dimensions and positions of nanostructures. There was a parallax method proposed to reconstruct a 3D representation of the NW based on two SEM images acquired at two angles (0 and 45 degrees) by tilting the NW holder. This method was not widely accepted because it required a lot of data analysis and a self-developed software [59, 123]. The best and simplest way to achieve 3D structure of NW is analyzing two SEM images captured at 0 and 90 degrees. For our SEM, the specimen stage is allowed to tilt -10° to 90°. However, the size of nanomanipulator stage restricts the tilt angle no more than 30° when it is mounted on the specimen stage. This is because the nanomanipulator stage will collide with detectors or chamber wall inside SEM if the specimen stage is tilted to a larger angle. So an independent rotation or tilting stage is required to fulfil it. The rotation stage was reported to be incorporated in a home-built nanomanipulator by others to tilt the NW holder [91, 123]. However, they were not capable of accurately controlling a 90 degree rotation. Although the calibration of the rotation stage could be performed by tracking the size change of the calibrated pattern attached on the rotation stage with a sequence of steps, the hysteresis of forward and backward rotations resulted in large uncertainties. Therefore, a straightforward approach is introduced here to meet this need.

A tungsten probe is attached on a piezoelectric plate bender with a rectangular cross section (FIGURE 3.10). A double-side copper tape is used to bind the tungsten tip and the piezo plate bender. The double-side copper tape is also electrically conductive, so that it can be applied to create an electrical connection between the tungsten tip and an electrical wire, and then to have an electrical open circuit together with another tungsten tip. With this thin copper tape, the tungsten tip is well aligned on the plate bender. When the plate bender is rotated to the position where only the side face is imaged, this position is called as 0 degree. Then 90 degree is the position where only the front face of plate bender is imaged after rotation, FIGURE 3.18. Using this method, the rotation of NW attached to the tungsten tip is precisely controlled at 0 and 90 degrees.
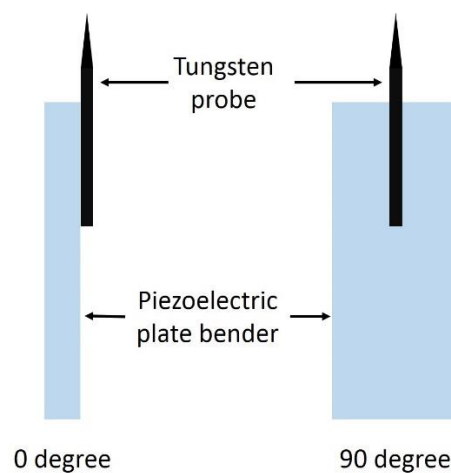
FIGURE 3.18: Schematics of a tungsten tip attached on a piezoelectric plate bender with side view (0 degree) and front view (90 degree).

Once SEM images of the NW at 0 and 90 degrees are captured, its true effective length of NW and positions can be determined. For instance, FIGURE 3.19 shows two captured SEM images of a NW at 0 and 90 degrees. Based on the offset angles (i.e., α and β of the NW both in XY and YZ planes) and the average length of NW (L) in Y axis measured from 0 and 90 degrees, the accurate determination of the effective length L_{eff} can be achieved according to the following equation

$$L_{eff} = \sqrt{(L \times tan\alpha)^2 + L^2 + (L \times tan\beta)^2} = L \times \sqrt{(1 + tan\alpha^2 + tan\beta^2)} \quad (24).$$

More details about determining the accurate effective length is present in Appendix C.
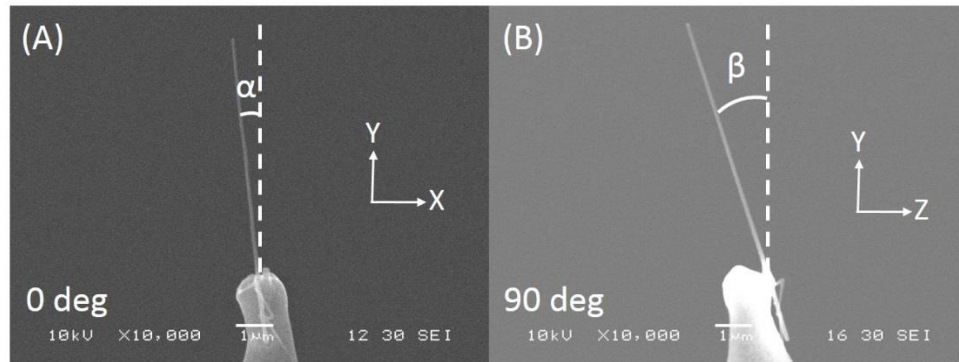
FIGURE 3.19: SEM images of a B$_4$C NW on a tungsten probe at (A) 0 degree and (B) 90 degree.

The introduction of the rotation stage not only increases the accuracy for determination of the effective length of the tested nanostructure, but also has other two benefits. First, the observation of NW at two different angles: 0 and 90 degrees can be used to evaluate the suitability of the NW for axial tensile or buckling tests. For example, the NW shown in FIGURE 3.19B (i.e., when it was viewed at 90 degrees) has a large offset angle in Z axis, which means this NW is not suitable for tensile or buckling tests. It is because the NW will have a large height misalignment when the free end of NW is fixed on an AFM tip. Second, the observation at different angles can verify whether the clamp by EBID is successful. For example, FIGURE 3.20A showed a NW was clamped on the tungsten probe by EBID. It seemed that the EBID clamp was deposited on the tungsten probe tightly when it was imaged at 0 degree. But a small gap was found between the EBID clamp and the probe when it was observed at 90 degree, FIGURE 3.20B. In order to have a valid clamp, more EBID was carried out in the gap at 90 degree to build up a connection, as illustrate in FIGURE 3.20C.
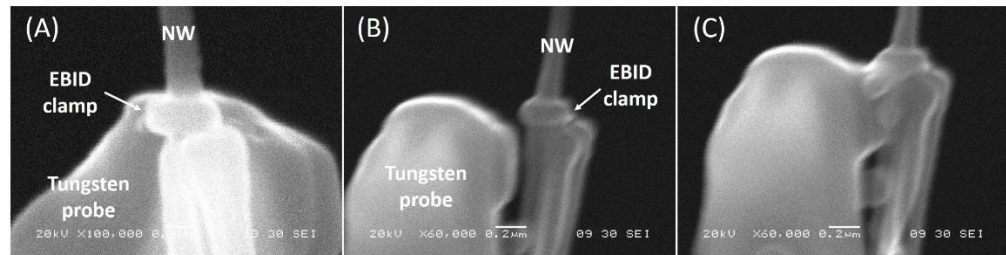
FIGURE 3.20: SEM images of a NW was clamped on a tungsten probe by EBID at (A) 0 degree and (B, C) 90 degree.

In short, by implementing a rotation stage with precise control of the probe rotation at 0 and 90 degrees, SEM images at these two angles can be acquired. This is beneficial to determine the accurate effective length of a NW, identify the suitability of NW for tensile or buckling tests, and verify the fidelity of EBID clamp.

3.4.4   Combination of Pre-test and Post-test TEM Analysis

It is known that accurate measurement in diameter of NW is essential to calculate the stress for tensile test and its second moment of area for resonance vibration and buckling tests. The typical resolutions for SEM and TEM are 3-7 nm and 0.1-1 nm, respectively [124], so we can achieve accurate diameter measurement for NWs with tens of nanometers in TEM, but not SEM. However, in most reports, diameters of NWs subject to *in situ* SEM tests were measured directly in SEM [28, 59, 61, 65, 91, 125]. Lin et al. had used cross sectional TEM imaging to determine the cross-sectional dimensions of NWs after *in situ* SEM tests. The tested NW together with the AFM tip was detached from the nanomanipulator and embedded into epoxy resin, and then sectioned by an ultramicrotome machine into a series of slices for TEM observation. Although very reliable dimensional measurement can be achieved by this method, it was challenging and , as a consequence, only one sample was present in the report [91].
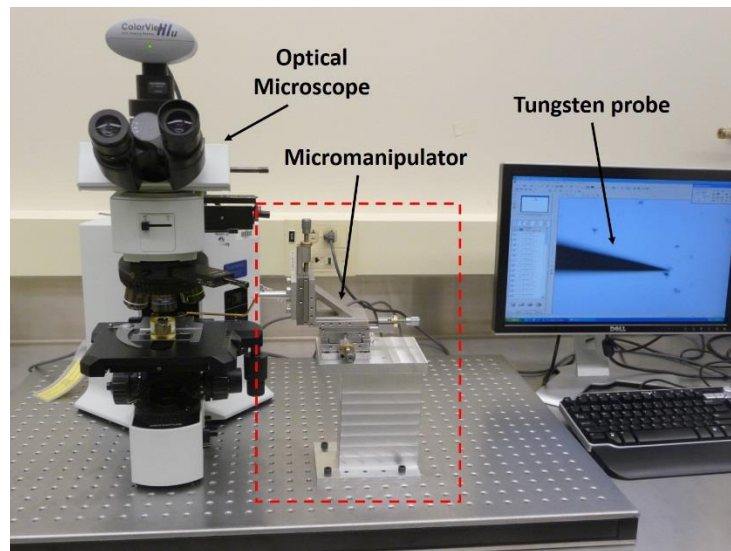
FIGURE 3.21: Photograph of the home-made micromanipulator. The tungsten probe shown the computer screen is used as an end effector to manipulate objects.

In this dissertation work, a different method was developed to use TEM to image individual NWs before and after *in situ* SEM tests. This method used a home-made micromanipulator under an optical microscope, as shown in FIGURE 3.21. The process of this study is schematically illustrated in FIGURE 3.22 and briefly described as following: (A) B_4C NWs were grown on a sample substrate. (B) NWs were transferred from the sample substrate onto a soft polydimethylsiloxane (PDMS) substrate by gently stamping the PDMS substrate against the sample substrate. (C) Individual NWs were picked up from the PDMS substrate by the home-made micromanipulator. (D) The picked NWs were laid on a TEM grid and imaged in TEM. (E) Suitable NWs after TEM imaging were detached from the TEM grid and transferred on the edge of a clean Si substrate by the micromanipulator. (F) The Si substrate along with NWs was mounted on the nanomanipulator stage. Then a NW was clamped on a tungsten tip and pulled out from the Si substrate for *in situ* tests. (G) The NW was subject to the resonance vibration test. (H) After the resonance vibration test, another end of the NW was clamped an AFM tip for tensile or buckling tests. (I) The NW after *in situ* tests was detached from the

AFM tip or tungsten probe and transferred on a TEM grid by the micromanipulator, and at last imaged again in TEM. Although this process is tedious, it gives useful information of individual tested NWs, including the cross-sectional size, the crystallographic defects, compositions, thickness of amorphous oxide layer, shape, and amorphous carbon layer formed during the tests. This comprehensive study for individual NWs offers accurate determination of their mechanical properties, and relations between the mechanical properties and their sizes, microstructures, compositions, shapes, and various effects.
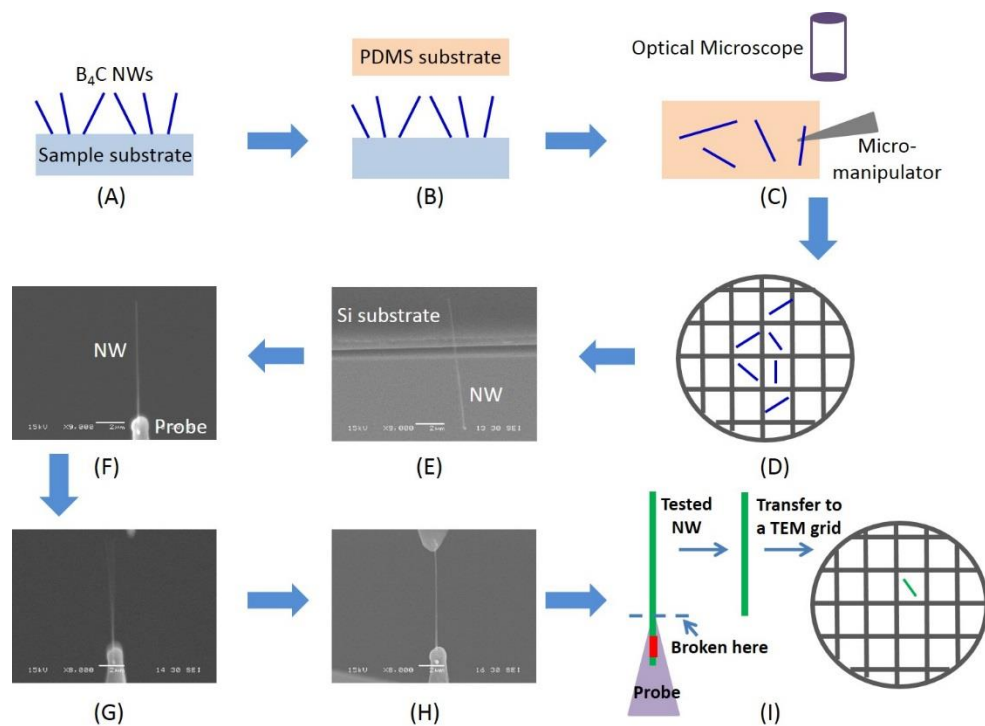
FIGURE 3.22: Schematics of the study process.

3.5   Conclusions

The details of building up a nanomanipulator inside the vacuum chamber of an SEM are specified in this chapter. The performance of the nanomanipulator system is studied and presented here. The technical specifications of this home-made nanomanipulator system have been evaluated. Since this system is used for *in situ* tests, many improvements have advanced the nanomanipulator system. Frist, each individual

nanowire can now be tested by two different techniques so that direct comparison of experimental data can be made. Second, the force measurement resolution is improved as compared to others' works. Third, the accuracy of determining the length of a tested nanowire is increased with the help of the additional rotational stage. Last, the pre-test and post-test imaging individual NWs by TEM are realized. These improvements facilitate more accurate mechanical characterization of 1D nanostructures.

CHAPTER 4:   IN SITU TESTING OF BORON CARBIDE NANOWIRES

4.1   Introduction of As-synthesized Boron Carbide Nanowires

As introduced in Chapter 1, crystalline B_4C NWs were produced by co-pyrolysis of B_2H_6 and CH_4 in a LPCVD system at temperatures zone of 964-997 °C in the laboratory. The majority of as-synthesized NWs had diameters between 15 and 90 nm, and lengths from a few micrometers up to ten micrometers [76]. It was later discovered that as-synthesized crystalline B_4C NWs possessed planar defects, such as stacking faults. The stacking faults were observed under TEM for some NWs, but were "hidden" in other NWs. A limited observation angle in the TEM was responsible for making the stacking faults appear invisible. Extensive experiments have been conducted and concluded that planar defects existed in B_4C NWs. The cause was a relatively lower stacking fault energy for B_4C materials [126]. Generally, the stacking faults on B_4C NWs can be divided into two categories: axial faults (AF) and transverse faults (TF). The axial faults are defined as the fault planes in a NW that are parallel to the preferred growth direction of the NW (FIGURE 4.1A), while the transverse faults are perpendicular to its preferred growth direction (FIGURE 4.1B).
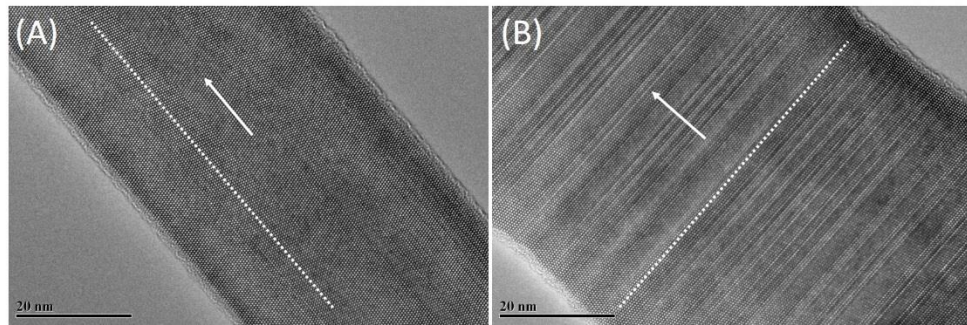
FIGURE 4.1: TEM images of (A) an AF NW and (B) a TF NW. The arrows represent the NWs' preferred growth directions, and the dash lines represent the fault planes.

It was reported that stacking faults in crystalline NWs play an important role in determining their mechanical properties [127, 128]. Therefore, it is necessary to study the mechanical properties for both AF and TF B_4C NWs. In this dissertation work, two types of B_4C NWs were carefully investigated by TEM, and characterized mechanically by *in situ* SEM tests.

4.2   Detailed Experimental Procedures

The experimental procedures were illustrated schematically in FIGURE 3.22 and also briefly described above. A further description is provide here. The optical microscope (OM) and SEM were used to identify long B_4C NWs grown on a SiO_2/Si substrate. Next a PDMS substrate gently contacted this area, such that many B_4C NWs were transferred to the PDMS substrate (FIGURE 4.2A). With the aid from the micromanipulator, selected NWs, which were chosen for *in situ* tests, were picked up, transferred to, and suspend on the carbon film on a TEM grid (FIGURE 4.2B). Then structural and compositional information for the NWs were studied by TEM and electron energy loss spectroscopy (EELS). Based on the TEM results, certain NWs were identified as suitable for mechanical tests. Those NWs were transferred to the edge of a clean Si substrate, and manipulated to protrude approximately vertically from the substrate edge using the micromanipulator (FIGURE 4.2C). Then the Si substrate and

overhanging NWs were mounted to the sample/tip holder on the nanomanipulator stage. A tungsten probe was moved close to pick up a NW that was to be tested (FIGURE 4.2D). The end of the NW that was suspended in air was clamped onto the probe by EBID. After a strong clamp between the NW and the probe was formed, the NW was pulled out from the Si substrate. Then the NW attached on the probe was resonated by mechanical or electrical excitations by applying an AC signal to the piezoelectric plate bender or between two tungsten probes respectively. The resonance frequency of the NW was determined by searching for its maximum vibration in SEM when sweeping the frequency range of the applied signal. After the resonance vibration test was concluded, the other free end of the NW was clamped to an AFM tip by EBID. A tensile or buckling test was carried out by moving the AFM tip away from or towards the tungsten probe. During this test, a series of high resolution SEM images were captured. The applied forces were determined by measuring the deflections of the AFM cantilever via SEM images. The change in NW's effective length was determined by analyzing SEM images too. In the last step of *in situ* tests, the NW was fractured by being stretched. Then the tungsten probe or the AFM tip, together with the fractured NW, was uninstalled from the nanomanipulator stage, and loaded under the OM. The remaining part of the NW on the probe or tip was broken at its root by the micromanipulator, and transferred to a TEM grid. Finally, a tested NW was imaged again in the TEM.
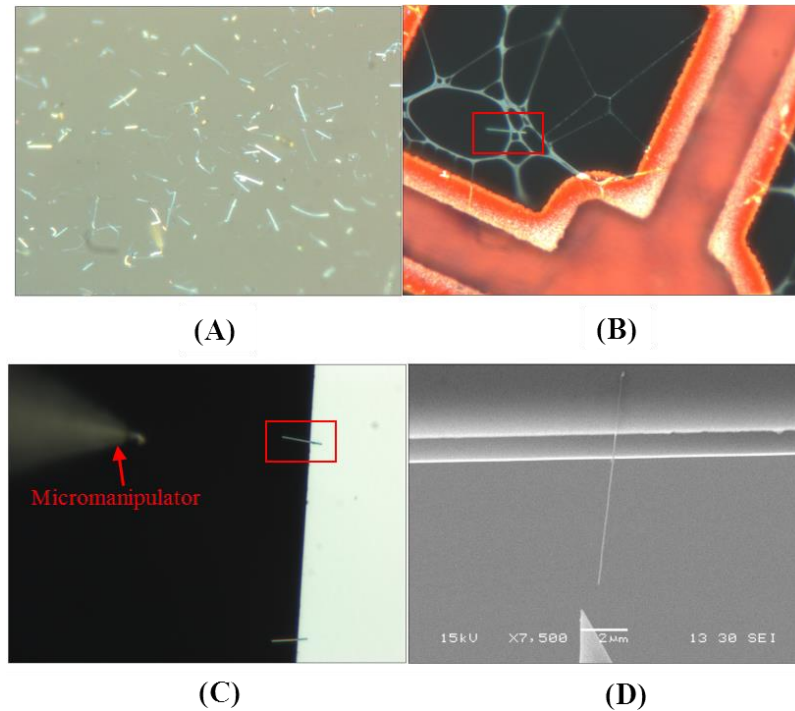
FIGURE 4.2: OM images of (A) B_4C NWs on a PDMS substrate; (B) one NW
suspended on carbon film on a TEM grid; (C) NWs protruded at the edge of a Si
substrate. (D) SEM image of the NW (same as the one marked with the red box in (B)
and (C)) on the edge of the Si substrate, and would be picked up using a tungsten tip.

4.3   Results and Discussion

4.3.1   Experimental Results of Resonance Vibration Test

After obtaining the resonance frequency of a B_4C NW from the resonance
vibration tests, the Young's modulus of that B4C NW was calculated in the process as
discussed in Appendix C. The experimental data and calculated results for all tested AF
NWs are presented in TABLE 4.1, while those for the tested TF NWs are presented in
TABLE 4.2. From these results, the calculated Young's modulus for AF NWs were in
the range of 253-510 GPa, while those for TF NWs ranged from 215-506 GPa.

TABLE 4.1: Experimental results for resonance vibration tests on B_4C AF NWs.

NW ID	D (nm)	L (µm)	f (MHz)	E (Gpa)	Note
062513#6	50.0 ± 0.7	9.02 ± 0.04	1.0127 ± 0.005	347 ± 12	
062513#5	49.1 ± 0.6	8.45 ± 0.28	1.1134 ± 0.005	334 ± 45	
051613#8	47.0 ± 0.9	4.87 ± 0.01	2.8008 ± 0.005	255 ± 10	a
080513#1	44.6 ± 0.6	6.71 ± 0.05	1.3940 ± 0.005	253 ± 10	b
Q080513#3	66.3 ± 0.6	5.00 ± 0.03	3.8205 ± 0.005	264 ± 8	c
051313#3	84.9 ± 0.9	6.69 ± 0.01	2.8694 ± 0.005	292 ± 6	
082113#5	94.0 ± 0.6	6.44 ± 0.04	3.6566 ± 0.005	333 ± 9	
082113#6	54.2 ± 0.6	8.16 ± 0.04	1.6239 ± 0.005	509 ± 15	d
082113#1	44.6 ± 0.5	3.98 ± 0.05	4.3701 ± 0.005	308 ± 17	
051313#6	59.3 ± 0.6	6.90 ± 0.02	2.1990 ± 0.005	397 ± 9	
082113#8	61.6 ± 0.7	6.14 ± 0.03	2.9473 ± 0.005	416 ± 12	
080713#5	68.0 ± 0.5	7.77 ± 0.02	2.2501 ± 0.005	510 ± 9	e
120413#8	52.0 ± 0.8	4.60 ± 0.01	3.5307 ± 0.005	264 ± 8	c

a: a small NW was attached on the part close to the free end of the tested NW;

b: the tested NW was distorted before *in situ* tests;

c: the tested NW was broken into two parts during the manipulation before tests;

d: a thick amorphous carbon layer formed on the part close to the clamp end of the tested NW;

e: a thick amorphous carbon layer and a small NW on the part close to the clamp end of the tested NW.

TABLE 4.2: Experimental results of resonance vibration tests on B_4C TF NWs.

NW ID	D (nm)	L (µm)	f (MHz)	E (Gpa)	Note
050913#3	74.3 ± 0.5	8.20 ± 0.05	2.1898 ± 0.005	500 ± 14	
051613#9	73.4 ± 0.3	5.42 ± 0.05	4.1021 ± 0.005	344 ± 12	c
051613#2	72.4 ± 0.6	6.53 ± 0.01	3.0302 ± 0.005	407 ± 7	
051613#4	73.2 ± 0.3	6.98 ± 0.04	2.8902 ± 0.005	473 ± 10	
080513#3	70.6 ± 0.3	6.83 ± 0.03	2.7045 ± 0.005	408 ± 6	
051613#6	88.0 ± 0.6	6.67 ± 0.01	3.1436 ± 0.005	323 ± 5	a
081313#2	53.6 ± 0.5	4.15 ± 0.03	5.3633 ± 0.005	379 ± 13	c
082113#2	58.0 ± 0.5	6.23 ± 0.01	2.5762 ± 0.005	380 ± 7	
080613#5	77.6 ± 0.6	5.72 ± 0.06	4.6374 ± 0.005	488 ± 23	
122013#4	54.0 ± 1.5	7.07 ± 0.14	1.4030 ± 0.005	215 ± 21	f
121813#6	73.4 ± 0.7	8.46 ± 0.15	1.9502 ± 0.005	462 ± 34	
121813#8	50.6 ± 0.9	6.66 ± 0.04	2.2700 ± 0.005	506± 22	

a: a small NW was attached on the part close to the free end of the tested NW;

c: the tested NW was broken into two parts during the manipulation before tests;

f: an additional mass or particle attached on the free end of the tested NW.

All calculated moduli for AF and TF NWs are plotted in one graph for a direct

comparison, FIGURE 4.3. The majority of TF NWs are located in the higher modulus

range of 400-500 GPa. But the majority of AF NWs are located in the lower modulus

range of 250-350 GPa.
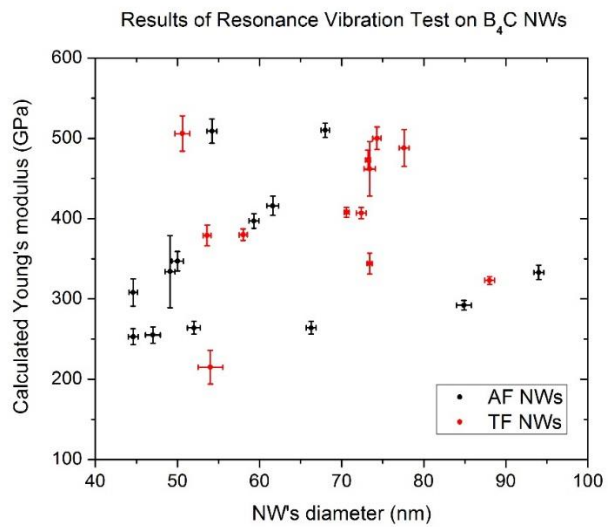
FIGURE 4.3: The results of calculated modulus for all tested AF and TF NWs.
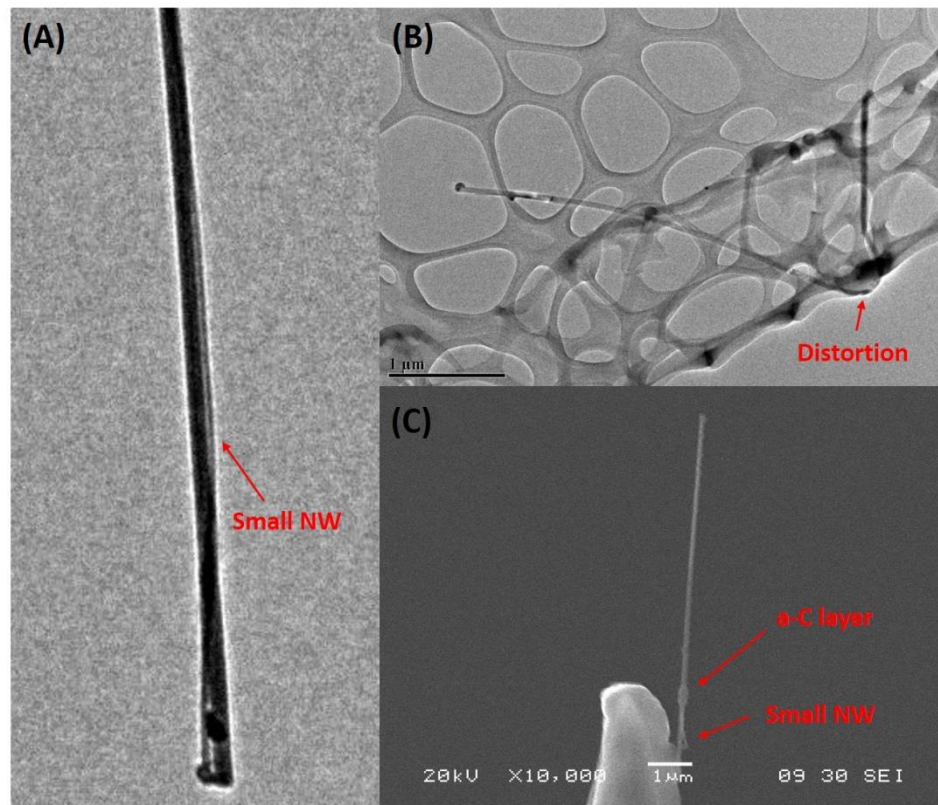
FIGURE 4.4: SEM images of factors affecting results of resonance vibration tests, such as (A) a small NW attached on the free end of a tested NW; (B) the NW was distorted before tests; and (C) a small NW and a-C layer on the part close to the clamp end of the tested NW.

The resonance vibration tests of NWs required that several factors should be carefully considered to verify the calculated moduli. For example, the letters on the Note columns in the above two tables represent different factors. The letter "a" represents a small NW attached on the part close to the free end of a tested NW, FIGURE 4.4A. This additional weight from the small NW reduced the resonant frequency of the tested NW, which lead to a lower calculated modulus. In other words, the calculated modulus of 255 $\pm$ 10 GPa was underestimated. The "b" indicates that a tested NW was distorted before that test, FIGURE 4.4B. The "c" denotes that a NW was broken into two parts during the manipulation before test and that the longer broken part was used for testing. These two factors, "b" and "c", indicate that the NWs were subject to plastic deformation

before *in situ* testing. Upon direct comparison with other tested NWs, it was apparent that plastic deformation softens the B_4C NWs. This phenomenon was also observed in buckling tests. The "d" denotes that a thick, amorphous carbon layer was formed on the part close to the clamped portion of the tested NW. The "e" represents a thick, amorphous carbon layer and a small NW both located close to the clamped end of the tested NW, FIGURE 4.4C. The factors "d" and "e" increased flexural rigidities of tested NWs, leading to an increased resonance frequency, which in turn, overestimated the Young's moduli of the NWs. The "f" represents that an additional mass or particle was attached on the free end of the NW, as well as the thinner portion of a tapered was clamped. These two aspects both decreased the resonance frequency of the tested NW, so its calculated modulus was highly underestimated. The factors introduced above cannot be used to quantitatively nor correctly calculate the modulus, because the details of these factors are undetermined. For example, the diameter and the length of a small, attached NW is unknown, so it is not possible to determine the mass of the small NW or to model the small NW with numerical modeling to provide corrections. However, they are useful for identifying the validity of the calculated results. Therefore, the invalid calculated results, owing to the existed factors, were filtered out. The results of remaining NWs are more reliable, and are plotted in FIGURE 4.5.
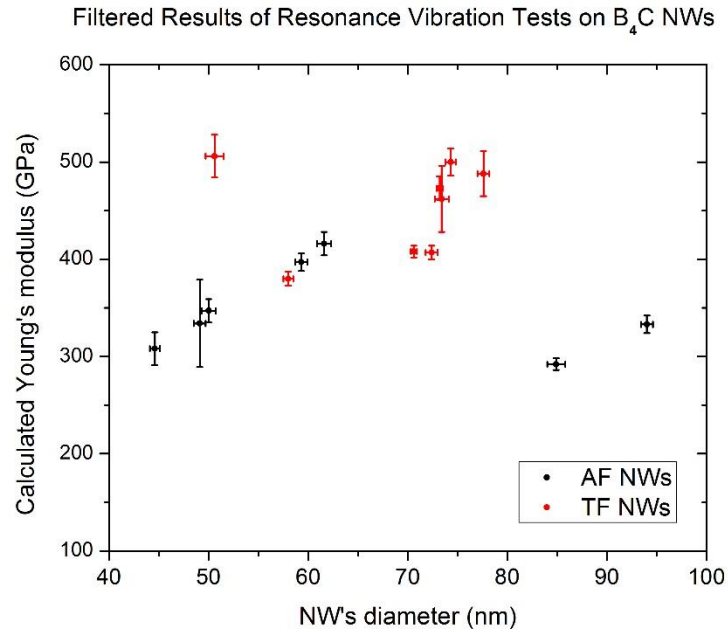
FIGURE 4.5: The results of calculated modulus for AF and TF NWs after some non-ideal tested NWs were filtered out.

The filtered results indicate that the Young's moduli for TF NWs are larger than those of AF NWs. It is found that more effects will influence the resonance vibration results, which are studied in later sections. However, the tests on these NWs were conducted with similar experimental conditions, so it can be concluded in general that TF NWs are stiffer than AF NWs. There are two possibilities to lead to this conclusion.

4.3.1.1 Anisotropy of Elasticity

The first suspicion for the difference in the Young's moduli of AF and TF NWs is the elastic anisotropy of B_4C NWs. Theoretically, the modulus measured by resonance vibration and buckling tests is the bending modulus, also known as the flexural modulus. The bending modulus is defined as the ratio of stress to strain in flexural deformation. However, when a NW was bent, the neighboring atoms were stretching or compressing each other, as shown in FIGURE 4.6A. It is known that most materials fail under tensile stress before they fail under compressive stress. Therefore, the flexural strength could

be considered the same as tensile strength for homogenous materials. In the linear region of the stress-strain curve for both tensile and compression tests, $\sigma = E \cdot \varepsilon$, where E is Young's modulus. Because the flexural modulus achieved from the resonance vibration or buckling tests were in the elastic region, the flexural modulus should be equal to the Young's modulus.

The Young's modulus for AF and TF NWs are along the axial directions, which have different crystallographic directions. For AF NWs, the crystallographic direction of the axial orientation is parallel to the (001) defect plane, which is [100] (FIGURE 4.6B). But for TF NWs, the crystallographic index of the axial direction perpendicular to (001) plane is $[\overline{0.297}, \overline{0.297}, 1]$, FIGURE 4.6C.
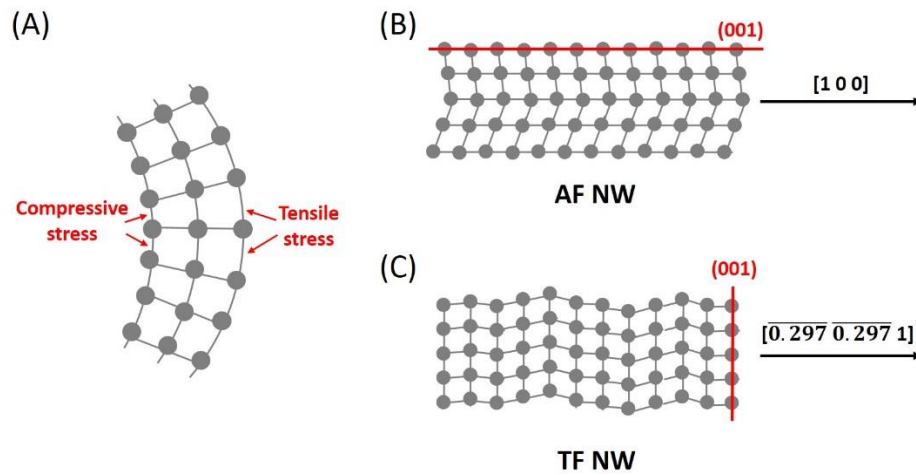
FIGURE 4.6: Atomic representations for (A) flexural deformation of a NW; (B) AF NW; and (C) TF NW.

The nonzero elastic constants for B_4C bulk materials have been found, and listed as following (in units of GPa): $C_{11} = 561.8$, $C_{21} = 123.6$, $C_{31} = 69.6$, $C_{51} = 17.8$, $C_{22} = 536.5$, $C_{23} = 63.3$, $C_{25} = -38.7$, $C_{33} = 517.7$, $C_{35} = -1.0$, $C_{44} = 164.8$. There are other relationships including: $C_{ij} = C_{ji}$, $C_{52} = -C_{51}$, $C_{66} = \frac{1}{2}(C_{11} - C_{12})$, $C_{44} = C_{55}$ [129, 130]. So the elastic constant matrix C for B_4C is:

$$C = \begin{bmatrix} 561.8 & 123.6 & 69.6 & 0 & 17.8 & 0 \\ 123.6 & 536.5 & 63.3 & 0 & -38.7 & 0 \\ 69.6 & 63.3 & 517.7 & 0 & -1.0 & 0 \\ 0 & 0 & 0 & 164.8 & 0 & -38.7 \\ 17.8 & -38.7 & -1.0 & 0 & 164.8 & 0 \\ 0 & 0 & 0 & -38.7 & 0 & 219.7 \end{bmatrix} \tag{25}.$$

Then the elastic compliance matrix ($S = C^{-1}$, in unit of 1/GPa) is:

$$S = \begin{bmatrix} 0.0019 & -0.0004 & -0.0002 & 0 & -0.0003 & 0 \\ -0.0004 & 0.0020 & -0.0002 & 0 & 0.0005 & 0 \\ -0.0002 & -0.0002 & 0.0020 & 0 & -0.0000 & 0 \\ 0 & 0 & 0 & 0.0063 & 0 & 0.0011 \\ -0.0003 & 0.0005 & -0.0000 & 0 & 0.0063 & 0 \\ 0 & 0 & 0 & 0.0011 & 0 & 0.0048 \end{bmatrix} \tag{26}.$$

Because B₄C has a complex rhombohedral crystal unit with space group $R\bar{3}m$, the direction-dependent Young's modulus for B₄C can be determined by the equation:

$$E_{uvw} = \frac{1}{(1-n_3^2)^2 S_{11} + n_3^4 S_{33} + n_3^2(1-n_3^2)(2S_{13} + S_{44}) + 2n_2 n_3(3n_1^2 - n_2^2)S_{14}} \tag{27}$$

where (n_1, n_2, n_3) is the unit vector for the crystallographic direction [uvw].

According to the above equations, the Young's modulus of [100] direction for AF NW is calculated by

$$E_{AF} = \frac{1}{0.0019} GPa = 526 GPa \tag{28}.$$

For the TF NW, the unit vector for the crystallographic direction $[\overline{0.297}, \overline{0.297}, 1]$ is (-0.274, -0.274, 0.922). Then the Young's modulus for the TF NW is calculated by

$$E_{TF} = \frac{1}{(1-0.922^2)^2 0.0019 + 0.922^4 0.0020 + 0.922^2(1-0.922^2)(-2 \times 0.0002 + 0.0063)} GPa \tag{29}.$$
$$= 446 GPa$$

Based on theoretical calculations, the Young's modulus of the AF NW should be larger than that of the TF NW. However, the theoretical results are contradictory to the experimental results. Therefore, another possibility is discussed below.

4.3.1.2 Effect of the Fault Orientation

Another possible explanation is due to the different fault orientation. It is generally believed that the mechanical properties of materials critically depends on their internal microstructures. There were many publications reported that the crystallographic defects played an important role on the mechanical properties of nanoscale materials from experimental [131, 132] or numerical results [128]. It was reported that the dense stacking faults (SFs) can strengthen nanocrystalline bulk [133] or brittle NWs [127]. It was discovered that the NWs with a high density of SFs had higher Young's modulus compared to NWs with perfect structures. This was explained by the variation of bond arrangement at the SF sites on a NW. The Young's modulus was directly related to the bond strength. And it was revealed that the bond strength depends on the location of bonds [134]. Therefore, the local interatomic interactions might be changed by the various possible arrangements of bonds stacking at the dense SF sites. Then consequently, the strengths of these bonds were altered. Since the TF B_4C NWs have more SF sites than AF NWs, which means that TF NWs could be stiffer than AF NWs.

4.3.2   Experimental Results of Buckling Test

In buckling tests of B_4C NWs, the data set of the deformation of a tested NW and the buckling forces were first concluded and plotted. The critical buckling force was found in the plot. And then the Young's modulus of B_4C NWs were calculated as the data analysis process illustrated in Appendix C. The experimental data and calculated results of four tested NWs (i.e., two AF NWs and two TF NWs) are present in TABLE

4.3. In the table, L is the effective length between two clamps, D is the overall diameter, P_{cr} is the critical buckling force, E_1 and E_2 are the Young's moduli calculated from the resonance vibration tests and buckling tests, respectively. From the calculated moduli of these four NWs for buckling tests, the same conclusion that the moduli of AF NWs are lower than those of TF NWs can be made.

These four B_4C NWs were subject to the resonance vibration tests first, and then to the buckling tests. Because the NWs were not undergone plastic deformations during the resonance vibration tests, the calculated moduli for the same NW from these two different tests should be consistent. In other words, the calculated values of E_1 and E_2 for each NW should be consistent. However, the direct comparison in the TABLE 4.3 demonstrates that two calculated values are not matched well, with the discrepancy up to 35%. The discrepancy may be due to the amorphous carbon layers formed on NWs during the tests, which is discussed in details in the section 4.3.4.3. In addition, the height misalignments of the NWs in buckling test was unknown, which results in large uncertainties in the results determined from buckling tests.

TABLE 4.3: Experimental data and results of buckling tests on B_4C NWs.

NW ID	Type	L (μm)	D (nm)	P_{cr} (nN)	E_2 (Gpa)	E_1 (Gpa)
062513#5	AF	5.95 ± 0.11	49.1 ± 0.6	79 ± 7	248 ± 29	334 ± 45
062513#6	AF	5.77 ± 0.08	50.0 ± 0.7	131 ± 8	360 ± 31	347 ± 12
080513#3	TF	6.52 ± 0.06	70.6 ± 0.3	510 ± 21	450 ± 22	408 ± 6
050913#3	TF	7.26 ± 0.06	74.3 ± 0.5	478 ± 19	427 ± 22	500 ± 14

In addition to the calculated Young's moduli, more results were also achieved from the buckling tests. When the NWs reached the initial buckling, it was still in the elastic region (also called as the elastic buckling), which meant the NWs could be fully recovered. The mechanical behaviors of NWs would not change even if NWs were loaded and unloaded in the elastic buckling multiple times. But if the NWs were

undergone plastic deformations, then the intrinsic properties of NWs would be altered. For instance, a NW was experienced with three cycles of loading-unloading processes. The experimental results are present in FIGURE 4.7. For the first loading, the NW was loaded to the elastic buckling, as shown in FIGURE 4.8A, and then unloaded to the initial position. For the second testing circle, the NW was compressed to the plastic buckling, as shown in FIGURE 4.8B, then it was completely unloaded. In the third loading, the NW was loaded to the elastic buckling. It is shown that the loading curves for the first and second loadings are consistent, which yields the same modulus values. However, the lower position for the third loading curve implies that the NW was softened after the plastic deformation in the plastic buckling. The calculated Young's modulus of the NW from the first and second buckling tests is 427 ± 22 GPa, while it is determined as 351 ± 20 GPa from the third buckling test, which is about 18% decrease in the elastic modulus after the NW was plastically deformed. The similar results were obtained when the multiple buckling tests were performed on other NWs. In general, the plastic deformation results in an 18-20% reduction in Young's moduli.
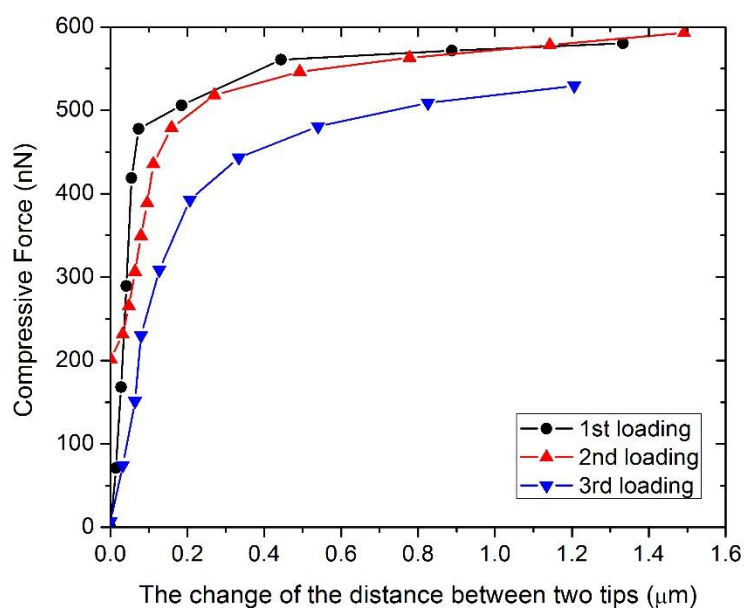
FIGURE 4.7: The results of three buckling loadings on a NW.
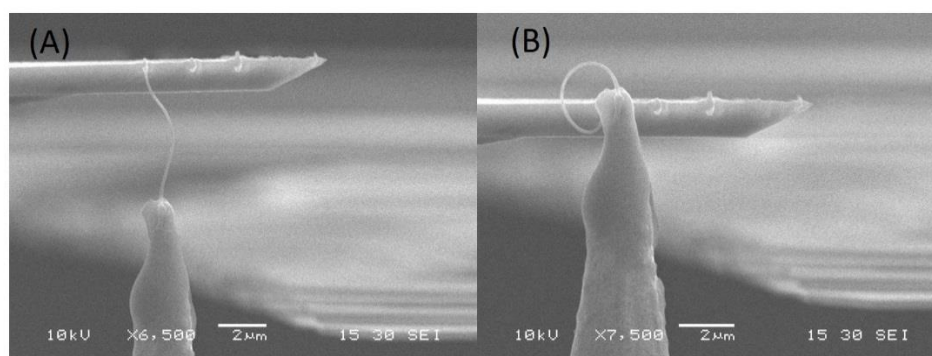
FIGURE 4.8: SEM images to show (A) the elastic buckling and (B) the plastic buckling.

The bulk B_4C is known as a hard and brittle material in nature [135]. But our results, as shown in FIGURE 4.9, reveal that the B_4C NWs are extremely flexible. Our observations are consistent with the reported results for *in situ* buckling of B_4C NWs from other groups [33, 101]. The excellent flexibilities of B_4C NWs may be due to the intrinsic properties in nanoscale size, or a higher aspect ratio.
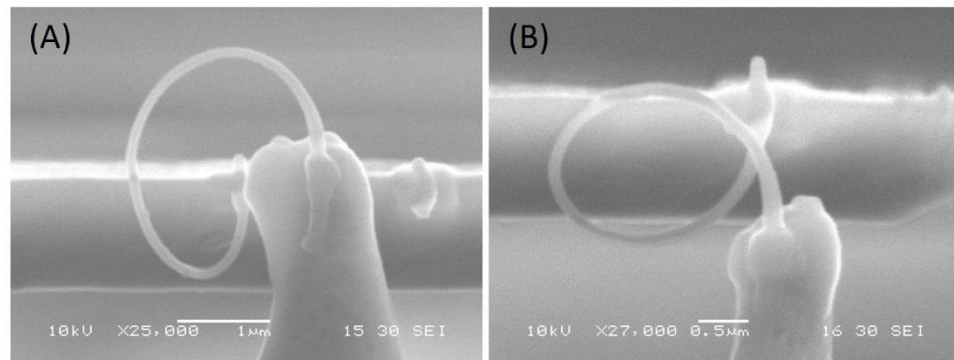
FIGURE 4.9: SEM images displaying two twisted NWs (A) and (B) to show their flexibility.

4.3.3   Experimental Results of Tensile Test

Similarly, some NWs were subject to tensile tests after resonance vibration evaluation. Many issues exist in the AFM cantilever based *in situ* tensile test, such as inaccurate measurement of the cantilever's deflection, the in-plane and height misalignments of the tested NW, the aggravation of the in-plane misalignment during the elongation, and so on.

The measurement accuracy of the deflection of the cantilever was enhanced with the help of a micro-feature near the sensing cantilever as a reference bar. And the issue of aggravation of the in-plane misalignment during the tension was finally solved by employing a relatively stiff cantilever with a reference microfiber. Although the improvements are introduced in the section 3.4.2, the comprehensive effect of the issue of aggravation of the in-plane misalignment is discussed here.

A NW was initially in-plane aligned before the tension. When the NW was under tension loading, the cantilever started to bend first, that leads to a relative shift of the position of the clamp on the cantilever. The shift amount causes a large in-plane misalignment, as shown in FIGURE 4.10A. It is noted that the NW with a large in-plane misalignment was not only under axial force (F), but also under a shear force (F_y). The

force F_x is determined by the deflection of the cantilever, and then used to calculate the axial force combining with the misalignment angle θ. It is not ideal to perform a tensile test if this distortion occurs, because the combined action of the tensile and shear forces will result in the formation of crack with less efforts. Thus, the obtained fracture strength will be highly underestimated. For example of this NW displayed in FIGURE 4.10, the NW was fractured at the strength of 0.34 GPa, which was much lower than the fracture strengths obtained from other tested NWs. There is another evidence to show that the fracture of this NW was due to the combined action of the tensile and shear forces. The fracture edge on NW was not flat for this NW (FIGURE 4.10B), which was different with the flat fracture edges observed on other NWs fractured under axial tension forces (FIGURE 4.10C). It is well known that the flat fracture surface is one characteristic for tensile test on brittle materials. It meant that the B_4C NWs exhibited the brittle nature in the tensile tests. This was proved from the stress-strain curve that the NW was fractured abruptly with no plastic deformation observed before failure. Therefore, according to the above discussion, results from tensile tests with large in-plane misalignments were considered to be unreliable and removed from analysis.
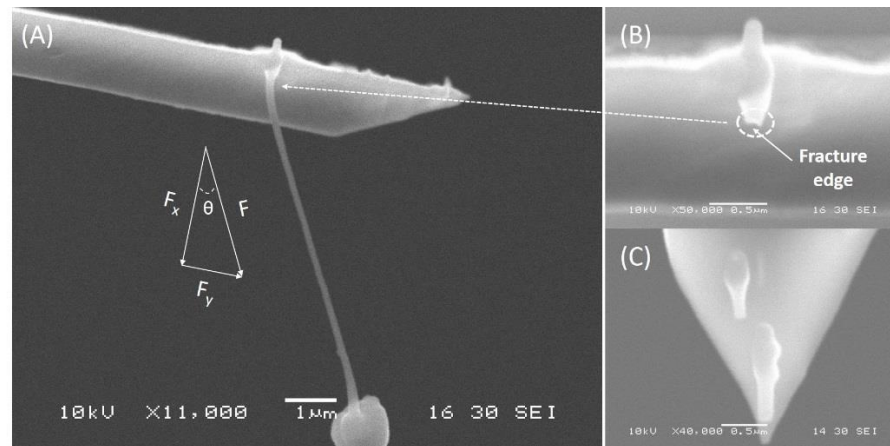
FIGURE 4.10: SEM images show (A) the in-plane misalignment during the tensile test; (B) the fracture edge for the NW shown in (A); and (C) fracture edges for other NWs after tensile tests.

Moreover, the height misalignment is also influential to the tensile results. For instance of a TF NW, it was first examined by the resonance vibration test. The Young's modulus obtained from the resonance vibration test was 407 ± 7 GPa. Then it was inspected by the tensile test. The Young's modulus calculated from tensile results was only 142 ± 4 GPa, which was about 65% reduction. The misalignment angle was measured in the beginning was about 18° in the height orientation. It was reported that the height misalignment might cause about 12% uncertainty errors in the calculated results [59]. But in our study, it showed that the height misalignment could result in larger errors to the calculated results, because of the larger height misalignment. Therefore, results from tensile tests with large height misalignments were removed too.
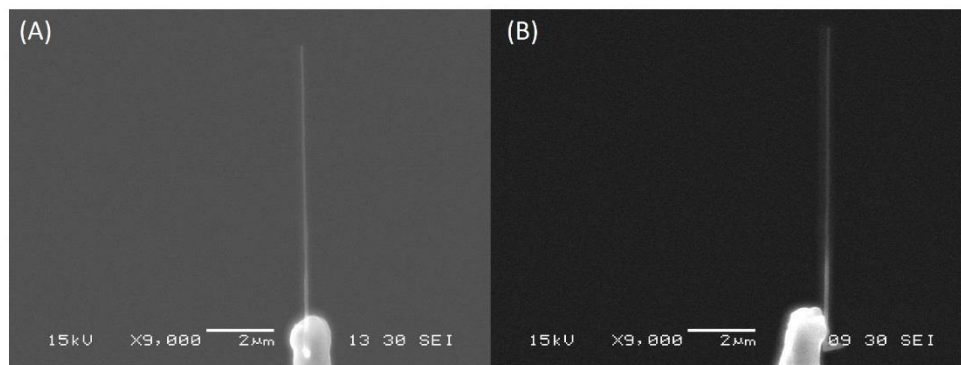
FIGURE 4.11: (A) top view and (B) side view of a one-end clamped NW.

A good candidate for tensile tests is one aligned NW. The aligned NW means the NW should be aligned both in-plane and height orientation. It is impossible so far to achieve the side view to verify the height alignment when both ends of a NW are clamped. Instead, the top (FIGURE 4.11A) and side views (FIGURE 4.11B) of a one-end clamped NW are observed before its second end is clamped. If the NW is aligned to within 5° both in-plane and height, then it is considered as a good specimen for tensile test.

After ruling out some unreliable results, results of two B_4C NWs (one AF NW and one TF NW) from tensile tests are present in the TABLE 4.4. The detailed data analysis of tensile tests is discussed in Appendix C.

TABLE 4.4: Results of tensile tests on B_4C NWs.

NW ID	Type	Diameter (nm)	Young's modulus (GPa)	Fracture strength (GPa)	Maximum strain (%)
080713#5	AF	68.0 ± 0.5	333 ± 6	19.5 ± 0.5	5.9 ± 0.3
121813#6	TF	73.4 ± 0.7	431 ± 4	14.5 ± 0.5	3.3 ± 0.2

The calculated modulus results are consistent with the obtained results from the resonance vibration tests, that Young's moduli of the AF and TF NWs are in the range of 300-400 GPa and 400-500 GPa, respectively. In addition, the fracture strength (i.e., tensile strength for brittle materials) of a B_4C NW is much higher than the reported value

0.26 GPa for B$_4$C bulk [136]. However, the fracture strength of the AF NW is larger than the TF NW. This may be owning to the fault orientation. It is apparent that the crack propagation direction is normal to the defect plane in the AF NW, while it is parallel to the defect plane in the TF NW. Since the dense boundaries of stacking faults in the AF NW can hinder the crack propagation, more energies are required to reach the failure. Therefore, an AF NW have a higher fracture strength and maximum strain.

There is one more interesting phenomenon observed in the tensile tests of B$_4$C NWs. The B$_4$C NWs were fractured at two positions simultaneously when they failed, FIGURE 4.12. In other words, the NW was broken into three pieces. It means the maximum stress occurs at two different locations on a tested NW at the same time. But why does it happen? The possible explanation is given in the following section 4.3.4.3.
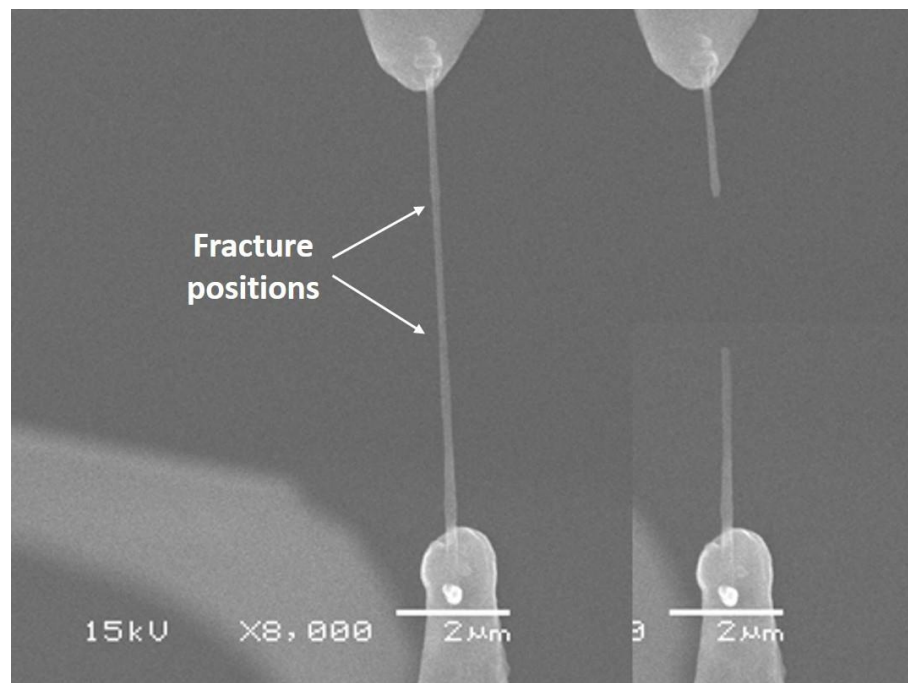
FIGURE 4.12: SEM images showing the two simultaneous fracture positions on a NW under tension.

4.3.4   Effects on experimental results

In addition to these experimental limitations, such as low resolutions of load and displacement, and existence of in-plane and height misalignments, there are some other effects hidden behind to influence experimental results.

4.3.4.1 The Non-uniformity of NW's Length

Under TEM imaging, different view angles were used to image individual B_4C NWs. For most NWs, their diameters were not varied with different view angles, which indicated that their cross sections were circular.

However, it was discovered in TEM that NWs were not grown with a constant diameter. The regular variation of diameter along the longitudinal axis of the NW was observed, so that the NW was considered as a tapered NW. There may be only a few nanometers difference between one end and another end of a NW. So it is extremely difficult to discover that this small tapered shape of NW is not uniform under SEM imaging. In our study, the diameter at the root end of a tapered NW was used for data analysis by assuming it as a cylindrical NW. Then how large the error would produce if we made this assumption? Therefore, both analytical solutions and FEM simulations were conducted to study this effect.

4.3.4.1.1 Analytical Solutions for Free Vibration of Tapered NWs

Before deriving the analytical solutions for free vibration of tapered NWs, the process of deriving the analytical solutions for uniform beams is briefly introduced. For a uniform beam, the second moment of area of the beam I and mass per unit length μ is independent of distance x on the beam away from the fixed end. So the well-known free vibration equation for a cantilevered beam is

$$EI\frac{\partial^4 Y(x,t)}{\partial x^4} = -\mu\frac{\partial^2 Y(x,t)}{\partial t^2} \tag{30}$$

where, E is the Young's modulus of the beam, $Y(x,t)$ is the vertical response of the beam which describes the deflection of the beam in y direction at position x at time t. A Fourier decomposition of the deflection is applied to rewrite the deflection as

$$Y(x,t) = y(x)e^{-i\omega t} \tag{31}$$

where $y(x)$ is the amplitude of harmonic vibration of the beam at position x, ω is the frequency of vibration. Then the above differential equation (28) becomes

$$EI\frac{\partial^4 y(x)}{\partial x^4} - \mu\omega^2 y(x) = 0 \tag{32}.$$

The general solution for the equation (30) is

$$y(x) = A\cosh(\beta x) + B\sinh(\beta x) + C\cos(\beta x) + D\sin(\beta x) \tag{33}$$

where β is the value determined by $\beta = (\frac{\mu\omega^2}{EI})^{\frac{1}{4}}$, and A, B, C, and D are constants. For the different modes of resonance, the general solution is typically written as

$$y_n(x) = A\cosh(\beta_n x) + B\sinh(\beta_n x) + C\cos(\beta_n x) + D\sin(\beta_n x) \tag{34}$$

with $\beta_n = (\frac{\mu\omega_n^2}{EI})^{\frac{1}{4}}$, where ω_n is the natural frequency at nth mode. For a fixed-free beam, the boundary conditions are

$$y_n = 0, \quad \frac{dy_n}{dx} = 0 \quad at\ x = 0,$$
$$\frac{d^2 y_n}{d^2 x} = 0, \quad \frac{d^3 y_n}{d^3 x} = 0 \quad at\ x = L. \tag{35}.$$

When these boundary conditions are applied into the equation (32), we can achieve the equation

$$\begin{bmatrix} 1 & 0 & 1 & 0 \\ 0 & 1 & 0 & 1 \\ \cosh(\beta_n L) & \sinh(\beta_n L) & -\cos(\beta_n L) & -\sin(\beta_n L) \\ \sinh(\beta_n L) & \cosh(\beta_n L) & \sin(\beta_n L) & -\cos(\beta_n L) \end{bmatrix}\begin{bmatrix} A \\ B \\ C \\ D \end{bmatrix} = 0 \tag{36}$$

The non-trivial solutions for the above matrix equation is existed only if the determinant of the first matrix is equal to zero, which is

$$det\begin{bmatrix} 1 & 0 & 1 & 0 \\ 0 & 1 & 0 & 1 \\ \cosh(\beta_n L) & \sinh(\beta_n L) & -\cos(\beta_n L) & -\sin(\beta_n L) \\ \sinh(\beta_n L) & \cosh(\beta_n L) & \sin(\beta_n L) & -\cos(\beta_n L) \end{bmatrix} = 1 + \cos(\beta_n L)\cosh(\beta_n L) = 0 \qquad (37)$$

This nonlinear equation has the solutions with the first four roots are $\beta_1 L = 1.8751, \beta_2 L = 4.6941, \beta_3 L = 7.8548, \beta_4 L = 10.9955$. Then the natural frequencies of vibration can be determined by

$$\omega_n = \beta_n^2 \sqrt{\frac{EI}{\mu}} = \frac{(\beta_n L)^2}{L^2}\sqrt{\frac{EI}{\mu}} \qquad (38)$$

Now, let us study the free vibration of a tapered beam. For a tapered beam as illustrated in FIGURE 4.13, the radius R_x for the circular cross section at the position x from the origin can be expressed as $R_x = r + \frac{R-r}{L}x = r(1 + \alpha x)$, where r is the radius at the fixed end, R is the radius at the free end, L is the length of the beam, and α is the constant with the value of $\alpha = \frac{R-r}{rL}$. Therefore, the second moment of area (I_x) and cross-sectional area (A_x) at the position x are calculated by $I_x = I_0(1 + \alpha x)^4$ and $A_x = A_0(1 + \alpha x)^2$, where I_0 and A_0 are the second moment of area and area for the cross section at the fixed end, respectively.
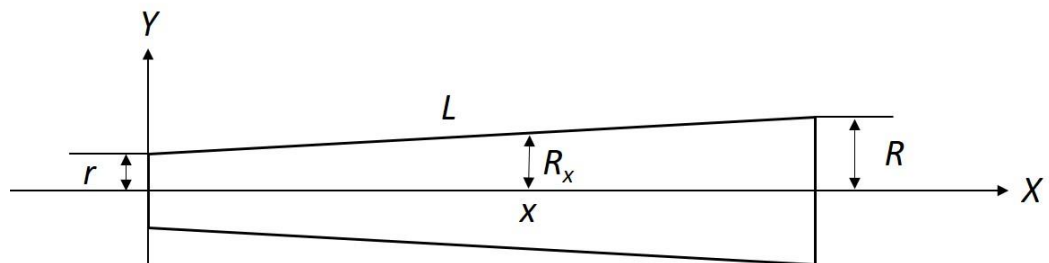
FIGURE 4.13: The schematics of a tapered NW with the left side fixed.

Therefore, the free vibration of a beam with varying cross-section is governed by the differential equation

$$\frac{d^2}{d^2 x}\left(EI_x \frac{d^2 y_n(x)}{d^2 x}\right) - \rho A_x \omega_n^2 y_n(x) = 0 \tag{39}$$

where ρ is the materials density. This equation (37) can be rewritten as

$$\frac{d^2}{d^2 x}\left(EI_0(1+\alpha x)^4 \frac{d^2 y_n(x)}{d^2 x}\right) - \rho A_0(1+\alpha x)^2 \omega_n^2 y_n(x) = 0 \tag{40}$$

Then, we introduce a new function $w_n(x) = (1 + \alpha x)^2 y_n(x)$. After applying this new function into the above equation (38), we achieve

$$EI_0 \frac{\partial^4 w_n(x)}{\partial x^4} - \rho A_0 \omega_n^2 w_n(x) = 0 \tag{41}.$$

Similarly, the general equation for this differential equation (39) is

$$w_n(x) = A\cosh(\beta_n x) + B\sinh(\beta_n x) + C\cos(\beta_n x) + D\sin(\beta_n x) \tag{42}$$

where β_n is the nth eigenvalue calculated by $\beta_n = (\frac{\rho A_0 \omega n^2}{EI_0})^{\frac{1}{4}}$. Then, the deflection $y(x)$ can be determined by

$$y_n(x) = \frac{1}{(1+\alpha x)^2}\left[A\cosh(\beta_n x) + B\sinh(\beta_n x) + C\cos(\beta_n x) + D\sin(\beta_n x)\right] \tag{43}$$

The boundary conditions for a fixed-free tapered beam are

$$y_n = 0, \quad \frac{dy_n}{dx} = 0 \quad at\ x = 0,$$
$$\frac{d^2 y_n}{d^2 x} = 0, \quad \frac{dy}{dx}\left(EI_x \frac{d^2 y_n}{d^2 x}\right) = 0 \quad at\ x = L. \tag{44}.$$

After applying these boundary conditions into the general solution equation (41), we can obtain a matrix equation

$$\begin{bmatrix} 1 & 0 & 1 & 0 \\ 0 & 1 & 0 & 1 \\ \dfrac{6n^2+m^2}{4nm}\cosh(m)-\sinh(m) & \dfrac{6n^2+m^2}{4nm}\sinh(m)-\cosh(m) & \dfrac{6n^2-m^2}{4nm}\cos(m)+\sin(m) & \dfrac{6n^2-m^2}{4nm}\sin(m)-\cos(m) \\ \dfrac{2n^2+m^2}{2nm}\sinh(m)-\cosh(m) & \dfrac{2n^2+m^2}{2nm}\cosh(m)-\sinh(m) & \dfrac{-2n^2+m^2}{2nm}\sin(m)+\cos(m) & \dfrac{2n^2-m^2}{2nm}\cos(m)+\sin(m) \end{bmatrix}\begin{bmatrix} A \\ B \\ C \\ D \end{bmatrix}=0 \quad (45)$$

where $m = \beta_n L$ as called eigenvalues, and $n = 1 - \dfrac{r}{R}$ when r/R is defined as the taper ratio for a tapered beam. The non-trivial solution for the above matrix equation (43) is

$$\det\begin{bmatrix} 1 & 0 & 1 & 0 \\ 0 & 1 & 0 & 1 \\ \dfrac{6n^2+m^2}{4nm}\cosh(m)-\sinh(m) & \dfrac{6n^2+m^2}{4nm}\sinh(m)-\cosh(m) & \dfrac{6n^2-m^2}{4nm}\cos(m)+\sin(m) & \dfrac{6n^2-m^2}{4nm}\sin(m)-\cos(m) \\ \dfrac{2n^2+m^2}{2nm}\sinh(m)-\cosh(m) & \dfrac{2n^2+m^2}{2nm}\cosh(m)-\sinh(m) & \dfrac{-2n^2+m^2}{2nm}\sin(m)+\cos(m) & \dfrac{2n^2-m^2}{2nm}\cos(m)+\sin(m) \end{bmatrix}=0 \quad (46),$$

which yields a non-linear equation:

$$\begin{aligned} &m^4(1+\cos(m)\cosh(m)+12n^4(1-\cos(m)\cosh(m)) \\ &+(12mn^3-4m^3n)\cos(m)\sinh(m) \\ &-(12mn^3+4m^3n)\cosh(m)\sin(m) \\ &+12m^2n^2 sin(m)\sinh(m)=0 \end{aligned} \quad (47).$$

If this beam is uniform (i.e., $n = 0$), then the above equation (45) becomes $1 + cos(m)cosh(m) = 0$, which is same with what is achieved above for a uniform beam. With this general characteristic equation (45) for a tapered beam, the eigenvalues m can be determined if the radii at the fixed and free ends of the beam are known. The results are independent of the beam length L. Compared to the equation (12), the Young's modulus of a tapered beam can be calculated by a modified equation as

$$E = \frac{16\pi^2\rho}{m^4}\frac{L^4}{r^2}f_0^2 \quad (48)$$

where, ρ and L are the density and length of the tapered beam respectively, r is the radius of cross section at the fixed end, f_0 is the measured fundamental frequency for the beam, and m is the first harmonic eigenvalue calculated by applying the taper ratio of the tapered beam into the characteristic equation. The eigenvalues were calculated corresponding to the varied taper ratios, and results were plotted in FIGURE 4.14.

Results were curve fitted by three functions: second order and third order polynomial fittings, and exponential fitting. The fitting curves show that the exponential fit is the most suitable to describe the relationship of the first harmonic eigenvalue and the taper ratio for cantilevered beams. The empirical formula for this relationship is

$$m = 4.1874 - 3.6644e^{-0.4604\left(\frac{r}{R}\right)} \tag{49}$$

This is a general relationship for all cantilevered beams, either uniform or tapered beams. For example, for the taper ratio (r/R) is 1, and the eigenvalue is calculated to be 1.8750, which is the well-known first harmonic eigenvalue for the free vibration of a cantilevered uniform beam. The purpose of this empirical equation is to help us estimate the Young's modulus of a tapered beam more effectively and accurately.
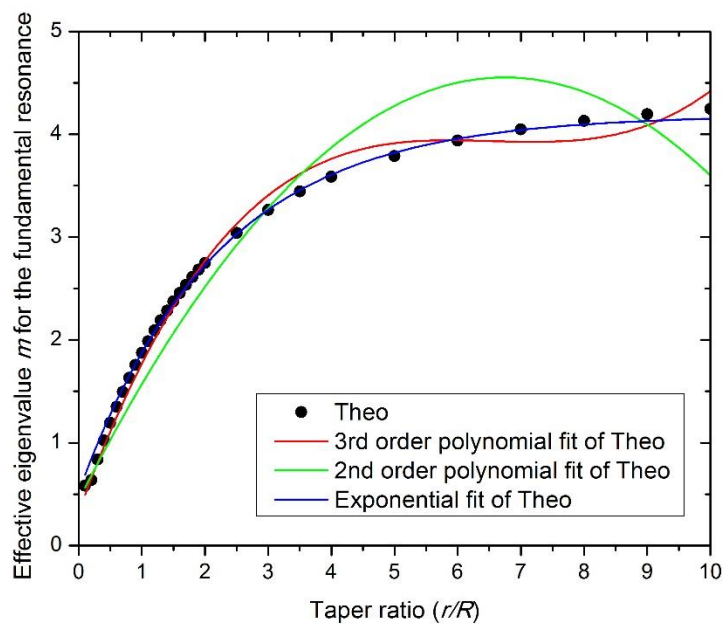
FIGURE 4.14: The curve of theoretical m values versus the taper ratio r/R, with three different fittings.

4.3.4.1.2 Study the Free Vibration of Tapered NWs by FEM

The free vibration of tapered NWs were also studied by using a numerical simulation tool (i.e., FEM). The specific parameters and conditions for FEM in this work is discussed in the convergence study in Appendix D. The model used in this study was a truncated conical solid structure. The radii at fixed and free ends were r and R respectively, as shown in FIGURE 4.15A. The value R was fixed, while r was changed to alter the taper ratio (r/R). From the analytical solution, it is known that the length of beam (L) is irrelevant to the relationship between the frequency shift (i.e., the shift of eigenvalue) and the tapered ratio. However, if the length of beam is small enough, it will not behavior like a slender beam, which is absolutely inappropriate for our case. So it is necessary to study how large the slenderness ratio (L/R) is appropriate for this study. With keeping the taper ratio and R value constant, the length of beam was altered to investigate the frequency response. The result of the length effect with a constant taper ratio (0.9) is shown in FIGURE 4.15B. The result demonstrates that the length affects the frequency shift for a short tapered beam as expected. With increasing the length of NW, the frequency ratio (i.e., f/f_0, where f and f_0 are the frequencies of a tapered and uniform NW, respectively.) is constant. Based on this result, a beam length of 100R was chosen for the FEM study.
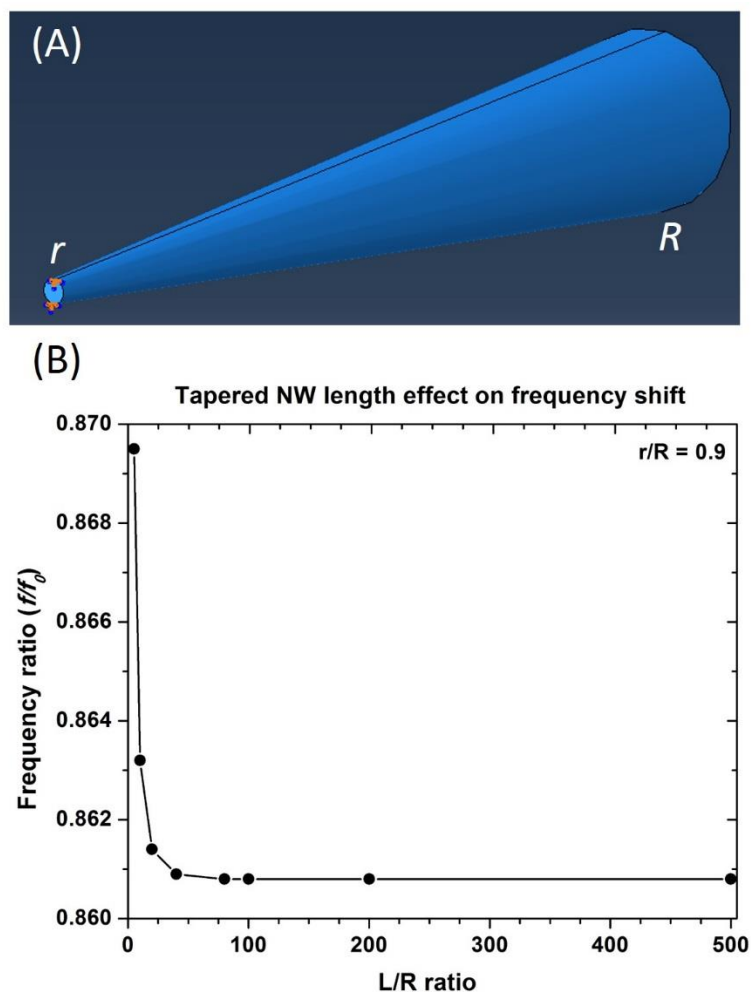
FIGURE 4.15: (A) A FEM solid model of a tapered NW. (B) The FEM results to show the length effect on the frequency shift for a tapered NW.

Results of this FEM study were obtained, and then compared with the analytical solutions (Theo), as illustrated in FIGURE 4.16. Results from FEM and analytical solutions are consistent with the taper ratio in the range of 0.1 – 1.5. The reason for the large discrepancy for the taper ratio larger than 1.5 is not clear. One possible explanation is due to the nature of discretization for finite element analysis. The solid element used in this model is 20-node quadratic brick element (C3D20R), which may be a limitation in the modeling of a tapered beam. But fortunately, for all observed NWs synthesized in our lab, their taper ratios are in the range of 0.5 – 1.5. The difference of results for

analytical solution and FEM in this range is not significant, as shown in FIGURE 4.17.
The results for both cases can be linearly fitted, with the fitting equations of $y = 1.2x - 0.2$ and $y = 1.2x - 0.2$ for analytical solution and FEM, respectively. In other words, the FEM results correspond to the analytical solutions with the taper ratio from 0.5 to 1.5.
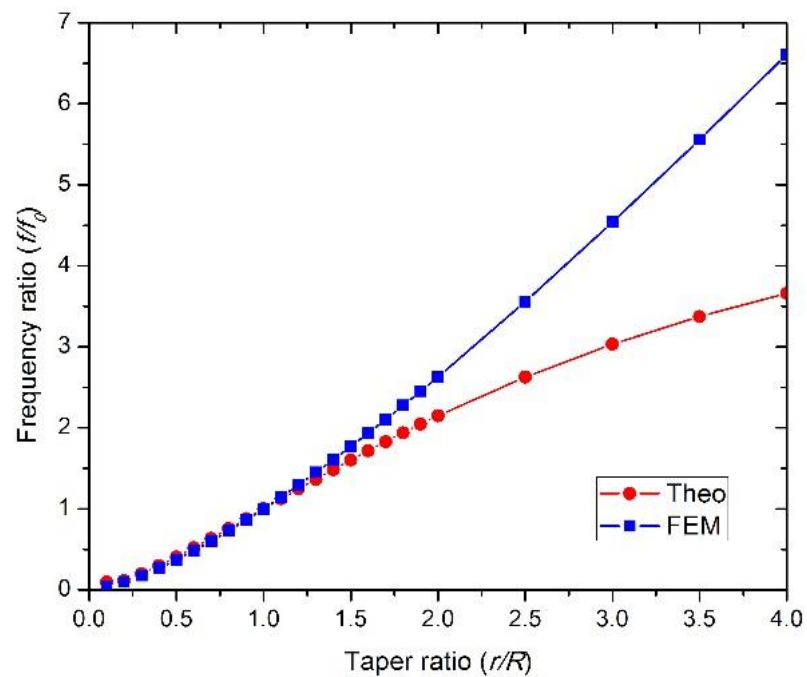
FIGURE 4.16: Comparison of theoretical (red) and modeling (blue) results of the frequency shift correlating with the taper ratio.
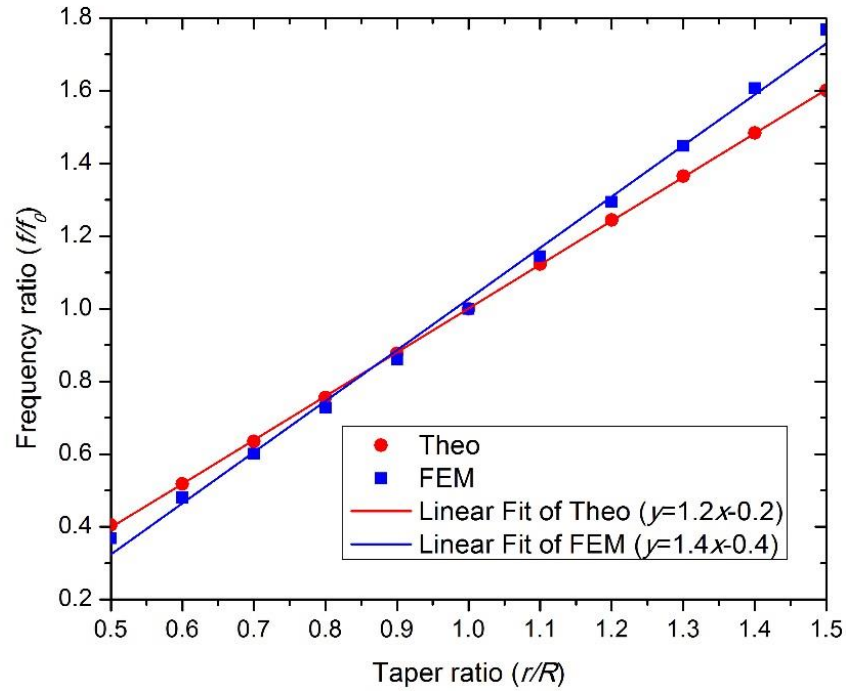
FIGURE 4.17: Comparison of theoretical (red) and modeling (blue) results of the frequency shift linearly correlating with the taper ratio in the range of 0.5-1.5.

For our tapered NWs, the linear fitting equation of the analytical solution is suitable for corrections. The linear relationship between the frequency ratio and taper ratio is

$$\frac{f}{f_0} = 1.2 \frac{r}{R} - 0.2 \tag{50},$$

which can be transformed to

$$\frac{\Delta f}{f_0} = \frac{f - f_0}{f_0} = 1.2(\frac{r}{R} - 1) \tag{51}$$

where Δf is the frequency shift amount if an uniform beam becomes a tapered beam. During the experiments, the resonant frequency of a tapered NW was measured, and used for the calculation of the Young's modulus E_0 by assuming the NW was uniform. This assumption certainly caused the estimation error in the calculated modulus.

According to the beam theory equation (12), the estimation error of Young's modulus ΔE and Δf has a relation of

$$\frac{\Delta E}{E_0} = 2\frac{\Delta f}{f_0} \tag{52}$$

Therefore, ΔE can be determined by

$$\frac{\Delta E}{E_0} = 2.4(\frac{r}{R} - 1) \tag{53},$$

where, the sign of ΔE (- and +) is used to determine if the calculated modulus is underestimated or overestimated, respectively. For instance of a NW with the taper ratio of 0.9 (i.e., r<R), the calculated Young's modulus with considering it as a uniform NW will be 24% underestimated. In conclusion, a slightly tapered NW is considered as a uniform one will result in a relatively large estimated error in the calculated Young's modulus.

4.3.4.2 Amorphous Oxide Layer

The amorphous oxide layer was observed and reported extensively on various nanostructures. The oxide layers were uniformly formed on the surfaces of nanostructures because the nanostructures had chemical reactions to oxygen in the atmosphere. The nanostructures with the oxide layers should be considered as core-shell structures, because the oxide layers and nanostructures usually have different properties. The oxide layer effect should be considered in the calculation of Young's modulus for all types of mechanical tests. Therefore, the correction formulas for each *in situ* tests were derived here.

4.3.4.2.1 The Effect of Oxide Layer on Tensile Test

In the tensile test, the external force *F* was applied on the oxide layer instead of on the core NW, as shown in FIGURE 4.18. When the oxide layer was stretched under the external force, the internal forces such as the bonding force at tangential direction

appeared at the core-oxide interface. The internal forces were equivalent but opposite action and reaction forces denoted as f and f'. Thus, the net force applied on the oxide layer (F_o) was equal to F-f', while the net force applied on the core NW (F_c) is f. The external force F was measured during the experiment, and used to calculate the stress.

FIGURE 4.18: Schematics of tensile test on a NW (blue) with an oxide layer (grey).

Without considering the oxide layer, the external force acting on a NW is

$$F = \sigma S \tag{54}$$

where, σ is the stress applied on the NW, and S is the cross-sectional area of the NW before correction. Now, if the oxide layer is taken into account, the external force has two parts: F_c and F_o, which act on the core and oxide layer respectively,

$$F = F_c + F_o = \sigma_c S_c + \sigma_o S_o \tag{55}$$

where, σ_c and σ_o are the stress applied on the core and the oxide layer of NW respectively, and S_c and S_o are the cross-sectional areas of the core and the oxide layer of NW respectively. The cross-sectional areas S, S_c and S_o, respectively, can be expressed as $S = \pi r_o^2$, $S_c = \pi r_c^2$, and $S_o = \pi(r_o^2 - r_c^2)$, where r_c is the core radius, and r_o is the overall radius of the NW. Then based on the Hooke's law (i.e., $\sigma = \varepsilon E$), the above equation (53) is rewritten as

$$\varepsilon E \times \pi r_0^2 = \varepsilon_c E_c \times \pi r_c^2 + \varepsilon_0 E_o \times \pi(r_0^2 - r_c^2) \tag{56}$$

where, E is the calculated Young's modulus of NW before correction, E_c and E_o are the Young's modulus of the core NW and the oxide layer, respectively. It is apparent that

the overall strain (ε) is same with the strain on the core NW (ε_c), or the strain on the oxide layer (ε_o) (i.e., $\varepsilon = \varepsilon_c = \varepsilon_o$). Therefore, the above equation can be simplied as

$$Er_o^2 = E_c r_c^2 + E_o \left(r_o^2 - r_c^2 \right) \tag{57}$$

In experiments, the overall diameter D_o and core diameter D_c of a NW were measured on captured TEM images of the NW. If we introduce a constant α to represent the diameter ratio or radius ratio (i.e., $\alpha = \frac{D_o}{D_c} = \frac{r_o}{r_c}$), then the Young's modulus of the core NW can be calculated by

$$E_c = E\alpha^2 - E_o \left(\alpha^2 - 1 \right) \tag{58}.$$

Next, the above equation (56) is simply manipulated by dividing E on both sides, and then it becomes

$$\frac{E_c}{E} = \alpha^2 - \frac{E_o}{E} \left(\alpha^2 - 1 \right) \tag{59}.$$

From this equation (57), it can conclude that when the Young's modulus of oxide layer is smaller than the uncorrected Young's modulus of the NW, the uncorrected Young's modulus is underestimated (i.e., when $\frac{E_o}{E} < 1$, $\frac{E_c}{E} > 1$.), and vice versa.

4.3.4.2.2 The Effect of Oxide Layer on Buckling and Bending Tests

For bending and buckling tests, the Young's modulus E of a NW can determined by equation (13) and equation (14), respectively. From these two equations, the flexural rigidity EI is only term that will be affected by the oxide layer. It is apparent that the overall flexural rigidity should combine the flexural rigidity of the core ($E_c I_c$) and that of the oxide layer ($E_o I_o$). Therefore, the relationship between the intrinsic Young's modulus of the core NW (E_c) and the uncorrected modulus of the NW (E) can be expressed as

$$EI = E_c I_c + E_o I_o \tag{60}$$

where, I, I_c , and I_o are, respectively, the second moment of areas for the cross section of the NW, the core, and the oxide layer, and E_o is the Young's modulus of the oxide alyer. Applying the formulas of these three second moment of areas into the above equation (58), it becomes

$$E \frac{\pi}{4} r_o^4 = E_c \frac{\pi}{4} r_c^4 + E_o \frac{\pi}{4} \left(r_o^4 - r_c^4 \right)$$ (61).

As aforementioned, by introducing the radius ratio α, the Young's modulus of the core NW can be corrected by

$$E_c = E\alpha^4 - E_o \left(\alpha^4 - 1 \right)$$ (62).

Therefore, it also can be concluded that if the Young's modulus of oxide layer is smaller than the uncorrected Young's modulus of the NW, the uncorrected Young's modulus will be underestimated, and vice versa.

4.3.4.2.3 The Effect of Oxide Layer on Resonance Vibration Test

The oxide layer has more complex effects on the resonance vibration test of a NW, because it both changes the flexural rigidity EI and the unit mass of the NW. The resonant frequency measured from the experiment was the frequency of a core-oxide NW, and was considered as a uniform homogenous NW. Based on the equation (11), the relationship between the uncorrected modulus of the NW (E) and the intrinsic Young's modulus (E_c) of the core NW can be expressed as

$$\frac{\rho S}{EI} = \frac{\rho_c S_c + \rho_o S_o}{E_c I_c + E_o I_o}$$ (63)

where, ρ, ρ_c and ρ_o are the density of the whole NW, the core NW, and the oxide layer ,respectively. The density of the whole NW was considered as the density of the core NW before the correction. Then the above equation can be rewritten as

$$\frac{\rho_c \pi r_o^2}{E \frac{\pi}{4} r_o^4} = \frac{\rho_c \pi r_c^2 + \rho_o \pi \left(r_o^2 - r_c^2\right)}{E_c \frac{\pi}{4} r_c^4 + E_o \frac{\pi}{4}\left(r_o^4 - r_c^4\right)} \tag{64}.$$

Then, the intrinsic Young's modulus of the core NW can be corrected by

$$E_c = E\alpha^2\left(1 + \frac{\rho_o}{\rho_c}\left(\alpha^2 - 1\right)\right) - E_o\left(\alpha^4 - 1\right) \tag{65}.$$

It is not clear to determine if the uncorrected modulus of a NW without consideration of the oxide layer was underestimated or overestimated. However, for B_4C NWs, the Young's modulus and density of amorphous boron oxide (B_2O_3) layer were reported to be 16 GPa and 1.8 g/cm^3 [59]. The thickness of the amorphous oxide layer was extensively investigated on individual NWs by TEM, and found in the range of 2-3 nm. The core radii of all tested NWs were ranged from 20 nm to 50 nm. Therefore, the radius ratio a was in the range of 1.04-1.15. From the resonance vibration results, the uncorrected Young's moduli were calculated to be in the range of 300-500 GPa. Then based on the above equation (63), the true Young moduli of the core B_4C NWs should be about 14%-60% higher than the uncorrected Young's moduli.

4.3.4.3 Amorphous Carbon Layer

The clamp should be very strong, so that the sliding of nanostructure will not occur during *in situ* tests. It is known that the nanostructures have high surface energy, so that the attractive forces (e.g., van der waals, electrostatic, and friction forces) between nanostructures and a tip or a flat substrate are moderately strong. So it could be used for clamping nanostructures if no strong interactions were required [137]. Adhesive was also used to develop a strong clamp between carbon nanotube (CNT) and an AFM tip [138]. But the difficulty of controlling CNT's orientation and the contamination of adhesive on CNT were the disadvantages for using adhesive. So far, electron-beam-induced deposition (EBID) has been extensively employed to develop strong nanoscale

clamps inside electron microscopes. The EBID was first observed inside SEM by Watson in 1947 [139]. It was common to observe that the surface became contaminated with a carbon-rich film when it was exposed to an electron beam in SEM. This contaminated film was presumed to be formed by secondary electrons induced polymerization of hydrocarbons that were present in the vacuum chamber and absorbed onto the surface. These hydrocarbons molecules might come from the residual hydrocarbons in the vacuum chamber, such as pump oil, or the contaminations absorbed on the surfaces of samples during the preparation and manipulation of samples. Hence, the nanoscale clamp could be done inside SEM with only residual hydrocarbon contaminates. But its major disadvantage was time consuming. Besides, it was difficult to guarantee that the clamping is strong enough. Therefore, it was improved either by incorporating a gas delivery system that provides the precursor molecules [140], or by using micromanipulator to deposit paraffin on the probe [141]. However, there is one critical issue by using EBID found in our experiments, which has been unexplored. That was an amorphous carbon (a-C) layer formed on a NW when the NW was clamped onto the tip by EBID. Moreover, the a-C layer could be formed too even when nanostructures were imaged with relatively large magnifications under electron beam irradiation (EBI). But it was found that the a-C layer induced by EBID was thicker than that induced by EBI. To understand the formation mechanism of the a-C layer on a NW, extensive tested NWs were post-test investigated by TEM.

4.3.4.3.1 The Non-uniformity of a-C Layer

Similar with the oxide layer, this additional a-C layer should have effects on all types of mechanical tests. However, will they have same effects? In other words, will the uncorrected Young's moduli of the NWs be underestimated?
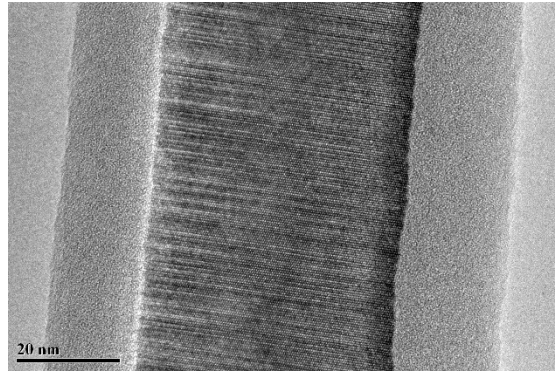
FIGURE 4.19: TEM image of a post-test NW with a non-uniform amorphous carbon layer.

From the experimental observations, the a-C layer was not formed uniformly either in the radial or longitudinal directions. FIGURE 4.19 shows that the left a-C layer formed on a tested NW is thinner than the right one. In the beginning, it was believed that the non-uniformity of the a-C layer in the radial direction was because the top-half NW exposed to the electron beam had a thicker a-C layer while the bottom-half NW hidden from the electron beam had a thinner one. This reason was plausible because more secondary electrons were generated on the top-half exposed surface. For a gas delivery system, the surface absorption played a dominant role in the EBID process, so the thickness of a-C layer was positively related to the amount of generated secondary electrons. Therefore, the top-half NW should have a thicker a-C layer, which was confirmed by the reported observation achieved with a gas-assisted ion beam induced deposition [142]. However, the fact from our observation was exactly the opposite. The bottom-half NW had a thicker a-C layer while the top-half NW had a thinner one, as shown in FIGURE 4.20A. This can be explained by the surface diffusion model, which was proved from many experimental results and accepted that it had more dominant role than the surface absorption model in the explanation of EBID mechanism [141, 143].
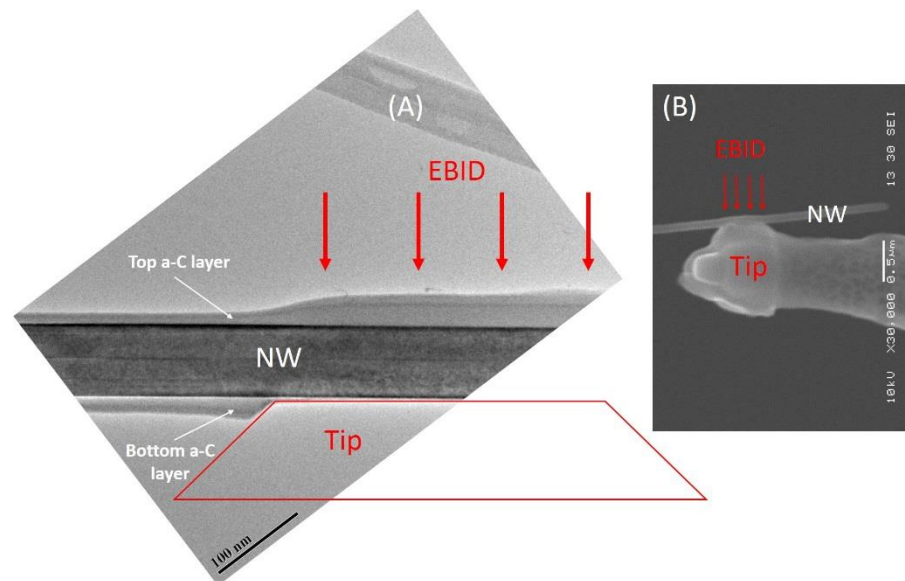
FIGURE 4.20: (A) TEM image demonstrates the difference between top and bottom a-C layers for a post-test NW, which was clamped to a tip by EBID in SEM, as shown in the SEM image (B).

In the longitudinal direction, the a-C layer was not uniform neither, FIGURE 4.21. The a-C layer was formed and completely covered on a tested NW. But the thickness of the a-C layer gradually decreased from the clamped end to the free end of the NW. It was believed that the decrement of its thickness along the length of NW was resulted from the combined effects of the nonlinear distribution of secondary electrons and the diffusion of decomposed hydrocarbon molecules along the length of NW. The a-C layer was also formed when the whole NW was exposed to the electron beam during the tests. But the a-C layer caused by this EBI process was believed as uniform, which was consistent with the experimental observation that the a-C layer on a tested NW far away (i.e., > 1 μm) the clamp end was almost uniform.
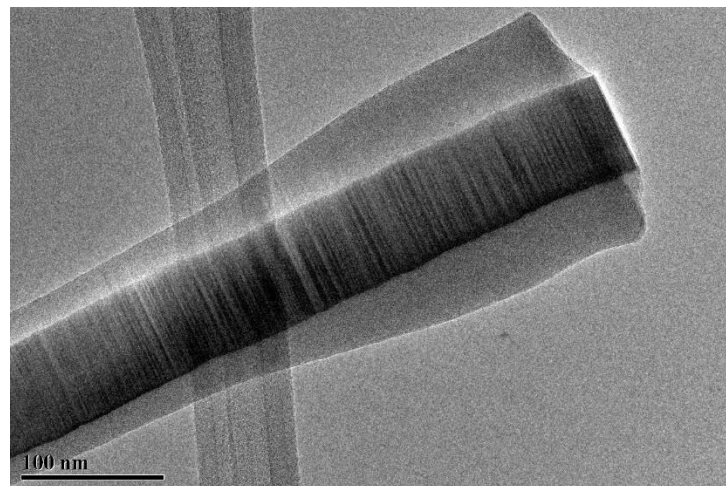
FIGURE 4.21: The TEM image to show a non-form a-C layer on a tested NW.
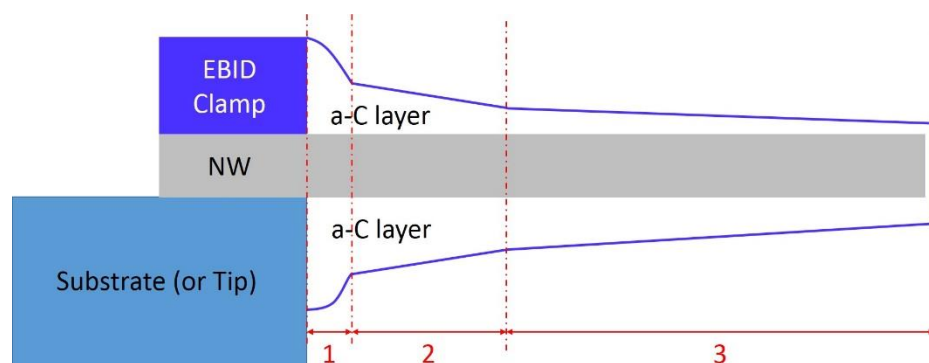
FIGURE 4.22: The model to demonstrate the thickness profile of a-C layer on a tested NW.

Because the a-C layer on a NW is non-uniform both in radial and longitudinal directions, it is extremely difficult to find an analytical solution for correcting the effects from the a-C layer. Therefore, FEM was employed to study the effect of a-C layer on experimental results. First of all, a model (FIGURE 4.22) was created to mimic the real thickness profile on a tested NW for FEM modeling. In this model, it represents that a NW is fixed on a substrate or a tip by EBID, and ready for resonance vibration test. Therefore, the NW is actually composed of three materials (i.e., a-C, amorphous B_2O_3,

and crystalline B$_4$C). For the a-C layer on the NW, it is divided into three parts, as illustrated in FIGURE 4.22. For the part1, its length is defined to be 50 nm, which is based on the experimental measurement 50 ± 10 nm. The profile of the part 1 is nonlinear, and described as a Gaussian curve, FIGURE 4.23. The profile of the a-C layer on part 1 is mainly caused by the distribution of the first type of secondary electrons (SE 1: produced when the primary electrons interact with the sample surface), which was generally thought as a Gaussian distribution [144]. For the part 2, its length is assumed to be 1 μm, which is based upon the post data analysis result, as shown in FIGURE 4.24. It demonstrates that in the distance range of 0.05-1 μm away from the clamp end, the thickness decreases dramatically. The profile of a-C layer on the part 2 is considered to consistent with the distribution of the second type of secondary electrons (SE II: produced when the backscattered electrons interact with the shallow portions of the sample). Interestingly, the value of 1 μm is consistent with the theoretical value (1.01 μm) of the maximum escape radius of secondary electrons on B$_4$C materials based on the model of Kanaya and Okayama [145]. In that model, the primary electron beam should hit on a flat substrate, and then it yielded the maximum escape radius of secondary electrons. However, for NWs having circular cross-sections with tens of nanometers in diameter, the theoretical calculation based on that model should not be fit for our case. Therefore, the other possibility that the decomposed hydrocarbon molecules diffused on the surface of a NW was considered, because the high surface energy of NW likely made it happen. To simplify the model, the thickness profile of this part is considered as a linear decrement with a relatively large slope. For the part 3, it is covered the rest length of the NW. The a-C layer on this part is formed mainly due to EBI on the whole NW during the testing. Based on the experimental results, the thickness profile of this part is considered as a linear decrement with a small slope. This

slight decrement should be the consequence of hydrocarbon molecules diffusing from the clamp end to the free end on the NW's surface.
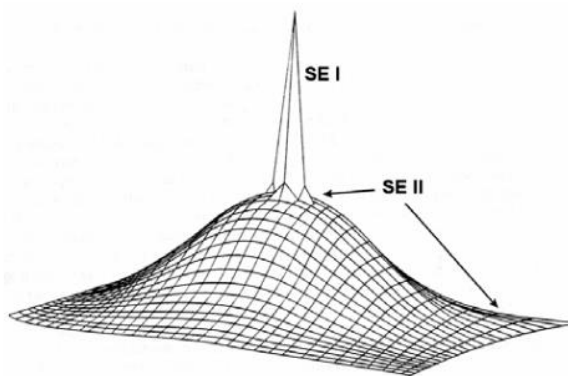
FIGURE 4.23: The illustration of 3D distribution profile of secondary electrons.
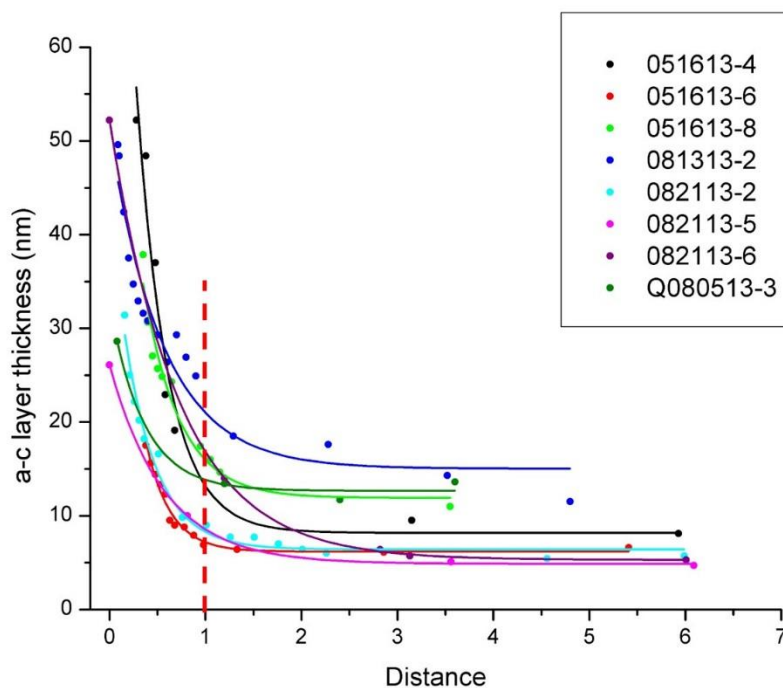
FIGURE 4.24: Measurement results of thickness of a-C layers on five post-test NWs to demonstrate the distributions of a-C layer profiles.

For NWs subject to different conditions of EBID and EBI, the a-C layer profiles formed on the NWs were different. In FIGURE 4.24, the average thickness distributions of a-C layers on NWs were fitted as exponential decay functions. It was also found that a thicker a-C layer was easier to form on a thin NW, because the mass of a-C materials deposited on a NW with similar condition should be equivalent. Therefore, instead of using thickness profile, the mass profile (i.e., volume profile) was applied to generalize the a-C layer profile. Because the volume profile along the length of NW is just the cross-sectional area varying along the longitudinal direction. Likewise, the cross-sectional area profile was also well fitted by an exponential decay distribution:

$$y = y_0 + Ae^{-\frac{x}{t}} \tag{66}$$

where, y_0 is the offset to represent the amount of a-C layer on the part 3, A is the amplitude representing the amount of a-C layer in the initial portion of the part 1, and t is the decay rate representing the profile shape. Based on the results of eight post-test NWs (TABLE 4.5), the general trends can be concluded. The amount of a-C layer on the part 3 (the offset) is positively related to the amount of hydrocarbon source (paraffin) and EBI time. And the amount of a-C layer in the initial portion of the part 1 (the amplitude) is proportional to the combination of paraffin amount and EBID time. However, it is difficult to extract quantitative formulas to express their correlations.

TABLE 4.5: Experimental conditions and results of a-C layer profiles.

NW ID	Voltage (KV)	EBID (mins)	EBI (mins)	Diameter (nm)	Paraffin amount	offset (y0)	Amplitude (A)	Decay rate (t)
051613#4	10	25	75	75	more	4	31.5	0.29
051613#6	10	23	48	90	less	1.6	4	0.24
081313#2	10	22	103	42	less	3.3	13.8	0.42
051613#8	20	33	73	45	less	2.5	6.6	0.25
082113#2	10	13	42	53	more	1.4	6.4	0.28
082113#5	10	35	59	102	less	1.4	9.1	0.54
082113#6	10	66	44	58	less	1.1	17.3	0.56
080513#3	10	22	113	62	less	3	6.6	0.34

4.3.4.3.2 The Effects of a-C Layer on *In-Situ* Tests

The radial non-uniformity of a-C layer on a NW will cause the split of resonance frequencies of the NW because the second moment of area will be different along the axis of in-plane and out-of-plane, FIGURE 4.25. For example, the different resonance frequencies were measured when the NW was vibrating in different orientations, FIGURE 4.26. The resonance frequency measured from the experiment was the one when the NW was vibrating in-plane, which is the plane perpendicular to the electron beam direction, FIGURE 4.26A. It was very difficult to observe the out-of-plane vibration because the vibration direction is parallel to the electron beam direction, FIGURE 4.26B. Since the in-plane frequency is the one wanted and measured from the experiment, the non-uniform thickness in the direction of out-of-plane is not important. Therefore, in order to simplify the model, the shape of a-C layer is considered as a circular pipe. Hence, the non-uniformity effect of a-C layer will be only discussed for the profile along the longitudinal direction.
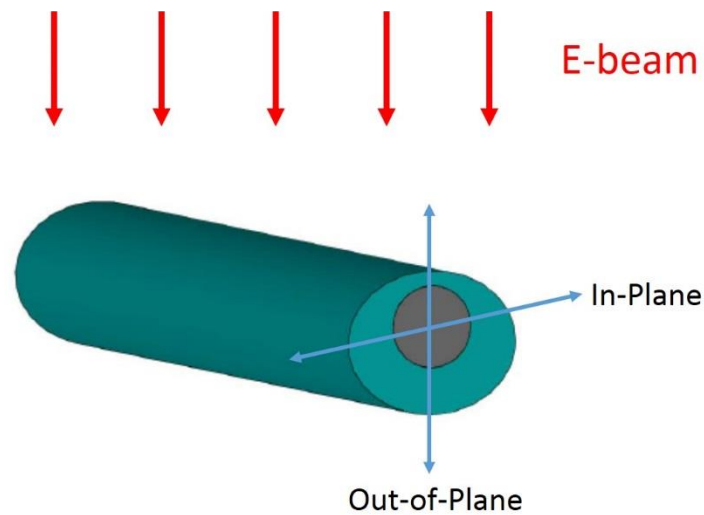
FIGURE 4.25: The schematics of non-uniform cross section after a-C layer (green) deposited on the NW (grey), resulting in two different resonances in-plane and out-of-plane.

In-plane: f_{ip}=2.1990 MHz   Out-of-plane: f_{op}=2.1134 MHz
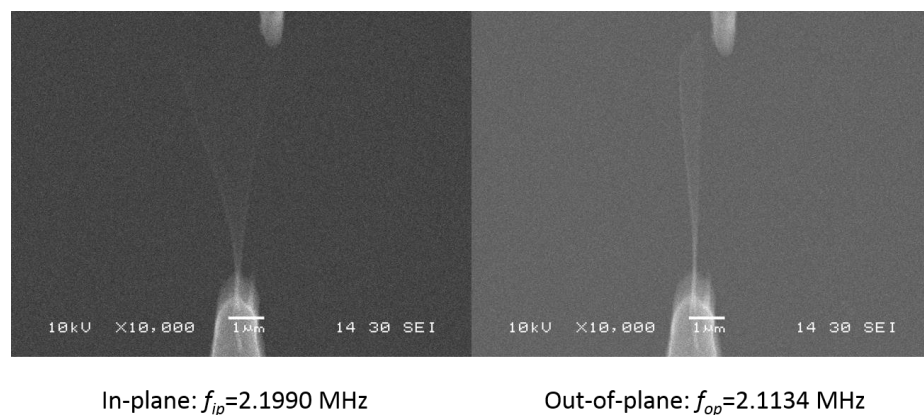
FIGURE 4.26: SEM images showing two different resonances for in-plane and out-of-plane.

For bucking and bending tests, the formation of the a-C layer on the NW increases the flexural rigidity *EI*, which requires a larger force to reach a desired deformation. Because the a-C layer was not considered for the calculation of *I* in the results, the calculated Young's modulus would be overestimated when a larger applied force was used for the calculation.

For a tensile test, a larger force is needed to extend a NW with the a-C layer to a certain elongation as compared to a NW without a-C layer, because it needs an extra force to elongate the a-C layer. In the tensile results, because the a-C layer was not considered, the stress was overestimated with using a larger force over a constant cross sectional area. Thus, the Young's modulus was overestimated because the overestimated stress was used to divide by a correct strain. In addition, the existence of a non-uniform a-C layer could affect other mechanical properties derived from tensile rests, such as tensile strength, ultimate strength. It was observed from many *in situ* SEM tensile tests of NWs in our group or other research groups. The NWs were always fractured at the positions close to the EBID clamp. It may be caused by the distortion of a tested NW at clamped ends, which is due to the in-plane or height misalignments of a NW, as discussed in the section 4.3.3. But the misalignment issue was not existed for MEMS-based tensile tests, then why the fracture positions were also close to the EBID clamps? Here, a new explanation related to the non-uniformity of a-C layer was provided. From the proposed model of a-C layer (FIGURE 4.22), the a-C layer thickness changes more rapidly on the part where is close to the EBID clamp. So it could have some points with very large discontinuity on the surface of the part close to the EBID clamp. It is well known that the discontinuity on the surface will generate a stress concentration under an applied force, which has a higher chance to produce cracks and fractures. This hypothesis was verified by one experimental result. In this experiment, two regions of a NW was exposed to electron beam before the second end was fixed for tensile test, FIGURE 4.27A. As a result, thicker a-C layer were formed on these two regions, and large discontinuities of a-C layer on the surface were found at boundaries of these two regions. When this NW was subjected to tension, it was eventually fractured the positions where the largest discontinuities located, FIGURE 4.27B. The reason for two

positions on NW failed simultaneously could be because they both reached the maximum stresses at the same time. Therefore, the non-uniform a-C layer is likely to reduce the fracture strength.
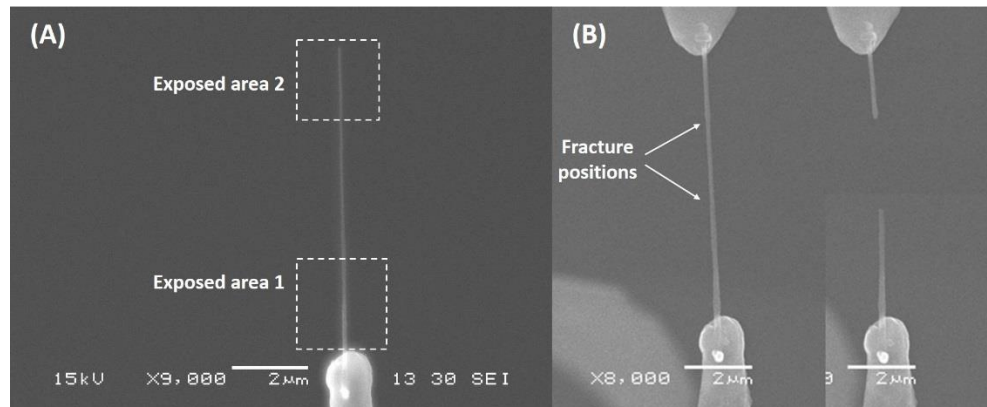
FIGURE 4.27: SEM images of a NW was fractured at two edge positions between a thick and a thin a-C layers.

For the resonance vibration test, the resonance frequency was measured to determine the Young's modulus of a tested NW. Therefore, it is important to find out the change of resonance frequency before and after the formation of a-C layer. Interestingly, the formation of a-C layer does not only increase the flexural rigidity, but also increase the mass of a test NW. According to the equation (11), it is shown that the flexural rigidity and mass are proportional and inversely proportional to the resonance frequency, respectively. Therefore, it is more complicated to determine the effects of the a-C layer on resonance vibration testing results. For example, the root part (close to the clamp end; exposed area 1) and the top part (close to the free end; exposed area 2) of a NW were exposed to electron beam for 5 minute repetitively, FIGURE 4.28A. It was discovered that the a-C layer formed on the root part of a NW increased the resonance frequency, while it formed on the top part of a NW decreased the resonance frequency, FIGURE 4.28B. This result was consistent with many other reported results related to

the mass sensing by cantilevers [146-148]. The additional mass by forming a-C layer on the top part plays a dominant role to reduce the resonance frequency, because the motion at the free end is the maximum. But the increased flexural rigidity by forming a-C layer on the root part plays a dominant role to increase the resonance frequency, because the bending moment at the clamp end is the maximum. Therefore, it is worthy to point out that extra attentions should be paid while imaging a small region of a NW in SEM, because the a-C layer is easy to form under a focused electron beam and to result in the frequency shift. FEM was also used here to study this effect. The modeling results were consistent with the experimental results. Furthermore, it was shown that in the modeling results, the partial a-C layer on the top part of a NW decreased the resonance frequency only due to the adding mass. Because the frequency did not change when the Young's modulus of a-C material was changed in the modeling. But when the density of a-C material was altered, the frequency shifted accordingly. Likewise, the partial a-C layer on the root part of a NW increased the resonance frequency only because of the increasing flexural rigidity. The resonance frequency shifted after the Young's modulus of a-C materials was changed, while it stayed unchanged after the density of a-C material was adjusted in the modeling.
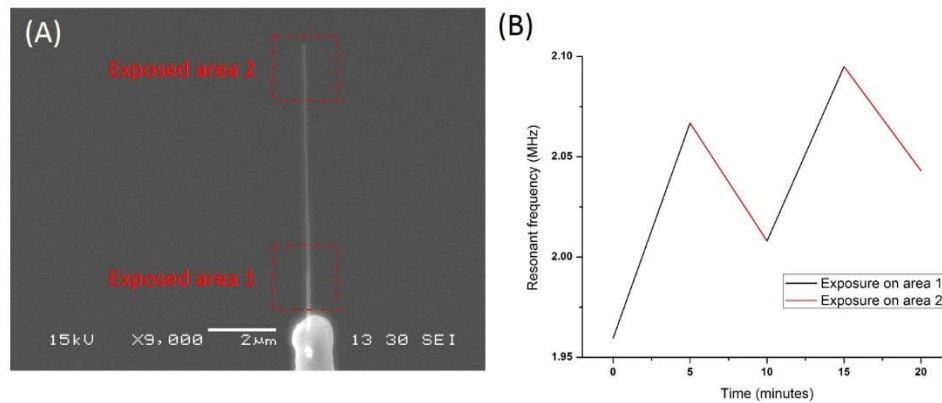
FIGURE 4.28: (A) SEM image of a NW with two regions exposed to EBI; (B) and its corresponding frequency shift after EBI to two different regions.

The a-C layer that affected on frequency measurement discussed above was formed by EBI. But, how does the EBID-induced a-C layer affect the frequency measurement? Since it is impossible to measure the frequency shift before and after making clamps by EBID, FEM was applied to study this effect. It is described above that the a-C layer formed by EBID is not uniform, and its profile is divided into three parts. For the part 1, its length is only around 50 nm. Moreover, scarce experimental data for the part 1 were obtained, because the tested NWs apart from the tip were usually broken at the part 2. For this reason, the a-C layer of the part 1 was not taken into account in FEM study. Then the a-C layer profile is composed of two tapered pipes representing the part 2 and 3, FIGURE 4.29. According to the measurement results, the thickness $t2$ was estimated to $1.5 \cdot t3$, and $t1$ was also written as $\alpha \cdot t3$, where α was in the range of 2.5 - 10, which depended on the combination of paraffin amount and EBID time. The thickness $t3$ was measured in the range of 4-12 nm, depending on the combination of paraffin amount and EBI time. The thickness of oxide layer was fixed to 2 nm. The effective lengths of all tested NWs were in the range of 4-9 μm, while their core diameters were ranged from 40 nm to 90 nm. Then all combinations

with each smallest and largest values for each parameters were applied to build various

models, so that the frequency shift range could be found.
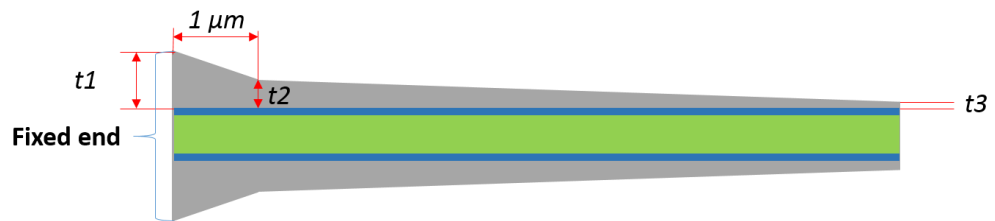
FIGURE 4.29: The simplified model of a-C layer (grey) after EBID on a NW (B$_4$C (green) and oxide layer (blue)). The parameters *t1*, *t2* and *t3* are the thicknesses of three boundaries which represent shapes of two tapered pipes.

TABLE 4.6: FEM results of frequency shift for different a-C layer profiles on NWs with different size.

NW type	L (µm)	D (nm)	t3 (nm)	α (t1=α·t3)	f (MHz)	Δf (+/- %)	Possible (Yes/No)
Short & Thin	4	40	0	0	3.8982	0.0	No
			4	2.5	3.9984	2.6	Yes
			4	10	5.1925	33.2	Yes
			12	2.5	5.0553	29.7	Yes
			12	10	6.8841	76.6	No
Short & Thick	4	90	0	0	9.0610	0.0	No
			4	2.5	8.9470	-1.3	Yes
			4	10	10.1929	12.5	Yes
			12	2.5	9.3117	2.8	Yes
			12	10	12.4840	37.8	No
Long & Thin	9	40	0	0	0.7700	0.0	No
			4	2.5	0.7708	0.1	Yes
			4	10	0.8628	12.1	Yes
			12	2.5	0.9161	19.0	Yes
			12	10	1.0183	32.2	No
Long & Thick	9	90	0	0	1.7898	0.0	No
			4	2.5	1.7542	-2.0	Yes
			4	10	1.8633	4.1	Yes
			12	2.5	1.7789	-0.6	Yes
			12	10	2.0106	12.3	No

The simulation results of this study by FEM are presented in TABLE 4.6. The last column is to clarify the possibility to observe that a-C layer in experiment. For cases "t3=0, α=0" and "t3=12, α=10", the "No" means the situations of "no a-C layer" and "120 nm thick a-C layer on the root end" were not observed from the experiments. The reason to include the case of "t3=0, α=0" is in order to verify the frequency alteration before and after forming a-C layer. And the purpose of studying the case of "t3=12, α=10" is to find out the upper limitation. For most models, the frequencies of NWs with a-C layers are larger than those without a-C layers. It is known that the added mass of the a-C layer formed on the top part of a NW reduced the frequency, while the increased flexural rigidity of the a-C layer on the root part of the NW raised the frequency. Similar with the effect of the oxide layer on frequency shift, a uniform a-C layer formed on a NW decreases the frequency of the NW. This means the added mass are more influential than the increased flexural rigidity on frequency shift for a uniform a-C layer. If the thickness of a-C layer close to the root end increases to a certain value, then two effects eventually will be balanced, meaning the frequency of NW with or without this a-C layer will remain same. In other words, the a-C layer has no effect on the resonance vibration test. For instance, a *long and thin* NW with the a-C layer ($t3 = 4$ nm and $\alpha = 2.5$) almost has no change (only 0.1%) on frequency. For most cases, because the thickness of a-C layer on the root part is larger than that that on the part close to the free end, the increased flexural rigidity from the a-C layer is more influential than the added mass, which results in an increment of frequency. By directly comparing the results in TABLE 4.6, two general rules can be extracted. (1) The frequency decreases or increases less for the longer and thicker NWs, because the increased flexural rigidity are more influential for shorter NWs, and the added mass are more dominant for thinner NWs. (2) With increasing the thickness $t3$ or α, the flexural rigidity increases more, so the frequency

increases more too. With these two rules, the frequency shift range can be determined through finding the lower and upper bounds. In general, the frequency shift percentage is found out in the range of -2.0% - 76.6%. Because the uncertainty of the Young's modulus is around twice much as that of measured frequency (i.e. $\frac{\Delta E}{E} \propto 2\frac{\Delta f}{f}$), the estimation error of the Young's modulus is in the range of -4.0% - 153.2%. In other words, the uncorrected Young's moduli may be slightly underestimated, or slightly overestimated, or significantly overestimated. This simulation results provide an explanation for the large variations of the calculated Young's moduli of nanostructures with same materials from *in situ* SEM tests. Because with inconsistence of EBID and testing times, the different profiles of a-C layer formed on nanostructures would vary the results for all *in situ* SEM tests, including resonance vibration, buckling, bending, and tensile tests.

To better understand the above discussion, an example of a tested NW (082113#6) is given here. The experimental results of this NW are presented in TABLE 4.1. The uncorrected Young's modulus of this NW is 509 GPa, which is much larger than those of other AF NWs (300-400 GPa). The reason of higher calculated modulus is due to a thicker a-C layer formed on its root end, as shown in FIGURE 4.30. Two dash lines represent the core B_4C NW. Via studying this NW with pre-test and post-test TEM imaging, the core diameter is around 51 nm, and the effective length is around 8 μm, and the thickness *t3* and α are 5 nm and 9, respectively. These parameters are very close the case "*L=9, D=40, t3=4, α=10*", which gives a rough 12.1% frequency increment. It also means the uncorrected Young's modulus 509 GPa is around 24.2% overestimated. Therefore, the Young's modulus can be corrected to 409 GPa (i.e., 509/(1+24.2%)), which is close to the range of 300-400 GPa.
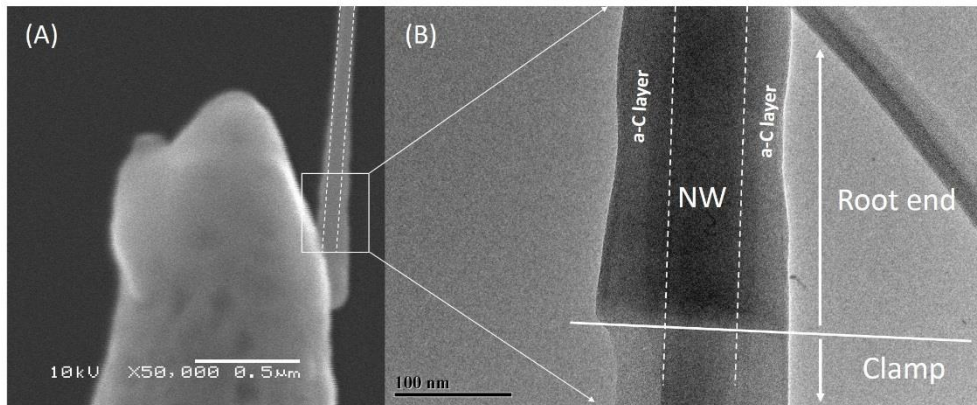
FIGURE 4.30: (A) SEM and (B) TEM images of the root end of 082113#6 NW to show the thick a-C layer on NW. The image (B) is the part marked in image (A). Two dash lines are used to represent the sides of core NW.

4.3.4.3.3 The Effect of Clamping on Resonance Vibration Test

It was reported that the frequency increased with adding more EBID time and then reached the plateau because the clamp became strong enough [125]. The reported results were based on the line clamp, which was different than the area clamp used more frequently by us and many other groups. The experimental studies of frequency shift with increasing EBID time were conducted initially in order to obtain strong clamps. But interestingly, the experimental results was different with that reported results. The frequency increased with adding EBID time, but did not reach the plateau, as shown in FIGURE 4.31.
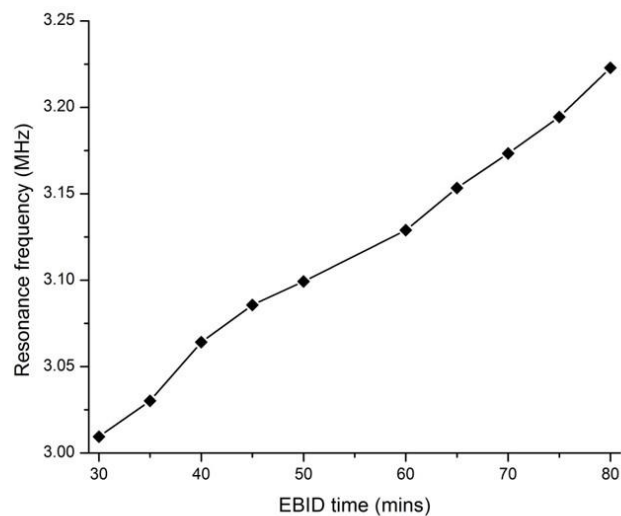
FIGURE 4.31: The experimental results of frequency shift with adding EBID time.

In order to find out the true cause for this different between the reported and our experimental results, FEM was used again to study the line and area clamps. The line clamp study was referred to the publication with same conditions and modeling settings [125]. 20-node quadratic brick elements (C3D20R) and 4-node linear tetrahedron elements (C3D4) were used for the NW and the line clamp, respectively. FIGURE 4.32 shows a created solid model (A) and the mesh on the clamp and NW (B), and also the simulation results (C). The bottom face of the line clamp was fixed, because the clamp was firmly attached on a secured tip in the experiments. The cross section of the line clamp was approximated to a Gaussian distribution, which was explained above for the profile of SE1. The analytical results of frequency shift was calculated by considering the decrease of the NW's effective length after widening the line clamp. The frequency increased significantly by broadening a narrow clamp, because the narrow clamp deformed under the maximum bending moment. The deformation on the clamp disappeared when the width increased. Then the frequency shift should be close to the

analytical result, as illustrated in FIGURE 4.32C. Our modeling result was consistent with the modeling results reported by Qin [125].
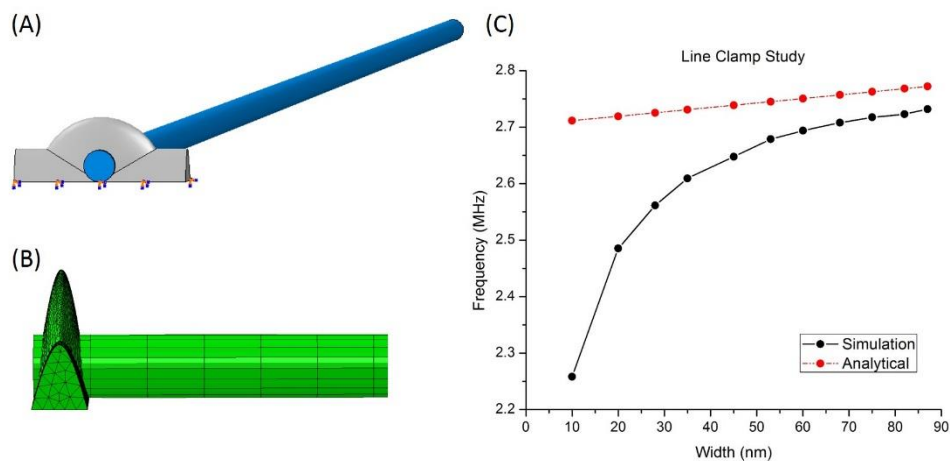
FIGURE 4.32: Line clamp study by FEM. (A) the created model for line clamp (grey) with a NW (blue); (B) side view of line clamp after mesh; (C) the modeling results of frequency shift with increasing the width of line clamp, comparing with the analytical results.

Once the line clamp study was verified, the area clamp study was then performed. A similar solid model (FIGURE 4.33A) was created, with a fixed bottom of the area clamp. The length and width of the area clamp were prescribed as 425 and 320, which was based on the actual size of the area clamp: 425 nm × 320 nm. The FEM results (FIGURE 4.33B) shows the frequency increased slightly by thickening a thin area clamp. The increment amount was much less as compared with the line clamp study. The frequency increased only 0.4% with increasing the thickness of the area clamp from 5 nm to 40 nm. After that, the frequency shift reached the plateau, which meant the resonance frequency of the NW would not increase with growing the thickness of the area clamp. The FEM resultant curve was lower than the theoretical value, implying that a small deformation inside the clamp was always existed because of the maximum bending moment existed on the fixed end of NW.
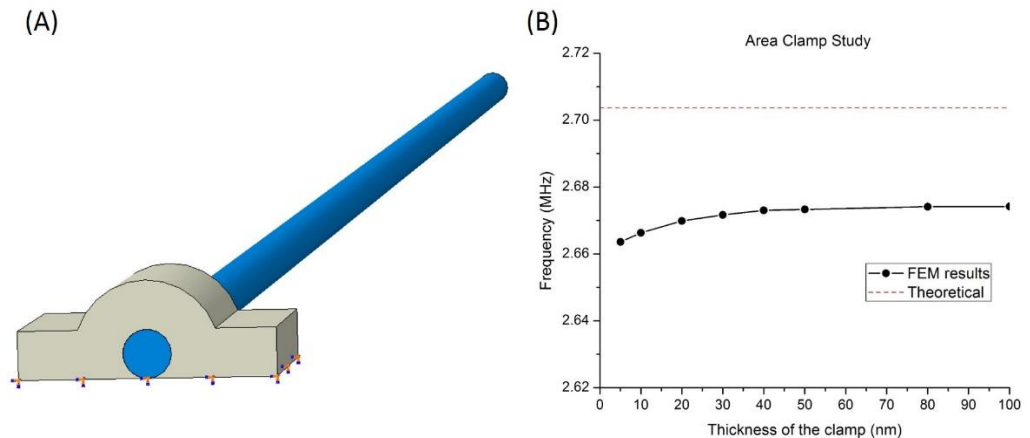
FIGURE 4.33: Area clamp study by FEM: (A) the solid model for an area clamp (grey) with a NW (blue); (B) the FEM results of frequency shift with increasing the thickness of the area clamp, comparing with the theoretical value.

It clearly demonstrates that the modeling results (FIGURE 4.33B) are not consistent with experimental results (FIGURE 4.31) for the area clamp. So, what is the true cause for the frequency increasing with adding EBID time? Is it possible that the effective length decreases with adding EBID time? The answer is no. For example of the experimental results present in FIGURE 4.31, the frequency increases about 8%, which means the effective length should decrease around 4% according to the equation of $\frac{\Delta f}{f} \propto 2\frac{\Delta L}{L}$. Since the effective length of this tested NW is 6.81 μm, the added width on the area clamp (i.e., the decrease amount of the effective length of NW) should be around 270 nm. However, this large amount of width increment on the area clamp was not observed within SEM.

After ruling out these two possible causes for the frequency increase: thickening the clamp and shortening the effective length, the only left cause is that the a-C layer on the root part of NW becomes thicker with adding EBID time. A series of SEM images

(FIGURE 4.34) demonstrates the diameter on the root part of NW increases with raising EBID time.
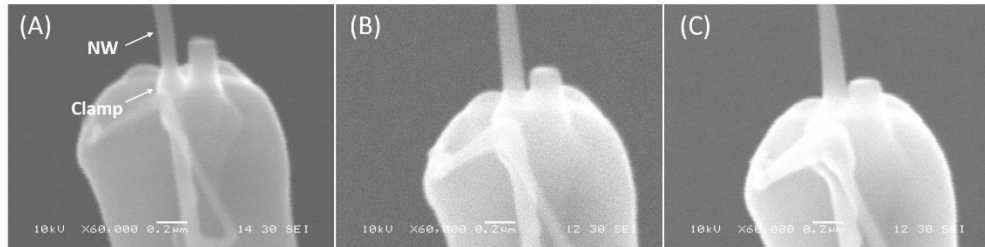
FIGURE 4.34: SEM images of the root part of a tested NW after different EBID time: (A) 30 minutes; (B) 50 minutes; (C) 80 minutes.

In conclusion, this study demonstrates extra cautions are needed when depositing clamps by EBID: (1) the strong clamp can be reached by applying more EBID time; (2) but the thicker a-C layer will be formed on the root part of NW if more EBID time is used. Thus, it is necessary to find the compromise between these two aspects.

4.3.4.3.4 A Direct Characterization of a-C Layer

It was reported that the density and Young's modulus of a-C materials were 2.0 g/cm^3 and 50 ± 10 GPa, respectively [141]. These two properties of a-C materials were also studied in this work. Through imaging a post-test NW in TEM, FIGURE 4.35, it was found that the thickness of the a-C layer increased about 5 nm after around 1.1 μm-long NW part was exposed to electron beam for 5 minutes. The frequency decreased about 4.2% after this exposure in the experiment. In FEM, a small pipe with length of 1.1 um and 5 nm thickness was tied on the top part of a NW to mimic the formation a partial a-C layer. The density of material was set to the reported value 2.0 g/cm^3. The modeling result shows that the frequency reduces about 4.8%, which is consistent with the experimental result. However, the modeling result of adding a 1.1 μm-long and 5 nm thick of pipe on the root part of a NW only yielded about 1.4 %

frequency increment, which was much less than the experimental value as 5.6%

frequency increment. It could have two reasons for the inconsistency: 1) the model for

the partial a-C layer on the root part was incorrect; 2) the reported Young's modulus of

a-C material was low. The first reason was considered because the a-C layer was

formed near the tungsten tip considered as a hydrocarbon source. Based on the surface

diffusion model, the a-C layer profile should be modeled as a tapered pipe. Therefore,

a 1.1 μm-long, 10 nm-thick at clamp end and 5 nm-thick at another end of a tapered

pipe was modeled and tied on the root part of the NW. The frequency increased about

2.3%, which was still less than the experimental value. The taper ratio was not allowed

to increase because the thickness at clamp end in the model should match that

measured in the experiment. Thus, the second reason was taken into account. The

value of Young's modulus of a-C materials was set to 50 GPa based on the publication

[141]. However, this reported value was less than another value (> 100 GPa) reported

elsewhere [149]. The lower Young's modulus of a-C material was obtained by

nanoindentation with tens of nanometer indentation depth. So the underestimation of a-

C material's Young's modulus was probably due to the uneven surface of a-C

deposition on a Si substrate, as shown in the AFM image in that publication [141]. So

the Young's modulus of a-C material was increased to 100 GPa for the modeling.

After completing the modeling, the frequency increased about 4.4%. If the Young's

modulus of a-C material kept to increase to 135 GPa, the frequency increased 5.6%

which was same with the experimental value. The accuracy of density and Young's

modulus of a-C layer is very important in the correction of Young's modulus of NWs

if the a-C layer is considered. This introduced a new method to measure the Young's

modulus and density of a-C layer if the correct shape of a-C layer on the NW can be

determined. It may be also possible to deposit a regular shape of a-C layer on an AFM

cantilever for determine its density and Young's modulus by measuring the frequency shift of cantilever.
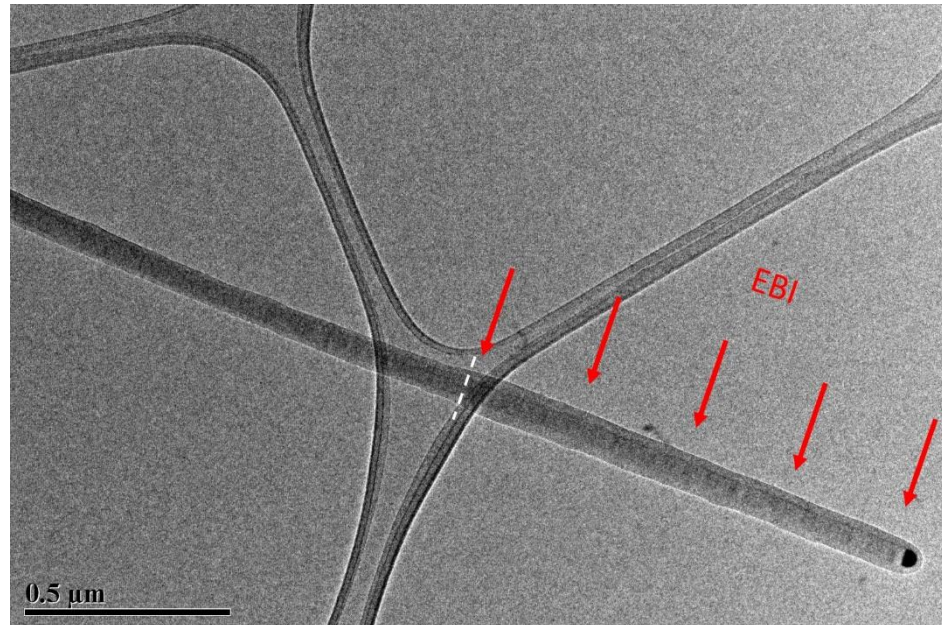
FIGURE 4.35: TEM image of a post-test NW showing the difference between EBI exposed and unexposed areas and the boundary (white dash line).

4.4   Conclusions

The mechanical properties of B_4C NWs were studied by *in situ* resonance vibration, buckling, and tensile tests inside SEM with the home-made nanomanipulator system. The detailed data analysis of experimental results for different testing techniques were conducted. Finite element modeling was extensively employed in this chapter to study the experimental results and understand some unexpected phenomena.

B_4C NWs were first investigated under TEM before subject to *in situ* tests. The diameters of core NWs and the thicknesses of the oxide layers were measured by processing captured TEM images with pixel resolution. The stacking faults on NWs were observed. NWs were categorized into AF and TF NWs based on the faults orientations. In the resonance vibration test, the calculated Young's moduli of AF NWs

are lower than those of TF NWs. The fault orientation is believed to be the cause. The conclusion is confirmed as well in the buckling and tensile tests. The experimental results for resonance vibration tests are influenced by many apparent effects, such as small NWs or particles attached on NWs, plastic deformation on NWs during the manipulation, and so on. However, there are some hidden effects existed to affect the experimental results.

For the effect of slight non-uniformity of NW's length, analytical and simulation works were carried out. The direct comparison of analytical solutions and FEM results demonstrates they are consistent in the small taperness. For the taper ratio in the range of 0.5-1.5, the estimation error of uncorrected Young's moduli has a linear relationship with the taper ratio.

TABLE 4.7: The summary of effects of amorphous oxide and carbon layers on the uncorrected Young's modulus.

Test	Amorphous oxide layer	Amorphous carbon layer
Buckling	Underestimated	Overestimated
Tensile	Underestimated	Overestimated
Resonance vibration	Underestimated	Under- or over-estimated

The effects of amorphous oxide and carbon layers on different tests are summarized in TABLE 4.7. For amorphous oxide layer, its effect on the achieved modulus can be quantified by applying the derived equations. However, the effect of amorphous carbon layer on the achieved results are more qualitative, because the profile of a-C layer on NW is not uniform, and furthermore the profile is changing during the testing process. Because it is difficult to quantify the effect of a-C layer, the quantitative corrections on the measured results cannot be done. Fortunately, the effect of amorphous oxide layer offsets the effect of amorphous carbon layer. Although it is impossible to know if two effects are neutralized, the net effect should not be significant as long as the

a-C layer is not very thick. The a-C layer effect is useful to explain some abnormal phenomena observed in experiments, and helpful to filter out the deviated data and results. Therefore, the filtered uncorrected Young's moduli from the resonance vibration tests are considered to be close to the intrinsic values. The Young's moduli of B_4C AF NWs are in the range of 300-400 GPa, while those of B_4C TF NWs are 400-500 GPa. The TF NWs are comparably stiff to the bulk B_4C (E_{bulk}= 432-480 GPa) [150]. But B_4C NWs have excellent flexibilities as for the brittle ceramic materials. In addition, the results of tensile tests suggests that B_4C NWs have much higher fracture strength comparing with the bulk counterpart.

CHAPTER 5:   CONCLUSIONS AND FUTURE WORKS

5.1   Conclusions

The systematic experimental study of nanoindentation was carried out to determine optimal experimental conditions for nanoindentations at tens of nanometers depth. Then boron platelets, instead of nanoribbons, with thickness at tens of nanometers were used for nanoindentation tests because surface flatness was required for the tests. A few conclusions were made based on the results of nanoindentations to boron platelets on sapphire substrate: (1) indentation depth should not exceed the thickness of a tested platelet, otherwise pile-up or crack might occur. (2) boron platelets were softer than the sapphire substrate; (3) the indentation depth at 10 nm or less was inappropriate for our case, because many effects played more profound roles at this shallow depth; (4) the substrate effect was existed for a nanoindentation with depth more than 10 nm on the boron nanoplatelets. Therefore, a new approach was developed to rule out the substrate effect from the experimental results. Nanoindentation experiments were further conducted on boron platelets on four different substrates. Then the experimental data were analyzed to extract the intrinsic Young's modulus of α-tetragonal boron nanostructures at 69 ± 4 GPa. The calculated intrinsic modulus of α-tetragonal boron nanostructures was comparable to the reported values for α-rhombohedral crystalline boron nanobelts.

A home-built nanomanipulator *in situ* SEM has been developed. The details of those building blocks were briefly discussed and summarized. The performance of key components was conducted, and then the technical specifications of this

nanomanipulator system were generated. The basic tests for all available *in situ* testing techniques were attempted, and proved the feasibility for all techniques. Many improvements by adding more functions on the system have been done after problems were encountered when using the nanomanipulator to test B_4C NWs. Frist, each individual nanowire could be tested by two different techniques so that direct comparison of experimental data can be made. Second, the force measurement resolution was improved as compared to others' works. Third, the accuracy of determining the length of a tested nanowire was increased with the help of the additional rotational stage. Last, the pre-test and post-test imaging individual NWs by TEM were realized by using a home-made micromanipulator. These improvements facilitated more accurate mechanical characterization of 1D nanostructures.

Individual B_4C nanowires were extensively studied by a transmission electron microscope (TEM) before *in situ* tests. The TEM imaging results revealed that dense stacking faults were existed in B_4C nanowires with two different orientations: axial and transverse. Therefore, B_4C nanowires were categorized into AF and TF nanowires according to the axial and transverse faults. The calculated Young's moduli of B_4C nanowires from *in situ* resonance vibration, buckling and tensile tests indicated that TF NWs were stiffer than AF NWs. There were some visible effects on *in situ* tests, such as small NWs and particles attached on NW, plastic deformation prior to tests, and so on. Besides, some invisible effects also had profound influences on the results. All these effects were completely studied in order to better interpret the obtained results. After filtering out unqualified results, The Young's moduli of B_4C AF NWs were in the range of 300-400 GPa, while those of B_4C TF NWs were in the range of 400-500 GPa. The TF NWs were comparably stiff to the bulk B_4C. But B_4C NWs had excellent flexibilities

as for a brittle ceramic materials. In addition, the results of tensile tests suggested that B$_4$C NWs had extraordinary fracture strength comparing to the bulk counterpart.

5.2   Future Works

There are some future research works that may be worthy to pursue.

The proposed approach for extracting the intrinsic modulus by ruling out the substrate effect was only tried on our boron platelets. The first assumption of this approach is that the contact between the platelets and substrate should be perfect bond. However, it is difficult to judge this assumption. In order to verify this approach, it may be necessary to perform a series of indentation tests on one type of thin films on different substrates. The thickness of thin film can be at micro-scale, such that the indentation depth should be larger, in turns that many effects existing at shallow indentation depth are avoided.

The effect of amorphous carbon layer on experimental results is only qualitatively determined. The profile of a-C layer on NW after EBID is proposed in this dissertation according to the experimental observation. However, more experiments should be carried out to determine explicit relationships between the thickness of formed a-C layer and experimental conditions by systematically controlling parameters. The explicit relationships are beneficial to a direct determination of a-C layer profile without imaging every tested NW by TEM, which is much more convenient and efficient.

The preliminary results of determining the Young's modulus of a-C materials showed that the obtained value in this work was different than that in other's report. Since it is critical to have accurate mechanical properties of a-C layer for analytical or modeling corrections, more experiments and simulations are needed to determine the accurate properties of a-C layer caused by EBID.

It is extremely difficult to control the height misalignment when the NW is clamped onto the tip. Since experimental results are influenced by the height misalignment, many unqualified results are filtered out. Therefore, the filtered results of buckling and tensile tests are insufficient. To have more confidence in the conclusions about the results from these two *in situ* tests, more B_4C NWs should be tested by buckling and tensile testing techniques.

REFERENCES

1. Iijima, S., *Helical microtubes of graphitic carbon.* Nature, 1991. **354**(6348): p. 56-58.

2. Xia, Y.N., et al., *One-dimensional nanostructures: Synthesis, characterization, and applications.* Advanced Materials, 2003. **15**(5): p. 353-389.

3. Wildoer, J.W.G., et al., *Electronic structure of atomically resolved carbon nanotubes.* Nature, 1998. **391**(6662): p. 59-62.

4. Weber, J., et al., *One-dimensional nanostructures: fabrication, characterisation and applications.* International Materials Reviews, 2008. **53**(4): p. 235-255.

5. Zhang, Z.B., et al., *Electronic transport properties of single-crystal bismuth nanowire arrays.* Physical Review B, 2000. **61**(7): p. 4850-4861.

6. Zhou, X.T., et al., *Thin beta-SiC nanorods and their field emission properties.* Chemical Physics Letters, 2000. **318**(1-3): p. 58-62.

7. Li, Y., et al., *Nanowire electronic and optoelectronic devices.* Materials Today, 2006. **9**(10): p. 18-27.

8. Cui, Y., et al., *Nanowire nanosensors for highly sensitive and selective detection of biological and chemical species.* Science, 2001. **293**(5533): p. 1289-1292.

9. Patolsky, F., G. Zheng, and C.M. Lieber, *Nanowire sensors for medicine and the life sciences.* Nanomedicine, 2006. **1**(1): p. 51-65.

10. Li, D.Y., et al., *Thermal conductivity of individual silicon nanowires.* Applied Physics Letters, 2003. **83**(14): p. 2934-2936.

11. Wang, J.F., et al., *Highly polarized photoluminescence and photodetection from single indium phosphide nanowires.* Science, 2001. **293**(5534): p. 1455-1457.

12. Duan, X.F., et al., *Single-nanowire electrically driven lasers.* Nature, 2003. **421**(6920): p. 241-245.

13. Huang, M.H., et al., *Room-temperature ultraviolet nanowire nanolasers.* Science, 2001. **292**(5523): p. 1897-1899.

14. Kind, H., et al., *Nanowire ultraviolet photodetectors and optical switches.* Advanced Materials, 2002. **14**(2): p. 158-+.

15. Yan, R.X., D. Gargas, and P.D. Yang, *Nanowire photonics.* Nature Photonics, 2009. **3**(10): p. 569-576.

16. Tian, B., T.J. Kempa, and C.M. Lieber, *Single nanowire photovoltaics.* Chemical Society Reviews, 2009. **38**(1): p. 16-24.

17. Krishnan, A., et al., *Young's modulus of single-walled nanotubes.* Physical Review B, 1998. **58**(20): p. 14013-14019.

18. Li, F., et al., *Tensile strength of single-walled carbon nanotubes directly measured from their macroscopic ropes.* Applied Physics Letters, 2000. **77**(20): p. 3161-3163.

19. Treacy, M.M.J., T.W. Ebbesen, and J.M. Gibson, *Exceptionally high Young's modulus observed for individual carbon nanotubes.* Nature, 1996. **381**(6584): p. 678-680.

20. Wong, E.W., P.E. Sheehan, and C.M. Lieber, *Nanobeam mechanics: Elasticity, strength, and toughness of nanorods and nanotubes.* Science, 1997. **277**(5334): p. 1971-1975.

21. Wu, B., A. Heidelberg, and J.J. Boland, *Mechanical properties of ultrahigh-strength gold nanowires.* Nature Materials, 2005. **4**(7): p. 525-529.

22. Wu, B., et al., *Microstructure-hardened silver nanowires.* Nano Letters, 2006. **6**(3): p. 468-472.

23. Han, X.D., et al., *Low-temperature in situ large strain plasticity of ceramic SiC nanowires and its atomic-scale mechanism.* Nano Letters, 2007. **7**(2): p. 452-457.

24. Han, X.D., et al., *Low-temperature in situ large-strain plasticity of silicon nanowires.* Advanced Materials, 2007. **19**(16): p. 2112-+.

25. Zhang, Y.F., et al., *Direct observation of super-plasticity of beta-SiC nanowires at low temperature.* Advanced Functional Materials, 2007. **17**(17): p. 3435-3440.

26. Agrawal, R., et al., *Elasticity Size Effects in ZnO Nanowires-A Combined Experimental-Computational Approach.* Nano Letters, 2008. **8**(11): p. 3668-3674.

27. Chen, C.Q., et al., *Size dependence of Young's modulus in ZnO nanowires.* Physical Review Letters, 2006. **96**(7).

28. Zhu, Y., et al., *Size effects on elasticity, yielding, and fracture of silver nanowires: In situ experiments.* Physical Review B, 2012. **85**(4).

29. He, J. and C.M. Lilley, *Surface effect on the elastic behavior of static bending nanowires.* Nano Letters, 2008. **8**(7): p. 1798-1802.

30. Miller, R.E. and V.B. Shenoy, *Size-dependent elastic properties of nanosized structural elements.* Nanotechnology, 2000. **11**(3): p. 139-147.

31. Wang, G.F. and X.Q. Feng, *Effects of surface elasticity and residual surface tension on the natural frequency of microbeams.* Applied Physics Letters, 2007.

90(23).

32. Law, M., J. Goldberger, and P.D. Yang, *Semiconductor nanowires and nanotubes.* Annual Review of Materials Research, 2004. **34**: p. 83-122.

33. Tao, X.Y., et al., *B4C-Nanowires/Carbon-Microfiber Hybrid Structures and Composites from Cotton T-shirts.* Advanced Materials, 2010. **22**(18): p. 2055-+.

34. Zhou, J., et al., *Flexible piezotronic strain sensor.* Nano Letters, 2008. **8**(9): p. 3035-3040.

35. Xu, S., et al., *Self-powered nanowire devices.* Nature Nanotechnology, 2010. **5**(5): p. 366-373.

36. Yu, M.F., et al., *Strength and breaking mechanism of multiwalled carbon nanotubes under tensile load.* Science, 2000. **287**(5453): p. 637-640.

37. Sundararajan, S., et al., *Mechanical property measurements of nanoscale structures using an atomic force microscope.* Ultramicroscopy, 2002. **91**(1-4): p. 111-118.

38. Li, X.D., et al., *Nanoindentation of silver nanowires.* Nano Letters, 2003. **3**(11): p. 1495-1498.

39. Poncharal, P., et al., *Electrostatic deflections and electromechanical resonances of carbon nanotubes.* Science, 1999. **283**(5407): p. 1513-1516.

40. Tan, E.P.S. and C.T. Lim, *Mechanical characterization of nanofibers - A review.* Composites Science and Technology, 2006. **66**(9): p. 1102-1111.

41. Oliver, W.C. and G.M. Pharr, *An improved technique for determining hardness and elastic-modulus using load and displacement sensing indentation experiments.* Journal of Materials Research, 1992. **7**(6): p. 1564-1583.

42. Hay, J.L., *Instrumented Indentation Testing.* ASM Handbook, 2000. **8**: p. 232-243.

43. MTS, *G200 Nanoindenter Manual.* 2007.

44. Li, X.D. and B. Bhushan, *A review of nanoindentation continuous stiffness measurement technique and its applications.* Materials Characterization, 2002. **48**(1): p. 11-36.

45. Mao, S.X., M.H. Zhao, and Z.L. Wang, *Nanoscale mechanical behavior of individual semiconducting nanobelts.* Applied Physics Letters, 2003. **83**(5): p. 993-995.

46. Li, X.D., et al., *Mechanical properties of ZnS nanobelts.* Nano Letters, 2005. **5**(10): p. 1982-1986.

47. Zhao, M.H., et al., *Probing nano-scale mechanical characteristics of individual semi-conducting nanobelts.* Materials Science and Engineering a-Structural Materials Properties Microstructure and Processing, 2005. **409**(1-2): p. 223-226.

48. Li, X.D., et al., *Direct nanomechanical machining of gold nanowires using a nanoindenter and an atomic force microscope.* Journal of Micromechanics and Microengineering, 2005. **15**(3): p. 551-556.

49. Feng, G., et al., *A study of the mechanical properties of nanowires using nanoindentation.* Journal of Applied Physics, 2006. **99**(7).

50. Wu, X.X., S.S. Amin, and T.T. Xu, *Substrate effect on the Young's modulus measurement of TiO2 nanoribbons by nanoindentation.* Journal of Materials Research, 2010. **25**(5): p. 935-942.

51. Li, X.D., I. Chasiotis, and T. Kitamura, *In Situ Scanning Probe Microscopy Nanomechanical Testing.* Mrs Bulletin, 2010. **35**(5): p. 361-367.

52. Heidelberg, A., et al., *A generalized description of the elastic properties of nanowires.* Nano Letters, 2006. **6**(6): p. 1101-1106.

53. Tan, E.P.S. and C.T. Lim, *Physical properties of a single polymeric nanofiber.* Applied Physics Letters, 2004. **84**(9): p. 1603-1605.

54. Lucas, M., et al., *Aspect ratio dependence of the elastic properties of ZnO nanobelts.* Nano Letters, 2007. **7**(5): p. 1314-1317.

55. Song, J.H., et al., *Elastic property of vertically aligned nanowires.* Nano Letters, 2005. **5**(10): p. 1954-1958.

56. Stan, G., et al., *Diameter-dependent radial and tangential elastic moduli of ZnO nanowires.* Nano Letters, 2007. **7**(12): p. 3691-3697.

57. Zhu, Y., C. Ke, and H.D. Espinosa, *Experimental techniques for the mechanical characterization of one-dimensional nanostructures.* Experimental Mechanics, 2007. **47**(1): p. 7-24.

58. Yu, M.F., et al., *Three-dimensional manipulation of carbon nanotubes under a scanning electron microscope.* Nanotechnology, 1999. **10**(3): p. 244-252.

59. Ding, W.Q., et al., *Mechanics of crystalline boron nanowires.* Composites Science and Technology, 2006. **66**(9): p. 1112-1124.

60. Dikin, D.A., et al., *Resonance vibration of amorphous SiO2 nanowires driven by mechanical or electrical field excitation.* Journal of Applied Physics, 2003. **93**(1): p. 226-230.

61. Calabri, L., et al., *Resonance of curved nanowires.* Journal of Physics-Condensed Matter, 2006. **18**(33): p. S2175-S2183.

62.   Meirovitch, L., *Elements of vibration analysis*. 1975, New York: McGraw-Hill.

63.   Hsin, C.L., et al., *Elastic Properties and Buckling of Silicon Nanowires.* Advanced Materials, 2008. **20**(20): p. 3919-+.

64.   Manoharan, M.P., et al., *Synthesis and elastic characterization of zinc oxide nanowires.* Journal of Nanomaterials, 2008.

65.   Xu, F., et al., *Mechanical Properties of ZnO Nanowires Under Different Loading Modes.* Nano Research, 2010. **3**(4): p. 271-280.

66.   Boustani, I., *Systematic ab initio investigation of bare boron clusters: Determination of the geometry and electronic structures of B-n (n=2-14).* Physical Review B, 1997. **55**(24): p. 16426-16438.

67.   Oganov, A.R., et al., *Ionic high-pressure form of elemental boron.* Nature, 2009. **457**(7231): p. 863-867.

68.   Albert, B. and H. Hillebrecht, *Boron: Elementary Challenge for Experimenters and Theoreticians.* Angewandte Chemie-International Edition, 2009. **48**(46): p. 8640-8668.

69.   Werheit, H., *BORON-RICH SOLIDS - A CHANCE FOR HIGH-EFFICIENCY HIGH-TEMPERATURE THERMOELECTRIC ENERGY-CONVERSION.* Materials Science and Engineering B-Solid State Materials for Advanced Technology, 1995. **29**(1-3): p. 228-232.

70.   Lin, Y.M. and M.S. Dresselhaus, *Thermoelectric properties of superlattice nanowires.* Physical Review B, 2003. **68**(7).

71.   Rabina, O., Y.M. Lin, and M.S. Dresselhaus, *Anomalously high thermoelectric figure of merit in Bi1-xSbx nanowires by carrier pocket alignment.* Applied Physics Letters, 2001. **79**(1): p. 81-83.

72.   Boukai, A.I., et al., *Silicon nanowires as efficient thermoelectric materials.* Nature, 2008. **451**(7175): p. 168-171.

73.   Harman, T.C., et al., *Quantum dot superlattice thermoelectric materials and devices.* Science, 2002. **297**(5590): p. 2229-2232.

74.   Venkatasubramanian, R., et al., *Thin-film thermoelectric devices with high room-temperature figures of merit.* Nature, 2001. **413**(6856): p. 597-602.

75.   Majumdar, A., *Thermoelectricity in semiconductor nanostructures.* Science, 2004. **303**(5659): p. 777-778.

76.   Guan, Z., et al., *Boron carbide nanowires: low temperature synthesis and structural and thermal conductivity characterization.* Journal of Materials Chemistry, 2012. **22**(19): p. 9853-9860.

77.   Xu, T.T., et al., *Crystalline boron nanoribbons: Synthesis and characterization.* Nano Letters, 2004. **4**(5): p. 963-968.

78.   Hayami, W. and S. Otani, *First-principles study of the crystal and electronic structures of alpha-tetragonal boron.* Journal of Solid State Chemistry, 2010. **183**(7): p. 1521-1528.

79.   Werheit, H., et al., *Raman effect in icosahedral boron-rich solids.* Science and Technology of Advanced Materials, 2010. **11**(2).

80.   Laubengayer, A.W., et al., *Boron. I. Preparation and properties of pure crystalline boron.* Journal of the American Chemical Society, 1943. **65**: p. 1924-1931.

81.   Lee, S., et al., *COMPUTATIONAL SEARCH FOR THE REAL TETRAGONAL B-50.* Physical Review B, 1992. **45**(7): p. 3248-3251.

82.   Will, G. and K. Ploog, *CRYSTAL-STRUCTURE OF I-TETRAGONAL BORON.* Nature, 1974. **251**(5474): p. 406-408.

83.   Liu, F., et al., *Fabrication and field emission properties of boron nanowire bundles.* Ultramicroscopy, 2009. **109**(5): p. 447-450.

84.   Liu, F., et al., *Fabrication of vertically aligned single-crystalline boron nanowire arrays and investigation of their field-emission behavior.* Advanced Materials, 2008. **20**(13): p. 2609-+.

85.   Wang, X.J., et al., *Single crystalline boron nanocones: Electric transport and field emission properties.* Advanced Materials, 2007. **19**(24): p. 4480-+.

86.   Kirihara, K., et al., *Mg-doping experiment and electrical transport measurement of boron nanobelts.* Journal of Solid State Chemistry, 2006. **179**(9): p. 2799-2804.

87.   Liu, F., et al., *Metal-like single crystalline boron nanotubes: synthesis and in situ study on electric transport and field emission properties.* Journal of Materials Chemistry, 2010. **20**(11): p. 2197-2205.

88.   Kirihara, K., et al., *Seebeck Coefficient and Power Factor of Single-Crystalline Boron Nanobelts.* Applied Physics Express, 2011. **4**(4).

89.   Yang, J.K., et al., *Enhanced and switchable nanoscale thermal conduction due to van der Waals interfaces.* Nature Nanotechnology, 2012. **7**(2): p. 91-95.

90.   Ni, H. and X.D. Li, *Synthesis, Structural and Mechanical Characterization of Amorphous and Crystalline Boron Nanobelts.* Journal of Nano Research, 2008. **1**: p. 10-22.

91.   Lin, C.H., et al., *In situ Nanomechanical Characterization of Single-Crystalline Boron Nanowires by Buckling.* Small, 2010. **6**(8): p. 927-931.

92.   Domnich, V., et al., *Boron Carbide: Structure, Properties, and Stability under Stress.* Journal of the American Ceramic Society, 2011. **94**(11): p. 3605-3628.

93.   Suri, A.K., et al., *Synthesis and consolidation of boron carbide: a review.* International Materials Reviews, 2010. **55**(1): p. 4-40.

94.   Thompson, R., *The Physics and Chemistry of Carbides: Nitrides and Borides*, ed. R. Freer. 1990, Netherlands: Kluwer Academic Publishers. 113.

95.   Domnich, V., et al., *Nanoindentation and Raman spectroscopy studies of boron carbide single crystals.* Applied Physics Letters, 2002. **81**(20): p. 3783-3785.

96.   Wood, C. and D. Emin, *CONDUCTION MECHANISM IN BORON-CARBIDE.* Physical Review B, 1984. **29**(8): p. 4582-4587.

97.   Stoto T., Z.L., Pelissier J., *Absence of defect clusters in electron irradiated boron carbide.* Radiation Effects, 1985. **90**(3-4): p. 161-170.

98.   Ulrich, S., et al., *Subplantation effect in magnetron sputtered superhard boron carbide thin films.* Diamond and Related Materials, 1998. **7**(6): p. 835-838.

99.   Werheit, H. and Ieee, *Thermoelectric properties of boron-rich solids and their possibilities of technical application.* ICT'06: XXV International Conference on Thermoelectrics, Proceedings. 2006, New York: Ieee. 159-163.

100.   Bao, L.H., et al., *Synthesis and photoluminescence property of boron carbide nanowires.* Chinese Physics B, 2008. **17**(12): p. 4585-4591.

101.   Huang, Y., et al., *Fabrication of patterned boron carbide nanowires and their electrical, field emission, and flexibility properties.* Nano Research, 2012. **5**(12): p. 896-902.

102.   Tian, J.F., et al., *Probing field emission from boron carbide nanowires.* Chinese Physics Letters, 2008. **25**(9): p. 3463-3466.

103.   Agrawal, R., O. Loh, and H.D. Espinosa, *The Evolving Role of Experimental Mechanics in 1-D Nanostructure-Based Device Development.* Experimental Mechanics, 2011. **51**(1): p. 1-9.

104.   Buckle, H., J. Westbrook, and H. Conrad, *The science of hardness testing and its research applications.* American Society for Metals, Metals Park, OH, 1973: p. 453.

105.   Nix, W.D., *MECHANICAL-PROPERTIES OF THIN-FILMS.* Metallurgical Transactions a-Physical Metallurgy and Materials Science, 1989. **20**(11): p. 2217-2245.

106.   Saha, R. and W.D. Nix, *Effects of the substrate on the determination of thin film mechanical properties by nanoindentation.* Acta Materialia, 2002. **50**(1): p. 23-38.

107. Mencik, J. and M.V. Swain, *ERRORS ASSOCIATED WITH DEPTH-SENSING MICROINDENTATION TESTS.* Journal of Materials Research, 1995. **10**(6): p. 1491-1501.

108. Gao, Y.F., et al., *Effective elastic modulus of film-on-substrate systems under normal and tangential contact.* Journal of the Mechanics and Physics of Solids, 2008. **56**(2): p. 402-416.

109. Fischei-Cripps, A.C., *The sharpness of a Berkovich indenter.* Journal of Materials Research, 2010. **25**(5): p. 927-934.

110. Sakharova, N.A., et al., *Comparison between Berkovich, Vickers and conical indentation tests: A three-dimensional numerical simulation study.* International Journal of Solids and Structures, 2009. **46**(5): p. 1095-1104.

111. MTS, *G200 Nanoindenter Manual.* 2007.

112. Fischer-Cripps, A.C., *Review of analysis and interpretation of nanoindentation test data.* Surface & Coatings Technology, 2006. **200**(14-15): p. 4153-4165.

113. Whitney, D.L., M. Broz, and R.F. Cook, *Hardness, toughness, and modulus of some common metamorphic minerals.* American Mineralogist, 2007. **92**(2-3): p. 281-288.

114. Salvetat, J.P., et al., *Elastic and shear moduli of single-walled carbon nanotube ropes.* Physical Review Letters, 1999. **82**(5): p. 944-947.

115. Marszalek, P.E., et al., *Atomic force microscopy captures quantized plastic deformation in gold nanowires.* Proceedings of the National Academy of Sciences of the United States of America, 2000. **97**(12): p. 6282-6286.

116. Ding, W., et al., *Rolling resistance moment of microspheres on surfaces: contact measurements.* Philosophical Magazine, 2007. **87**(36): p. 5685-5696.

117. JEOL, *JSM-6480 Instruction Manual.* 2002.

118. Chang, M., et al., *Mechanical properties of microwave hydrothermally synthesized titanate nanowires.* Nanotechnology, 2008. **19**(2).

119. Nakabayashi, D., et al., *Low-cost nanomanipulator for in situ experiments in a SEM.* Microscopy and Microanalysis, 2006. **12**(4): p. 311-316.

120. Nakabayashi, D., P.C. Silva, and D. Ugarte, *Inexpensive two-tip nanomanipulator for a SEM.* Applied Surface Science, 2007. **254**(1): p. 405-411.

121. Ding, W., et al., *Modulus, fracture strength, and brittle vs. plastic response of the outer shell of arc-grown multi-walled carbon nanotubes.* Experimental Mechanics, 2007. **47**(1): p. 25-36.

122. Li, X.D., et al., *Effect of tensile offset angles on micro/nanoscale tensile testing.* Review of Scientific Instruments, 2005. **76**(3).

123. Huang, Z., et al., *Three-dimensional representation of curved nanowires.* Journal of Microscopy, 2004. **216**: p. 206-214.

124. Ribeiro, E. and M. Shah, *Computer vision for nanoscale imaging.* Machine Vision and Applications, 2006. **17**(3): p. 147-162.

125. Qin, Q.Q., et al., *Measuring True Young's Modulus of a Cantilevered Nanowire: Effect of Clamping on Resonance Frequency.* Small, 2012. **8**(16): p. 2571-2576.

126. Guan, Z., et al., *Observation of 'hidden' planar defects in boron carbide nanowires and identification of their orientations.* Nanoscale Research Letters, 2014. **9**.

127. Chen, B., et al., *Strengthening Brittle Semiconductor Nanowires through Stacking Faults: Insights from in Situ Mechanical Testing.* Nano Letters, 2013. **13**(9): p. 4369-4373.

128. Wang, J., et al., *Influence of microstructures on mechanical behaviours of SiC nanowires: a molecular dynamics study.* Nanotechnology, 2012. **23**(2).

129. Lee, S., D.M. Bylander, and L. Kleinman, *ELASTIC-MODULI OF B-12 AND ITS COMPOUNDS.* Physical Review B, 1992. **45**(7): p. 3245-3247.

130. McClellan, K.J., et al., *Room temperature single crystal elastic constants of boron carbide.* Journal of Materials Science, 2001. **36**(14): p. 3403-3407.

131. Jang, D.C., et al., *Deformation mechanisms in nanotwinned metal nanopillars.* Nature Nanotechnology, 2012. **7**(9): p. 594-601.

132. Lu, L., et al., *Revealing the Maximum Strength in Nanotwinned Copper.* Science, 2009. **323**(5914): p. 607-610.

133. Youssef, K., et al., *Effect of stacking fault energy on mechanical behavior of bulk nanocrystalline Cu and Cu alloys.* Acta Materialia, 2011. **59**(14): p. 5758-5764.

134. Umeno, Y., Y. Kinoshita, and T. Kitamura, *Ab initio DFT simulation of ideal shear deformation of SiC polytypes.* Modelling and Simulation in Materials Science and Engineering, 2007. **15**(2): p. 27-37.

135. Chen, M.W., J.W. McCauley, and K.J. Hemker, *Shock-induced localized amorphization in boron carbide.* Science, 2003. **299**(5612): p. 1563-1566.

136. Johnson, G.R. and T.J. Holmquist, *Response of boron carbide subjected to large strains, high strain rates, and high pressures.* Journal of Applied Physics, 1999. **85**(12): p. 8060-8073.

137. Cuenot, S., S. Demoustier-Champagne, and B. Nysten, *Elastic modulus of polypyrrole nanotubes.* Physical Review Letters, 2000. **85**(8): p. 1690-1693.

138. Dai, H.J., et al., *Nanotubes as nanoprobes in scanning probe microscopy.* Nature, 1996. **384**(6605): p. 147-150.

139. Watson, J.H.L., *AN EFFECT OF ELECTRON BOMBARDMENT UPON CARBON BLACK.* Journal of Applied Physics, 1947. **18**(2): p. 153-161.

140. Lau, Y.M., et al., *Properties and applications of cobalt-based Material produced by electron-beam-induced deposition.* Journal of Vacuum Science & Technology a-Vacuum Surfaces and Films, 2002. **20**(4): p. 1295-1302.

141. Ding, W., et al., *Mechanics of hydrogenated amorphous carbon deposits from electron-beam-induced deposition of a paraffin precursor.* Journal of Applied Physics, 2005. **98**(1).

142. Yashinski, M.S. and C.L. Muhlstein, *The role of deposited layers in the nonlinear constitutive behavior of Si nanowires.* Journal of Applied Physics, 2013. **114**(19).

143. Amman, M., et al., *Atomic force microscopy study of electron beam written contamination structures.* Journal of Vacuum Science & Technology B, 1996. **14**(1): p. 54-62.

144. van Dorp, W.F. and C.W. Hagen, *A critical literature review of focused electron beam induced deposition.* Journal of Applied Physics, 2008. **104**(8): p. 42.

145. Kanaya, K. and S. Okayama, *PENETRATION AND ENERGY-LOSS THEORY OF ELECTRONS IN SOLID TARGETS.* Journal of Physics D-Applied Physics, 1972. **5**(1): p. 43-&.

146. Calleja, M., et al., *Challenges for nanomechanical sensors in biological detection.* Nanoscale, 2012. **4**(16): p. 4925-4938.

147. Craighead, H., *Nanomechanical systems - Measuring more than mass.* Nature Nanotechnology, 2007. **2**(1): p. 18-19.

148. Gil-Santos, E., et al., *Nanomechanical mass sensing and stiffness spectrometry based on two-dimensional vibrations of resonant nanowires.* Nature Nanotechnology, 2010. **5**(9): p. 641-645.

149. Tersoff, J., *STRUCTURAL-PROPERTIES OF SP3-BONDED HYDROGENATED AMORPHOUS-CARBON.* Physical Review B, 1991. **44**(21): p. 12039-12042.

150. Dodd, S.P., G.A. Saunders, and B. James, *Temperature and pressure dependences of the elastic properties of ceramic boron carbide (B4C).* Journal of Materials Science, 2002. **37**(13): p. 2731-2736.

151. Pharr, G.M., J.H. Strader, and W.C. Oliver, *Critical issues in making small-depth mechanical property measurements by nanoindentation with continuous stiffness measurement.* Journal of Materials Research, 2009. **24**(3): p. 653-666.

152. Oliver, W.C. and G.M. Pharr, *Measurement of hardness and elastic modulus by instrumented indentation: Advances in understanding and refinements to methodology.* Journal of Materials Research, 2004. **19**(1): p. 3-20.

153. Kalidindi, S.R. and S. Pathak, *Determination of the effective zero-point and the extraction of spherical nanoindentation stress-strain curves.* Acta Materialia, 2008. **56**(14): p. 3523-3532.

154. Senden, T.J. and W.A. Ducker, *EXPERIMENTAL-DETERMINATION OF SPRING CONSTANTS IN ATOMIC-FORCE MICROSCOPY.* Langmuir, 1994. **10**(4): p. 1003-1004.

155. Torii, A., et al., *A method for determining the spring constant of cantilevers for atomic force microscopy.* Measurement Science & Technology, 1996. **7**(2): p. 179-184.

156. Cleveland, J.P., et al., *A NONDESTRUCTIVE METHOD FOR DETERMINING THE SPRING CONSTANT OF CANTILEVERS FOR SCANNING FORCE MICROSCOPY.* Review of Scientific Instruments, 1993. **64**(2): p. 403-405.

157. Sader, J.E., et al., *METHOD FOR THE CALIBRATION OF ATOMIC-FORCE MICROSCOPE CANTILEVERS.* Review of Scientific Instruments, 1995. **66**(7): p. 3789-3798.

158. Sader, J.E., J.W.M. Chon, and P. Mulvaney, *Calibration of rectangular atomic force microscope cantilevers.* Review of Scientific Instruments, 1999. **70**(10): p. 3967-3969.

APPENDIX A: OPTIMAL NANINDENTATION CONDITIONS

The nanoindenter used in the laboratory was studied and present in this section. The primary purpose of this study was to investigate the suitability of this commercial nanoindenter for indentation tests with tens of nanometers penetration depth, and also to find out the optimal experimental settings to achieve the most reliable results for tens of nanometers nanoindentations.

A.1 Experimental Details

The nanoindentation testing machine was the Nano Indenter G200 (Agilent Technologies, MTS Nano Instruments, Knoxville, TN). It has Standard XP Module (XP) and Dynamic Contact Module (DCM) with two different tips. The software associated with the nanoindenter was TestWorks 4 in the beginning, and then upgraded to NanoSuite. Basic mode (the original Pharr-Oliver partial method [41]) and Continuous Stiffness Measurement (CSM) mode in each module were individually operated on a reference sample (fused silica), 1-micrometer-thick silicon dioxide on silicon (1μm SiO_2/Si), silicon (100), and sapphire (0001). All experiments were performed using these two modes. Each experiment was executed with only changing one test parameter while keeping others the same. All sample tests were saved automatically, and then the whole package of original data was exported to Microsoft Excel. All graphs were then plotted from the data package using OriginPro.

For all experiments, the parameter "allowable drift rate" was set to 0.05 nm·s⁻¹. This value was automatically monitored by the machine before the test, and then the test was carried out until the drift rate reached this value or a slightly lower value. The loading and unloading processes in all experiments followed the same procedure: the Berkovich indenter approached the sample surface with a 10 nm·s⁻¹ approach velocity from a distance around 1000 nm above the sample surface; the indenter detected the

surface with 25% or 40% sensitivity; loaded into the sample with a constant strain rate of 0.05 s^{-1} to a desired depth which was determined by the load control or displacement control; held on the maximum load for 10 s; unloaded to 10% of the maximum load with the same strain rate, and held for 100 s to correct thermal drift; then completed the unloading.

A.2 Results and Discussions

A.2.1 Comparison of Basic and CSM Methods

As described above, nanoindentation with basic method only produces one value of mechanical property at the maximum depth, but nanoindentation with CSM method can provide continuous mechanical properties as a function of indentation depth. FIGURE A.1 shows the results of four 800 nm indentations on 1 μm SiO$_2$/Si substrate done under XP module with Basic and CSM methods. For two indentations with Basic method, two modulus values are given at 800 nm depth. But two curves of modulus versus indention depth are produced for two indentations with CSM methods. The curves clearly show the substrate effect increases with increasing the penetration depth. Because the substrate effect will be definitely existed for further nanoindentations on boron nanoplatelets, CSM method should be used for extracting the continuous mechanical properties to study the substrate effect.
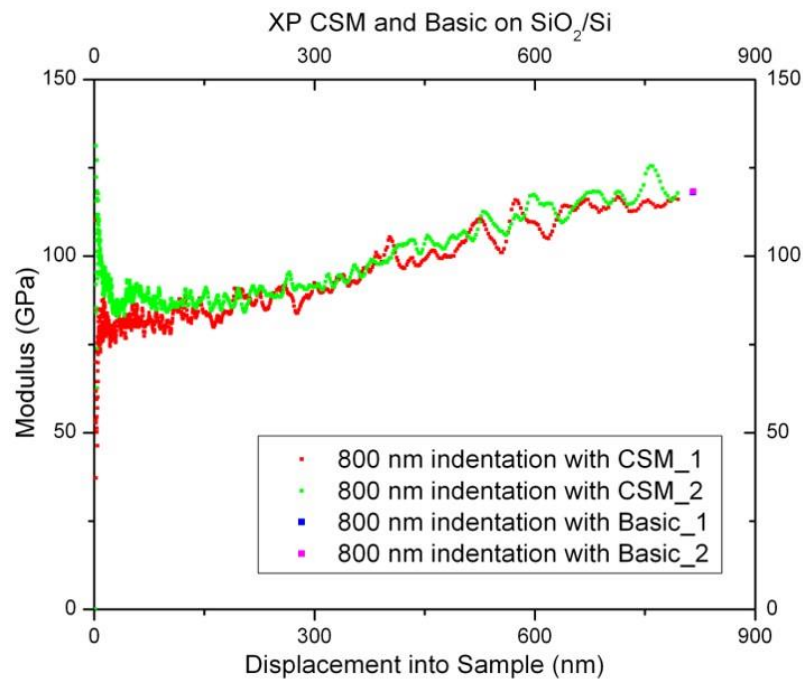
FIGURE A.1: Results comparison of Basic and CSM methods.

A.2.2 Comparison of XP and DCM Modules

For the XP and DCM heads, they both were Berkovich indenters, but the difference between the XP and DCM was studied and concluded as following.

According to the user's manual, the maximum load of the XP and DCM are 500 mN and 10 mN respectively. The load and displacement resolutions of a standard XP head are 50 nN and 0.01 nm, but those of DCM head are 1 nN and 0.0002 nm [111]. To make tens of nanometers indentations, the larger load limit is not important, but the better load and displacement resolutions are more preferred. FIGURE A.2 shows six 100 nm indentations on 1 μm SiO_2/Si substrate done with CSM method under XP and DCM modules. For three indentations under XP module with three different harmonic oscillation amplitude (z_0), all three curves are much rougher than those for three indentations under DCM module. Therefore, the comparison of results indicates that DCM module is a better choice for a small depth indentations.
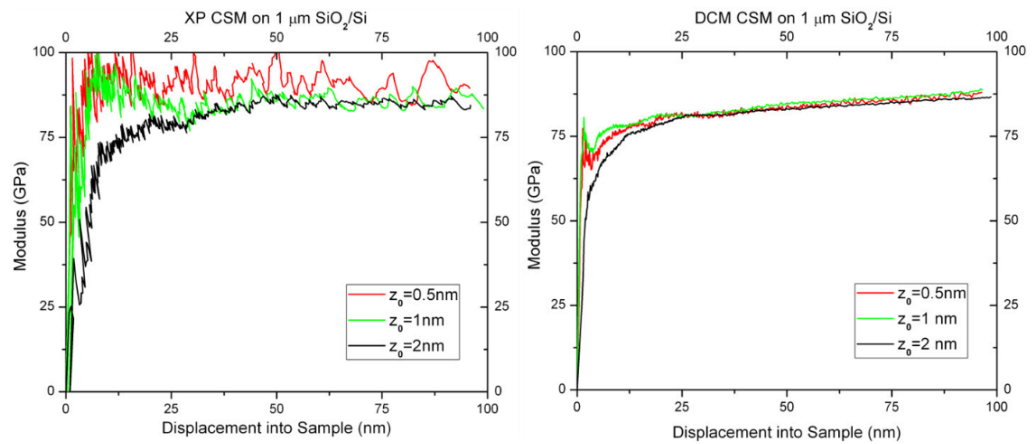
FIGURE A.2: Results comparison of XP and DCM modules.

A.2.3 Harmonic Displacement Target

A harmonic displacement target is the required input for the amplitude of displacement oscillation for CSM method. As described in above, the harmonic displacement oscillation is caused by superimposing a small sinusoidally varying load to the primary load signal. So the amplitude of displacement oscillation should be small enough that its effects on the overall loads and displacements can be ignored. But it should not be too small, otherwise the data gained in each oscillation cycle may not be insufficient for precise calculations. FIGURE A.3 presents the curves of elastic modulus and the displacement oscillation amplitude versus displacement for 100 nm indentations on 1µm SiO_2/Si substrate under DCM module with CSM method by varying the oscillation amplitudes.
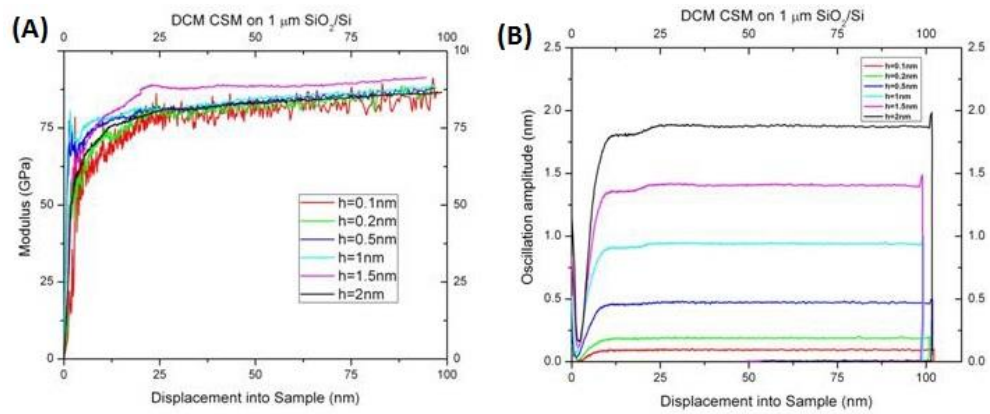
FIGURE A.3: Plots of (A) the elastic modulus and (B) the oscillation amplitude as a function of indention depth for DCM module with CSM method on 1µm SiO_2/Si substrate (h is the displacement oscillation amplitude).

Note that the initial parts of the displacement oscillation amplitude versus displacement curves scatter dramatically (FIGURE A.3B). The points at the bottoms where oscillation amplitudes stop decreasing are referred to as the tapping depth. The tapping depth results from the fact that the indenter loses contact with sample when it lifts up during the unloading cycles of the oscillation at the beginning of penetration [151]. After passing over the tapping depth, the value of the oscillation amplitude increases to a constant magnitude. This increase is due to the feedback control system which takes a certain amount of time to hold the oscillation amplitude constant. However, it is still unknown why the achieved oscillation amplitude values are 5% to 20% less than the prescribed values.

The results derived from these tests indicate that neither the largest oscillation amplitude nor the smallest amplitude is the best choice for nanoscale indentation. There is an optimal range for the oscillation amplitude, which is always dependent on the prescribed depth and the materials. FIGURE A.3A indicates that the magnitude of displacement vibration of 0.1 nm is not good for the DCM head to perform 100 nm

indentation tests on 1µm SiO$_2$/Si, because the corresponding modulus curve have relatively large variations.

A.2.4 Nanoindentation at 20 nm Depth

Because most of boron nanostructures are in the range of 20 ± 10 nm, nanoindentations with penetration depth of 20 nm on substrate are studied. In order to select an appropriate value for the amplitude of displacement oscillation for 20 nm indentation depth, a series of experiments were performed. Twenty-nanometer- deep indentation tests under DCM module with CSM method were performed on silicon and sapphire substrate at various harmonic displacements. The resultant curves are presented in FIGURE A.4. For silicon, the oscillation magnitudes of 0.1 nm and 2 nm are not suitable because these two modulus curves have large variations, FIGURE A.4A. For sapphire which has a considerably higher elastic modulus, only for the amplitude of displacement oscillation at 0.1 nm is not suitable, FIGURE A.4B. Considering that a higher tapping depth coincides with a higher oscillation amplitude, the oscillation amplitude of 0.2 nm or 0.5 nm was proper for making indentations with depth of 20 nm.
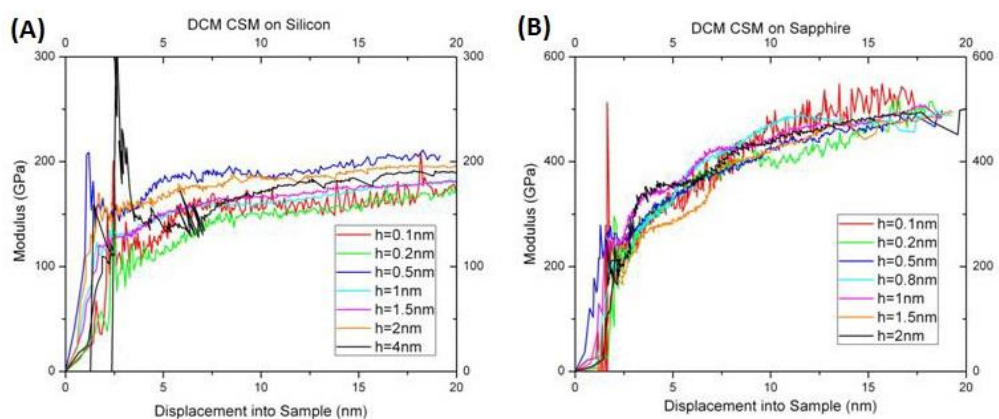

FIGURE A.4: Results of nanoindentation under DCM module with CSM method on silicon (A) and sapphire (B) at 20 nm depths.

A.2.5 Determination of Initial Surface Contact

It is well known that the determination of initial contact is an essential step before analyzing the data. The determination of the zero point of the surface indirectly affects the accuracy of the contact stiffness and contact area by changing the contact depths. Oliver et al. assumed that the minimum observed value at the beginning of the harmonic stiffness versus displacement curve to be the point of contact [152]. Nonetheless, in very small depth indentation, such as 20 nm or less, the initial parts of the harmonic stiffness versus displacement curves are very scattered which makes it difficult to identify the minimum point. Another approach is the default procedure for identifying the point of initial contact in the software, which picks up the first data point when the harmonic contact stiffness reaches or exceeds 200 N/m [153]. Based on the results of tens of nanometers indentations on substrates, this approach is appropriate for defining the surface point. Normally, software sets the surface point by picking up a point with stiffness closest to 200 N/m, but it sometimes mistakenly sets the surface point far away from 200 N/m. For example, for a 20 nm indentation on Si(100) substrate, the given Young's modulus by software (blue line) is higher than its intrinsic modulus (dash line), because the software is not defining the surface point at stiffness close to 200 N/m. After manually setting it to point with contact stiffness closest to 200 N/m, the modulus curve (red line) is flatter and close to its intrinsic value, FIGURE A.5. Therefore, it is important to check the surface point every time after the indentation is done.
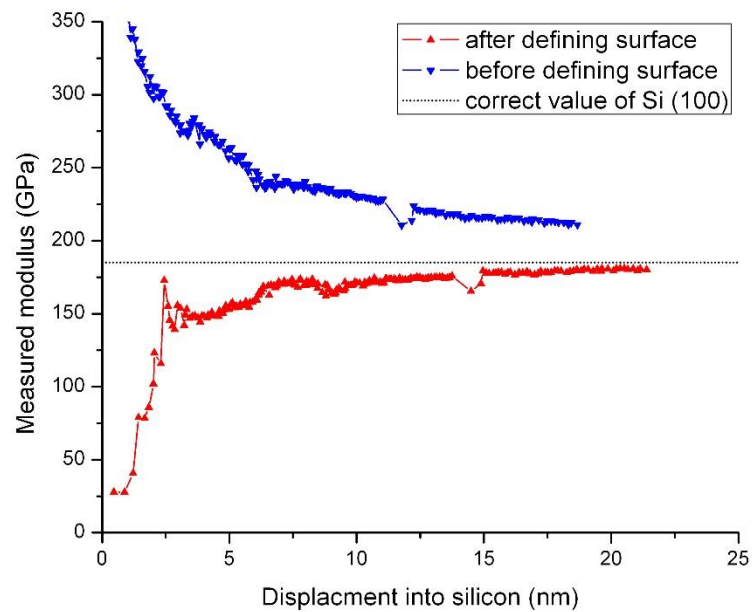
FIGURE A.5: Comparison of modulus curves before and after defining surface point with the intrinsic modulus value for a 20 nm indentation on a Si(100) substrate.

A.3 Summary

CSM method is more useful than Basic method when continuous mechanical properties is wanted. DCM module is a better choice than XP module for indentation tests with the penetration depth of 100 nm or less. It is found that the displacement oscillation amplitude has a profound effect on the derived properties, so finding an optimal range of displacement oscillation amplitudes for nanoindentation tests with CSM method is crucial. In addition, an appropriate approach to define the zero-point of surface contact is important to ensure the results reliable.

APPENDIX B: BASIC TESTS BY A NANOMANIPULATOR

Before this nanomanipulator was used to perform *in situ* testings on nanostrucutres, it was necessary to execute basic tests to check the feasibility of various *in situ* testing methods. Therefore, the details and results of these basic tests on this nanomanipulator was described in this section.

B.1 Basic Test for Tensile Testing Technique

The nanomanipulator was capable of stretching an individual nanostructure with quasi-static tensile loading by stepwise controlling the linear motion of XY stages or piezoelectric plate bender. First of all, individual nanostructures should be well prepared for being picked up easily by the probe. A half-cut TEM grid with holey carbon film was scratched on the sample substrate with the cut-edge against the substrate. Statistically, there were some nanostructures partially protruding outward at the cut-edge of the TEM grid, FIGURE B.1a. The nanostructures perpendicular to the cut-edge were selected to be good candidates for the consecutive mechanical characterizations. Then the AFM tip was moved to contact the nanostructure, and sequentially electron beam induced deposition (EBID) technique was used to deposit a clamp for helping nanostructure tightly attach to the AFM tip. The nanostructures were pulled out from the substrate or the cluster when the AFM was moved away from the edge, FIGURE B.1b.
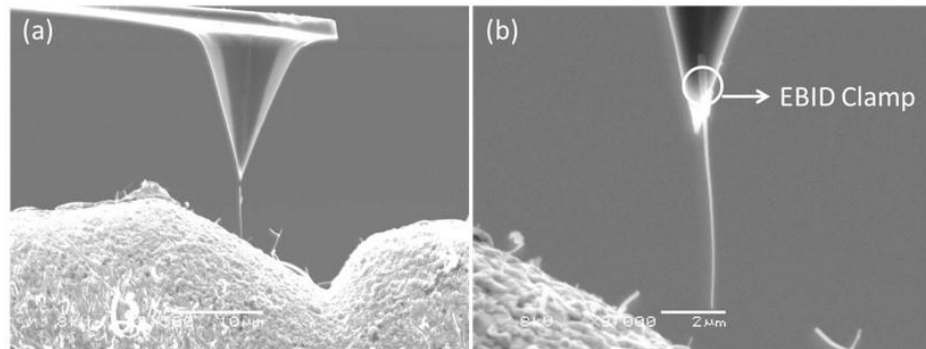
FIGURE B.1: (a) AFM tip is close to one boron nanowire perpendicularly protruding at the edge; (b) the boron nanowire is pulled out from the edge by AFM tip.

After that, the AFM tip with the nanostructure was moved to another AFM tip or probe. EBID was applied again to clamp another free end of the nanostructure to the AFM tip. Then the nanostructure was stretched when one AFM tip was driven away from another AFM tip, until the nanostructure was fractured, FIGURE B.2a-c. In this test, the tested nanowire was not aligned with AFM tips, because it was not perpendicular to the substrate edge before it was pulled out by an AFM tip. It was just a demonstrative test presented here to prove that the nanomanipulator is capable of performing tensile test as long as a good candidate can be found.

The tension process is recorded by taking a series of high-resolution SEM images, as discussed in Chapter one and shown in FIGURE 1.7. The deflection of the soft cantilever and elongation of nanostructure is determined by analyzing these captured SEM images.
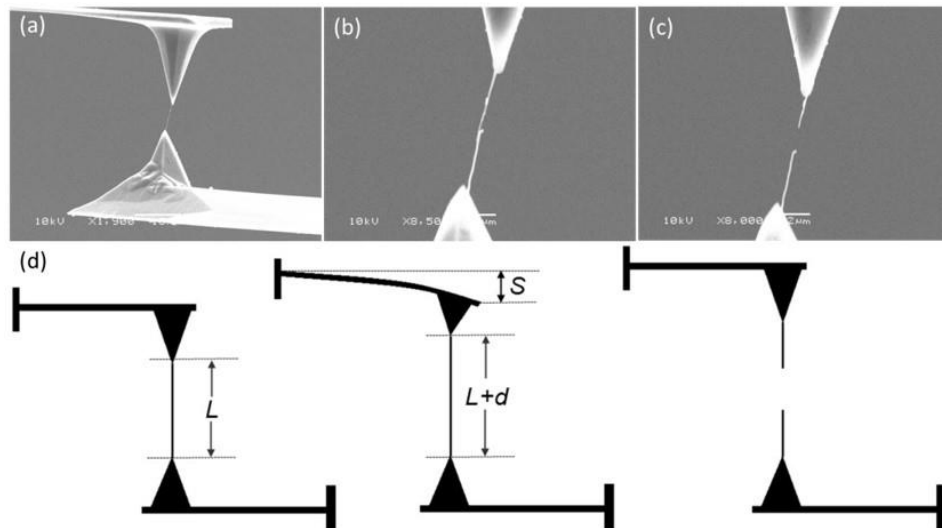
FIGURE B.2: SEM images (a-c) show the process of tensile test on a nanostructure; (d) schematic representations of tension process.

As representatively shown in the FIGURE B.2d, the stress σ and strain ε are calculated by equation (67) and (68),

$$\sigma = \frac{F}{A_0} = \frac{k \cdot S}{A_0} \tag{67}$$

$$\varepsilon = \frac{(L+d)-L}{L} = \frac{d}{L} \tag{68}$$

where F is the applied load, A_0 is the cross-section area of nanostructure, k is the spring constant of cantilever, S is the deflection of the cantilever at the free end, L and d are the original length and elongation of the nanostructure, respectively. Then, the tensile properties of nanostructure such as the elastic modulus, yield strength, tensile strength, and maximum strain can be achieved by analyzing the strain-stress curve. Therefore, the result of this basic test shows the feasibility of *in situ* tensile testing technique with this nanomanipulator system.

B.2 Basic Test for Resonance Vibration Testing Technique

Mechanical resonance tests of nanostructures were attempted by this nanomanipulator inside SEM combined with a piezoelectric plate bender and a function

generator. The protruded nanowires were picked up by the AFM tip with it perpendicular to tip direction (FIGURE B.3a), which was different with the way of picking up for tensile tests (FIGURE B.1a). The picking way chosen for this resonance test was in order to ensure that transverse wave was propagated in the beam-like nanostructures, because it was much easier to observe the vibration reverberated by the transverse wave than the longitudinal wave. One nanowire was initially expected to be pulled out, but there were two extra nanowires attached on it, FIGURE B.3b. Since it is difficult to get rid of these two extra nanowires, the whole nanofeature was used to perform the demonstrative resonance vibration test. The driving signal was applied to the piezoelectric plate bender to oscillate the AFM cantilever, in turns to vibrate the nanostructures. The range of driving frequency from the function generator was swept. The resonant frequency could be narrowed in a very small range, and then the precise value was determined by adjusting the function generator manually.
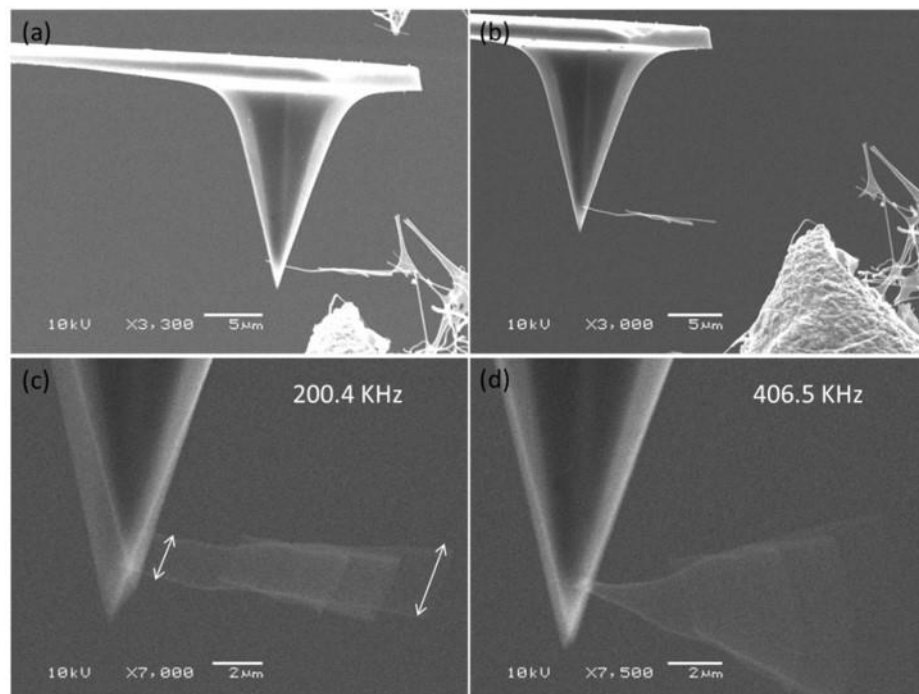
FIGURE B.3: The process of resonance vibration test: (a) a nanofeature was attached to AFM tip; (b) the nanofeature was pulled out from a TEM grid; (c) the third

resonance mode of AFM cantilever at 200.4 kHz; (d) the first resonance mode of this nanofeature at 406.5 kHz.

Sometimes, the nanostructure was oscillated too when the AFM tip was in the resonance state, as present in FIGURE B.3c. It was easy to distinguish whether the nanostructure was vibrated by the resonance of AFM cantilever. As two white two-arrow lines indicated in FIGURE B.3c, since the sizes of them were very close, which meant the nanostructure was vibrated by the resonance of AFM cantilever. The case shown in FIGURE B.3d is completely different. The vibration amplitude at the free end of nanostructure was much larger than that at the fixed end. The slight oscillation of AFM cantilever was because of the appearance of bending moment when nanostructure was vibrating.

Based upon the description of resonance vibration test in chapter one, once the resonance frequencies and geometric information of nanostructures are measured, then their Young's moduli can be determined.

B.3 Basic Test for Buckling Testing or Bending Testing Techniques

To perform buckling or bending tests, the first step is to pick up a nanostructure as described previously, shown in FIGURE B.1. Then the nanostructure is moved to the rigid cantilever, and eventually attached to its surface and perpendicularly against the surface. The nanostructured attached to an AFM tip was driven to push against the rigid cantilever, FIGURE B.4. Because it is a demonstrative test here, there is no measurement to calculate the applied force and axial displacement of nanostructure. The same method as calculating tensile force is used to determine the applied force for these two testing techniques. In addition, another free end of nanostructure needs to be clamped during the buckling tests in order to avoid sliding problem.
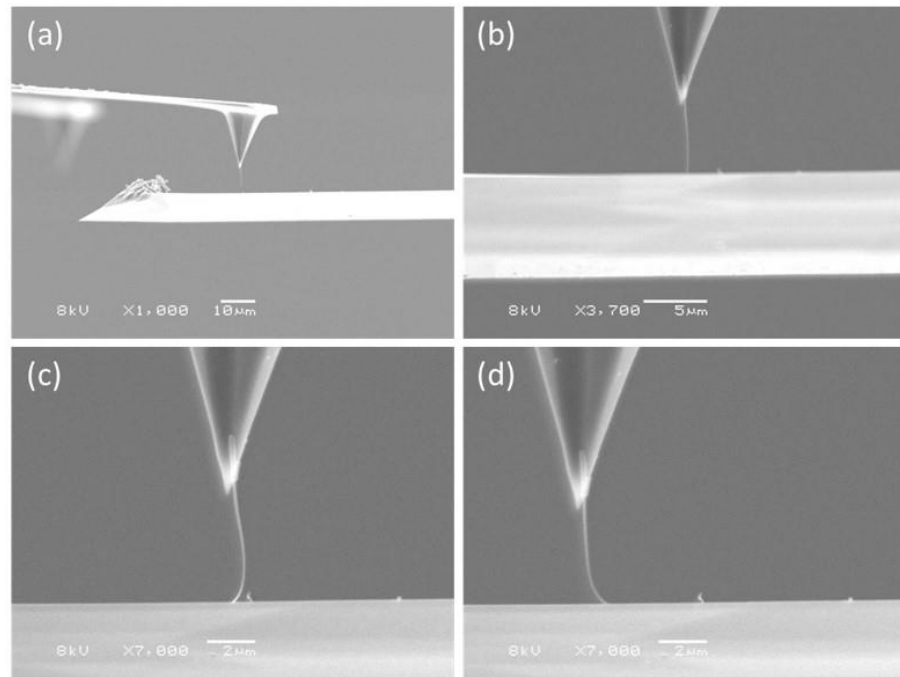
FIGURE B.4: The process of buckling test: (a) AFM tip with nanostructure was moved to the rigid cantilever; (b) nanostructure attached to the surface; (c) and (d) represent the nanostructure bend in two different orientations under load.

B.4 Basic Test for Measuring Spring Constant of AFM Cantilevers

It is known that the applied forces in *in situ* tensile, buckling and bending tests is calculated by multiplying the deflection of AFM cantilever with its spring constant. The spring constant must be accurately measured to determine applied forces with less uncertainty. There are many approaches to measure the spring constant of AFM cantilever, including methods that measured the deflection when a known mass or force was loaded on the cantilever [154, 155], and that determined the spring constant from the change of resonant frequency when an end mass is added to the cantilever [156], and from measuring the unloaded resonant frequency of the cantilever in vacuum or in liquid [157, 158], etc. In our case, we chose the Sader's method [157] because it is easily incorporated into the SEM nanomanipulator. It determines the spring constant of a rectangular AFM cantilever in vacuum by the equation (69),

$$k = M_e \rho_c bhL\omega_{vac}^2 \tag{69}$$

where k, ρ_c, h, b and L are the spring constant, density, thickness, width and length of the cantilever, respectively, and ω_{vac} is the fundamental radial resonant frequency of the cantilever in vacuum ($\omega_{vac} = 2\pi f_{vac}$, where f_{vac} is the fundamental resonant frequency), and M_e is the normalized effective mass which is 0.2427 if L/b>5 [157].

For the AFM cantilevers used in our research, the ratio of length over width is higher than 5, so the normalized effective mass gives 0.2427. The accurate width and length of the cantilever can be measured either under optical microscope or SEM, but its thickness has to be measured in SEM because it is only around 1 μm. The density of cantilever depends on the material made of the cantilever. For example, the soft AFM tips chosen for our experiments is MikroMasch CSC38/noAl, which is made by silicon without any coating, then it gives the density of cantilever is the density of silicon 2.3290 g/cm^3. The challenge of this method is to measure the resonant frequency of the cantilever in vacuum.

Through using the piezoelectric plate bender connected to a function generator (Tektronix AFG310), the AFM cantilevers can be oscillated at any frequency. The resonant frequency is determined when the maximum oscillation of the cantilever is observed under SEM, as shown in FIGURE B.5. The resonant frequencies of the cantilevers in vacuum from the shortest to the longest are 19.29 kHz, 14.64 kHz and 10.46 kHz, which is close to the nominal values of 20 kHz, 14 kHz and 10 kHz.
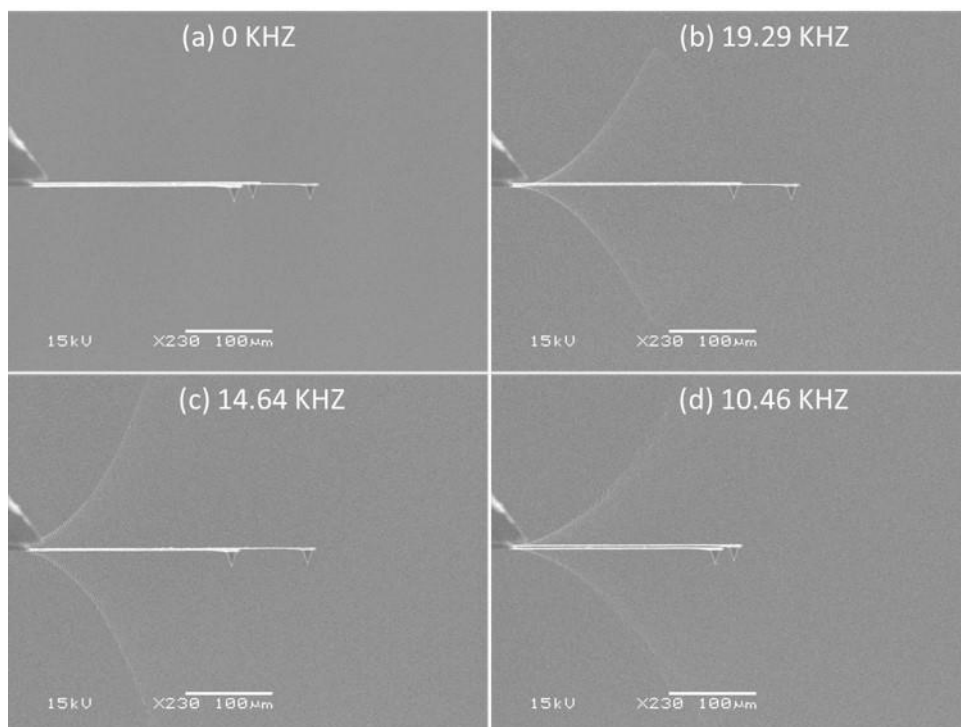
FIGURE B.5: SEM images of AFM cantilevers at their resonant frequencies (a) neither one at resonant mode; (b) the longest cantilever; (b) the medium one; (c) the shortest one at fundamental mode of resonance.

Based on these results, the spring constants of these three cantilevers are calibrated, and the differences with the nominal values provided by the manufacturer, are shown in TABLE B.1.

TABLE B.1: The nominal and calibrated data for CSC38/noAl.

AFM Cantilever	Shortest		Medium		Longest	
	Nominal	Calibrated	Nominal	Calibrated	Nominal	Calibrated
Length (μm)	250 ± 5	**239.6 ± 0.5**	300 ± 5	**289.8 ± 0.5**	350 ± 5	**340.9 ± 0.5**
Width (μm)	35 ± 3	**30.6 ± 0.3**	35 ± 3	**30.6 ± 0.3**	35 ± 3	**31.0 ± 0.3**
Thickness (μm)	1.0 ± 0.5	**1.0 ± 0.1**	1.0 ± 0.5	**1.0 ± 0.1**	1.0 ± 0.5	**1.0 ± 0.1**
Resonant Freq. (kHz)	14-28	**19.29 ± 0.05**	9.5-19	**14.64 ± 0.05**	7.0-14	**10.46 ± 0.05**
Spring Constant (N/m)	0.02-0.2	**0.059 ± 0.007**	0.01-0.1	**0.043 ± 0.005**	0.03-0.08	**0.027 ± 0.003**

APPENDIX C: DETAILED DATA ANALYSIS FOR IN SITU TESTS

C.1 Dimensional Analysis

The dimensional quantities of a nanowire are measured by image analysis software ImageJ, which helps count pixels of a distance on captured EM images. The followings are details about how to measure nanowire's overall length, effective length, overall diameter, core diameter, and amorphous layers.

C.1.1 Measuring Distance by Using ImageJ

When an image is opened in ImageJ, it is decomposed by $M \times N$ pixels. Each pixel point can be specified with coordinates of (X, Y) after the image is zoomed out to the maximum. To measure a real distance in the image, the amount of pixels covering the known scale bar must be determined first. A scale bar of known length (M) spans from the leftmost pixel of ($X1, Y$) to the rightmost pixel of ($X2, Y$), which means there are totally ($|X2-X1|+1$) pixels to represent this scale length. In other words, each pixel equals to M/($|X2-X1|+1$).

For an example of a SEM image with 12000X magnification (FIGURE C.1), the left red spot representing the leftmost pixel of 1 μm scale bar is (584,848), and right red one representing its rightmost pixel is (703,848). Therefore, there are 120 (i.e.703-584+1) pixels in total to represent the length of 1 μm, which is 8.3 nm for each pixel.

FIGURE C.1: The illustration to represent a scale bar by pixels.

C.1.2 Measuring the length of a nanowire

To measure a length between two points, the coordinates of two endpoints' pixels should be found. For example, there are (*X1,Y1*) and (*X2,Y2*) for these two points. Then the amount of pixels between these two points is $L = \sqrt{(|X2 - X1| + 1)^2 + (|Y2 - Y1| + 1)^2}$. Assuming it is *N* pixels to represent a scale of *M*, thus the length between these two points is *M×(L/N)*.

For an example of measuring overall length of a kinked nanowire (FIGURE C.2), the nanowire can be divided into two segments (AB and BC). The pixels at point A, B, and C are (163,731), (280,695) and (1919, 558), respectively. Therefore, the length of AB is $\sqrt{(280 - 163 + 1)^2 + (|695 - 731| + 1)^2}$ =123.66 pixels, and the length of BC is $\sqrt{(1919 - 280 + 1)^2 + (|558 - 695| + 1)^2}$ =1645.80 pixels. Then the overall length of the nanowire is AB+BC=123.66+1645.80 pixels = 1769.46 pixels. Since the scale bar of 2 μm equals to 359 pixels, the overall length is (1769.46/359)×2 μm ≈9.86 μm. The measurement error for this length measurement is expected to be 4 pixels (i.e. two pixels error for each end). Thus the error value is (4/359)×2 μm=0.02 μm. The overall length of this nanowire is 9.86 ± 0.02 μm.
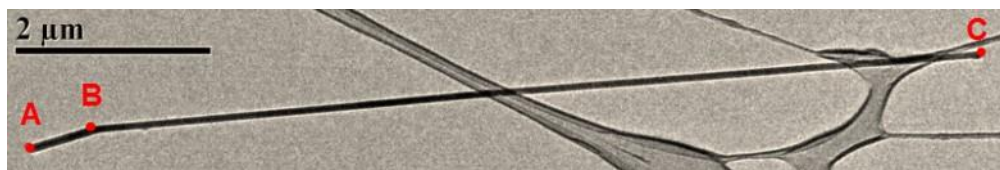

FIGURE C.2: The illustration of length measurement.

C.1.3 Measuring diameters of nanowires

The core and overall diameters of a nanowire are measured differently comparing with the approach of measuring its length. The diameter of a nanowire should

be perpendicular to nanowire's growth direction. So the angle θ (-90°< θ <90°) between its growth direction and the horizontal in the image should be found first. Then the measuring line spanning across the diameter should have an angle of $\pm(|\theta|$-90°) with the horizontal. The ImageJ helps measure distance of desired line when the angle between the line and the horizontal is given too. Therefore, three different diameter-lines starting from three spots at one edge of nanowire were measured as *X1*, *X2*, and *X3*. The diameter is defined as the average value of *X*, where *X=(X1+X2+X3)/3*. The estimated error is the largest difference value (i.e. max(|*X1-X*|, |*X2-X*|, |*X3-X*|)).

FIGURE C.3: The illustration of diameter measurement.

For example of measuring diameters based on a TEM image with 200K magnification (FIGURE C.3), the angle of nanowire's growth direction with the horizontal is approximately 27°. So the line to measure its diameter must have an angle of around -63° with the horizontal, shown as the white solid arrow line on the Figure 8.3. During the measurement of the core diameter, it was measured three times from three different spots. These values are in the form of pixels, as 1396, 1389, and 1392. The mean of these three values is 1392 pixels, with the error of 4 pixels. Since the pixel amount for this 10 nm scale bar is 308 pixels, the core diameter is 45.2 ± 0.1 nm. For

the overall diameter of this nanowire, it is difficult to measure it directly because the limitation of the image. So the overall diameter can be determined by summation of thicknesses of left and right amorphous layers and its core diameter. Via the same process, the thicknesses of amorphous layers on both side are measured. For the thickness of left amorphous layer, three values are obtained: 87, 83and 72 pixels. Then its mean value 81 pixels and the error 9 pixels lead to its thickness should be 2.6 ± 0.3 nm. Similarly, the thickness of right amorphous layer is found to be 2.5 ± 0.2 nm. Therefore, the overall diameter of the nanowire is 50.3 nm (i.e. 45.2+2.6+2.5 nm). For the error of the overall diameter, it is 0.4 nm determined by the following equation:

$$\nabla D = \sqrt{0.1^2 + 0.3^2 + 0.2^2} \, nm = 0.37 \, nm \approx 0.4 \, nm.$$

C.2 Analyzing Results from Resonance Vibrational Tests

For resonance vibration test, Young's modulus E of nanowire is determined by simple beam equation (12). From this equation, it is obvious indicated that the effective length L, the diameter of the nanowire D, and the resonance frequency f are required to determine the modulus of the tested nanowire.

C.2.1 Determining the Effective Length for Resonance Vibration Test

There are two prototypes to estimate the effective length: (a) tip-fixed case, and (b) tip-rotated case. The reason that we have two prototypes is because the tip can not be rotated at beginning. But since it is very essential to measure the effective length accurately, the testing stage was improved in order to have a tip rotation function. Such that the orientation of NW at any degree of observation can be determined. Nanowires attached on the tip are always misaligned, FIGURE C.4. When this NW is fixed on the tip, it has θ degree misalignment with Y direction, FIGURE C.4a. But is it parallel to the XY plane? Without a tip rotation function, it is very difficult to find out. There is one approach proposed to estimate the misalignment with Z direction is by compared the

overall lengths measured by SEM and TEM images, which will be discussed in following tip-fixed case. But with a tip rotation function, it is much easier to find out if the NW is parallel to the XY plane. By rotating the tip for 90 degree, the plane that we are viewing is the YZ plane, FIGURE C.4b. Now it is straightforward to find out there is a φ degree of misalignment between the NW with Z direction. Therefore, it is simpler and more accurate to determine the effective length for this tip-rotated case. There are some NWs tested before the tip rotation function was added. So the details about how to determine the effective length for both cases are discussed below.
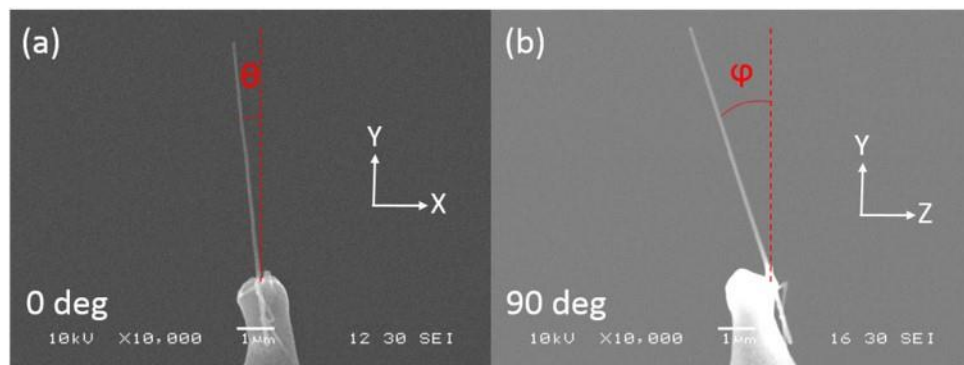
FIGURE C.4: SEM images show two orientations of a NW attached on a tip at 0 degree (a) and 90 degree (b).

(a) Tip-fixed Case

When the tungsten tip is fixed, the orientation of nanowire can only be known in two-dimensional (2D) plane. When a nanowire (red line) is not perfectly perpendicular to the electron beam (arrows), its true length (C) must be larger than the projected length (B), FIGURE C.5. Similarly, the projected effective length (A) must be smaller than the true effective length (X). To correct the value, a simple geometric model is applied, as shown in FIGURE C.5. The true effective length X can be calculated by $(A/B) \cdot C$. The

projected lengths of *A* and *B* can be measured on SEM images. The maximum measured length of the nanowire from TEM images is considered as its true length (*C*).
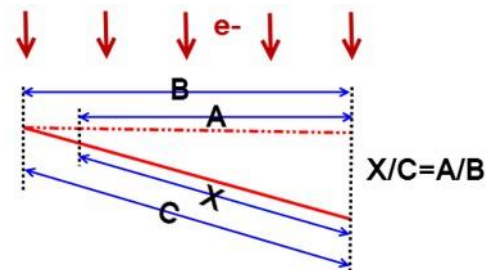

FIGURE C.5: The illustration of determining effective length (tip-fixed case).

For example, the maximum measured length of a nanowire on TEM images is 9.86 ± 0.02 μm, which is considered as its true length (*C*). The measured overall length (*B*) and effective length (*A*) on SEM images are 9.11 ± 0.03 μm and 8.33 ± 0.02 μm, respectively. Then the true effective length should be 9.02 ± 0.04 μm, where 9.02 μm is calculated by $(8.33/9.11) \times 9.86$ μm, and the error of 0.04 μm is determined by $\Delta X =$

$$X \times \sqrt{(\frac{\Delta A}{A})^2 + (\frac{\Delta B}{B})^2 + (\frac{\Delta C}{C})^2} = 9.02 \times \sqrt{(\frac{0.02}{8.33})^2 + (\frac{0.03}{9.11})^2 + (\frac{0.02}{9.86})^2}\text{μm} \approx 0.04\text{μm}.$$

(b) Tip-rotated Case

When the tip can be rotated, a nanowire attached on the tip can be rotated too, FIGURE C.6. Based on two SEM images captured from 0 and 90 degrees, two projected effective length *l0* and *l90* can be measured in the form pixel coordinates (*X0,Y0*) and (*X90, Y90*). During the rotation, the testing stage remained at the same height, so the tip's height changed because the tip was not aligned to the rotation axis. Then the NW was focused at different working distance for these two degrees. It is necessary to calibrate the length measurement at different working distance in SEM in order to obtain accurate effective length during the post-test data analysis. The calibration for different working distance was done by imaging a standard AFM grating sample in SEM. It was

found out from the calibration results that the length measurement for different working distance was inconsistent. So conversion factors were derived by dividing the measured length by the standard pitch length. So the true projected length *L0* and *L90* are calculated by *l0/a* and *l90/b*, where *a* and *b* are conversion factors for the working distances at 0 and 90 degrees, respectively. Then the angles of the nanowire with the vertical direction θ and φ at 0 and 90 degrees can be determined by *arctan(X0/Y0)* and *arctan(X90/Y90)*, respectively. Theoretically, the projections of a nanowire in Y axis at both 0 and 90 degrees are not changed, which means *L0*cos(θ)* should be equal to *L90*cos(φ)*. But in reality, due the existence of experimental errors, these two values will not be exactly same. So the average value (*L*) of *L0*cos(θ)* and *L90*cos(φ)* is used as the projection of nanowire in Y axis. The error ΔL for *L* is chosen from the larger difference value (i.e. $\Delta L = \max(|L- L0*cos(\theta)|, |L- L90*cos(\varphi)|)$). Thus the coordination of the nanowire in 3D space should be (*L*tanθ, L, L*tanφ*), which makes its true effective length *L_eff* calculated by

$$L_{eff} = \sqrt{(L * tan\theta)^2 + L^2 + (L * tan\varphi)^2} = L\sqrt{1 + tan^2\theta + tan^2\varphi}$$.   The

uncertainty of *L_eff* is $\Delta L\sqrt{1 + tan^2\theta + tan^2\varphi}$, if the errors of these two angles are not considered.
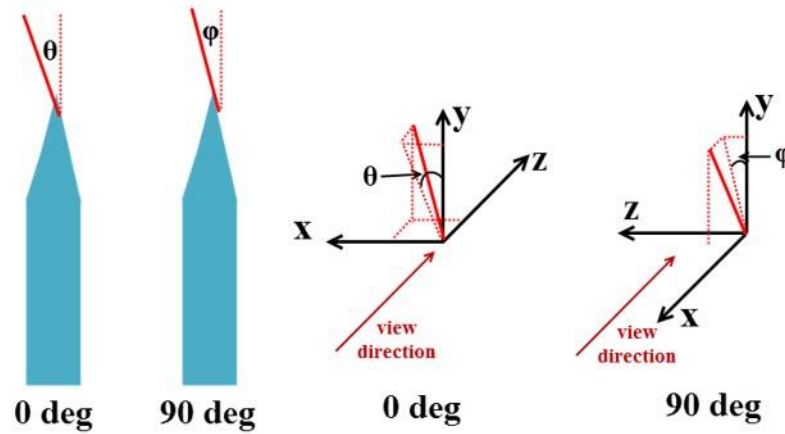
FIGURE C.6: The illustration of determining effective length (tip-rotated case).

For example of the results shown in FIGURE C.4, the measured effective length *l0* and the angle θ at 0 degree are 6.39 μm and 5.7°, respectively. For 90 degree, the measured effective length *l90* and the angle φ are 6.86 μm and 17.9°, respectively. Then the projected length *L* at Y axis is the average of 6.36 μm (i.e. 6.39 μm $\times$ cos(5.7°)) and 6.53 μm (i.e. 6.86 μm $\times$ cos(17.9°)), which is 6.45 μm. Then the estimation error of *L* is 0.9 μm (i.e. 6.45 μm − 6.36 μm). Therefore, according to the above equation, the true effective length *L*$_{eff}$ is calculated to be 6.81 μm (i.e. $L_{eff} = L\sqrt{1 + tan^2\theta + tan^2\varphi} =$ 6.45 $\mu m \times \sqrt{1 + tan^2(5.7°) + tan^2(17.9°)} = 6.81 \ \mu m$). Then the estimation error of *L*$_{eff}$ can be calculated to be 0.10 μm. So the true effective length used for further modulus calculation is 6.81 ± 0.10 μm. This is derived without considering the error resulted from the length measurement at different working distance. It has a large discrepancy in the result if this error is considered. For instance, on the FIGURE C.4, the working distances shown at 0 and 90 degrees are 12 mm and 16 mm, which gives the conversion factors of 1.025 and 1.053, respectively. Then the projected length *L* at Y axis is 6.19 μm, which is the average of 6.20 μm (i.e. (6.39 μm/1.025) $\times$ cos(5.7°)) and 6.19 μm (i.e. (6.86 μm/1.053) $\times$ cos(17.9°)). And the estimation error of *L* is 0.1 μm. With the same calculation, the true effective length is 6.53 ± 0.01 μm. In this example, about 4.3%

overestimation in the calculation of effective length, which eventually leads to about 17.2% overestimation of Young's modulus (i.e. $4 \times 4.3\%$). It is apparent that an accurate effective length is required to determine carefully.

C.2.2 Determining the Resonance Frequency

The resonance frequency is determined in the experiment by observing the vibration of the NW at its resonance under SEM. The NW is stationary until the frequency of applied AC signal is close to the resonant frequency of the NW. The sweep mode is changed to the manual mode when the rough range of the NW's resonant frequency is located. By manually increasing or decreasing the frequency stepwise, the maximum vibration of the NW is observed. Then this frequency is the resonant frequency of the NW. The relatively low resolution of real-time SEM and the vibration of the NW, make it more difficult to determine the maximum oscillation easily. The estimation error is considered as five steps here. For example, a resonant frequency of one NW is found at 1.0127 MHz, which means the minimum adjustable step is 0.0001 MHz. Then the estimation error is 0.0005 MHz. Therefore, the resonant frequency of the tested NW is 1.0127 ± 0.0005 MHz.

C.2.3 Calculating the Young's Modulus for Resonance Vibration Test

How to achieve needed parameters for determining the Young's modulus of a tested NW for resonance vibration test are discussed above. Then the Young's modulus can be calculated by the equation (12). These two values are considered as actual values without any uncertainties. Hence, the estimation error of the calculated Young's modulus should be $\Delta E = E \times \sqrt{(4\frac{\Delta L}{L})^2 + (2\frac{\Delta D}{D})^2 + (2\frac{\Delta f}{f})^2}$, where ΔL, ΔD, and Δf are the estimation errors of the effective length, diameter, and resonant frequency, respectively.

For instance, there is a tested NW with diameter of 50.0 ± 0.7 nm, the effective length of 9.02 ± 0.04 μm, and the fundamental resonant frequency of 1.0127 ± 0.0005 MHz. According to the above equation, the calculated Young's modulus is 347 GPa. So the estimation error of this calculated Young's modulus is 12 GPa (i.e. $\Delta E == 347 \times \sqrt{(4\frac{0.04}{9.02})^2 + (2\frac{0.7}{50.0})^2 + (2\frac{0.0005}{1.0127})^2} \approx 12$ GPa). As a result, the Young's modulus of this tested NW is 347 ± 12 GPa.

C.3 Analyzing Results from Buckling Tests

For buckling test, Young's modulus E of nanowire is determined by the equation: $E = \frac{16L^2}{\pi^3}\frac{P_{cr}}{D^4}$. So the effective length L, its diameter D and the critical buckling force P_{cr} should be found to calculate its modulus.

C.3.1 Determine the Effective Length L for Buckling Tests

The effective length of a tested NW for buckling test is different than that for resonance vibration test, because the NW is fixed at both ends for buckling test. So its effective length is the distance of its two fixed ends. Assuming that the pixel coordinates of these two fixed ends are *(X1,Y1)* and *(X2,Y2)* for these two points. Then the amount of pixels between these two points is $L = \sqrt{(|X2 - X1| + 1)^2 + (|Y2 - Y1| + 1)^2}$. Considering the uncertainty to find exact points for both fixed ends, if ΔL pixels estimation for each end was taken, then there are totally *2ΔL* pixels of measurement error for measuring the effective length. Sometimes, this estimation error ΔL may be relatively large, because EBID makes the clamp edges vague. If it is *N* pixels to represent a scale of *M*, thus the effective length between these two ends is *M×(L/N) ± M×(2ΔL/N)*.

For example, the effective length is the distance of point B and C at the zero-loading condition, shown in FIGURE C.7. In ImageJ, the pixel coordinates of B and C are found as (642,110) and (615,801), respectively. Then the pixels for BC is 693 (i.e.

$$\sqrt{(|615 - 642| + 1)^2 + (|801 - 110| + 1)^2} \approx 693).$$ If the uncertainty for each end is

considered as 5 pixels, then the measurement error is 10 pixels. Since the scale bar of 1

μm equals to 120 pixels, the overall length is 5.78 μm (i.e. (693/120) × 1 μm ≈ 5.78

μm). The measurement error for this length measurement is 0.08 μm (i.e. (10/120) × 2

μm ≈ 0.08 μm). Therefore, the effective length of this tested nanowire is 5.78 ± 0.08

μm.
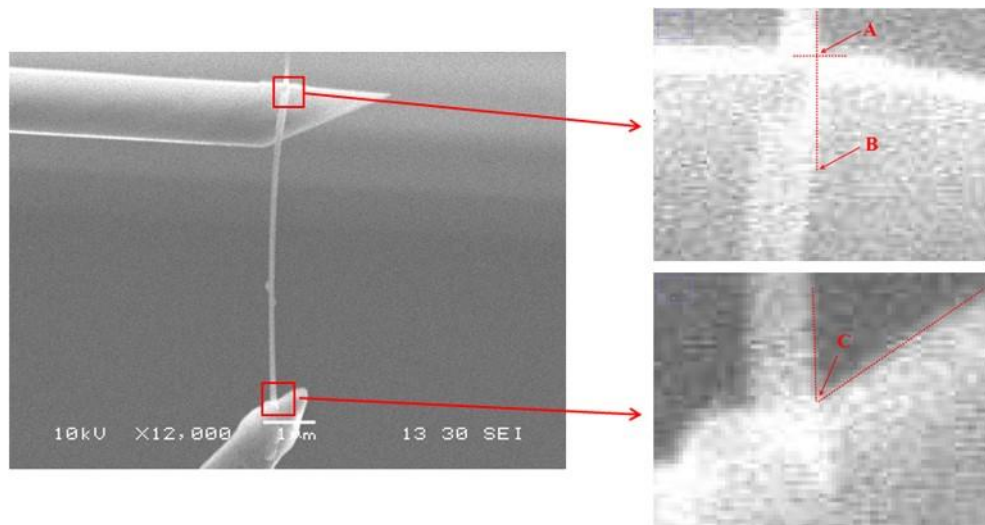
FIGURE C.7: The left image is original SEM image of buckling test at zero-loading; the right images are zoom-in images marked on the left.

C.3.2 Determining the Critical Buckling Force P_{cr}

To find the critical buckling force, the buckling point should be found first during

the compression of a nanowire. The point where buckling occurs can be found at the

bifurcation point on the correlation curve between applied force and the distance of two

fixed ends. The applied force is measured by observing the deflection of an AFM

cantilever with calibrated force constant. The distance of two fixed ends can be directly

determined, but the uncertainly is relatively larger because it is hard to find the exact

clamped points. Since the change of the distance of these two fixed ends during buckling

test is same with the change of the distance of any two points on two tips, the correlation

of applied force and distance of two fixed ends can be replaced by that of applied force and the distance between two tips.

C.3.3 Determining Applied Force

The force constant (i.e. stiffness or spring constant) of the cantilever is needed to be well calibrated, so that the applied force can be accurately calculated. The force constant of AFM cantilever can be calibrated by $k = M_e \rho_c bhL\omega_{vac}^2$, where k, ρ_c, h, b and L are the spring constant, density, thickness, width and length of the cantilever, respectively, and ω_{vac} is the fundamental radial resonant frequency of the cantilever in vacuum ($\omega_{vac} = 2\pi f_{vac}$, where f_{vac} is the fundamental resonant frequency), and M_e is the normalized effective mass which is 0.2427 if $L/b > 5$. Then the uncertainty of its spring constant is $\Delta k = k \times \sqrt{(\frac{\Delta b}{b})^2 + (\frac{\Delta h}{h})^2 + (\frac{\Delta L}{L})^2 + (2\frac{\Delta \omega}{\omega})^2}$. The dimensions of a cantilever are measured on SEM images too.

After the deflection of cantilever (d_i) at each moment ($t=i$) is determined, the applied force at each moment is calculated by $P_i = k \times d_i$. And its error at each moment is

$$\Delta P_i = P_i \times \sqrt{(\frac{\Delta k}{k})^2 + (\frac{\Delta d}{d})^2}.$$

For example of buckling test on a NW, the applied forces and their errors are present in TABLE C.1. In the table, L denotes the distance between two cantilevers, and its measurement error is estimated to be $\Delta L = (5/120) \times 1\mu m \approx 40$ nm, where 5 pixels are taken as the estimation error, and 120 pixels represent the scale bar of 1μm. The deflection of cantilever at each moment is $d_i = L_i - L_0$, and its error is $\Delta d = \sqrt{2(\Delta L)^2} \approx 60$ nm. The applied force at each moment is $P_i = k \times d_i$, where the spring constant of cantilever k is calibrated to be 0.118 N/m, with error of 0.004 N/m. Then the estimation error of applied force ΔP_i can be calculated based on the equation above.

TABLE C.1: The data for determining the applied force and its error at each moment.

test #	L (nm)	d (nm)	P (nN)	ΔP (nN)	k (N/m)	ΔL (nm)
0	1830	0	0	0	0.118	40
1	1950	120	14	7		
2	2120	290	34	7	Δk (N/m)	Δd (nm)
3	2310	480	57	7	0.004	60
4	2630	800	94	8		
5	2940	1110	131	8		
6	3030	1200	142	9		
7	3130	1300	153	9		
8	3180	1350	159	9		
9	3220	1390	164	9		
10	3250	1420	168	9		
11	3260	1430	169	9		
12	3240	1410	166	9		

C.3.4 Determining the Distance between Two Tips

The distance between two tips can be considered as the distance from any point at one tip to any point on another tip. These two points are two reference points, and they should be almost vertically aligned. For example in Figure 4.8, the point A and C are selected as two reference points, because they are both intersection points of nanowire with tips, which are easy to be located. The similar process for determining the effective length is used to determining the distance of AC. Since A and C points are more definitive, so 2 pixels estimation error is considered as measurement error.

For example, the distances between two tips at each moment are present in TABLE C.2. The pixel coordinates of point A (Xa, Ya) and C (Xc, Yc) are found out in

ImageJ. The coordination represent the line segment AC is determined as ($|Xc\text{-}Xa|$+1,

$|Yc\text{-}Ya|$+1). Since the scale bar of 1 μm has 120 pixels for all these SEM images captured

at the same magnification, the distance between two tips is $L =$

$\left[(\sqrt{(|Xc - Xa| + 1)^2 + (|Yc - Ya| + 1)^2})/120\right] \times 1\,\mu m$. The change of two tips'

distance dL_i at each moment (t=i) is calculated by $L_0\text{-}L_i$. Two pixels estimation error is

considered as measurement uncertainty, so the error of two tips' distance is $\Delta L = (2/120)$

$\times$ 1μm $\approx$ 0.02 μm. Then the error of the change of two tips' distance is $\Delta(dL) = \sqrt{2(\Delta L)^2}$

$\approx$ 0.03 μm.

TABLE C.2: The data for determining the distance between two tips and its error at
each moment.

test #	Point A	Point C	AC	L (μm)	dL=L0-L(μm)	ΔL (μm)
0	(642, 71)	(615, 801)	(28, 731)	6.10	0.00	0.02
1	(645, 72)	(613, 801)	(33, 730)	6.09	0.01	
2	(646, 73)	(611, 801)	(35, 729)	6.08	0.01	Δ(dL) (μm)
3	(646, 74)	(608, 801)	(40, 728)	6.08	0.02	0.03
4	(650, 73)	(604, 799)	(47, 727)	6.07	0.03	
5	(653, 77)	(604, 796)	(50, 720)	6.01	0.08	
6	(653, 84)	(602, 794)	(52, 711)	5.94	0.16	
7	(654, 95)	(602, 792)	(53, 698)	5.83	0.26	
8	(653, 106)	(600, 790)	(54, 685)	5.73	0.37	
9	(655, 114)	(598, 788)	(58, 675)	5.65	0.45	
10	(655, 125)	(597, 788)	(59, 664)	5.56	0.54	
11	(655, 137)	(595, 788)	(61, 652)	5.46	0.64	
12	(655, 147)	(594, 788)	(62, 642)	5.37	0.72	

Therefore, the correlation data between the applied load and the change of two

tips' distance is present in TABLE C.3. And the corresponding correlation curve is

illustrated in FIGURE C.8. Based on this correlation curve, the bifurcation point is found

and considered as critical buckling moment. The applied force at this moment is

commonly called critical buckling force. In this test, the critical buckling force is $P_{cr} \approx$

131 ± 8 nN.

TABLE C.3: The applied force and the change of two tips' distance, and their errors at each moment.

| test #	P (nN)	ΔP (nN)	dL=L0-L(μm)	Δ(dL) (μm)
0	0	0	0.00	0.02
1	14	7	0.01	
2	34	7	0.01	
3	57	7	0.02	
4	94	8	0.03	
5	131	8	0.08	
6	142	9	0.16	
7	153	9	0.26	
8	159	9	0.37	
9	164	9	0.45	
10	168	9	0.54	
11	169	9	0.64	
12	166	9	0.72	
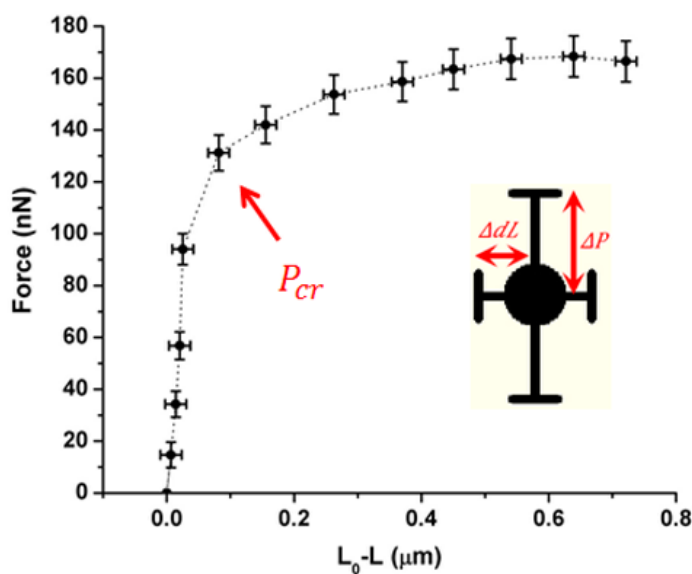
FIGURE C.8: The correlation curve of applied force and the change of two tips' distance.

C.3.5 Calculating Young's Modulus of Nanowire for Buckling Test

The effective length of the tested nanowire is $L \pm \Delta L$. The overall diameter of nanowire is $D \pm \Delta D$. The critical buckling force is $P_{cr} \pm \Delta P_{cr}$. So the Young's modulus

of this nanowire is calculated by $E = \frac{16L^2}{\pi^3} \frac{P_{cr}}{D^4}$, with uncertainty of $\Delta E = E \times$

$\sqrt{(2\frac{\Delta L}{L})^2 + (4\frac{\Delta D}{D})^2 + (\frac{\Delta P_{cr}}{P_{cr}})^2}$.

For example of this tested nanowire, the effective length is 5.77 ± 0.08 µm, its overall diameter is 50.0 ± 0.7 nm, and the critical buckling force is 131 ± 8 nN. Then the Young's modulus is calculated to be 360 ± 31 GPa.

It is worthy to note that the uncertainty of the distance between two tips was not included into the final calculation of Young's modulus. Thus, it is acceptable that this uncertainty is not determined for the data analysis of buckling tests, which makes the post-test data analysis more straightforward and efficient.

C.4 Analyzing Results from Tensile Tests

The mechanical properties are extrapolated from the relationship of the stress and the strain for the tensile tests. According to the definitions of the stress and strain, the axial load, the cross sectional area of NW, the effective length of a tested NW, and its elongation should be measured to achieve the stress versus strain correlation. Since it is extremely difficult to measure the instantaneous cross sectional area after the NW is stretched, the engineering stress and strain are used to extract mechanical properties for tested NWs.

The axial tensile load is determined by multiplying the deflection of the cantilever with its calibrated spring constant. This process is as same as that used for determining buckling force that is discussed above. The diameter of NW is used to calculate its cross sectional area when the cross section of NW is considered as circular. The effective length is the distance between two EBID clamps. Two pixels are defined as the positions of these two clamps. Then the distance between the two pixels is the effective length. The uncertainty of the effective length is determined by the estimation

error originated from uncertain edges of EBID clamps. The elongation of the effective length is measured by its increment after it is extended. Because the two ends of the effective length is fixed on two tips, the change of the effective length should be equal to the change of the distance between two tips.

For example a NW experienced tensile test, the experimental data and results are present in TABLE C.4. The diameter and effective length of the tested NW are 73.4 ± 0.7 nm and 8.18 ± 0.02 µm, respectively. The strain and stress are calculated based on the definitions. The uncertainty of strain is calculated by the equation of $\Delta\varepsilon = \varepsilon \times \sqrt{(\frac{\Delta(L-L_0)}{L-L_0})^2 + (\frac{\Delta L_0}{L_0})^2}$, where L_0 and L are the effective length between two clamps at unloaded and loaded moments, respectively; and Δ is the uncertainty of measurement for different terms.

TABLE C.4: Experimental results of tensile test on a NW.

Steps	Strain	Force (µN)	Stress (GPa)
0	0	0	0
1	0.003 ± 0.002	2.52 ± 1.06	0.60 ± 0.25
2	0.005 ± 0.002	6.72 ± 1.06	1.59 ± 0.25
3	0.006 ± 0.002	9.24 ± 1.06	2.18 ± 0.25
4	0.008 ± 0.002	13.94 ± 1.07	3.30 ± 0.26
5	0.009 ± 0.002	16.46 ± 1.08	3.89 ± 0.26
6	0.011 ± 0.002	21.17 ± 1.09	5.00 ± 0.27
7	0.014 ± 0.002	26.70 ± 1.11	6.31 ± 0.29
8	0.017 ± 0.002	29.40 ± 1.12	6.95 ± 0.29
9	0.018 ± 0.002	33.43 ± 1.13	7.90 ± 0.31
10	0.020 ± 0.002	37.13 ± 1.15	8.78 ± 0.32
11	0.023 ± 0.002	42.67 ± 1.17	10.09 ± 0.34
12	0.026 ± 0.002	47.21 ± 1.20	11.16 ± 0.35
13	0.029 ± 0.002	50.90 ± 1.22	12.03 ± 0.37
14	0.031 ± 0.002	56.11 ± 1.25	13.27 ± 0.39
15	0.033 ± 0.002	61.15 ± 1.29	14.46 ± 0.41

The achieved stress and strain values at each step are plotted in FIGURE C.9. The data are then linear fitted, as present by the red dash line on the graph. The fitting

line should intercept with the origin point. The slope of the fitting line is the Young's

modulus of the tested NW, and the uncertainty of the slope is used as the uncertainty of

its Young's modulus. For this example, the linear fitting equation is $y = 431x$. The

uncertainty of the slope is about 4. Therefore, the Young's modulus of this tested NW

is 431 ± 4 GPa. Furthermore, the last data point represents the fracture moment. So the

fracture strength is around 14 GPa, with the maximum strain around 3.3%.
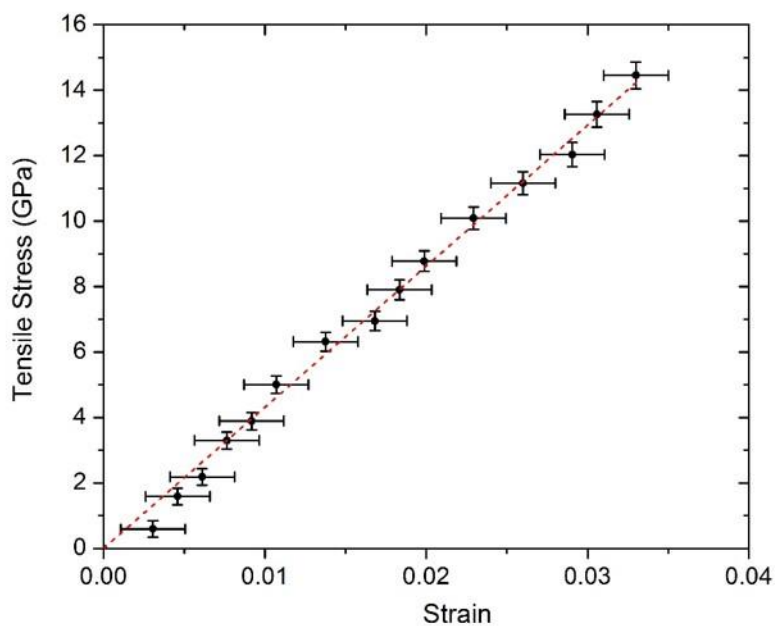
FIGURE C.9: The stress-strain relationship a B4C NW under tension.

APPENDIX D: FEM OF RESONANCE VIBRATION TESTS

There are many effects that will influence the experimental results, such as weak clamp, non-uniformity of NW, amorphous outer layer on NW, additional mass, etc. Some effects can be corrected mathematically, while some effects are not. Therefore, numerical modeling can be employed to correct the experimental results and explain some interesting phenomena in the experimental results. The numerical modeling method used for this study is finite element modeling (FEM) with a commercial software Abaqus 6.11.

To produce reliable results from FEM, reasonable models for NWs and correct boundary and contact conditions should be created in the software. Therefore, mesh convergence study is conducted to verify the rationality of models and to find optimal meshing conditions.

D.1 Mesh Convergence Study

The nanowire to be modeled: Radius $R=25$ nm; length $L=9.02$ μm; density $\rho=2.5 \times 10^3$ kg/m^3; experimental resonant frequency $f=1.0127$ MHz.

According to simple beam theory, the nth mode resonance frequency f_n for a cantilevered uniform beam is calculated by equation $f_n = \dfrac{\beta_n^2}{2\pi}\sqrt{\dfrac{E_b I}{mL^4}}$, where, E_b is the bending modulus of the beam, I is the second moment of area, m is the mass per unit length, and L is the beam length. The β_n is the eigenvalue of the characteristic equation: $\cos\beta_n \cosh\beta_n + 1 = 0$, which determines $\beta_0=1.875$, $\beta_1=4.694$, $\beta_2=7.855$ and $\beta_3=1.099.6$ correspond to the first four modes of resonance frequency.

Based on above equation, the bending modulus (Young's modulus) of the nanowire is calculated to be around 350 GPa. This is the value we used in FEM.

D.1.1 Mesh Convergence Study Using Beam Elements in ABAQUS:

The beam element is first chosen for the study is because a beam is similar with an uniform NW. For a beam model, the cross section is considered as one unit, but its length can be meshed into infinitesimal elements. If the elements are not small enough, the modeling results will be inaccurate. However, the number of elements is increased if the element size is reduced, then it takes more time to run the model. Therefore, it is necessary to start with mesh convergence study.

The detailed modelling steps of this study are described:

1. Sketch a wire with length of 9020;

2. Input materials property with density of 2500, Young's modulus of 350E9, and Poisson ratio of 0.2;

3. Define the section as a beam with circular cross section, with the radius of 25;

4. Assign the section and define the beam orientation;

5. Create it as an independent instance;

6. Set a boundary condition (Encastre) on one end, and apply a concentrated force of 10 in another end, as shown in the following image (FIGURE D.1);

7. Mesh the beam from 10 elements to100 elements with the increment of 10 elements, and mesh the beam from 100 to 200 elements with the increment of 50 elements;

8. Create a job and submit it (Totally 12 jobs with different number of elements);

9. View and report the results (FIGURE D.2);

10. Collect the data and plot them as a curve (FIGURE D.3).

FIGURE D.1: The beam with boundary condition and a concentrated load.

FIGURE D.2: Result of a beam bending under this load (10 elements).
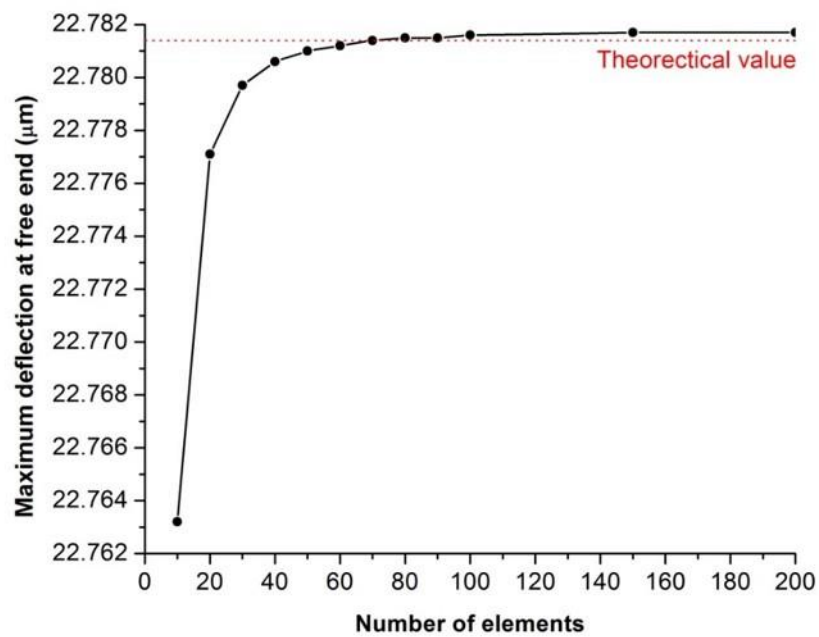
FIGURE D.3: The resultant curve of the free end node displacement versus number of elements

For the lateral bending, the lateral displacement y is calculated based on Euler

Bernoulli beam theory by the equation $y = \dfrac{PL^3}{3EI}$, where, P is the applied load, L is the

length from the fixed end to the point where the lateral force is applied, y is the lateral

displacement perpendicular to nanostructure, and I is the second moment of area of nanostructure ($I = \pi R^4 \big/ 4$ for nanowire, where R is the radius of nanowire). Based on this equation, when 10 N is applied to the free end of this nanowire, the lateral displacement at the free end is calculated to be 22.78141 μm, which is consistent with the FEA results. Therefore, it indicates that this model is correct.

Then, this model is used to extract the natural frequencies and eigenvalues, and also to study the mesh convergence. The frequency extracted from this modeling is very close to the experimental value. The eigenvalue provided by Abaqus is not the classical eigenvalue in simple beam theory, but a value related to the frequency by the following relationship: Value = (frequency×2×π)^2, which is just the square of circular frequency ω. This value can be used as eigenvalue is based on the eigenvalue equation for free vibration of beam theory $\beta = (\frac{\mu \omega^2}{EI})^{1/4}$, where β is the classical eigenvalue, μ is the mass per unit length, E is the Young's modulus, and I is the second moment of area. Once the model is built, all these parameters μ, E, and I are fixed, so the above equation becomes $\beta = (a \cdot \omega^2)^{1/4}$, where a is a constant. So the eigenvalue can be simply present as the square of circular frequency ω^2 in Abaqus.

A method called linear perturbation step is used to extract the resonance frequencies. The beam is meshed from 10 to 80 elements to do the mesh convergence study. The results are present in the following graph (FIGURE D.4).
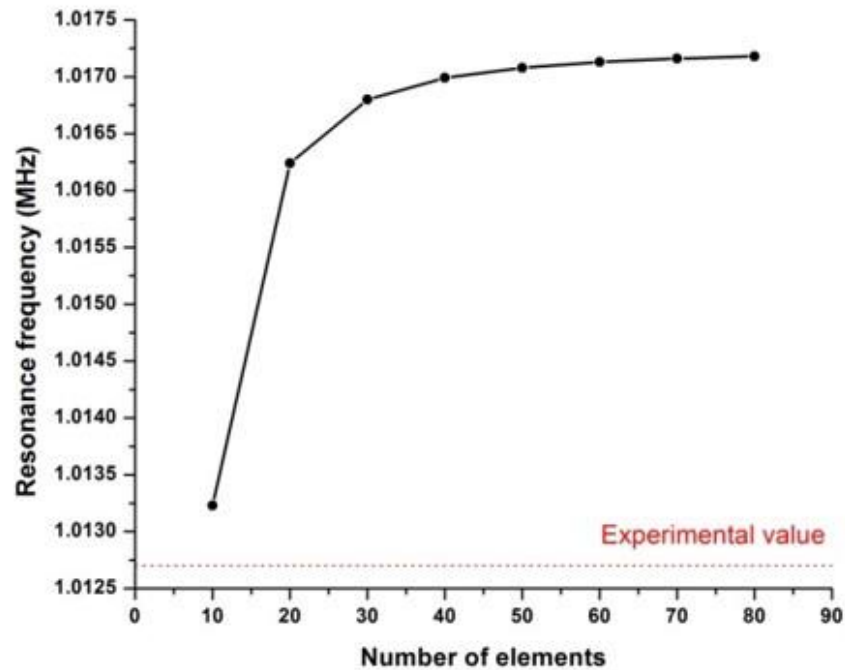
FIGURE D.4: The resultant curve of resonance frequency versus number of elements.

From the above figure, we find out the numerical modeling results are larger than the experimental value, and converge toward to the opposite way. So there should be sometime wrong with it. I double checked the input parameters, and realized that I simply estimated the Young's modulus as 350 GPa, instead of 347 GP that is exactly calculated from the simple beam theory equation. Hence, the Young's modulus of 347E9 was used to replace 350 GPa in this model. Then we achieved the more consistent results, as shown in FIGURE D.5.
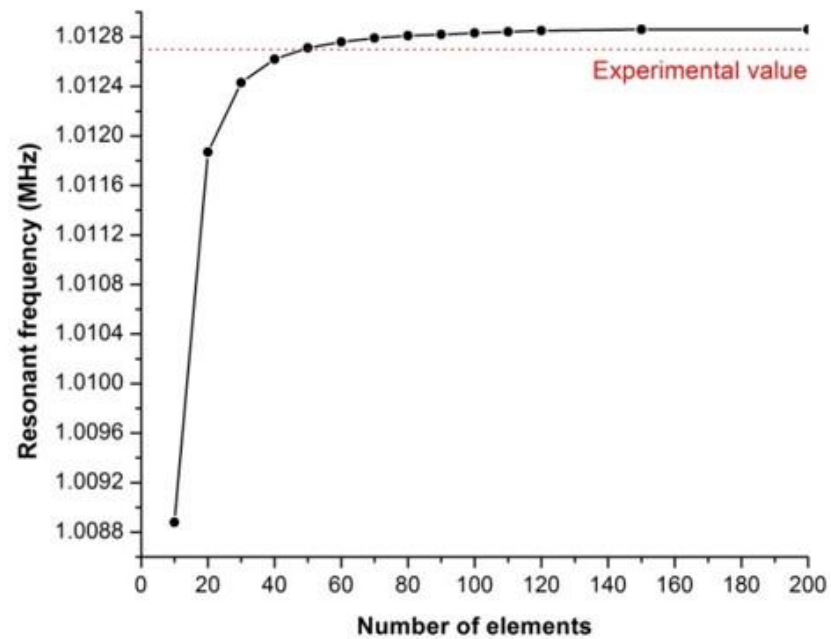
FIGURE D.5: The curve of resonance frequency versus number of elements.

From the result, we see the frequency is sensitive to the Young's modulus input value, so the sensitivity analysis was studied. The beam was modeled with 200 elements. The Young's modulus input value was increased from 346.5 GPa to 347.5 Gpa with increment of 0.1 GPa. The sensitivity analysis result is present in FIGURE D.6. In small range of Young's modulus, the resonant frequency is linearly increased as increasing the Young's modulus.
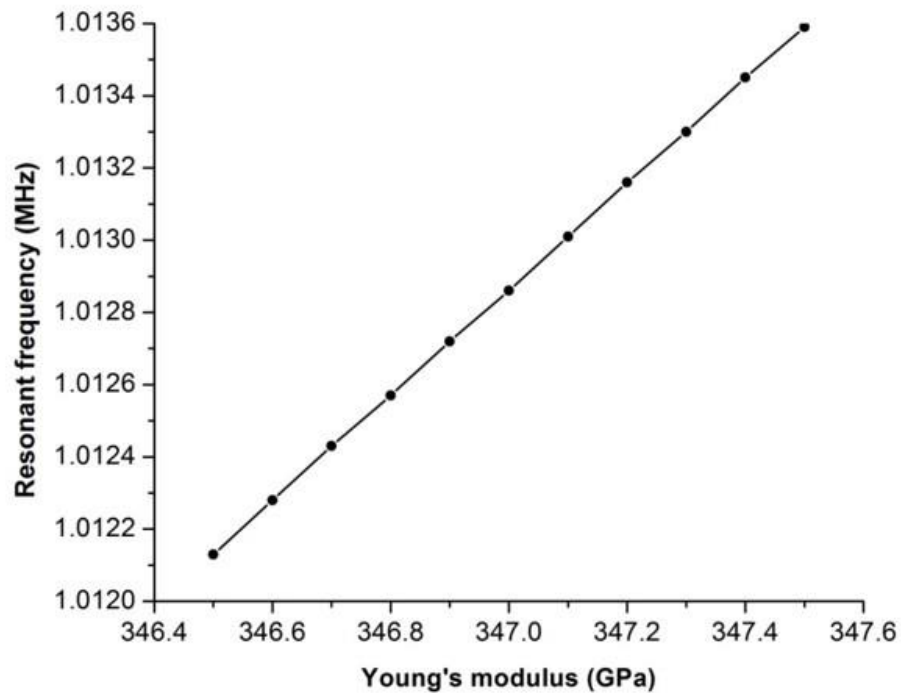
FIGURE D.6: The result of sensitivity analysis study.

D.1.2 Mesh Convergence Study Using Solid Elements in ABAQUS

The mesh convergence study on beam elements shows that FEA can be used as an effective tool to verify or correct the experimental results. The main purpose of using FEA in this study is to explain some unexpected results and make a necessary corrections. There are many effects found in the experiments, such as irregular shapes of NWs, non-uniform amorphous layers formed on NWs, and etc. Therefore, instead of beam elements, solid elements should be used in Abaqus for this study because they are more flexible to model irregular shapes. To determine the optimal conditions to mesh the solid elements, the mesh convergence studies both on cross-section and length are conducted at the beginning.

D.1.2.1 Mesh Convergence Study on Cross Section

The modelling steps for this study are described:

1. Create a cylinder with length of 9020, and radius of 25; Create a line along the length;

2. Input materials property with density of 2500, Young's modulus of 350E9, and Poisson ratio of 0.2;

3. Create and assign the section;

4. Create it as an independent instance;

5. Set a boundary condition (Encastre) on one end surface, and apply a concentrated force of 10 at another end point, as shown in the following image (FIGURE D.7);

6. Fix the seed number of 100 for length, and then seed the circular edge of cross-section from 5 to 30, which makes the number of elements in cross-section increase from 3 to 100, FIGURE D.8;

7. Create a job and submit it (Totally 12 jobs with different number of elements);

8. View and report the results;

9. Collect the data and plot them as a curve (FIGURE D.9);

In addition, the resonant frequency was studied too. In order to compare the experimental result, the Young's modulus was changed to 347E9. The results are present in FIGURE D.10.

FIGURE D.7: The solid wire with a boundary condition and a concentrated force.
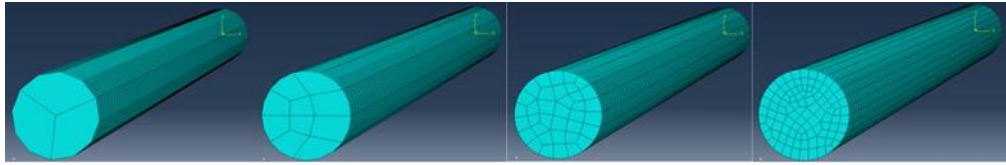
FIGURE D.8: Increase elements in cross-section when the element in length is fixed.
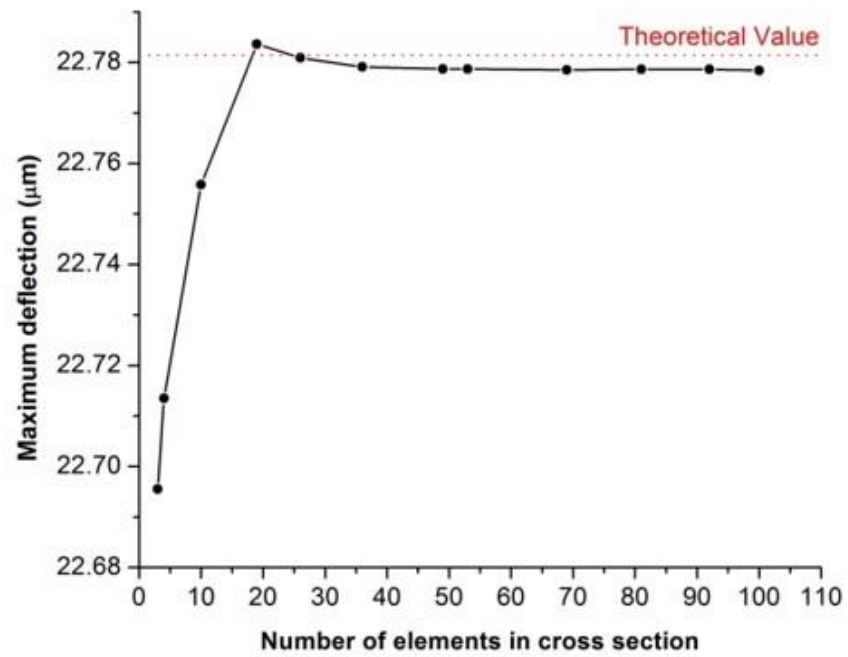
FIGURE D.9: The resultant curve of maximum deflection versus number of elements in cross-section.
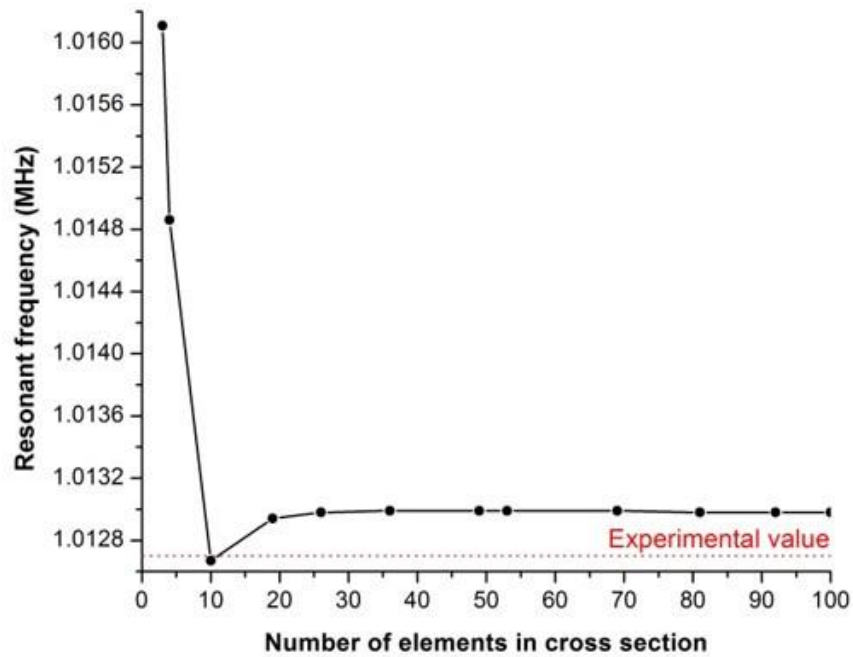
FIGURE D.10: The resultant curve of resonant frequency versus number of elements in cross-section.

D.1.2.2 Mesh Convergence Study on Length

The modelling steps for this part are descripted:

1. Create a cylinder with length of 9020, and radius of 25; Create a line along the length;

2. Input materials property with density of 2500, Young's modulus of 350E9, and Poisson ratio of 0.2;

3. Create and assign the section;

4. Create it as an independent instance;

5. Set a boundary condition (Encastre) on one end surface, and apply a concentrated force of 10 at another end point, as shown in the following image;

6. Fix the element number of 36 for cross-section (seed edge number 18), and then mesh length number from 10 to 400, FIGURE D.11;

7. Create a job and submit it (Totally 12 jobs with different number of elements);

8. View and report the results;

9. Collect the data and plot them as a curve (FIGURE D.12);

The convergence of resonant frequency was studied too, and its results are shown in FIGURE D.13.
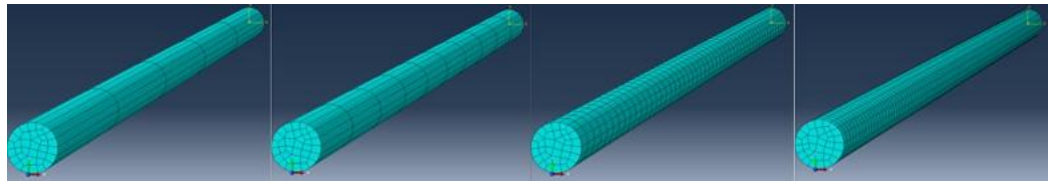
FIGURE D.11: Increase elements in length when the number of elements in cross-section is fixed.
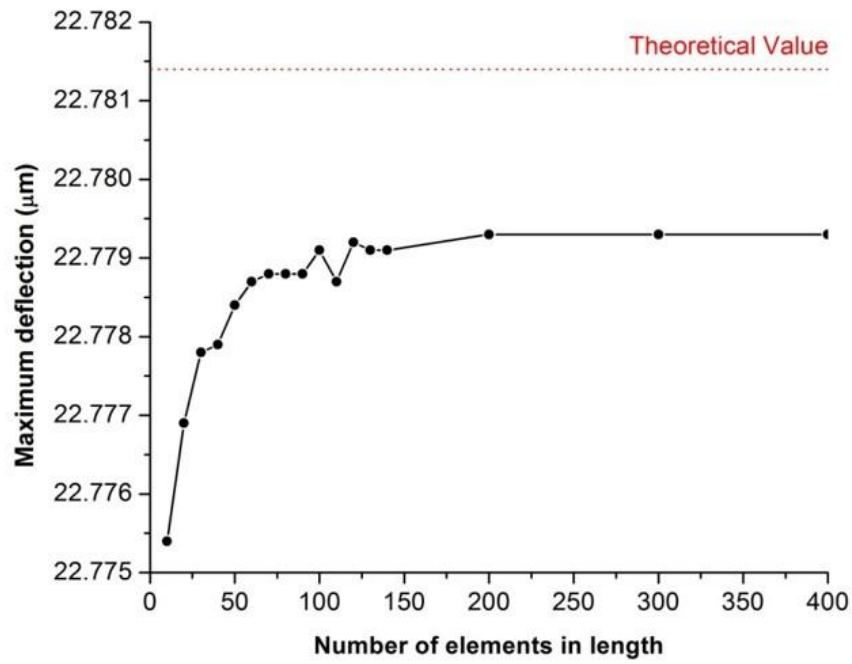
FIGURE D.12: The resultant curve of maximum deflection versus number of elements in length.
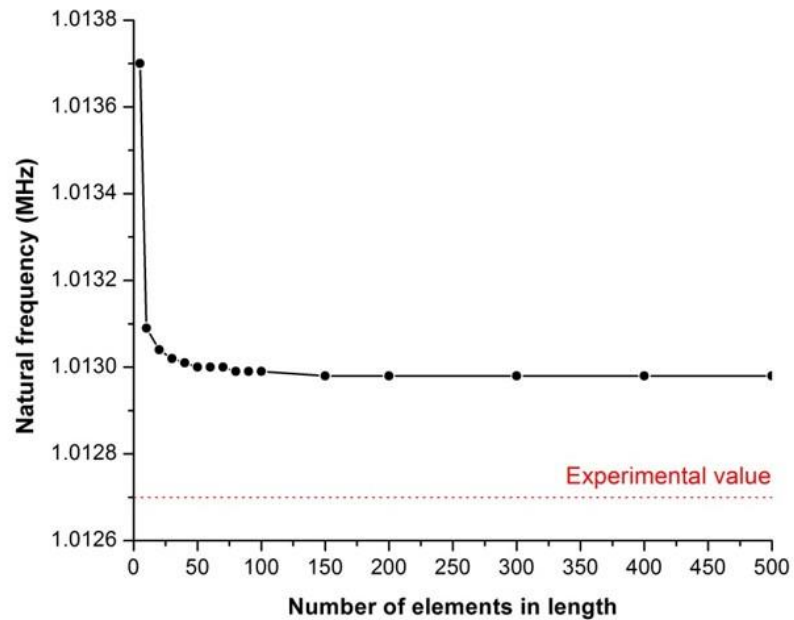

FIGURE D.13: The resultant curve of resonant frequency versus number of elements in length.

D.2 Summary

Based on the results of these convergence studies, the elements for cross-section should be more than 36, which means the seed edge number for the circular edge is 18. And the elements for length should be more than 200. Moreover, the results, that the curves do not converge to the theoretical value, show that solid elements are a little stiffer than beam elements. For an example of solid elements, if we use 346.8 GPa instead of 347 GPa, then the curves can converge to the theoretical value.

However, since our objective is to estimate the effects of some factors, such as amorphous shell, tapered structure, and extra mass attached on nanowire, it should be okay to use solid elements to model nanowires. In addition, if we have 100 elements in cross-section and 200 elements in length, then there are 20000 elements in total. The element we used was quadratic brick (C3D20R). Then, we have 89731 nodes, which are not reaching the limitation of 100000 nodes. So we can simply use the academic teaching version of Abaqus under Mosaic account to do the work, instead of running the jobs under Cluster account.